

Boria Effects on the High Temperature Oxidation of Silicon Carbide

A Dissertation

Presented to
the faculty of the School of Engineering and Applied Science
University of Virginia

in partial fulfillment
of the requirements for the degree

Doctor of Philosophy

by

Bohuslava McFarland

May

2017

APPROVAL SHEET

The dissertation
is submitted in partial fulfillment of the requirements
for the degree of
Doctor of Philosophy



AUTHOR

The dissertation has been read and approved by the examining committee:

Elizabeth Opila, Advisor

Advisor

Dean Pamela Norris

Professor Petra Reinke

Professor William Soffa

Professor Peter Kroll

Accepted for the School of Engineering and Applied Science:



Craig H. Benson, Dean, School of Engineering and Applied Science

May
2017

Acknowledgements

This work was sponsored in part by Roll-Royce, funding source award number 5003063802/15UVA18. I would like to thank the project manager from Roll-Royce, Dr. Adam Chamberlain. This work was also sponsored in part by the Technical Corrosion Collaboration, contract # FA7000-10-2-0011, FA7000-12-2-0017. I would like to thank Mr. Adam Goff at Luna Innovations, Charlottesville, VA for providing me access to their FTIR. I would like to express my deepest gratitude to my advisor, Prof. Elizabeth Opila, for her full support and unwavering commitment in helping me excel and for providing me the opportunity to work on a very fun research project. I am also thankful for having had the opportunity to work with an exceptional undergraduate student, Madeline Morales, who helped out with characterization. I am deeply indebted to my family. Without their support I would not have gotten this far. I thank my parents, Bohuslav and Maria Bacik, my husband Erin, and my sweet little bird, Wren.

Table of Contents

Abstract.....	21
1 Aim of the research project.....	24
1.1 Objectives.....	24
1.2 Brief description of tasks.....	25
1.2.1 Task 1: Boron nitride effects on the high temperature oxidation of silicon carbide fibers	25
1.2.2 Task 2: Role of boron concentration and pressure on the oxidation kinetics of reaction-bonded silicon carbide.....	25
1.2.3 Task 3: Optimization of sol-gel synthesis parameters for the application of sol-gel derived borosilicate glass coatings on silicon carbide substrates	25
1.2.4 Task 4: High temperature stability of the sol-gel derived borosilicate glasses	26
1.2.5 Task 5: Effects of sol-gel derived borosilicate glasses on SiC oxidation	26
2 Introduction.....	27
2.1 CMC oxidation reactions.....	27
2.2 Motivation of this research project.....	28
2.3 Oxidation studies on CMC components.....	29
2.3.1 Background on SiC and BN oxidation kinetics	30
2.3.2 Oxidation studies on SiC fibers	35
2.3.3 Boron effects on matrix oxidation	40
2.3.4 Accelerated oxidation of Si-based systems due to the presence of boron	40
2.4 Background on borosilicate glass.....	41
2.4.1 Structures of binary borosilicate glass building blocks	41
2.4.2 Borosilicate glass: Binary SiO ₂ -B ₂ O ₃ phase diagram.....	44
2.4.3 Borosilicate glass viscosity	45
2.5 Challenges faced in elucidating the effects of a borosilicate thermally grown oxide on SiC oxidation kinetics	47
2.5.1 Compositional dependence of borosilicate glass properties	47
2.6 Summary of gaps in the present knowledge of the borosilicate thermally grown oxide and methodologies undertaken in this research project to resolve them.....	49
2.6.1 Modeling the borosilicate thermally grown effects on SiC oxidation with sol-gel derived borosilicate glass coatings	50

2.6.2	Previous oxidation study on Si substrates coated with sol-gel derived borosilicate glass layers ⁴¹	51
3	Experimental procedure	56
3.1	Silicon-based materials.....	56
3.1.1	Silicon carbide fibers	56
3.1.2	Reaction-bonded silicon carbide coupons	57
3.1.3	High purity silicon carbide coupons for sol-gel coating experiments	58
3.1.4	High purity silicon coupons for sol-gel coating experiments	58
3.1.5	Preparation procedures conducted prior to coating application or oxidation	59
3.2	Sol-gel procedure for silica and borosilicate coatings and glasses	59
3.2.1	Detailed synthesis procedure	60
3.3	Substrate coating techniques	62
3.3.1	Pre-oxidation conditions conducted on CVD-SiC coupons.....	63
3.3.2	Freestanding glass casting and drying procedures.....	63
3.4	High temperature oxidation procedures	65
3.4.1	Gel-to-glass conversion analysis.....	67
3.4.2	Oxidation exposures.....	67
3.4.3	Freestanding glass high temperature instability studies.....	68
3.5	Characterization techniques.....	68
3.5.1	Scanning Electron Microscopy (SEM)	68
3.5.2	X-Ray Diffraction (XRD)	70
3.5.3	Fourier Transform Infrared spectroscopy	71
3.5.4	Raman spectroscopy	71
3.5.5	Combustion Infrared (IR) Spectrometry	72
3.5.6	Inductively Coupled Plasma – Optical Emission Spectrometry	72
3.5.7	X-ray Photoelectron Spectroscopy (XPS)	75
3.5.8	FactSage thermochemical software	75
3.5.9	Image J software for image processing and analysis	75
4	Task 1: Boron nitride effects on the high temperature oxidation of silicon carbide fibers	76
4.1	Objectives of Task 1	77
4.2	Experimental re-cap.....	77

4.3	Results	79
4.3.1	Characterization of fibers prior to oxidation.....	79
4.3.2	Oxidation results	81
4.4	Discussion	98
4.4.1	Effects of the oxide boron concentration on oxygen transport	98
4.4.2	Boria volatility	99
4.4.3	Implications for ceramic matrix composites.....	102
4.5	Conclusions	103
4.6	Recommendations for future work.....	103
5	Task 2: Effects of boron, pressure, and temperature on the oxidation behavior of reaction-bonded SiC coupons	104
5.1	Objectives of Task 2.....	104
5.2	Experimental recap.....	105
5.3	Results	106
5.3.1	Coupon characterization prior to oxidation exposure	106
5.3.2	Crystal structure	115
5.3.3	Oxidation exposures.....	116
5.3.4	Characterization of oxidized RB-SiC coupons	119
5.4	Discussion	140
5.4.1	Boron effects on RB-SiC oxidation kinetics in 1 atm O ₂ environments.....	140
5.4.2	Pressure effects on RB-SiC oxidation kinetics	143
5.4.3	Implications of B effects on CMC matrix material oxidation resistance.....	144
5.5	Conclusions	145
5.6	Recommendations for future work.....	145
6	Task 3: Optimization of sol-gel synthesis, coating application, and freestanding glass fabrication	147
6.1	Objectives of Task 3.....	147
6.2	Experimental procedure, recap.....	147
6.3	Results	149
6.3.1	Gelation.....	149
6.3.2	Maximizing B retention	149
6.3.3	Optimization of the gel-to-glass conversion	151

6.3.4	Glass structure molecular bonding, Fourier transform infrared spectroscopy	156
6.3.5	XRD phase characterization of glasses following heat treatment.....	160
6.3.6	Carbon incorporation in glass structure	160
6.3.7	Substrate coating optimization for thin silica and borosilicate films.....	162
6.3.8	Optimization of freestanding glass fabrication	168
6.4	Discussion	169
6.4.1	Boron retention and borosilicate bond formation	170
6.4.2	Carbon incorporation in the glass structure	172
6.5	Conclusions	173
6.6	Recommendations for future work.....	175
7	Task 4: High temperature stability of sol-gel derived borosilicate glasses in dry O ₂	176
7.1	Objectives of Task 4.....	177
7.2	Experimental recap.....	177
7.3	Results	179
7.3.1	Weight change profiles from 800°C exposures in dry O ₂ for 100 h	179
7.3.2	Weight change profiles from 1200°C exposures in dry O ₂ for 100 h	181
7.3.3	Post exposure characterization of freestanding glasses	183
7.3.4	Summary of volatilization reactions that occurred in the sol-gel derived freestanding glasses from exposures to the TGA environment.....	189
7.4	Discussion	190
7.4.1	Weight loss.....	190
7.4.2	Viscosity and melting	193
7.5	Conclusions	193
7.6	Recommendations for future work.....	194
8	Task 5: Oxidation of SiC substrates coated with borosilicate sol-gel derived glass layers.....	195
8.1	Objectives	196
8.2	Experimental recap.....	197
8.2.1	Sol-gel synthesis	197
8.2.2	Substrates and coating application.....	198
8.2.3	Oxidation exposures.....	201

8.2.4	Characterization techniques	201
8.3	Results	202
8.3.1	Effects of borosilicate glass composition on CVD-SiC oxidation kinetics .	203
8.3.2	Benchtop specific weight change.....	207
8.3.3	Oxide microstructures	208
8.3.4	Oxide thickness	212
8.3.5	Bulk oxide composition	216
8.3.6	Efforts to reproduce Schlichting's experiments: oxidation of sol-gel derived borosilicate glass coated Si substrates	219
8.3.7	Oxidation of sol-gel derived borosilicate glass coated Sylramic SiC fibers	221
8.4	Discussion	230
8.4.1	Boria fluxing of SiC: a review of chemical reactions.....	230
8.4.2	Role of SiO ₂ on the B ₂ O ₃ chemical reactivity with SiC	231
8.4.3	Structural insights into the fluxing mechanism	232
8.4.4	Implications of the boria fluxing mechanism on CMC degradation.....	234
8.4.5	Critique of Schlichting's approach ⁴¹	235
8.5	Conclusions	236
8.6	Recommendations for future work.....	237
9	Summation of research project findings	239
	References.....	242
	Appendix: Sol-gel formulation examples	250

List of Tables

Table 1: Summary of gaps in the present understanding of the thermally grown borosilicate glass and its effects on SiC oxidation kinetics and methodologies undertaken in this research project to advance the present state of knowledge.	50
Table 2: Issues that arose in replicating Schlichting’s study ⁴¹ and methodologies undertaken in this study to address these issues	55
Table 3: Select list of sol-gel synthesis formulations	61
Table 4: ICP-OES emission lines used for detecting B, Si, and Ti from digestion solutions	74
Table 5: Compiled linear (k_l) and parabolic (k_p) oxidation rate constants determined from TGA data, oxide thickness and fiber recession measurements. Asterisks refer to the Sylramic <i>iBN</i> TGA traces where an initial transient was observed. The corresponding Sylramic <i>iBN</i> rate constants were calculated from the slopes of the linear dependence established after the transient.....	85
Table 6: Compiled reaction limited and diffusion limited activation energies for oxidation of Sylramic fibers compared to literature values for related SiC materials	87
Table 7: Consolidated list of characterization techniques utilized in Task 2	106
Table 8: FactSage data for compounds consistent with EDS Points 1 and 2 in Figure 42 left	114
Table 9: Point EDS elemental compositions from 0.5 and 4 wt.% B coupon surfaces oxidized in the TGA instrument at 900°C for 100 h in 1 atm dry O ₂ . Point 1 (top left) and Point 2 (top right) collected from the 0 wt.% B coupon; Point 3 (bottom left) collected from the 0.5 wt.% B coupon; and Point 4 (bottom right) collected from the 4 wt.% B coupon, as shown by labels 1 – 4 in Figure 55.	128
Table 10: Mean oxide thicknesses measured from coupon cross-sections oxidized at 1200°C for 100 h in 1 and 4.4 atm dry O ₂ . Average dome heights measured from oxides formed on B-containing coupons were also included – parentheses represent the number of domes measured.	136
Table 11: Parabolic rate constants calculated from oxide thickness.....	139
Table 12: Select sol-gel synthesis formulations conducted in Task 3	148
Table 13: ICP-OES results of B concentrations in thin gel films and freestanding glasses, nominally 52 mol%	150

Table 14: ICP-OES results of actual B concentration as a function of maximum heat treatment temperature in converted glasses	151
Table 15: ICP-OES results testing for B reproducibility in borosilicate (F 7) gels and freestanding glasses	155
Table 16: ICP-OES results comparing B concentrations in freestanding glasses synthesized from TMBX and B ₂ O ₃ precursors	156
Table 17: Select sol-gel synthesis formulations conducted in Task 4	178
Table 18: Characterization methods carried out on individual freestanding glasses from isothermal exposures to the high temperature dry O ₂ environment conducted at 800 and 1200°C for 100 h.....	179
Table 19: Combustion IR results of the carbon concentration in silica- (F 2) and TMBX-synthesized borosilicate (F 8) freestanding glasses following TGA exposures at 1200°C for 100 h in dry O ₂ . The carbon concentrations were compared to glasses that were not exposed to the TGA environment, but were cast from the same sol-gel synthesis.	184
Table 20: Borosilicate FSG B concentration prior to and after TGA exposure at 800 and 1200°C for 100 h in dry O ₂ determined by ICP-OES	186
Table 21: Sol-gel synthesis formulations.....	198
Table 22: Substrates and coatings investigated in Task 5.....	200
Table 23: Consolidated list of characterization techniques utilized in Task 5	202
Table 24 : Specific weight change results from benchtop weight change measurements following TGA exposures at 800 and 1200°C for 100 h in dry O ₂	208
Table 25: Comparison of average oxide thicknesses measured from uncoated and silica- and borosilicate glass coated CVD-SiC coupons oxidized at 1200°C for 100 h in dry O ₂	214
Table 26: Average oxide thicknesses measured from boria glass coated CVD-SiC coupons oxidized at 800°C for 100 h in dry O ₂	216
Table 27: ICP-OES results of the bulk B concentration in oxides digested from borosilicate glass coated CVD-SiC coupons oxidized for 100 h in dry O ₂ at 800 and 1200°C.....	217
Table 28: ICP-OES results of the bulk B concentration in oxides digested from boria glass coated CVD-SiC coupons oxidized for 100 h in dry O ₂ at 800°C	218

Table 29: Average oxide thicknesses measured from uncoated and glass coated Sylramic fibers oxidized at 1200°C for 100 h in dry O₂ 225

Table 30: Raman peak assignments 228

Table 31: ICP-OES results of the bulk B concentration in oxides digested from unocated and glass coated Sylramic fibers oxidized for 100 h in dry O₂ at 800 and 1200°C 229

List of figures

Figure 1: Scanning Electron Microscopy (SEM) images of CMC's after high temperature oxidation at 1316°C, 6 atm total pressure, 0.6 atm H₂O partial pressure, 21 m/s gas velocity for 100h³. A) Interior portion of CMC imaged away from a surface crack, and B) CMC portion imaged near a surface crack illustrating excessive glass formation, fiber and matrix degradation. 29

Figure 2: Oxide thickness measurements provided in the study by Ramberg et al. reported as a function of time following isothermal oxidation exposures of (111) CVD-SiC in dry oxygen ranging from 800 -1100°C²¹. The figure was annotated from the original to highlight the different oxidation mechanisms..... 32

Figure 3: Parabolic weight change observed in the study by Jacobson et al. on the oxidation of high order BN at 900°C in dry O₂ (water impurity ranged from 7 – 44 ppm)¹¹. The original image was annotated here to highlight the parabolic weight gain and linear weight loss regimes..... 35

Figure 4: Plot of isothermal weight change profiles observed in the study by Wilson and Opila on the oxidation of Hi-Nicalon™ fibers in dry O₂ at temperatures ranging from 700 – 1300°C³⁰. The original image was annotated here differentiate the linear and parabolic oxidation regimes..... 36

Figure 5: Plot of isothermal weight change profiles observed in the study by Opila and Boyd on the oxidation of SiC fibers with a BN layer in dry argon with 5 vol% oxygen at temperatures ranging from 816 – 1343°C¹³. Deviation from SiC oxidation behavior due to the presence of the BN is highlighted by the black box signifying a transient period of rapid weight gain. The original image was annotated here to highlight the transient period of rapid weight gain. 39

Figure 6: STM analysis of v-SiO₂ films from the study by Lichtenstein et al.⁴⁴. A) Zachariassen's schematic of v-SiO₂ structure of interconnected Si-O rings, B) STM image showing Si atom positions, and C) STM image showing O atom positions. Original image was annotated here to differentiate between Si and O atoms and to highlight the range of ring sizes. 42

Figure 7: Annotated schematic of v-B₂O₃ from Hwang et al. proposing a 1: 1 ratio of triangular BO₃ (triangle) to B₃O₆ boroxol ring (circle) units formed from three BO₃ units⁴⁸. Original image was annotated here to differentiate between boroxol ring and planar triangle arrangements..... 43

Figure 8: Binary SiO₂-B₂O₃ phase diagram by Rocket and Foster⁴⁶. Figure was annotated from the original to highlight flattening of the liquidus. 44

Figure 9: Reduction in SiO₂ viscosity by B₂O₃ incorporation plotted as viscosity on a log₁₀ axis versus inverse temperature ranging from 800 to 1390°C for varying borosilicate glass compositions. Viscosities were calculated from data reported by Yan et al. (0, 3, 6, and 48 mol% B₂O₃, balance SiO₂)⁵⁵ and Bruckner and Navarro (98 mol% B₂O₃, balance SiO₂)⁴²..... 45

Figure 10: Comparison of parabolic oxidation rates for silicon. A) O₂ diffusion rates calculated from parabolic rate constants determined from the oxidation of silicon substrates coated with sol-gel derived glass layers (re-plotted from Schlichting⁴¹). B) Deal and Grove parabolic oxidation rate constants of silicon²² compared to the parabolic oxidation rate constants of silicon coated with sol-gel derived silica layers from Schlichting’s study..... 52

Figure 11: Macrograph of a Sylramic *iBN* fiber lanyard..... 57

Figure 12: Macrograph of a RB-SiC coupon..... 58

Figure 13: Macrograph of a CVD-SiC coupon..... 58

Figure 14: Macrograph of a Si coupon 59

Figure 15: SiC substrate immersion in sol coating by dip-coat method. A) CVD- SiC coupon, and B) SiC fibers twisted into a lanyard 62

Figure 16: Photograph of TGA Instrument..... 66

Figure 17: Furnace hot zone schematic 66

Figure 18: Example of sol-gel derived freestanding glass after conversion suspended from the alumina hanger in the TGA apparatus..... 67

Figure 19: Sylramic *iBN* lanyard suspended in the TGA apparatus with the furnace in the lowered position. The sample thermocouple is located below the lanyard. The furnace is raised to initiate oxidation exposure. 78

Figure 20: Secondary electron micrographs of A) Sylramic *iBN* and B) Sylramic fibers surfaces. 79

Figure 21: Backscatter electron image of Sylramic *iBN* cross-section illustrating the BN layer (between arrows). The cross represents point EDS sampling of the BN coating. .. 80

Figure 22: Elemental EDS maps of the Sylramic *iBN* fiber cross-section imaged from backscattered electrons. 80

Figure 23: TGA specific weight change results as a function of time for Sylramic fibers exposed to 1 atm of dry O₂ for 100 h under isothermal temperatures ranging from 800 – 1300°C..... 82

Figure 24: TGA specific weight change results as a function of time for Sylramic *iBN* fibers exposed to 1 atm of dry O₂ for 100 h under isothermal temperatures ranging from 800 – 1300°C..... 83

Figure 25: TGA specific weight change results as a function of the square root of time for fibers exposed to 1 atm of dry O₂ for 100 h under isothermal temperatures ranging from 1100 – 1300°C. A) Sylramic and B) Sylramic *iBN*. Linear fits shown by dashed lines... 84

Figure 26: Plot of Sylramic oxidation rate constants versus inverse temperature for linear (mg cm⁻² h⁻¹, squares) and parabolic (mg² cm⁻⁴ h⁻¹, circles) oxidation mechanisms determined from TGA weight change data following isothermal oxidation for 100 h in dry O₂ at 900 – 1300°C..... 86

Figure 27: Micrographs of oxidized fiber cross-sections after 100 h exposures in dry O₂. Top row: Sylramic fiber cross-sections - A) 900°C, B) 1300°C. Bottom row: Sylramic *iBN* fiber cross-sections - C) 900°C, D) 1300°C. Oxidized fiber cross-sections were imaged by SEM with secondary electrons..... 88

Figure 28: Oxide thickness measurements as a function of temperature for Sylramic *iBN* (open squares) and Sylramic (filled squares) oxidized fibers exposed for 100 h in dry O₂ under isothermal conditions ranging from 900 – 1300°C..... 89

Figure 29: Plot of Sylramic oxidation rate constants versus inverse temperature for linear (μm h⁻¹, squares) and parabolic (μm² h⁻¹, circles) oxidation mechanisms determined from oxide thickness measurements..... 91

Figure 30: Secondary electron micrographs of fiber cross-sections after digestion. Top row: Sylramic fiber cross-sections A) Unoxidized fiber, and after oxidation for 100 h in dry O₂ at B) 900°C, C) 1300°C. Bottom row: Sylramic *iBN* fiber cross-sections D) Unoxidized fiber, and after oxidation for 100 h in dry O₂ at E) 900°C, F) 1300°C..... 92

Figure 31: Mean fiber diameters for Sylramic *iBN* (open squares) and Sylramic (filled squares) following digestion after exposures for 100 h in isothermal dry O₂ exposures ranging from 800 – 1300°C..... 93

Figure 32: Plot of Sylramic fiber recession rate constants versus inverse temperature for linear (μm h⁻¹, squares) and parabolic (μm² h⁻¹, circles) oxidation mechanisms determined from fiber diameter measurements..... 94

Figure 33: ICP-OES results for average B concentration in digested oxides from fibers as a function of temperature after 100 h isothermal exposures in dry O₂. Sylramic *iBN* – open squares; Sylramic – filled squares..... 95

Figure 34: Sylramic *iBN* oxide thickness measurements: 1300°C represented by filled squares, 1200°C represented by open squares, and 900°C represented by open circles. A) Sylramic *iBN* oxide thickness plotted versus time for 900, 1200, and 1300°C exposures in dry O₂. Calculated oxide thicknesses from the parabolic rate constant reported by Ogbuji and Opila for the dry O₂ oxidation of CVD-SiC at 1200°C¹⁷ represented by the dashed line. Calculated oxide thicknesses from the linear and parabolic rate constants are reported by Ramberg et al. for the dry O₂ oxidation of ($\bar{1}\bar{1}\bar{1}$) CVD-SiC at 900°C²¹ are represented by the dotted line. B) Oxide thickness versus the square root of time for 1200 and 1300°C exposures. Note the symbols for oxide thicknesses following 1 h 1200 and 1300°C exposures are superimposed. 97

Figure 35: ICP-OES results for Sylramic *iBN* oxide B concentration as a function of oxidation time at three different temperatures in dry O₂: 900, 1200, and 1300°C. 98

Figure 36: FactSage calculated partial pressure temperature dependence for predominant volatile species from vaporization and volatilization reactions of a 24 mol% B₂O₃ borosilicate glass composition (dashed line) and pure liquid B₂O₃ (solid line) in 10 ppm water vapor, balance O₂, and in dry O₂..... 101

Figure 37: Representative macrograph of unoxidized RB-SiC coupons..... 107

Figure 38: Plan-view micrographs of RB-SiC coupons. A) 0 wt.% B, B) 0.5 wt.% B, and C) 4 wt.% B..... 108

Figure 39: Elemental EDS maps of C, Si, and Al taken from the baseline 0 wt.% B coupon microstructure 109

Figure 40: EDS elemental maps taken in plan view from 0.5 wt.% B RB-SiC coupon. 110

Figure 41: EDS elemental maps taken in plan view from 4 wt.% B RB-SiC coupon.... 110

Figure 42: Left) Point ID EDS analysis of the black (Point 1) and dark grey (Point 2) phases present in the micrograph taken from the 4 wt.% B-containing RB-SiC coupon. Top right) spectrum corresponding with the point ID analysis of Point 1. Bottom right) spectrum corresponding with the point ID analysis of Point 2..... 112

Figure 43: Binary phase diagrams of systems B-Al, B-Ca, and Ca-Si, and B-C¹⁰⁰ 113

Figure 44: Quantification of B area fraction by Image J particle size analysis of B elemental maps. A) Particle outlines of the B phase of the B elemental EDS map taken from the RB-SiC coupon containing 0.5 wt.% B (Figure 40) Particle outlines of the B

phase of the B elemental EDS map taken from the RB-SiC coupon containing 4 wt.% B (Figure 41). 114

Figure 45: XRD analysis of RB-SiC coupons. From top-to-bottom: Diffraction patterns from RB-SiC coupons containing 0, 0.5, and 4 wt.% B. 115

Figure 46: TGA weight profiles of RB-SiC coupons containing 0, 0.5, and 4 wt.% B from exposures at 900°C for 100 h in 1 atm dry O₂. 117

Figure 47: TGA weight profiles of RB-SiC coupons containing 0 and 4 wt.% B from exposures at 1200°C for 100 h in 1 atm dry O₂. A) Plots of specific weight change versus time. B) Plots of specific weight change versus root time. Forced linear fits are denoted by dotted lines. TGA weight change profiles of RB-SiC coupons containing 0.5 wt.% B are unavailable for exposures at 1200°C. 118

Figure 48: Specific weight change from benchtop weight measurements following TGA and high pressure rig exposures of RB-SiC coupons containing 0, 0.5, and 4 wt.% B. A) Specific weight change from 900 and 1200°C TGA exposures for 100 h in 1 atm dry O₂. B) Specific weight from 900 (solid lines) and 1200°C (dashed lines) high pressure rig exposures in 1 and 4.4 atm dry O₂. Lines are to guide the eye. 119

Figure 49: Optical macrographs of RB-SiC coupons containing 4 wt.% B. A) Unoxidized coupon, B) Oxidized coupon following the 1200°C TGA exposure, C) Oxidized coupon following 1200°C high pressure rig exposure at 1 atm dry O₂, and D) Oxidized coupon following 1200°C high pressure rig exposure in 4.4 atm dry O₂. 120

Figure 50: Optical profilometry of the surface roughness of RB-SiC coupons containing 4 wt.% B. A) Unoxidized coupon, B) Oxidized coupon following the TGA exposure at 1200°C in 1 atm dry O₂, and C) Oxidized coupon following the high pressure rig exposure at 1200°C in 4.4 atm dry O₂. (Courtesy of Madeline Morales) 121

Figure 51: Plan-view micrographs of oxidized RB-SiC coupons following TGA exposures at 900°C for 100 h in 1 atm dry O₂. A) 0 wt.% B baseline coupon, B) 0.5 wt.% B coupon, and C) 4 wt.% B coupon. Labels 1- 3 correspond with areas analyzed by EDS. 122

Figure 52: Point EDS spectra and elemental compositions from 0.5 and 4 wt.% B coupon surfaces oxidized in the TGA instrument at 900°C for 100 h in 1 atm dry O₂. Point 1 (top spectrum) and point 2 (middle spectrum) collected from the 0.5 wt.% B coupon, as shown in Figure 51 B. Point 3 (bottom spectrum) collected from the 4 wt.% B coupons, as shown in Figure 51 C. 123

Figure 53: Elemental EDS maps of B and Si taken of oxides formed on RB-SiC coupons containing 0.5 and 4 wt.% B after oxidation in the TGA instrument at 900°C for 100 h in 1 atm dry O₂, shown Figure 51 B and C. Left column) B map (top) and Si map (bottom)

from the 0.5 wt.% B coupon oxidized surface, and Right column) B map (top) and Si map (bottom) from the 4 wt.% B coupon oxidized surface..... 124

Figure 54: Elemental EDS maps of Al taken of oxides formed on RB-SiC coupons containing 0, 0.5 and 4 wt.% B oxidized in the TGA instrument at 900°C for 100 h in 1 atm dry O₂, shown in Figure 51 A, B, and C, respectively. A) 0 wt.% B baseline coupon, B) 0.5 wt.% B coupon, and C) 4 wt.% B coupon. 125

Figure 55: Plan-view micrographs of oxidized RB-SiC coupons following TGA exposures at 900°C for 100 h in 1 atm dry O₂ showing a bright oxide phase prone to cracking and pitting. A) 0 wt.% B baseline coupon, B) 0.5 wt.% B coupon, and C) 4 wt.% B coupon. Labels 1- 4 correspond with areas analyzed by Point ID EDS..... 126

Figure 56: Point EDS spectra and elemental compositions from 0.5 and 4 wt.% B coupon surfaces oxidized in the TGA instrument at 900°C for 100 h in 1 atm dry O₂. Point 1 (top left) and Point 2 (top right) collected from the 0 wt.% B coupon; Point 3 (bottom left) collected from the 0.5 wt.% B coupon; and Point 4 (bottom right) collected from the 4 wt.% B coupon, as shown by labels 1 – 4 in Figure 55. 127

Figure 57: Plan-view micrographs of oxidized RB-SiC coupons following TGA exposures at 1200°C for 100 h in 1 atm dry O₂. A) 0 wt.% B baseline coupon, B) 0.5 wt.% B coupon, and C) 4 wt.% B coupon. 129

Figure 58: Plan-view micrographs of oxidized RB-SiC coupons following high pressure rig exposures at 900°C for 100 h. Top row: A) 0 wt.% B baseline coupon, B) 0.5 wt.% B coupon, and C) 4 wt.% B coupon exposed in 1 atm dry O₂. Bottom row: D) 0 wt.% B baseline coupon, E) 0.5 wt.% B coupon, and F) 4 wt.% B coupon exposed in 4.4 atm dry O₂. 130

Figure 59: Plan-view micrographs of oxidized RB-SiC coupons following high pressure rig exposures at 1200°C for 100 h. Top row: A) 0 wt.% B baseline coupon, B) 0.5 wt.% B coupon, and C) 4 wt.% B coupon exposed in 1 atm dry O₂. Bottom row: D) 0 wt.% B baseline coupon, E) 0.5 wt.% B coupon, and F) 4 wt.% B coupon exposed in 4.4 atm dry O₂. 131

Figure 60: X-ray diffraction patterns collected from 0, 0.5, and 4 wt.% B coupons oxidized at 1200°C for 100 h in dry O₂ in the TGA and in the high pressure rig in 1 and 4.4 atm dry O₂. The diffraction pattern from the unoxidized 0 wt.% B coupon is included for comparison with patterns from oxidized coupons..... 133

Figure 61: Oxide cross-section BEI of oxidized RB-SiC coupons following TGA exposures at 1200°C for 100 h in 1 atm dry O₂. A) 0 wt.% B baseline coupon, B) 0.5 wt.% B coupon showing oxide dome-shape, C) 4 wt.% B coupon showing oxide dome-shape, and D) 4 wt.% B coupon showing oxide pit..... 134

Figure 62: Elemental EDS maps of dome-shaped oxide cross-section from an oxidized 4 wt.% B coupon following TGA exposure at 1200°C for 100 h in 1 atm dry O ₂	135
Figure 63: Oxide thickness measurements of RB-SiC coupons containing 0, 0.5, and 4 wt.% B following high pressure rig exposures at 1200°C for 100 h in 1 and 4.4 atm dry O ₂ . Lines are to guide the eye.	137
Figure 64: Micrograph (top left) taken from an oxidized 0.5 wt.% B coupon cross-section representing subsurface oxidation. The coupon was oxidized at 1200°C for 100 h in 4.4 atm dry O ₂ . The micrograph is shown with corresponding maps collected from EDS analysis of the microstructure.	138
Figure 65: Ellingham diagram from Lynch ¹¹⁰ . Oxide reactions relevant to this study are highlighted by arrows.	141
Figure 66: Heat treatment in the TGA instrument used to establish the gel-to-gel conversion heat treatment- weight loss results as a function of time and temperature for borosilicate (F 7) gel-to-glass conversion: Black) Top plot showing hold time of 1 h at 400°C with maximum temperature of 600°C; Green) Middle plot showing hold time of 8 h at 400°C with maximum temperature of 550°C; and Red) Bottom plot showing hold time of 16 h at 400°C with maximum temperature of 500°C.	152
Figure 67: Evolution of borosilicate (F 7) gel-to-glass bonding: FTIR spectra as a function of maximum heat treatment temperature (max HTT) and gas environment. ...	157
Figure 68: XRD results of converted glass powders from high-B (F 6) formulations: Top) maximum HTT of 600°C in Ar gas stream, Middle-Top) maximum heat treatment temperature of 600°C in Ar/ H ₂ gas stream, Middle-Bottom) maximum heat treatment temperature of 550°C in Ar/ H ₂ gas stream, and Bottom) maximum heat treatment temperature of 400°C in Ar/ H ₂ gas stream.	160
Figure 69: Optical image of high-B glass (F 8) cold pressed into a pellet.	161
Figure 70: Raman spectrum of a dark intercalate from the borosilicate formulation F 8 glass pellet.....	162
Figure 71: Micrographs of silica and borosilicate coated coupons. A) Silica (F 2) coating surface synthesized with 90 vol% solvent concentration applied without prior pre-oxidation, B) Borosilicate (F 10) coating surface synthesized with TMBX precursor and 95 vol% solvent concentration applied without prior pre-oxidation, C) Borosilicate (F 10) coating surface synthesized with TMBX and 95 vol% solvent concentration applied by three dip coats following pre-oxidation for 5 min at 1000°C, and D) Borosilicate (F 12) coating surface synthesized with the B ₂ O ₃ precursor and 95 vol% solvent concentration applied without prior pre-oxidation. Coupons were imaged in plan view by SEM with secondary electrons.	163

Figure 72: Micrograph of a borosilicate coating synthesized with the B_2O_3 precursor and 95 vol% solvent concentration (F 12) applied by three successive dip coats onto a Si coupon. Coupon was imaged in plan view by SEM with secondary electrons. 164

Figure 73: Micrographs of glass coated Sylramic fiber cross-sections. A) Silica (F 2) coating synthesized with 90 vol% solvent concentration applied by a single immersion, B) Borosilicate (F 7) coating synthesized with 90 vol% solvent concentration applied by a single immersion, C) Borosilicate (F 7) coating synthesized with 95 vol% solvent concentration applied by three consecutive immersions, and D) Borosilicate (F 12) coating synthesized with 90 vol% solvent concentration applied by a single immersion. Cross-sectioned fibers were imaged by SEM with secondary electrons. 165

Figure 74: Micrographs of fiber lengths showing the comparison of fiber pre-oxidation effects on improving coating surface coverage. Coatings were synthesized with TMBX precursor and a 95 vol% solvent concentration that were vacuum coated three times in succession. A) Sylramic fiber not per-oxidized prior to being coated, B) Sylramic fibers pre-oxidized for 5 min at 1000°C prior to being coated, C) Sylramic *iBN* fibers not per-oxidized prior to being coated, and D) Sylramic *iBN* fibers pre-oxidized for 5 min at 1000°C prior to being coated. Fiber surfaces were imaged by SEM with secondary electrons. 166

Figure 75: A) Micrograph of a borosilicate coating synthesized with the TMBX precursor and 92.7 vol% solvent concentration (F 9) applied by three successive dip coats onto a CVD-SiC coupon. Coupon was imaged in plan view by SEM with secondary electrons. B) Micrograph of a boria coating synthesized with the TMBX precursor and 70 vol% solvent concentration (F 13) applied by seven successive dip coats onto a CVD-SiC coupon. Coupon was imaged in plan view by SEM with backscattered electrons..... 168

Figure 76: Examples of ambient dried versus oven dried gels synthesized from borosilicate formulation (F 5). A) Ambient dried gels post conversion, B) Oven dried gel prior to conversion and C) The same oven dried gel converted to a glass. 169

Figure 77: Plots of the freestanding glass specific weight change versus time from TGA exposures at 800°C for 100 h in dry O_2 180

Figure 78: Macrographs of silica and borosilicate freestanding glasses taken before and after TGA exposures at 800°C for 100 h in dry O_2 181

Figure 79: Plots of the freestanding glass specific weight change versus time from TGA exposures at 1200°C for 100 h in dry O_2 182

Figure 80: Macrographs of silica and borosilicate freestanding glasses taken before and after TGA exposures at 1200°C for 100 h in dry O_2 183

Figure 81: Raman spectrum from analysis of the TMBX-synthesized borosilicate glass (F 8) following TGA exposures for 100 h at 1200°C in dry O₂. 185

Figure 82: Surface composition of O, Si, and B determined from surface depth profiling of a TMBX-synthesized borosilicate freestanding glass (F 7) by XPS following TGA exposure at 1200°C for 100 h in dry O₂. A) Surface concentrations of O, Si, and B (at. %) as a function of surface depth. B) Surface concentration of boron as a function of sputter depth shown superimposed to highlight the boron concentration gradient, which extends more than 0.3 µm into the glass surface. 187

Figure 83: FTIR spectra from borosilicate freestanding glasses synthesized from the TMBX precursor (F 7 – F 9) and from the boria precursor (F 11). A) Stacked spectra from converted freestanding glasses. B) Stacked spectra of the freestanding glasses after dry O₂ exposures at 800°C (F 9 and F 11, top two spectra, respectively) and after dry O₂ exposures at 1200°C (F 7 – F9 and F 11, bottom four spectra) for 100 h..... 189

Figure 84: Weight change profiles plotted as specific weight change versus time recorded from TGA exposures at 800°C for 100 h in dry O₂. A) Weight change profiles from uncoated and silica coated CVD-SiC coupons. B) Weight change profiles from uncoated and borosilicate glass coated CVD-SiC coupons. C) Weight change profiles of uncoated and boria glass CVD-SiC coated coupons. Two of the boria glass coated coupons were pre-oxidized in dry O₂ prior to coating application. The pre-oxidation conditions are individually described in the plots. 205

Figure 85: Weight change profiles from TGA exposures of uncoated, silica- (F 3) and TMBX-synthesized borosilicate (F 9 and F 10) glass coated CVD-SiC coupons oxidized at 1200°C for 100 h in dry O₂. Weight change profiles from thin boria-synthesized borosilicate glass coated CVD-SiC coupons are unavailable. 207

Figure 86: Micrographs of thin silica glass coated CVD-SiC coupons (F 3) oxidized for 100 h in dry O₂ at (A) 800°C and (B) 1200°C. Microstructures were observed by SEM in plan view with secondary electrons. 209

Figure 87: Micrographs of thin boria-synthesized borosilicate glass coated CVD-SiC coupons (F 12) oxidized for 100 h in dry O₂ at (A) 800°C and (B) 1200°C. Microstructures were observed by SEM in plan view with secondary electrons. 209

Figure 88: Micrographs of thin TMBX-synthesized borosilicate glass coated CVD-SiC coupons (F 10) oxidized for 100 h in dry O₂ at (A) 800°C and (B) 1200°C. Microstructures were observed by SEM in plan view with secondary electrons. 210

Figure 89: Micrographs of thick TMBX-synthesized borosilicate glass coated CVD-SiC coupons (F 10) oxidized for 100 h in dry O₂ at (A) 800°C and (B) 1200°C. Microstructures were observed by SEM in plan view with secondary electrons. 210

Figure 90: Micrographs of thick boria glass coated CVD-SiC coupons (F 13) oxidized for 100 h in dry O₂ at 800°C. A) Oxide microstructure of boria coated coupon not pre-oxidized prior to coating application. B) Oxide microstructure of a boria coated coupon pre-oxidized at 1000°C for 1 h prior to coating application. C) Oxide microstructure of a boria coated coupon pre-oxidized at 800°C for 100 h prior to coating application. Arrows represents spots where the oxide was analyzed by EDS. Microstructures were observed by SEM in plan view with backscattered electrons. 211

Figure 91: Micrographs of cross-sectioned uncoated and coated CVD-SiC coupons oxidized for 100 h in dry O₂ at 1200°C. A) Uncoated coupon, B) thin silica glass coated coupon (F 3), C) thin boria-synthesized borosilicate glass coated coupon (F 12), and D) thick TMBX-synthesized borosilicate glass coated coupon (F 9). Cross-sections were observed by SEM with secondary electrons. Micrographs showing the oxidized cross-section of the thin TMBX-synthesized glass coated coupon (F 10) was not shown. 213

Figure 92: Micrographs of cross-sectioned boria coated CVD-SiC coupons (F 13) oxidized for 100 h in dry O₂ at 800°C. A) Coupon not pre-oxidized prior to coating application, B) coupon pre-oxidized at 1000°C for 1 h prior to coating application, and C) coupon pre-oxidized at 800°C for 100 h prior to coating application. Cross-sections were observed by SEM with backscattered electrons..... 215

Figure 93: Weight change profiles from TGA exposures of uncoated and boria-synthesized borosilicate glass coated (F 12) Si coupons oxidized at 800 and 1200°C for 100 h in dry O₂. A) Weight change profiles from 800°C exposures plotted as specific weight change versus time. B) Weight change profiles from 1200°C exposures plotted as specific weight change versus time..... 219

Figure 94: Weight change profiles from TGA exposures of uncoated and boria-synthesized borosilicate glass coated (F 13) Si coupons oxidized at 1200°C for 100 h in dry O₂ plotted as specific versus the square root of time. Dashed lines denote linear fits to the plotted weight change data. Parabolic rate constants, k_p , were calculated from the squared slopes of the linear fits..... 220

Figure 95: Micrographs of thin boria-synthesized borosilicate glass coated Si coupons (F 12) oxidized for 100 h in dry O₂ at (A) 800°C and (B) 1200°C. Microstructures were observed by SEM in plan view with secondary electrons. 221

Figure 96: Weight change profiles from TGA exposures of uncoated and boria-synthesized borosilicate glass coated (F 13) Sylramic fibers oxidized at 800 and 1200°C for 100 h in dry O₂. A) Weight change profiles from 800°C exposures plotted as specific weight change versus time. B) Weight change profiles from 1200°C exposures plotted as specific weight change versus time..... 223

Figure 97: Micrographs of cross-sectioned uncoated and coated Sylramic fibers oxidized for 100 h in dry O₂ at 800°C. A) Uncoated fibers, B) silica glass coated fibers (F 3), C) boria-synthesized borosilicate glass coated fibers (F 12). Microstructures were observed by SEM in plan view with secondary electrons..... 224

Figure 98: Micrographs of cross-sectioned uncoated and coated Sylramic fibers oxidized for 100 h in dry O₂ at 1200°C. A) Uncoated fibers, B) silica glass coated fibers (F 3), C) boria-synthesized borosilicate glass coated fibers (F 12). The oxides fused the fibers together. Microstructures were observed by SEM in plan view with secondary electrons. 225

Figure 99: Raman spectra of uncoated and boria-synthesized borosilicate glass coated Sylramic fibers (F 12) before and after oxidation at 1200°C for 100 h in dry O₂. A) uncoated, unoxidized Sylramic SiC fiber, B) unoxidized boria-synthesized borosilicate glass coated Sylramic SiC fiber (F 12), C) uncoated, oxidized Sylramic SiC fiber, and D) oxidized boria-synthesized borosilicate glass coated Sylramic SiC fiber (F 12)..... 228

Figure 100: Proposed structures of boria. A) Proposed structure of ν -B₂O₃ by Hwang et al.⁴⁸, and B) Proposed changes in the molten B₂O₃ structure by Mackenzie showing further decomposition of BO₃ triangles into B=O bonds resulting from increased heating of the glass⁵². Figure was annotated from the original to identify B and O atoms and B=O bonds.. 233

Abstract

Ceramic matrix composite (CMC) components were introduced into civilian aircraft engines in 2016. CMCs are comprised of silicon carbide (SiC) fibers coated with a boron nitride layer embedded in a SiC matrix. SiC and boron nitride will react with oxygen upon exposure to the engine's high temperature oxidizing environment, forming silica and boria oxidation products, respectively, which together form a borosilicate glass. In the presence of water vapor the boria and silica can also react with water to form B-O-H and Si-O-H gaseous species. These reactions can result in the depletion of the boron nitride interphase and excessive borosilicate glass formation leading to rapid recession of the SiC fibers and CMC degradation. The thermally grown borosilicate glass compositions are presently unknown, as well as the time, temperature and gas environment that result in excessive borosilicate glass formation. Two approaches were taken in this research project to understand the role of boria concentration and exposure conditions that lead to accelerated SiC oxidation kinetics so that the mechanistic understanding and prediction of CMC degradation rates can be elucidated.

In the first approach, the microstructure, composition, bonding and phase of thermally grown borosilicate glasses were investigated through the oxidation of two different types of boron-containing SiC materials. The role of a boron nitride layer on the oxidation behavior of SiC fibers was investigated. The boria concentrations in the oxides were correlated with the weight change behavior, oxide thickness, and fiber recession of the oxidized fibers. Higher boria concentrations led to initial rapid oxidation rates of SiC fibers that were 3 – 10 times faster than observed for pure SiC. Slower oxidation rates followed as the oxide surface became increasingly enriched with silica due to boria

volatilization, thereby limiting the observation of boria effects on SiC fiber oxidation kinetics. Reaction-bonded SiC (RB-SiC) ceramics were investigated next to understand the role of boron (B) concentration on the RB-SiC oxidation behavior. Varying concentrations of B were processed into RB-SiC coupons, comprised of SiC particles embedded in a silicon melt-infiltrated matrix. High temperature oxidation studies were conducted in ambient and in elevated oxygen pressure environments. The increased B concentration and elevated oxygen pressure increased the RB-SiC oxidation kinetics. Oxides from B-containing coupons were up to four times thicker than oxides from B-free coupons. Subsurface oxidation was also observed in oxidized B-containing coupons.

In the second approach, glass coatings with well-defined B concentrations were synthesized by a sol-gel method and applied onto SiC substrates to simulate a thermally grown borosilicate glass. Three B concentration ranges were investigated: 0, 24 – 55, and > 95 mol %, balance silica. Coating B concentrations > 95 mol% resulted in fluxing of the SiC substrate, which accelerated the SiC oxidation kinetics by up to 800 times faster than observed for pure SiC. Boria effects on SiC oxidation were not observed with application of borosilicate glass coatings due to a combination of 1) silica incorporation in the boria glass network, which slowed oxygen transport; and 2) boria volatility, which led to reduced B concentrations in the oxide. Sol-gel derived borosilicate glass coatings differed in composition and bonding from thermally grown borosilicate glasses, which limited this approach to directly model the thermally grown borosilicate glass. However, this approach allowed for investigating the interactions of boria with SiC and with the thermally grown silica glass that cannot be investigated by thermally grown borosilicate glasses alone.

The findings in this study demonstrated that high B concentrations flux the SiC, leading to accelerated SiC oxidation kinetics. Oxygen transport in B-rich borosilicate glass is several times faster than in silica by comparison, but is limited when boria volatilization occurs. Thus, the borosilicate glass at CMC free surfaces will likely be protective, but high concentrations of boria formation within the CMC will lead to significant SiC degradation.

1 **Aim of the research project**

Demands for high performing, more fuel efficient aircraft engines are driving the development of state-of-the art ceramic materials to replace the metallic alloys presently used in engine components^{1,2}. Stationary turbine shrouds constructed of non-oxide silicon carbide (SiC)-based ceramic matrix composites(CMCs) were introduced into the CFM LEAP engines in 2016¹. Optimum application of CMCs include their use as rotating components, such as turbine blades in the engine hot section, operating at temperatures up to 1500°C¹. The advantages of CMCs over the nickel-based superalloys presently used as turbine blades are their lighter weight and ability to tolerate higher temperatures¹. These advantages translate into higher fuel efficiencies, lower emissions, and cost savings². Many material challenges must be overcome before these goals can be realized, one of which being instability to the combustion gases. The CMCs, constructed of boron nitride (BN) coated SiC fiber weaves infiltrated with a SiC matrix, were found to substantially degrade when the BN coating was oxidized by the combustion gases to form a boron-rich glass³. The presence of boron accelerated the oxidation of SiC resulting in the excessive formation of a thermally grown borosilicate glass. This research project sought to determine the boron effects on the SiC oxidation kinetics that lead to CMC degradation.

1.1 Objectives

The objectives of this research project were threefold. The first objective was to determine the composition of the thermally grown borosilicate glass resulting from systematic oxidation exposures of B-containing SiC materials in the presence of BN. The second objective was to identify the environmental conditions that increase the boron

effects on SiC oxidation kinetics leading to excessive borosilicate formation. The third objective was to determine the mechanisms that cause accelerated SiC oxidation. These objectives were met by performing five tasks, briefly described in the following sections.

1.2 *Brief description of tasks*

1.2.1 **Task 1:** Boron nitride effects on the high temperature oxidation of silicon carbide fibers

Systematic oxidation studies were conducted on SiC fibers with a BN surface layer to determine the borosilicate glass composition under varying oxidation conditions. Results were compared against a baseline SiC fiber without a BN layer. The effects of the oxide boron concentration on the oxide thickness and fiber recession were evaluated.

1.2.2 **Task 2:** Role of boron concentration and pressure on the oxidation kinetics of reaction-bonded silicon carbide

Reaction-bonded silicon carbide (RB-SiC) coupons processed with varying concentrations of boron were used as model materials to determine the role of the boron concentration on oxidation kinetics. The oxidation temperatures and pressures were varied over ranges relevant to combustion environments. The RB-SiC oxidation behavior was evaluated by weight change and oxide thickness, microstructure, and composition.

1.2.3 **Task 3:** Optimization of sol-gel synthesis parameters for the application of sol-gel derived borosilicate glass coatings on silicon carbide substrates

Synthesis of sol-gel derived glass coatings were investigated as model materials for thermally grown borosilicate glasses. The sol-gel synthesis parameters were optimized for the application of well-defined glass coatings onto SiC substrates for subsequent oxidation testing. The sol-gel derived glasses were extensively characterized

for composition, molecular bonding, and phase. Issues with using the sol-gel method for producing glass coatings were addressed.

1.2.4 **Task 4:** High temperature stability of the sol-gel derived borosilicate glasses

The effects of the high-temperature environment on the sol-derived glasses in isolation from the underlying substrate were conducted by exposing sol-gel derived freestanding glasses to the same oxidation environment as the glass coated SiC substrates. Instabilities of the sol-gel derived glasses to the high temperature oxidizing environment were identified by characterizing the exposed glass for changes in weight, composition, molecular bonding, and phase. The implications of the sol-gel derived glass instability on the behavior of the sol-gel derived glass coatings in the high temperature oxidizing environments were presented.

1.2.5 **Task 5:** Effects of sol-gel derived borosilicate glasses on SiC oxidation

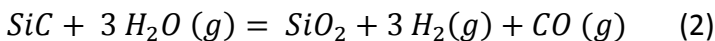
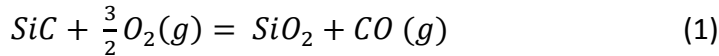
Oxidation studies were conducted on SiC substrates coated with sol-gel derived glass coating compositions varying in boron concentration. The effects of the glass coating boron concentration on the substrate oxidation kinetics were evaluated. The ability of the glass coatings to model thermally grown oxides was assessed.

2 Introduction

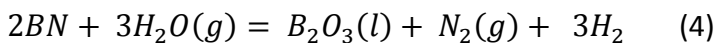
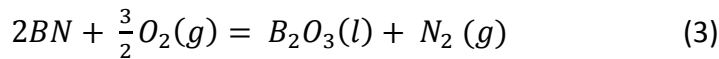
SiC-based ceramic matrix composites (CMCs) are replacing Ni-based superalloys in aircraft turbine engine hot section components due to their lighter weight and higher temperature operational capabilities, resulting in higher fuel efficiency². The CMCs consist of woven silicon carbide (SiC) fibers coated with a weakly bonded interphase,⁴ typically boron nitride (BN)⁵. The fiber weaves are embedded in a matrix that consists of SiC particulates and melt infiltrated silicon Si⁵. An environmental barrier coating protects the CMCs from engine's combustion gases⁶.

2.1 CMC oxidation reactions

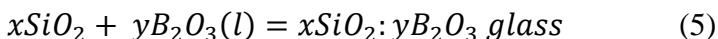
Microcracks in the CMC components are a concern for long term use in the engine hot section¹. Migration of the combustion gases through cracks will result in both SiC and BN oxidation. The predominant oxidizing gases in a combustion environment that will degrade the SiC and BN constituents are oxygen and water vapor⁷. SiC oxidizes in oxygen and water vapor to form silica (SiO₂), as given by Reactions 1 – 2^{8,9}.



BN will oxidize in oxygen and water vapor to form boria (B₂O₃), as given by Reactions 3 – 4¹⁰⁻¹³.

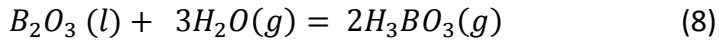


The silica oxidation product (Reactions 1, 2) reacts with the liquid boria oxidation product (Reactions 3, 4) to form a borosilicate glass, shown by Reaction (5)^{14, 15}:



Boria is unstable in high temperature environments, where it volatilizes as given by

Reactions 6 – 8¹⁶:



2.2 *Motivation of this research project*

The presence of the BN layer was ascribed to accelerating SiC oxidation at rates greater than observed for SiC oxidation alone^{13, 15, 17}, leading to thick borosilicate glass formation that caused significant CMC thermochemical^{3, 18, 19} and thermomechanical^{5, 20} degradation. A study by Opila et al. carefully archived significant CMC degradation from three different CMC architectures oxidized in a simulated engine environment³.

Exemplary features of CMC degradation are shown in Figure 1. On the left is a micrograph of a portion of a CMC that was imaged away from a surface crack where some matrix oxidation occurred, highlighted by the dotted arrow. On the right is a micrograph of a portion of the same CMC coupon imaged near a surface crack, where depletion of the BN interphase, excessive borosilicate glass formation, and rapid recession of the SiC fibers were observed.

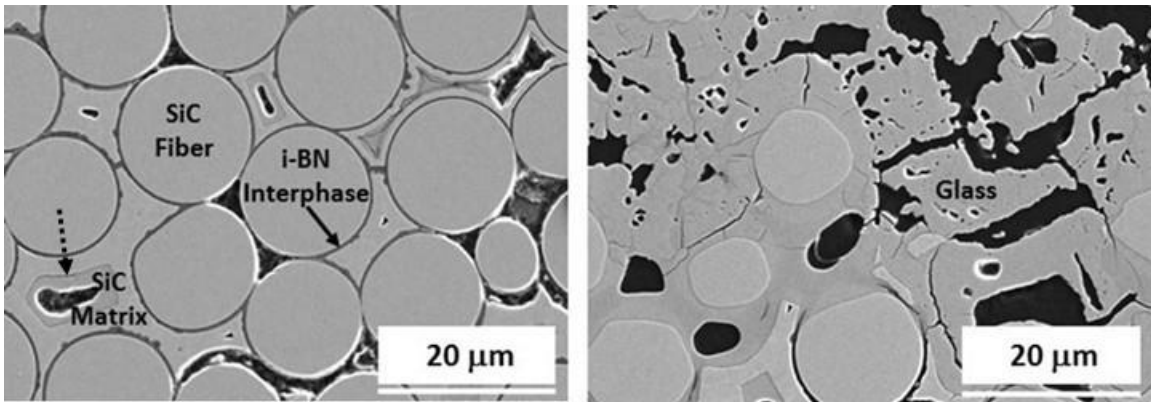


Figure 1: Scanning Electron Microscopy (SEM) images of CMC's after high temperature oxidation at 1316°C, 6atm total pressure, 0.6 atm H₂O partial pressure, 21 m/s gas velocity for 100h³. A) Interior portion of CMC imaged away from a surface crack, and B) CMC portion imaged near a surface crack illustrating excessive glass formation, fiber and matrix degradation.

This research project seeks to understand the effects of boria that increase CMC degradation, including answers to the following questions: 1) what are the borosilicate glass compositions that cause CMC degradation; 2) what are the time, temperature, and gas environment that lead to excessive borosilicate glass formation; and 3) what are the mechanisms that cause accelerated SiC oxidation? The following sections review the current state of knowledge on the role of boria on the oxidation of SiC. Gaps in the understanding of boria's role on SiC oxidation kinetics from these prior works are described.

2.3 *Oxidation studies on CMC components*

The CMC is a complex architecture of fibers, interphase, and matrix. Understanding the contributions of the oxidation behavior of the individual components to the oxidation behavior of the composite is large in scope. Hence, this section aims to deconstruct the complexity of CMC oxidation into smaller pieces. This section begins with a background on the present understanding of SiC and BN oxidation kinetics. Oxidation studies conducted on individual CMC components are then reviewed. This

section closes by including oxidation studies in which accelerated oxidation of Si-based systems was observed when boron (B) was present.

2.3.1 Background on SiC and BN oxidation kinetics

2.3.1.1 SiC oxidation kinetics

In high temperature dry oxygen environments, high purity SiC was shown to exhibit the passive oxidation kinetics of a slow growing oxide that acts as a barrier to further oxygen ingress¹⁷. A systematic evaluation conducted by Ramberg et al. showed that the oxidation behavior of SiC in dry oxygen environments ranging from 800 – 1100°C followed the linear-parabolic oxidation model developed by Deal and Grove on the oxidation of Si²¹. Silicon-based materials that oxidize in accord with Deal and Grove oxidation kinetics shows two rate-limiting regimes²². In the first regime, the oxidation rate is rate limited by the reaction kinetics of the oxidant and substrate. This oxidation mechanism dominates at either short times or for thin oxides. The oxide grows linearly with time, as given by Equation 9²³, where x is the oxide thickness and t is time:

$$x = k_l t^{n=1} \quad (9)$$

Oxidation in this regime is referred to as linear oxidation kinetics, where k_l in Equation 9 represents the linear oxidation rate constant. A phenomenological description of the linear rate constant is given by Equation 10, where k is the surface-reaction rate, C^* is the equilibrium concentration of oxidant in the oxide, and N_l is the concentration of oxidant molecules per unit volume of oxide²²:

$$k_l = \frac{C^* k}{N_l} \quad (10)$$

In the second regime, the oxidation rate transitions from being governed by the oxidant-substrate surface reaction kinetics to being governed by diffusion through the oxide

occurring at longer times when the oxide is sufficiently thick²². This regime is referred to as parabolic oxidation kinetics, as given by Equation 11²³:

$$x = (k_p t)^{n=0.5} \quad (11)$$

The parabolic oxidation rate constant is represented by k_p , which is related to the product of the oxidant diffusivity, D_{eff} , through the oxide and the solubility of the oxidant in the oxide, C^* , as given by Equation 12²²:

$$k_p = \frac{2D_{eff}C^*}{N_1} \quad (12)$$

Linear parabolic oxidation kinetics for SiC have been observed. Oxide thickness measurements for single crystal C-terminated ($\bar{1}\bar{1}\bar{1}$) CVD-SiC as a function of time for isothermal oxidation exposures ranging from 800 – 1100°C are shown in Figure 2. Note the fits to the oxide thickness data, which are 1) linear with time when oxidation kinetics are governed by the kinetics of the surface reaction and, 2) parabolic when the oxidation kinetics are governed by rate of oxidant transport through the growing oxide. Surface reaction kinetics dominate at 800°C, where the CVD-SiC oxidation kinetics are too slow to grow an oxide with sufficient thickness to limit the oxygen transport rate through the scale. The transition to the diffusion-limited mechanism occurs at shorter times with increasing temperature for exposure temperatures $\geq 900^\circ\text{C}$.

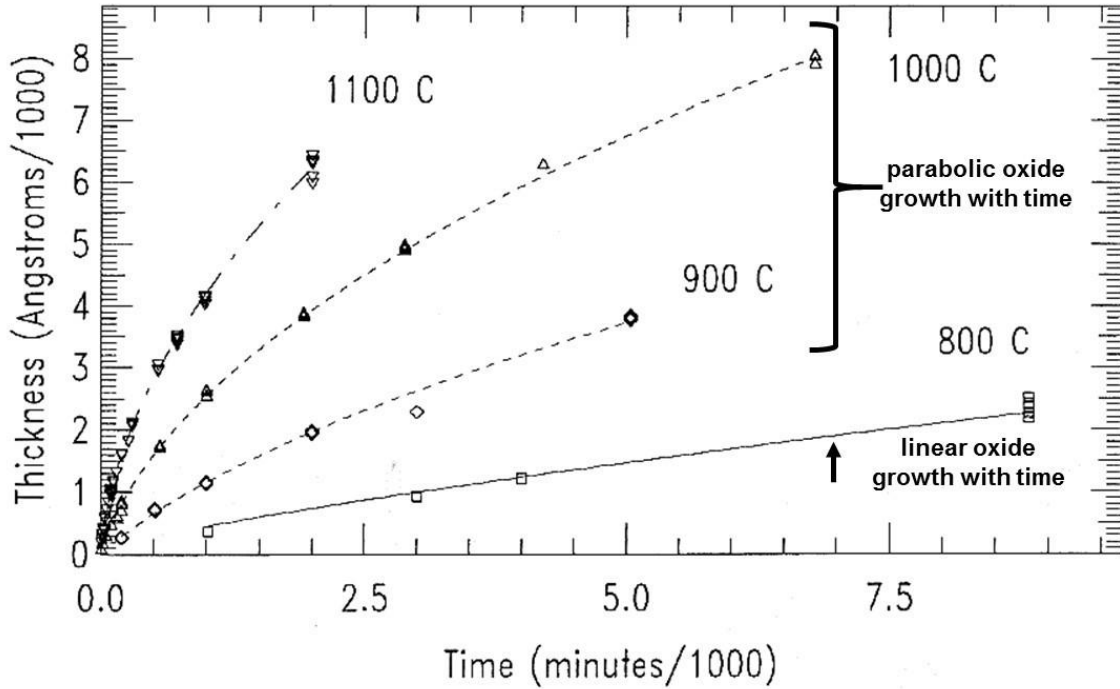


Figure 2: Oxide thickness measurements provided in the study by Ramberg et al. reported as a function of time following isothermal oxidation exposures of $(\bar{1}\bar{1}\bar{1})$ CVD-SiC in dry oxygen ranging from 800 -1100 °C²¹. The figure was annotated from the original to highlight the different oxidation mechanisms.

The SiC oxidation rate constants calculated from oxide thickness measurements can be converted to rate constants calculated from weight change measurements since the overall weight gain is derived from the oxidation reaction (i.e., in the case of the oxidation of SiC the overall weight gain is the difference between the gain in two oxygens and loss of one carbon)^{23, 24}. When oxidation is accompanied by volatilization reactions, the use of weight change can be applied only when contributions to the overall weight change from the volatilizing species are negligible.

Molecular oxidant transport through the thermally grown silica glass was demonstrated by Deal and Grove, given by the close agreement between the activation energy of the parabolic oxidation (119 kJ/ mol)²² and the activation energy of oxygen permeation through a vitreous silica membrane (113 kJ/ mol)²⁵. These results are evidence for the equivalency between 1) the thermally silica and silica glass structures,

and 2) k_p and Equation 12²². The combined mechanisms of surface-reaction kinetics and diffusion-limited kinetics in Deal and Grove's linear-parabolic model are given by

Equation 13:

$$x^2 + \frac{k_p}{k_l} x = k_p t \quad (13)$$

The mechanisms that control passive SiC oxidation kinetics are well understood, from which oxygen diffusivity through the thermally grown silica can be accurately deduced.

2.3.1.2 Pressure effects on SiC oxidation kinetics

Both SiC and Si oxidation rate constant were determined to have a power law dependence on the oxygen pressure, as given by Equation 14^{24, 26}:

$$k_p \propto P_{O_2}^n \quad (14)$$

The SiC and Si parabolic oxidation rate constants are both linearly proportional to the oxygen pressure. The oxidation rate constant and the pressure are related by the dependence of the solubility of oxygen, C^* , in the oxide on pressure, as given by Equations 15 and 16, where K is a coefficient of proportionality and $n = 1$ ²⁶:

$$C^* \propto K P_{O_2}^n \quad (15)$$

$$k_p \propto D_{eff} C^* \propto P_{O_2}^n \quad (16)$$

The parabolic rate constants will vary linearly with pressure.

2.3.1.3 Boron nitride oxidation kinetics

The oxidation kinetics of BN are not as well defined as the oxidation kinetics of SiC. The hexagonal α -BN polymorph is typically used as the interphase coating on SiC fibers^{4, 11} because the weak bonding in its layered structure allows for fracture deflection and fiber pull out from a stressed composite, increasing CMC toughness⁵. Oxygen impurity levels and degree of order (two dimensional lattice ordering versus three

dimensional lattice ordering) in the chemical vapor deposited (CVD) hexagonal α -BN were pertinent factors influencing BN oxidation behavior^{11, 18}. For instance, oxygen impurity in the BN interphase were shown to induce silica formation in the CMC at the interface of the SiC fiber and BN interphase in inert argon annealing environments¹⁸. With respect to lattice order, α -BN with a low degree of order oxidized at 900°C exhibited linear oxidation kinetics in contrast with highly ordered α -BN, which sometimes exhibited parabolic weight gain and at other times exhibited paralinear oxidation kinetics for the same oxidation conditions¹¹. Paralinear oxidation kinetics have a parabolic weight gain component that is accompanied by a linear weight loss component due to volatilization reactions²⁷. The observation of paralinear weight change in the study by Jacobson et al.¹¹ is shown in Figure 3. The weight gain component in paralinear oxidation kinetics is governed by parabolic oxidation kinetics, shown in Figure 3. The linear weight loss results from the high temperature instability of boron, given earlier by Reactions 6 – 8¹⁶.

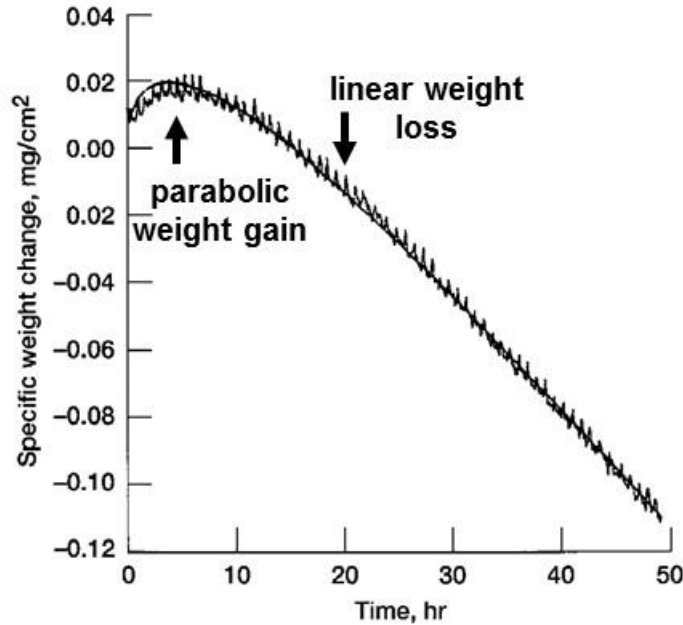


Figure 3: Paralinear weight change observed in the study by Jacobson *et al.* on the oxidation of high order BN at 900°C in dry O₂ (water impurity ranged from 7 – 44 ppm)¹¹. The original image was annotated here to highlight the parabolic weight gain and linear weight loss regimes.

The paralinear oxidation kinetics are characteristics of a non-protective oxide¹¹. Lavrenko determined rates of boria volatilization to equal the rates of BN oxidation during dry oxygen exposures at 1300°C²⁸, meaning that boria vaporized as soon as it had formed.

2.3.2 Oxidation studies on SiC fibers

2.3.2.1 Fiber oxidation in the absence of boron

Non-oxide polymer derived ceramic SiC fibers with μm-range diameters are preferred for CMC fabrication due to their high tensile strength, thermal stability, and creep resistance provided when the grain microstructure is fine, the Si: C ratio is stoichiometric, and the oxygen content is low²⁹. A recent study by Wilson and Opila showed that commercially available Hi-Nicalon™ SiC fibers demonstrated Deal and Grove oxidation kinetics when exposed to dry oxygen environments³⁰. The Hi-Nicalon™ fiber oxidation observed in the study by Wilson and Opila was governed by linear kinetics at temperatures below 900°C that then transitioned to parabolic kinetics at higher

temperatures, as shown in Figure 4³⁰. The temperature dependence of the oxidation rate constants in Wilson and Opila's study³⁰ were found to be in good agreement with the rate constants reported by others on the oxidation of CVD-SiC in dry O₂^{17, 21}.

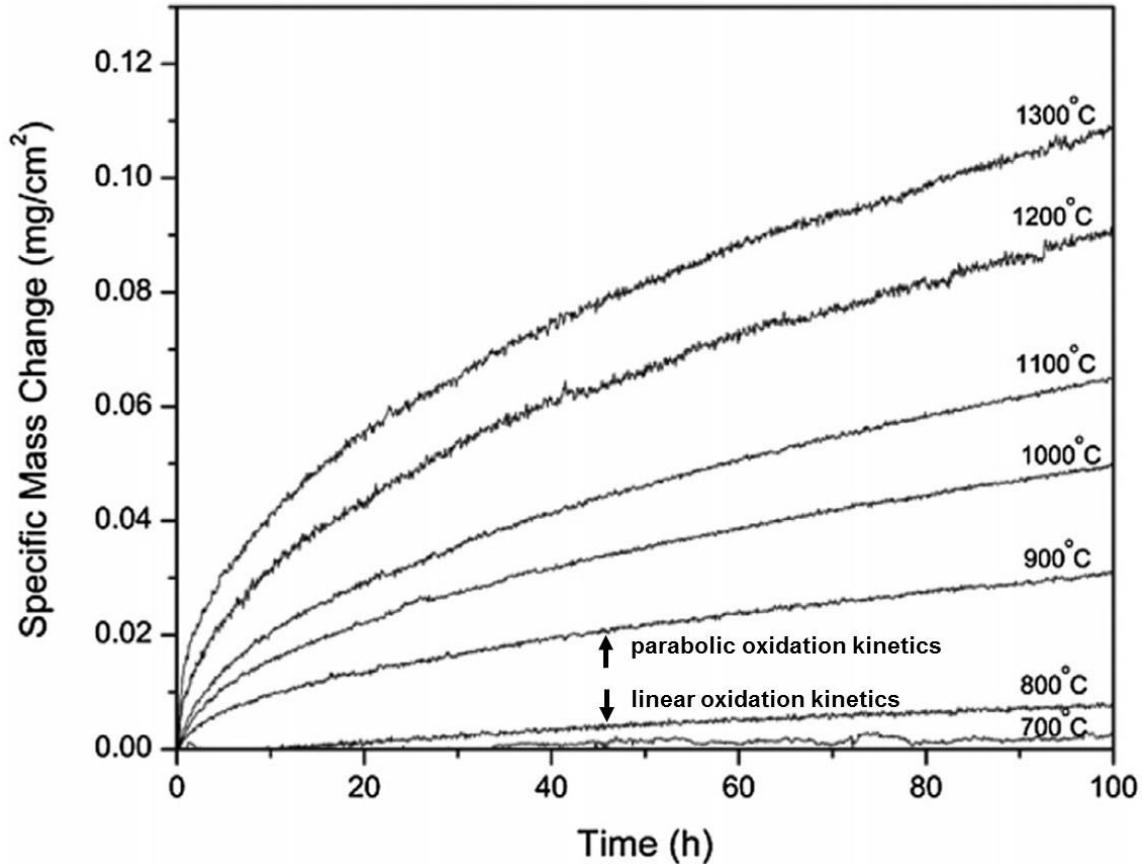


Figure 4: Plot of isothermal weight change profiles observed in the study by Wilson and Opila on the oxidation of Hi-Nicalon™ fibers in dry O₂ at temperatures ranging from 700 – 1300 °C³⁰. The original image was annotated here to differentiate the linear and parabolic oxidation regimes.

2.3.2.2 Fiber oxidation behavior in the presence of boron

Oxidation studies on non-oxide polymer-derived fibers with a Si-Hf-B-C-N composition reported very low parabolic rate constants that were attributed to the formation of a borosilicate glass thought to be more protective to oxidation than silica³¹. But, the rate constants from their study, reported to range from 1.5×10^{-9} – 8.4×10^{-9} mg² cm⁻⁴ h⁻¹, were calculated from weight change alone³¹. This is problematic in that volatile

oxides were predicted for this system at the oxidation conditions that were conducted, but weight loss from these species was neglected. The overall weight change may have been depressed by the weight loss from these volatile oxides, which could have led to underestimated oxidation rate constants calculated from the weight change results. Their study reported the oxide thicknesses to range from $\sim 2.3 - 3 \mu\text{m}$ following exposures for 200 h in air. The parabolic rate constants were calculated from their reported oxide thicknesses in this study. The calculated parabolic rate constants ranged from $2.6 \times 10^{-2} - 4.5 \times 10^{-2} \mu\text{m}^2/\text{h}$. Although a conversion from oxide growth to weight gain cannot be done in this case due to the formation of multiple volatile oxidation products, qualitatively the rate constants determined by weight change underestimate the actual oxide growth. Therefore, a quantitative microstructural evaluation of oxide thickness and fiber recession is needed to accurately assess oxidation behavior when high temperature oxidation exposures involve volatilization^{32, 33}.

A study by Lipowitz et al. used oxide thickness measurements to evaluate the oxidation behavior of SiC fibers containing B₄C and TiB₂ constituents that form a borosilicate glass when oxidized in air³⁴. The parabolic rate constant, k_p , reported by Lipowitz et al.³⁴ was extrapolated in this work to a value $2.9 \times 10^{-2} \mu\text{m}^2 \text{h}^{-1}$ by multiplying by a factor of $1 \text{ atm} / 0.2 \text{ atm}$ ³⁵ to account for the higher O₂ partial pressure used in this study. This calculated k_p is greater than the k_p reported for stoichiometric CVD-SiC oxidized at 1200°C in dry oxygen¹⁷ by a factor of 1.6. Under these conditions, the presence of B from the TiB₂ and B₄C constituents had a minor effect on the SiC fiber kinetics, but since the oxidation experiments were limited to a single temperature

(1200°C) in dry air³⁴, predictions on oxidation behavior at different temperatures, times, or environments cannot be deduced from these results.

The few studies available on the oxidation of BN-coated SiC fibers added new insights to the understanding of SiC oxidation kinetics in the presence of BN^{13, 36–38}. For instance, when the oxygen partial pressure (P_{O_2}) is low, such as at oxide-substrate interfaces where P_{O_2} levels hypothetically can be as low as $\approx 7 \times 10^{-17}$ atm, preferential SiC oxidation occurs and BN is left intact³⁸. Weight change results of BN-coated fibers exposed to P_{O_2} levels in which both silica and boria oxides are stable were inconsistent, and the weight change results did not appear to follow any known oxidation rate law^{13, 37}. For example, in a study by Naslain et al.³⁷, there was an induction period of ~ 1 h before B_2O_3 formed during exposures of BN-coated SiC fibers at 950°C in dry air (20 vol% O_2), which was then followed by more rapid B_2O_3 formation rates. In a study by Opila and Boyd, a transient period of rapid weight gain was observed during isothermal exposures of BN-coated SiC fibers in dry argon containing 5 vol% oxygen at temperatures ranging from 816 – 1343°C, which was then followed by weight change behavior resembling the oxidation behavior of SiC¹³. The weight profiles from the Opila and Boyd studies showing the transient period of rapid weight gain are provided here in Figure 5. The slowing rates of weight change following the transient period resulted from boria volatilization from the thermally grown borosilicate glass, determined by sputter depth profiling of the oxide surface with X-ray photoelectron spectroscopy. Boria volatilization leads to a greater silica concentration at the oxide surface, which slows the O_2 transport rate to that of a passivating silica oxide¹³. The transient weight change behavior was confirmed by the observance of measurable oxide thicknesses during microstructural

analysis of oxidized fibers that were removed from test after only 0.5 h of exposure. The oxide thicknesses were not reported.

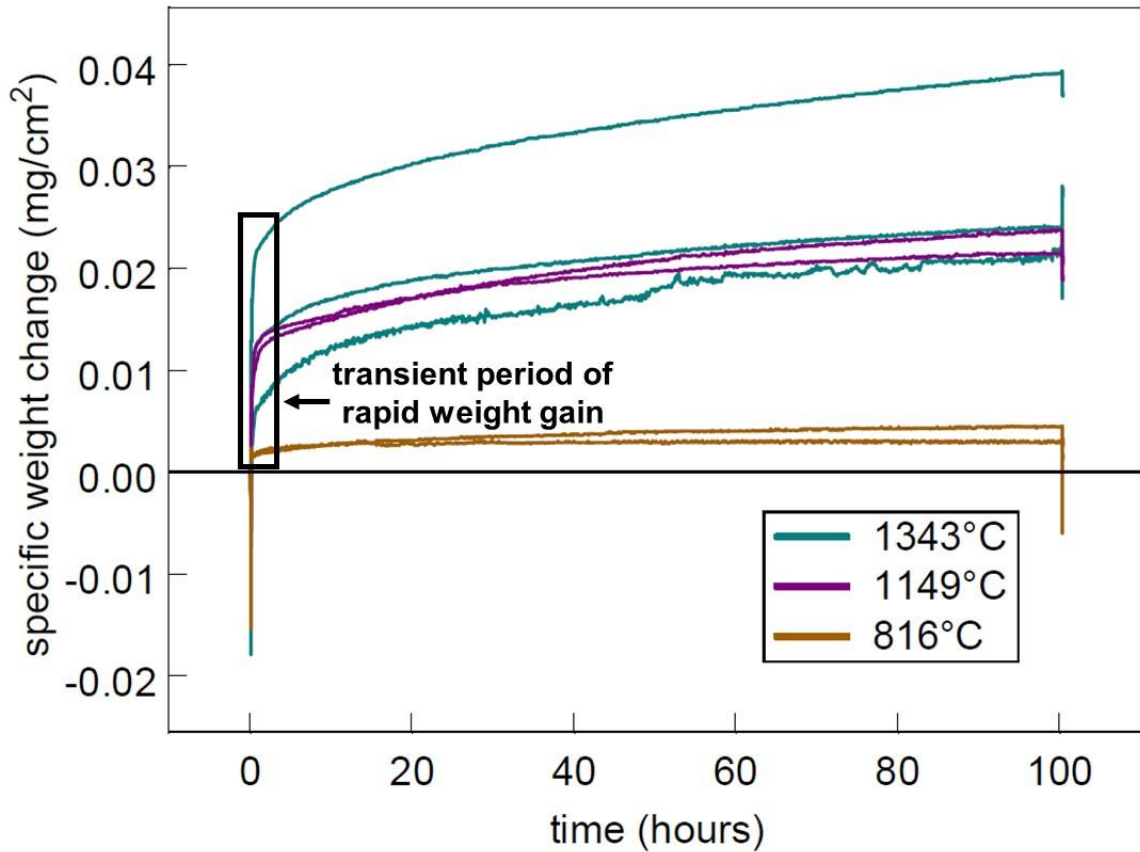


Figure 5: Plot of isothermal weight change profiles observed in the study by Opila and Boyd on the oxidation of SiC fibers with a BN layer in dry argon with 5 vol% oxygen at temperatures ranging from 816 – 1343 °C¹³. Deviation from SiC oxidation behavior due to the presence of the BN is highlighted by the black box signifying a transient period of rapid weight gain. The original image was annotated here to highlight the transient period of rapid weight gain.

It must be noted that BN layers and SiC fibers were different in the studies by Naslain et al.³⁷ and Opila and Boyd¹³, which could explain the differences in the observed oxidation behavior. The point is, however, that in both of these studies the presence of BN altered the oxidation behavior of the SiC fibers, which otherwise follows the well-defined Deal and Grove oxidation kinetic model, as shown in the study by Wilson and Opila³⁰.

Another study by Naslain et al. showed that during static fatigue testing of BN-coated fibers, the cracks present on fiber surfaces were filled in by the borosilicate glass,

which afforded better fiber oxidation resistance than if the cracks were unsealed⁴. The combination of these findings by Naslain^{4,37} and Opila and Boyd¹³ indicate that BN recession and SiC oxidation rates are rapid, leading to formation of a thermally grown borosilicate glass that is thick enough to seal cracks. As with the study by Lipowitz et al.³⁴, these studies are, however, limited in scope in terms of the set of exposure conditions and characterization methods that were conducted post oxidation. A systematic assessment of BN-coated SiC fiber oxidation weight gain, oxide thickness, and fiber recession following exposures to a range of conditions that vary in time, temperature, and gas environment is needed to determine the mechanisms that lead to accelerated SiC oxidation kinetics.

2.3.3 Boron effects on matrix oxidation

To our knowledge, reports of oxidation studies on the matrix material in the absence of fibers are not available.

2.3.4 Accelerated oxidation of Si-based systems due to the presence of boron

Oxidation studies on various Si systems that contained B-based components also found accelerated oxidation rates of the Si-based components with the formation of a thermally grown borosilicate glass^{13, 23, 39-41}. Parabolic rate constants (k_p) from a few of these studies conducted at 800°C are highlighted here and extrapolated to 1 atm of dry oxygen (O_2)^{23, 39, 41}. The k_p values were $2 \times 10^{-4} \text{ mg}^2 \text{ cm}^{-4} \text{ h}^{-1}$ for SiC-B₄C composites³⁹, $30 \times 10^{-4} \text{ mg}^2 \text{ cm}^{-4} \text{ h}^{-1}$ for B₂O₃ covered Hi-Nicalon™ fibers²³, and $60 \text{ mg}^2 \text{ cm}^{-4} \text{ h}^{-1}$ for Si coupons coated with a borosilicate glass having a nominal B₂O₃ concentrations ranging from 1 – 30 mol% B₂O₃⁴¹. The k_p values in the last mentioned study⁴¹ are orders of magnitude higher than the k_p value of $8 \times 10^{-6} \text{ mg}^2 \text{ cm}^{-4} \text{ h}^{-1}$ calculated for the oxidation of

chemical vapor deposited SiC (CVD-SiC) at 800°C in dry O₂²¹. Accelerated oxidation of Si-based systems in the presence of boria appears to be ubiquitous. While oxidation studies on Si and SiC coupons were able to relate O₂ transport in the thermally grown silica glass to O₂ permeation in silica glass^{17, 21, 22, 30}, the thermally grown borosilicate glass has not been methodically characterized and O₂ transport through a thermally grown borosilicate glass is largely not understood. Relationships between a thermally grown borosilicate glass and borosilicate glass properties have not been determined. Therefore, known borosilicate glass properties are utilized to elucidate the thermally grown borosilicate glass behavior and its effects on SiC oxidation kinetics. These properties are described below.

2.4 *Background on borosilicate glass*

2.4.1 Structures of binary borosilicate glass building blocks

A borosilicate glass is formed by the reaction between silica and boria, as described earlier by Reaction 5⁴². In Zachariassen's model for vitreous silica, viewed in two dimensions, the silica unit is comprised of SiO₃ triangles that interconnect with varying bond angles to form a continuous random network of interconnected Si-O rings that vary in size⁴³. Lichtenstein et al. were able to resolve the atomic structure of vitreous silica (v-SiO₂) utilizing Atomic Force Microscopy (AFM) in combination with Scanning Tunneling Microscopy (STM) on an atomically flat film deposited on single crystal Ruthenium⁴⁴. They not only confirmed Zachariassen's continuous random network model for v-SiO₂, as shown in Figure 6 A, but also determined that the pore sizes ranged from 4 – 9 membered rings, as annotated in Figure 6 C⁴⁴. The Figure 6 B and C are their STM

images resolving the arrangement of Si and O atoms, respectively, analyzed from v-SiO₂ films⁴⁴.

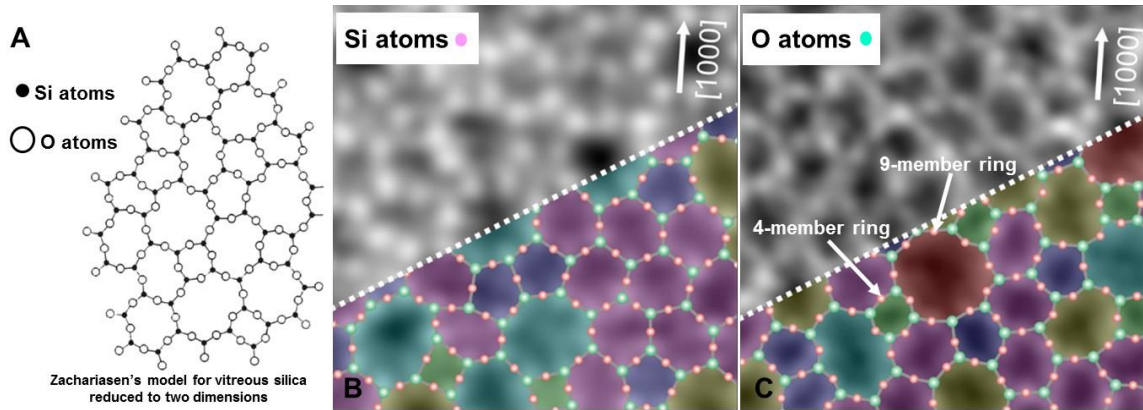


Figure 6: STM analysis of v-SiO₂ films from the study by Lichtenstein et al.⁴⁴. A) Zachariasen's schematic of v-SiO₂ structure of interconnected Si-O rings, B) STM image showing Si atom positions, and C) STM image showing O atom positions. Original image was annotated here to differentiate between Si and O atoms and to highlight the range of ring sizes.

The v-SiO₂ structure is stable up to temperatures < 1300°C, whereupon it transforms into crystalline β-cristobalite⁴⁵. Cristobalite is comprised of uniform 6-membered rings⁴⁴.

Silica has a melting temperature (T_m) of 1723°C.

Boria is mainly found in the vitreous state (v-B₂O₃)⁴⁶ and is comprised of trigonally coordinated BO₃ units⁴⁷. The v-B₂O₃ structure has been under considerable debate⁴⁷⁻⁵⁰. Neutron diffraction experiments conducted by Hannon et al. supported previous findings that the majority of B atoms make up planar B₃O₆ boroxol ring structural units and the remaining B atoms make up BO₃ triangular structural units⁴⁷. The neutron diffraction results determined 80% of B atoms were occupied in boroxol rings⁴⁷. Hwang et al. determined from nuclear magnetic resonance (NMR) analysis that 75% of B atoms made up B₃O₆ boroxol ring units, from which a 1: 1 ratio of triangular to boroxol ring units was proposed, as shown schematically in Figure 7. Raman and NMR results finding 75% of B atoms residing in boroxol ring units were consistent with molecular dynamics simulations of a “boroxol rich” model⁵¹.

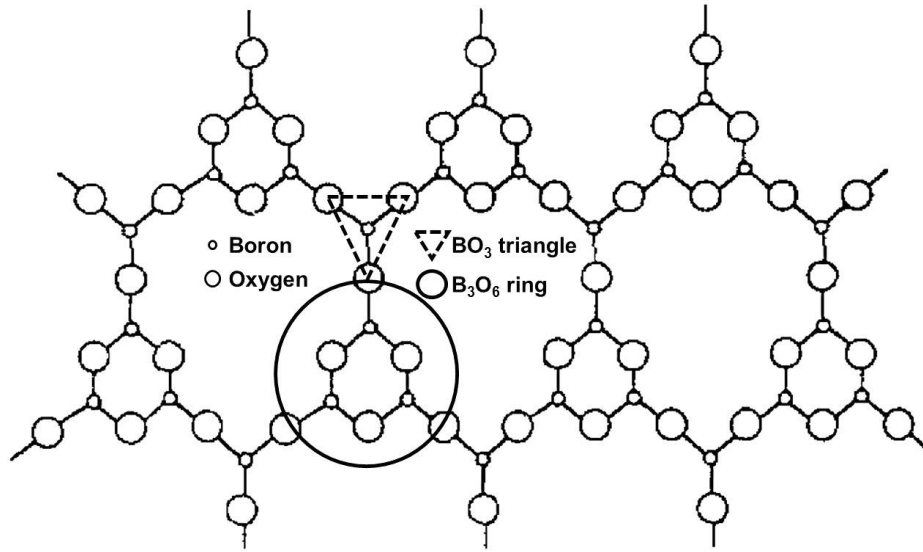


Figure 7: Annotated schematic of v-B₂O₃ from Hwang et al. proposing a 1:1 ratio of triangular BO₃ (triangle) to B₃O₆ boroxol ring (circle) units formed from three BO₃ units⁴⁸. Original image was annotated here to differentiate between boroxol ring and planar triangle arrangements.

Unlike silica, v-B₂O₃ has a low melting temperature of 450°C⁵². The structure of molten boria has also been greatly debated^{49, 50, 52–54}. Various boria properties change with temperature, which are indications of temperature-dependent structural changes that take place in molten boria⁴⁹. These structural changes, described in a review article by Krogh-Moe, were hypothetically ascribed to disruption of the boroxol ring units into to a more random network arrangement of BO₃ triangular units as temperature was increased⁴⁹. Raman spectroscopic studies on molten boria experimentally supported Krogh-Moe's hypothesis by demonstrating that intensity contributions from modes representing the BO₃ network increased with increasing temperature while intensity contributions from the boroxol ring mode decreased with increasing temperature^{50, 54}. At the 450°C melting temperature, the boroxol ring concentration calculated by Hassan et al. had reduced from 60% in the glass to ~45% in the liquid, and continued to decrease linearly as temperature was further increased to 1000°C⁵⁴. Molecular dynamics simulations supported experimental findings that observed the reduction in boroxol ring

concentration with increasing temperature⁵¹. A model constructed by Ferlat et al. was shown to be consistent with experimental results that determined the fraction of B atoms in boroxol rings to decrease from 75% in the vitreous state to ~ 15 – 20% at 1627°C⁵¹. It is postulated here that the boria oxidation product of B-based constituents may similarly undergo considerable structural changes at different exposure temperatures.

2.4.2 Borosilicate glass: Binary SiO₂-B₂O₃ phase diagram

Rockett and Foster constructed the binary SiO₂-B₂O₃ phase diagram, shown in Figure 8, by mixing different compositions of SiO₂ crystalline phases that would be stable at the firing temperature with predominantly v-B₂O₃⁴⁶. The phase diagram shows, most notably, that slight additions of B₂O₃ to SiO₂ sharply reduce the liquidus to lower temperatures. Although concavity was observed along the liquidus, liquid immiscibility was not detected in the amorphous glass phase.

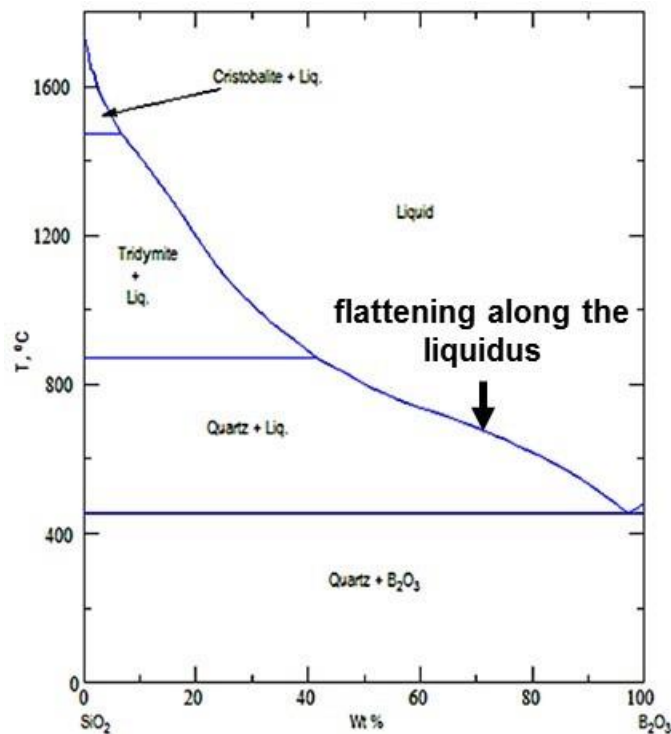


Figure 8: Binary SiO₂-B₂O₃ phase diagram by Rockett and Foster⁴⁶. Figure was annotated from the original to highlight flattening of the liquidus.

2.4.3 Borosilicate glass viscosity

Increasing boria concentrations not only lead to significant reductions in the borosilicate glass melt temperature, as shown by the phase diagram in Figure 8, but also results in a correspondingly significant reduction in the borosilicate glass viscosity^{42, 55}. For example, additions of up to 44 mol% B₂O₃ to SiO₂ were found to reduce the SiO₂ viscosity by up to *seven* orders of magnitude at temperatures ranging from 1000 – 1390°C⁵⁵. The sharp viscosity reductions that occur in SiO₂ with increasing B₂O₃ additions were plotted in Figure 9.

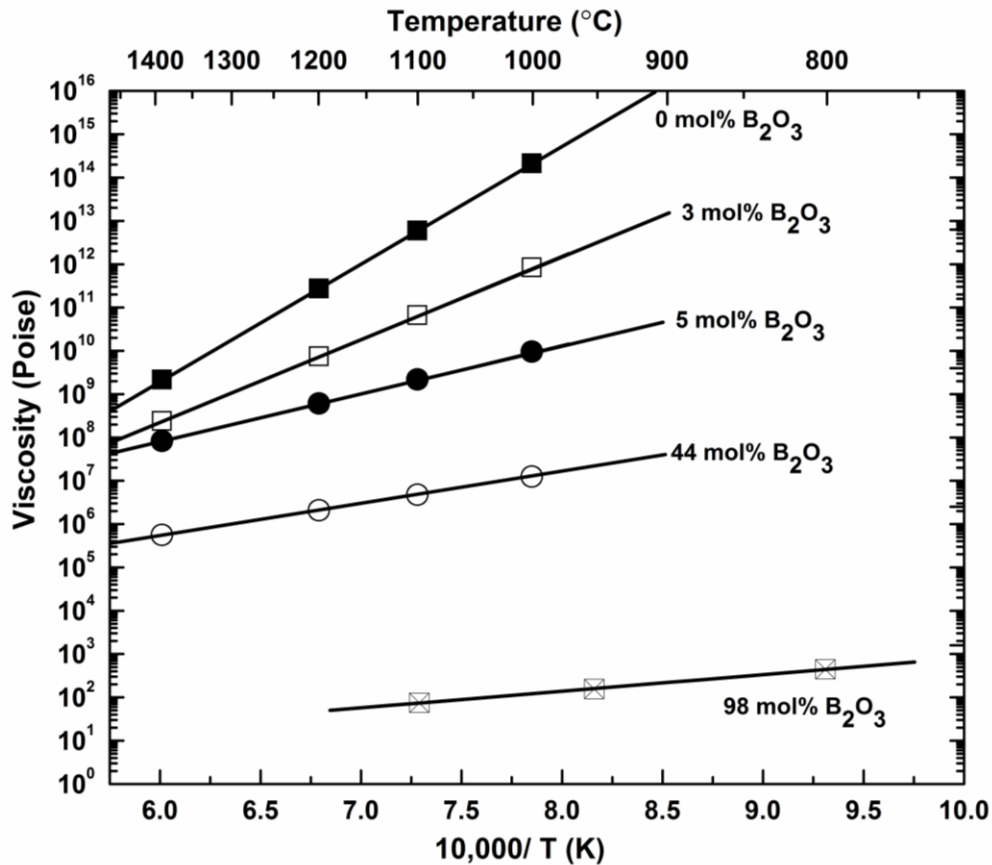


Figure 9: Reduction in SiO₂ viscosity by B₂O₃ incorporation plotted as viscosity on a log₁₀ axis versus inverse temperature ranging from 800 to 1390°C for varying borosilicate glass compositions. Viscosities were calculated from data reported by Yan et al. (0, 3, 6, and 48 mol% B₂O₃, balance SiO₂)⁵⁵ and Bruckner and Navarro (98 mol% B₂O₃, balance SiO₂)⁴².

Several studies found that formation of a low viscosity thermally grown borosilicate glass protected carbon (C) fibers or C-coated SiC fibers from rapid oxidation⁵⁶⁻⁶⁰. The fibers were infiltrated with a SiC matrix, which was prone to crack, thus exposing the fibers to O₂ by ingress through the cracks⁵⁶⁻⁶⁰. Boron-based interlayers were incorporated in the SiC matrix⁵⁶⁻⁶⁰. Similar to the oxidation of BN to boria, shown by Reactions 3 – 4, the oxidation of the boron-based interlayers produced boria. Silica that formed from SiC oxidation reacted with the boria to form a borosilicate glass. The formation of the borosilicate glass, having a lower viscosity than silica, sealed the SiC cracks, and thereby cut off O₂ ingress.

Some studies that used this crack-sealing approach also observed considerable SiC fiber recession adjacent to areas where a thick borosilicate glass had formed from the oxidation of the B-based interlayers in the matrix^{58, 59}. The recession was attributed to dissolution of the SiC fiber by the adjacent borosilicate glass^{58, 59}. A study by Hatta et al. determined that boria coatings were better in sealing SiC cracks and less prone to dewetting than borosilicate glass coatings, both of which were synthesized by a sol-gel method⁶⁰. Oxidation of boria-coated SiC plates in dry air from 1200 – 1600°C resulted in the unexpected development of a much thicker SiO₂ scale than had formed an uncoated SiC plate exposed to the same oxidation conditions⁶⁰. The increased SiO₂ growth was attributed to a reaction between SiC and B₂O₃ to form SiO₂ and to greater O₂ diffusivity through the borosilicate scale⁶⁰. These findings are in accord with Schlichting who showed orders of magnitude increases in Si oxidation rates to occur in dry O₂ environments when coated with sol-gel derived borosilicate glass layers⁴¹. Schlichting

attributed the faster Si oxidation kinetics to boria facilitating more rapid O₂ transport through the oxide by opening up the silica glass structure⁴¹.

2.5 Challenges faced in elucidating the effects of a borosilicate thermally grown oxide on SiC oxidation kinetics

A large body of research that supports boria-assisted accelerated oxidation of SiC was presented. And yet, the mechanisms that lead to accelerated SiC oxidation kinetics remain unanswered. Many questions persist, the foremost being an unknown thermally grown borosilicate glass composition. Gas transport rates through the thermally grown borosilicate glass likely depend on the borosilicate composition, which in turn affects SiC oxidation kinetics. Composition-dependent borosilicate glass properties with respect to gas transport, glass structure, and glass stability are reviewed below to provide insight into thermally grown borosilicate glass behavior in high temperature oxidation environments.

2.5.1 Compositional dependence of borosilicate glass properties

2.5.1.1 Gas transport through a borosilicate glass

Gas transport through vitreous boria and silica occurs via molecular diffusion. The gas diffusion coefficient is the quotient of the gas permeability and its solubility coefficient in the glass, as shown in Equation 17^{61, 62}.

$$D = \frac{P}{S} \quad (17)$$

Brown and Doremus determined an O₂ diffusion rate of 2.3 x 10⁻⁷ cm² s⁻¹ through molten boria at 550°C⁶³. This O₂ diffusion rate is significantly higher than the O₂ diffusion rate in vitreous silica determined by Norton²⁵, extrapolated here to 1.8 x 10⁻¹¹ cm² s⁻¹ at 550°C, assuming that O₂ solubility remains unchanged. Additions of boria to silica are expected

to increase the O₂ diffusivity; however, correlations between the boria concentration in the borosilicate glass and O₂ diffusion rates are presently unavailable.

2.5.1.2 High temperature stability of the borosilicate glass structure

Since the construction of the binary SiO₂-B₂O₃ phase diagram⁴⁶, advances in solid-state nuclear magnetic resonance (NMR) and Raman spectroscopy enabled researchers to probe the bonding environment in borosilicate glasses. Such studies determined that the borosilicate glass structure is a mixture of silica (Si-O-Si), boria (B-O-B), and borosilicate (Si-O-B) network units⁶⁴⁻⁶⁶. Room temperature Raman spectra of borosilicate glasses with varying boria concentration found occurrence of an Si-O-B bonding peak at 935cm⁻¹ for boria concentrations ≥ 40 mol%, balance silica⁶⁶. NMR spectra from Lee and Stebbins showed that B atoms residing in BO₃ planar triangles and in B₃O₆ boroxol rings both contribute to bonding with the SiO₄ silica unit⁶⁵. They further determined that the concentration of boroxol rings increase with increasing boria concentration in the borosilicate glass⁶⁵.

The Raman studies by Furukawa and White found that considerable structural changes occurred in the borosilicate glasses when heated above the glass transition temperature, T_g⁶⁶. As with ν -B₂O₃, the 808 cm⁻¹ mode assigned to the boroxol ring in an equimolar glass composition was shown to decrease in intensity when the borosilicate glass was exposed to temperatures $\geq 300^\circ\text{C}$. The decomposition of boroxol rings was attended by an increase in the 475 cm⁻¹ band, assigned to B-O-Si and B-O-B bonds⁶⁶. These results show that the temperature dependent structural changes that occur with ν -B₂O₃ are carried over when boria is dispersed in a silicate network. The combination of the O₂ diffusion studies in molten boria with the structural changes that occur in with the

boria components in a borosilicate glass suggests that oxidant transport increases with increasing concentrations of BO_3 units in the glass network. The varying thermally grown borosilicate glass structure adds to the challenges in defining O_2 transport mechanisms in a borosilicate thermally grown oxide.

In addition to the ramifications involved in understanding O_2 transport in an oxide that may undergo structural changes similar to borosilicate glasses, the thermally grown borosilicate glass is also unstable in high temperature environments due to boria volatilization^{42, 57}. Boria volatilization reactions, given earlier by Reactions 6 – 8¹⁶, are also known to occur in borosilicate glasses^{57, 60}. The occurrence of these reactions in a thermally grown borosilicate glass can alter its surface composition at the gas-oxide interface. Evidence of boria volatilization was found in oxidation studies of Si-B based materials that did not characterize the thermally grown borosilicate glass for composition, wherein boria was either absent entirely^{8, 12}, or it was present below the scale surface at concentrations up to 20 mol%^{13, 40, 59, 67}. Thus, boria volatilization will lead to a boria concentration gradient in the thermally grown borosilicate glass, which may in turn change O_2 transport rates across the scale.

2.6 *Summary of gaps in the present knowledge of the borosilicate thermally grown oxide and methodologies undertaken in this research project to resolve them*

Table 1 summarizes the gaps in the available knowledge of the borosilicate thermally grown oxide. Methodologies that were undertaken in this research study to fill in those gaps is also presented.

Table 1: Summary of gaps in the present understanding of the thermally grown borosilicate glass and its effects on SiC oxidation kinetics and methodologies undertaken in this research project to advance the present state of knowledge.

Gaps in present knowledge of thermally grown borosilicate glass	Methodologies undertaken to advance the present state of knowledge
Thermally grown borosilicate glass properties	<ul style="list-style-type: none"> • Systematic oxidation exposures were conducted on SiC materials containing boron that oxidize to form a borosilicate glass • Extensive characterization techniques were employed on the oxidized specimens to uncover thermally grown borosilicate glass properties for microstructure, composition, and structure following each oxidation exposure • Borosilicate glass coatings with well-defined composition and structure were applied onto SiC substrates to understand the effects of a known boron concentration in the glass coating on the SiC oxidation kinetics • The oxide formed from oxidation of borosilicate glass coated SiC substrates was compared to the oxide formed from the oxidation of boron-bearing SiC materials to determine if synthetic borosilicate glass coatings model the thermally grown borosilicate glass
Oxidation conditions that lead to accelerated SiC oxidation kinetics	<ul style="list-style-type: none"> • Oxidation studies were carried out in dry O₂ to maximize boron retention by minimizing boron volatilization reactions to improve resolution of boron effects on SiC oxidation kinetics • Isothermal oxidation exposures were carried out from 800 – 1300°C to determine temperature-dependent effects on accelerated SiC oxidation in the presence of boron • Isothermal oxidation exposures were also carried out from 1 – 100h to determine time – dependent effects on accelerated SiC oxidation in the presence of boron
Mechanisms causing accelerated SiC oxidation kinetics	<ul style="list-style-type: none"> • Weight change, oxide thickness, and substrate recession were methodically carried out for each oxidation exposure to determine mechanisms that lead to accelerated SiC oxidation kinetics as a function of oxidation conditions and oxide composition

Application of sol-gel derived borosilicate glass coatings on SiC substrates for the goal of understanding the effects of the known boron (B) concentration in the borosilicate glass coatings on the SiC oxidation kinetics is based on a previous study by Schlichting⁴¹. Schlichting’s study showed that the borosilicate glass coatings, applied onto Si substrates, accelerated the Si oxidation kinetics significantly. These results and the validity of adapting his approach to this research project is reviewed in the next section.

2.6.1 Modeling the borosilicate thermally grown effects on SiC oxidation with sol-gel derived borosilicate glass coatings

The motivation in modeling the borosilicate thermally grown oxide in this study is to facilitate the current understanding of how borosilicate glass affects SiC oxidation kinetics. Borosilicate glass coatings of known B concentration were applied onto SiC substrates to replicate the borosilicate thermally grown oxide. Methods that reliably

produced well-defined coatings with sufficient B concentration were required. These methods also had to enable the application of $<1 \mu\text{m}$ thin glass layers that represent oxide thickness at early stages of oxidation. These requirements for thin glass layers automatically precluded melt methods with silica and boria powders. Alternatively, sol-gel derived borosilicate glass coatings showed promise to meet the criteria of both aforementioned requirements.

2.6.2 Previous oxidation study on Si substrates coated with sol-gel derived borosilicate glass layers⁴¹

Schlichting⁴¹ performed a study to understand O_2 transport in high-temperature oxidizing environments through various borosilicate glass film compositions coated onto Si substrates, as summarized in Figure 10 A. The coating compositions were prepared by a sol gel method. The effects of boria concentration in sol-gel derived borosilicate glass coatings on the transport rate of O_2 as compared to O_2 transport in silica glass films on Si were investigated. The increase in the O_2 diffusion rate was found to be significant: a 1 mol% boria addition to silica increased the oxygen diffusion coefficient by nearly four orders of magnitude (Figure 10 A). The Si oxidation rates determined experimentally for a substrate coated with a pure SiO_2 sol-gel derived glass coating were compared with the classic Deal and Grove results for thermally grown oxides on Si in Figure 10 B²². Despite the steeper slope of the sol-gel derived silica glass layer, the parabolic rate constants in both studies are within the same order of magnitude. This comparison validates Schlichting's approach to understanding oxidation of Si-based materials through application of sol-gel derived glass layers as models for thermally grown oxides followed by standard oxidation experiments.

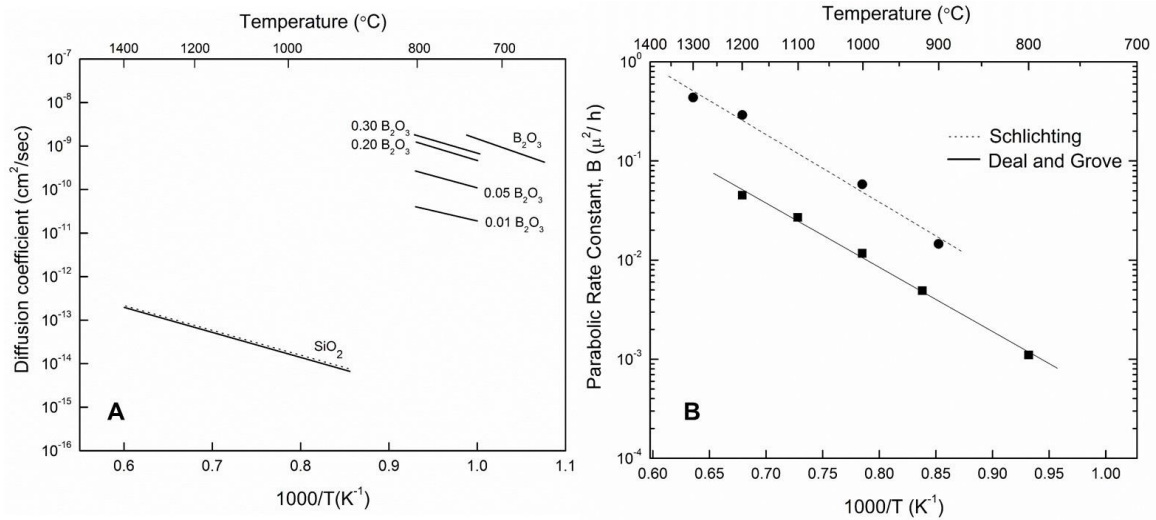


Figure 10: Comparison of parabolic oxidation rates for silicon. A) O₂ diffusion rates calculated from parabolic rate constants determined from the oxidation of silicon substrates coated with sol-gel derived glass layers (re-plotted from Schlichting⁴¹). B) Deal and Grove parabolic oxidation rate constants of silicon²² compared to the parabolic oxidation rate constants of silicon coated with sol-gel derived silica layers from Schlichting's study.

The utilization of sol-gel derived glasses that are well-defined in composition, bonding, and phase are paramount so that insights into the thermally grown borosilicate glass behavior can be obtained from the effects of sol-gel derived borosilicate glasses on SiC oxidation. These requisites led to several important questions about the sol-gel derived borosilicate glass coatings used in the Schlichting study that were addressed here.

Firstly, Schlichting reported only nominal compositions of sol-gel derived borosilicate glasses, which were synthesized by boria additions to hydrolyzed silane. The problem with reporting nominal concentrations is that the boria concentrations may have been significantly overestimated. Boron loss is a well-known problem associated with borosilicate synthesis procedures, leading to actual glass compositions with more than 40% to nearly 100% loss of boron⁶⁸⁻⁷¹. The limited yield of reacting precursors and the concomitant precipitation of boric acid resulting in boron loss in converted glasses were described early on by Nogami and Moriya⁶⁹. Irwin attributed borosiloxane bond instability in gels to hydrolysis by the presence of water, but spectrally observed the integration of hydrolyzed species into borosilicate bonds with the thermal removal of

water⁷². The water and silane ratio were additional factors used to limit boric acid precipitation in the gels⁷³. Advances in increasing boron retention in the gels were achieved by Soraru (1999), who further pushed the state of the art to decrease boron loss by increasing catalyst pH and by replacing methylated silane with ethyl/ vinyl silanes, which seemed to shield the Si-O-B bond from hydrolysis by steric hindrance⁷⁰. Recent synthesis procedures by Grandi advanced boron retention in borosiloxane gels by replacing trialkylborate with trimethoxyboroxine and by substituting a portion of the methylated silicon alkoxide with aminopropyltriethoxysilane, leading to boron concentrations in the xerogel that approached nominal values⁶⁸. While these works provided gainful insight into chemistries that led to increasing boron retention in sol-gel derived borosilicate systems, studies on boron concentration reproducibility and its stability in glasses are not presently available.

Secondly, Schlichting utilized coating film thicknesses of $\sim 10 \mu\text{m}$, determined by scanning electron microscopy (SEM) or from coating weight estimates. This film thickness is problematic because it is difficult to get a crack-free, adherent coating at thicknesses above $1 \mu\text{m}$ ⁷⁴. A $10 \mu\text{m}$ silica coating thickness is a long diffusion pathway for oxygen ingress for further oxidation, and is representative of thermally grown silica thicknesses exposed to an oxidation environment for 500 h at 1100°C , the upper temperature limit reported by Schlichting for oxidation experiments. Schlichting's oxidation exposures for the coated Si were 20 h in duration, which are short times to measure significant weight changes with such thick films.

Thirdly, carbon retention from organic volatilization during the gel-to-glass conversion is common to sol-gel derived silica and borosilicate glasses, particularly when

heat-treated in an inert atmosphere^{75, 76}. Although a dark appearance to the glass layers, indicative of carbon retention, was not mentioned in Schlichting's study, retained carbon oxidation has since been shown to occur in bulk sol-gel derived and crosslinked polysiloxane-siliconoxycarbide (SiOC) specimens at elevated temperature in air⁷⁷. Carbon minimization in the sol-gel derived glass layers is sought in this study so that boron effects on SiC oxidation are not shielded by retained carbon oxidation from the sol-gel derived glass layers expected to occur during oxidation studies. Volatilization of the organics in oxygenated and water vapor gas environments was found to reduce carbon retention in the heat treated glasses⁷⁸⁻⁸⁰. A preferable approach to reducing carbon retention in sol-gel coatings that would avoid SiC substrate oxidation during glass conversion is exposure of the coatings to hydrogen during glass conversion, which was found to decrease carbon concentration SiOC ceramics derived from silicone resin by the evolution of methane gas⁸¹⁻⁸³. Determining the carbon bonding to the glass structure as part of the glass network or segregation in elemental forms⁸⁴ is an area of active investigation⁸⁵, and it can have notable effects on the microstructure and high temperature properties of silica⁸⁶ and borosilicate sol-gel derived glasses⁷⁵.

A comprehensive study addressing these issues surrounding sol-gel derived glass coatings intended here to model thermally grown borosilicate glasses was undertaken in this work. In summary, the multiple advantages of synthesizing glass compositions by sol-gel method include room temperature synthesis, thin coating application (< 1 μm), and casting of monolithic freestanding glasses. However, the borosilicate sol-gel technique is prone to B loss leading to actual B concentrations that are considerably lower than nominal values⁶⁸. The synthesis also does not replicate binary SiO_2 -

B₂O₃ glasses, primarily due to carbon retention from partial organic volatilization during the gel-to-glass conversion⁷⁵. The retained carbon is expected to oxidize in the high temperature oxygen environment^{80, 82, 83} and might affect oxygen transport through the glass coating during exposure. Boria volatilization is also expected to occur during high temperature exposure⁵⁷, thus changing the glass composition over the duration of the test. Consequently, thorough characterization of sol-gel derived glasses was conducted prior to and after oxidation testing. These issues amongst others (Table 2) were addressed during this research project development.

Table 2: Issues that arose in replicating Schlichting’s study⁴¹ and methodologies undertaken in this study to address these issues

Issues	Schlichting’s Study ⁴¹	Addressed in This Research Project
Sol-Gel Derived Glass Characterization	<ul style="list-style-type: none"> Boron loss from sol-gel synthesis not mentioned Characterization of sol-gel derived glasses not reported Carbon retention by sol-gel process not mentioned 	<ul style="list-style-type: none"> Optical spectrometry quantified Si, B concentrations Vibrational spectroscopy mapped glass bonding Diffraction confirmed amorphous structure Retained carbon confirmed for content and phase
Coating Thickness	<ul style="list-style-type: none"> Utilized 10 μm coating thicknesses 	<ul style="list-style-type: none"> Coating thicknesses applied down to ≤ 1 μm minimized film cracks and were more representative of actual TGO thicknesses
High-Temperature Oxidation Procedure	<ul style="list-style-type: none"> Borosilicate coated coupon oxidation studies conducted at 700°C – 800°C for 20h 	<ul style="list-style-type: none"> Silica and borosilicate coated substrates exposed to 800°C, plus 1200°C relevant combustion engine use temperatures for 100 h
Interpretation of Oxidation Results	<ul style="list-style-type: none"> High-temperature boria volatilization reactions were not accounted for Carbon oxidation from carbon retention in sol-gel derived glasses not mentioned 	<ul style="list-style-type: none"> Change in boron concentration in borosilicate coatings and glasses quantified before and after oxidizing exposures Change in carbon concentration quantified in glasses after oxidizing exposures

3 Experimental procedure

The experimental procedure is organized into four sections. The first section describes the silicon-based materials that were used in the oxidation studies. The second section describes the equipment used for heat treatment and oxidation exposures. The third section describes the sol-gel methods that were optimized for the coating of silicon-based substrates and the casting of freestanding glasses. The final section describes the characterization techniques used in carrying out the five tasks of the research project.

3.1 Silicon-based materials

Four different types of silicon-based materials were used for the oxidation studies. The materials sequentially described in the following sections are: SiC fibers, reaction-bonded SiC coupons, high purity SiC coupons and Si wafers.

3.1.1 Silicon carbide fibers

Two types of SiC fibers were investigated. The first type is Sylramic™ fiber having 800 fibers/ tow (COI Ceramics, Inc., San Diego, CA). This fiber, hereafter referred to as Sylramic, was reported by Lipowitz et al. to be comprised of 95 wt% stoichiometric SiC, 3 wt% TiB₂, 1.3 wt% B₄C, 0.8 wt% O, and 0.7 wt% BN³⁴. The fibers also contain free carbon^{29, 87}. The Sylramic fiber tow was supplied with a protective polyvinyl alcohol (PVA) sizing. The lanyard was desized, removing the PVA, by volatilization in a horizontal tube furnace (MTI Corporation, Richmond CA) in 99.999% ultra-high purity Ar (Praxair Distribution, Inc., Richmond, VA) at 400°C for two hours. The second type of SiC fiber investigated was a Sylramic fiber tow with a BN surface layer that was grown *in-situ* by exposing the Sylramic fiber (800 fibers/ tow) to nitrogen gas as described by DiCarlo^{88, 89}. In this process, the boron-based constituents diffuse to

the fiber surface, react with the nitrogen gas, and form an *in-situ* boron nitride (iBN) layer with a thickness of ~150 nm⁸⁸. This second fiber type is referred to hereafter as Sylramic *iBN*. The Sylramic *iBN* fibers were not sized after the *iBN* treatment and was used as-received. The fiber specimens were prepared for oxidation by cutting 10 cm fiber lengths from each respective spool, which were produced from different lots. The Sylramic and Sylramic *iBN* fibers were then twisted into lanyards, as shown in Figure 11.



Figure 11: Macrograph of a Sylramic iBN fiber lanyard.

3.1.2 Reaction-bonded silicon carbide coupons

The reaction-bonded silicon carbide (RB-SiC) coupons were supplied by Rolls-Royce, Indianapolis. The RB-SiC coupons were processed with three different boron concentrations: 0, 0.5, and 4 wt.%. They are visually indistinguishable to the eye. A representative micrograph of a RB-SiC coupon is shown in Figure 12. Prior to oxidation, the coupons were sequentially cleaned in soapy de-ionized water, pure de-ionized water, 200 proof ethanol, and acetone for 2 minutes in a VWR Symphony™ ultrasonic cleaner with digital timer and heater (VWR, Radnor, PA). They were dried under ambient air conditions.



Figure 12: Macrograph of a RB-SiC coupon.

3.1.3 High purity silicon carbide coupons for sol-gel coating experiments

The high purity silicon carbide coupons investigated were chemical vapor deposited – SiC (CVD-SiC) that is >99.9995% pure and pore-free (Coorstek Advanced Carbides, Golden, CO). The CVD-SiC tiles were machined by Bomas (Bomas Machine Specialties, Inc., Somerville, MA) into coupons (1 cm x 2.54 cm x 0.375 cm with a 0.375 cm hole for coupon suspension). The RB-SiC coupon cleaning procedure was followed for cleaning the CVD-SiC coupons. A macrograph of the CVD-SiC coupon is shown in Figure 13.



Figure 13: Macrograph of a CVD-SiC coupon

3.1.4 High purity silicon coupons for sol-gel coating experiments

The silicon (Si) coupons investigated were 1 cm x 1 cm x 0.2 cm <100> oriented Si coupon from a scored 15 cm diameter Si wafer (Ted Pella, Inc., Redding, CA). A 0.32 cm hole was drilled into each Si coupon with an Gatan Model 601 ultrasonic disk cutter

(Gatan, Pleasanton, CA) using a slurry of SiC grit. The RB-SiC coupon cleaning procedure was followed for cleaning the Si coupons. A macrograph of the Si coupon is shown in Figure 14.

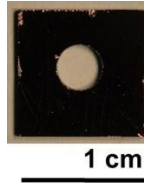


Figure 14: Macrograph of a Si coupon

3.1.5 Preparation procedures conducted prior to coating application or oxidation

The silicon carbide materials and silicon coupons were weighed before being coated and/ or oxidized on a Mettler-Toledo MS105DU analytical balance (Mettler-Toledo, LLC, Columbus, OH). The geometric surface area of the lanyards was determined from fiber diameter measurements, described later. The geometric surface area of the RB-SiC, CVD-SiC, and Si coupons was determined from dimensional measurements using a Mitutoyo Series 293 digital micrometer with a 0.001 mm resolution (Mitutoyo America, Aurora, IL). The substrates that were coated with sol-gel derived glass layers, described in more detail later, were re-weighed and the coating weight was calculated from the difference between their coated and bare weights. All oxidized specimens were weighed after oxidation exposures. The weight change results were normalized to the geometric surface area.

3.2 *Sol-gel procedure for silica and borosilicate coatings and glasses*

A synthesis route following Grandi et al.⁶⁸ was used to produce high boron containing glasses that gelled quickly with minor cracking. While the synthesis procedure was adapted from Grandi et al., the compositions and calculations for the formulations presented here were based on world patent WO/ 198942627A1⁹⁰. The silicon precursors,

tetraethyl orthosilicate (TEOS) and (2-aminopropyl)triethoxysilane (APTES) (Sigma-Aldrich St. Louis, MO) were used as-received. Two boron precursors were investigated. The first boron precursor, trimethoxyboroxine (TMBX), was also used in the study by Grandi et al.⁶⁸ and in the aforementioned patent⁹⁰ as well as others⁹¹. The second boron precursor, boria powder, has only been used by Schlichting⁴¹ for the sol-gel synthesis of borosilicate gels and glasses.

3.2.1 Detailed synthesis procedure

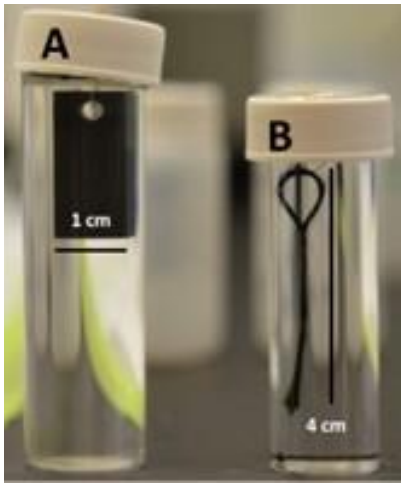
The hydrolysis of TEOS was carried out first. The acidified water catalyst was added to a mixture of TEOS with half the total volume of 200 proof ethanol. The reaction proceeded for 2-4 hours for small batch sizes (< 60 mL) and 4-24 h for large batch sizes (> 60 mL) in a two-port, 250mL Pyrex® round-bottom flask, placed in a water bath secured onto a magnetic stir/ hot plate. For elevated temperature syntheses, the hot plate temperature was set such that the synthesis temperature was raised at roughly 0.3°C/ min until stabilized to 40°C or 60°C, measured by a thermometer sealed in one port of the flask. The B precursor and the remaining volume of ethanol were added next. The sol was stirred for an additional 2-4 h for small batch volumes and 4-24 h for large batch volumes. The heat was then turned off, APTES was added, and the sol was mixed for another 5-15 minutes. Several formulation variants were executed that differed by silicon to boron (Si: B) ratio (1:0 – 0.3:1), solvent loading (10-95 vol%), catalyst type (HCl, HNO₃) and concentration (0.03 – 3N). A list of select formulations is provided in Table 3. Formulation and synthesis examples are provided in the Appendix.

Table 3: Select list of sol-gel synthesis formulations

Formulation (F)	Mol% TEOS; APTES	Mol Silane/ TMBX or Boria	Mol Si/ B	Nominal mol% B	Mol H₂O/ TEOS	Catalyst	Solvent (vol%)	Batch Temperature (°C)	
Silica-only	1	99; 1.0	---	---	---	2.7	0.06N HNO ₃	70-90	22
	2	94.5; 5.5	---	---	---	2.7	1N HCl	90	22
	3	92.5; 7.5	---	---	---	2.7	1N HCl	95	22
Boro-silicate 52-62 mol% B; TMBX pre-cursor	4	78; 22	2.8	0.9	52	1.5	0.03N HNO ₃	30-70	22
	5	76; 24	2.5	0.8	55	1.5	0.03N HNO ₃	70-90	22
	6	85; 15	2.2	0.6	62	1.5	1N HCl	90	40
Boro-silicate 67-75 mol% B; TMBX pre-cursor	7	75; 25	1.5	0.5	67	1.5	1N HCl	90	40
	8	75; 25	1.5	0.5	67	1.5	0.03N HNO ₃	90	40
	9	75; 25	1.5	0.5	67	1.5	1N HNO ₃	92.5	40
	10	75; 25	1.0	0.3	75	1.5	3N HCl	95	40-60
Boro-silicate 67-75 mol% B; Boria pre-cursor	11	75; 25	1.0	0.5	67	1.5	1N HCl	90	60
	12	75; 25	1.0	0.3	75	1.5	3N HCl	90-95	60
Boria >98 mol% B; TMBX pre-cursor	13	75; 25	0.06	0.02	98	1.5	1 N HCl	70	40

3.3 *Substrate coating techniques*

The sol-gel derived glass coatings were applied onto Sylramic fibers, CVD-SiC coupons, and Si coupons. These substrates were coated by a dip-coat method, in which the substrates were immersed in the sol, as shown in Figure 15 for an immersed CVD-SiC coupon (Figure 15 A) and SiC fibers twisted in a lanyard (Figure 15 B). Vacuum was applied during immersion of the SiC fibers in the sol⁶⁰ using a Buehler Cast N' Vac Castable Vacuum System Model 201384-115 (Buehler Lake Bluff, IL) to optimize formation of a thin, homogeneous coating onto each individual fiber. The vacuum was slowly increased to – 85 KPa (-25 in. Hg) in the vacuum desiccator, then slowly released back to ambient pressure. The substrates were then slowly removed from the sol manually. The coating thickness was controlled by the number of dip coats, which varied from 1 and 7. The wet coatings on the coupons were allowed to dry for five minutes in between dip coats. After the coating application was complete, the wet coatings on the



substrates were dried to a gel while suspended in covered containers for 1 week in ambient lab conditions. The coated substrates underwent a heat treatment procedure to convert the gel to a glass. The heat treatment procedures are described in more detail later. Following heat treatment, the coated substrates were reweighed and the coating weight was calculated.

Figure 15: SiC substrate immersion in sol coating by dip-coat method. A) CVD- SiC coupon, and B) SiC fibers twisted into a lanyard

3.3.1 Pre-oxidation conditions conducted on CVD-SiC coupons

Additional SiC substrate preparation procedures were carried out that are referred to hereafter as pre-oxidation. The pre-oxidation of the substrates resulted in the formation of a thermally grown silica glass on the substrate surface that was present prior to coating application with the sol-gel derived glass coatings. The oxidation procedures used to conduct the pre-oxidation are described in more detail later. The CVD-SiC coupons and SiC fibers were pre-oxidized prior to coating application for several reasons. One reason was to improve substrate wetting of the sol-gel coating to the SiC substrate⁴¹. The second reason was to investigate the interaction between the sol-gel derived boria glass coating and the thermally grown silica glass during oxidation exposures. Three different pre-oxidation conditions were carried out. The first applies to improved substrate wetting, in which a quick oxidation of CVD-SiC coupons or SiC fibers was conducted in dry O₂ at 1000°C for five minutes to grow an immeasurably thin thermally grown silica glass, <150 nm, calculated from the rate constant data determined by Ramberg et al. on the oxidation of CVD-SiC coupons²¹. The second and third pre-oxidation conditions were conducted on CVD-SiC coupons only, for the intent of investigating the boria glass coating – thermally grown silica glass interactions. These entailed oxidation of the coupons at 1) 1000°C for 1 h, or at 2) 800°C for 100 h. The calculated thicknesses of the silica thermally grown oxides are 0.06 μm for the 1000°C pre-oxidation condition and 0.3 μm for the 800°C pre-oxidation condition, again using the rate constant data from Ramberg et al.²¹

3.3.2 Freestanding glass casting and drying procedures

Freestanding glasses were fabricated by pipetting 7 mL of the sol into polyethylene specimen molds (7.4 mL, O.D. x H.: 38x13 mm, Fisher Scientific Waltham,

MA), where they gelled overnight in ambient fume hood conditions. Drying of the monolithic gels in their molds was optimized to minimize cracking while the gels undergo significant shrinkage during drying⁷⁴. The following drying procedure was found followed: 1) a 1.5 mm diameter hole to allow for solvent evaporation was pierced into the mold lid; 2) the sol was pipetted into several molds; 3) the covered sols were left to gel and dry in an ambient fume hood environment for 5-7 days; 4) the gels, in their capped molds, were placed in a 25-liter forced-air convection oven (MTI Corporation, Richmond, CA) in an ambient air environment at 40°C for 24h, followed by 48h at 50°C and 60°C, respectively, and finally for 24-48h at 40°C. The dried gels were then removed from their molds. A hole was drilled in their centers with a 1.6 mm diameter diamond drill bit using a Dremel rotary tool set to low speeds (5,000 rpm) to enable suspension of discs for further processing and characterization. The densified xerogels withstood drilling without breaking or shattering.

Next, the dried gel discs were suspended on alumina rods (99.5 w% purity, CoorsTek, Golden CO) and placed in a horizontal tube furnace (MTI Corporation, Richmond CA) for heat treatment to convert the gels to glasses. Two different gas environments were compared: 99.999% purity argon (Ar) gas (Praxair Distribution, Inc., Richmond, VA) or a gas mixture of 95 vol% argon to 5 vol% hydrogen (Ar/ H₂, Praxair Distribution, Inc., Richmond, VA), both flowing at 200 sccm through an alumina tube with a 30 mm inner diameter. Prior to entering the furnace, the gases were further purified in a laboratory gas drying unit (Model 26800, W. A, Hammond DRIERITE Co. LTD, Xenia, OH). The temperature of the furnace was increased to 400°C at 10°C/h in the first stage of conversion. The isothermal dwell time at 400°C ranged from 1-16 hours.

The temperature was then increased to the maximum temperature at a rate of 15°C/ h. The maximum heat treatment temperature differed as a function of nominal boron content. For silica glasses (F 1 – F 3) the maximum temperature ranged from 800 – 1000°C. The maximum temperature for mid - range boron content (F 4 – F 6) ranged from 400-800°C. For high range boron content (F 7 – F 13) the maximum temperature ranged from 400-600°C. Dwell time at the maximum temperature was 2 – 6 h followed by cooling to room temperature at 0.75°C/min.

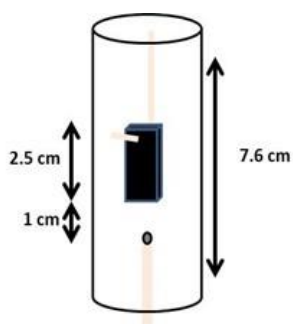
3.4 *High temperature oxidation procedures*

Thermogravimetric analysis (TGA) measures weight change as a function of time under isothermal conditions. The TGA studies were operated in a custom built apparatus⁷ shown in Figure 16. Samples were suspended on an alumina hanger (99.5 wt.% purity, Coorstek, Golden, CO) in the TGA instrument, centered within a fused quartz tube (99.995% purity, 22 mm inner diameter, Quartz Scientific, Inc. Fairport Harbor, OH), and positioned such that the sample was located in the furnace (Lab-Temp Furnace Model LSL-2.5-0-6-1M-J11214/1A, Thermcraft Winston-Salem, NC) hot zone, as shown in Figure 17.



Figure 16: Photograph of TGA Instrument

A Type R thermocouple placed 6 – 12 mm below the sample measured the sample temperature during test. The weight change was continuously measured by a Setaram B SETSYS 100g Microbalance (Setaram, Inc., Hillsborough, NJ). The microbalance was located well above the furnace to minimize signal disturbances from furnace operation.

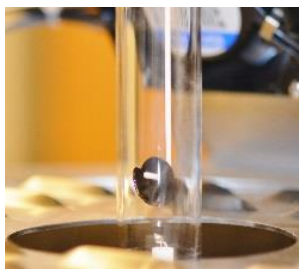


Voltage signals from the balance and temperatures from the sample thermocouple were continuously collected by an Agilent 34970A Data Acquisition/ Switch Unit (Agilent Technologies, Santa Clara, CA). Voltage signals were converted to weight change.

Figure 17: Furnace hot zone schematic

3.4.1 Gel-to-glass conversion analysis

The gel-to-glass conversion studies were conducted in the TGA instrument in Ar or Ar/ H₂ environments flowing at 100 sccm to characterize weight change of the



freestanding gels as a function of temperature and time. The time-profiles conducted in the horizontal tube furnace were also followed in the TGA instrument. The glass samples were suspended in the TGA apparatus as shown in Figure 18.

Figure 18: Example of sol-gel derived freestanding glass after conversion suspended from the alumina hanger in the TGA apparatus

3.4.2 Oxidation exposures

The oxidation exposures, and pre-oxidation exposures described earlier, were carried out in a dry 99.5% purity oxygen gas (Praxair Danbury, CT) environment that flowed at 1 atm through a MKS 247 Four Channel Readout flow controller (MKS Instruments Andover, MA) set to 100 sccm, previously calibrated to determine the actual flow rate. Isothermal oxidation exposures were conducted at 800 – 1300°C for 1 – 100 h durations. The linear gas velocities ranged from 1.6 cm/ s for 800°C and 2.3 cm/ s for 1300°C. The furnace was initially in the lowered position during heating to the set temperature programmed by a Eurotherm 2404 temperature controller/ programmer (Eurotherm Ashburn, VA). The data acquisition was initiated ~ 5 minutes after the furnace reached the set temperature. The furnace was then raised five minutes after the data acquisition was initiated. The weight change and sample temperature were captured under fast acquisition (~ 1 weight measurement/ second) for 15 minutes while the sample was heating up to the set temperature, and again during cooling at the end of test. A

weight measurement was collected every five minutes during normal acquisition in a 100 h test.

3.4.3 Freestanding glass high temperature instability studies

The freestanding glasses synthesized from sol-gel synthesis formulations F 2, F 7 - 9, and F 11 (Table 3) were exposed to the dry O₂ TGA environment at 800 and 1200°C, for 100 h. The weight change was used to understand the sol-gel derived glass instability, namely weight loss from boron volatilization and retained carbon oxidation expected to occur in the TGA environment. A combination of glass characterization techniques was performed to decouple weight loss from boron volatilization and carbon oxidation. Detailed descriptions of characterization techniques conducted in this study are provided next.

3.5 *Characterization techniques*

Several characterization techniques were conducted for each task. Variations on an individual technique were tailored to the specific type of specimen under analysis. These specimen-specific variations on an individual technique were systematically designated in the following sections describing the characterization techniques conducted in this study.

3.5.1 Scanning Electron Microscopy (SEM)

3.5.1.1 Sylramic and Sylramic *iBN* SiC fibers: bare and coated with sol-gel derived glass layers

Scanning electron microscopy (FEI Quanta LV650, FEI Hillsborough, OR) was used to characterize the uncoated and coated fibers prior to oxidation. Images were acquired with both secondary and backscattered electrons from the desized and uncoated

Sylramic and as-received Sylramic *iBN* fiber lengths and cross-sections. Energy Dispersive x-ray Spectroscopy (EDS, AZtec X-Max^N 150 Silicon Drift Detector; AZtecEnergy EDS software, Oxford Instruments, Concord, MA) was utilized for compositional analysis of the fibers and the BN coating. Measurements of the Sylramic and Sylramic *iBN* fiber diameters were made using the SEM software measurement tool, calibrated to NIST standards. Fiber diameters were measured from the cross-sections of a minimum of 25 fibers. The standard error was calculated on the mean fiber diameter with a 95% confidence interval. The fiber diameter sample mean was used to calculate the geometric surface area of a 10 cm long fiber assuming the surface area of a cylinder. The total geometric surface area of the lanyard was then estimated by multiplying the fiber surface area by the number of fibers in the tow (800). The lanyard weight change was normalized to its geometric surface area. The sol-gel derived glass coated fibers were imaged in cross-section to characterize the coating surface coverage and to measure the coating thickness. The coating thickness mean and true error were measured from the cross-sections of a minimum of 25 coated fibers.

After oxidation, the oxide thickness and fiber diameters were measured in the SEM from fiber cross-sections fractured from the lanyards. The sample mean and true error were determined from measurements on a minimum of 25 fibers. The amount of fiber recession was quantified from the mean difference between fiber diameter before and after oxidation.

3.5.1.2 Reaction-bonded silicon carbide coupons

Prior to oxidation, RB-SiC coupons were pre-characterized for phase distribution utilizing Scanning Electron Microscopy (SEM). The coupons were imaged in plan view

by SEM with backscattered electrons. The phase distribution was characterized by EDS. The EDS elemental maps were analyzed for area fraction as a function of the B concentration with Image J software. After oxidation the coupons were imaged in plan view with backscattered electrons to detect for phase distribution in the oxide. EDS maps were acquired for evidence of multiple phases in the oxides. Coupons were then cross-sectioned and oxide thicknesses were measured in SEM with the software measurement tool. Oxide cross-sections were also analyzed by EDS.

3.5.1.3 High purity CVD-SiC and silicon coupons: bare and coated with sol-gel derived glass layers

Micrographs of the bare and sol-gel derived glass coated CVD-SiC and Si coupons were acquired with secondary and backscattered electrons in plan view prior to and after oxidation. Oxidized CVD-SiC coupons were cross-sectioned and the oxide thickness mean and true error were determined from a minimum of 25 measurements spaced 0.5 – 1 mm apart along the coupon lengths. Oxide compositions were analyzed by EDS.

3.5.2 X-Ray Diffraction (XRD)

Diffraction patterns were collected from Sylramic and Sylramic *iBN* fibers, RB-SiC coupons, sol-gel derived freestanding glasses, and sol-gel derived glass coated CVD-SiC coupons with a powder diffractometer (PANalytical X'Pert Diffractometer, Westborough MA). Unoxidized fiber lanyards were first crushed into a powder using an agate mortar and pestle (Sigma-Aldrich Corp, St. Louis, MO). The fiber powder samples were analyzed to detect for the crystalline phases, namely SiC, TiB₂, and B₄C, reported by Lipowitz et al.³⁴ Sol-gel derived borosilicate glasses were also analyzed in powder

form before and after TGA exposure. Powder samples were transferred to the well (10 mm diam. x 1.0 mm depth) of a silica zero diffraction plate (30 x 30 x 2.5 mm, MTI Corporation, Richmond, CA) for analysis. The RB-SiC coupons were analyzed before and after oxidation without further modification. The sol-gel derived glass coated CVD-SiC coupons were analyzed after oxidation, also without further modification. The instrument was operated at 45 kV and 40 mA and the spectra were collected from a 2θ range of 10 - 110°, with a step size of 0.0167° held at 20.1 s per step. Crystalline diffraction peaks were identified using HighScore software (PANalytical, Westborough, MA).

3.5.3 Fourier Transform Infrared spectroscopy

Fourier transform infrared (FTIR) spectra (Thermo-Nicolet FT-IR Model 6700, Thermo Scientific, Waltham MA) were collected at Luna Innovations, Charlottesville, to identify molecular bonds in gel and in sol-gel derived glass samples before and after TGA exposure. Dried gels, converted glasses, and exposed glass samples were prepared by the KBr method and recorded in transmittance using OMNIC™ Series software (Thermo Scientific, Waltham MA). Scans were taken between 4000 cm^{-1} to 400 cm^{-1} operating under the following settings: total of 64 scans per sample and resolution 8 (3.857 cm^{-1}). A background was taken prior to every sample analysis.

3.5.4 Raman spectroscopy

Raman spectra were collected from bare and coated Sylramic fibers, Sylramic *iBN* fibers and from sol-gel derived freestanding glasses. These samples were analyzed both before and after TGA exposure. The spectra were collected between 50 – 1800 cm^{-1} using a Renishaw (Renishaw Inc. Hoffman Estates, Illinois) inVia Raman microscope under

room temperature ambient environment conditions. The fibers were mounted on a 90° SEM stub (Ted Pella, Redding, CA) and analyzed in cross-section. The freestanding glasses were crushed to a fine powder using an agate mortar and pestle, then pressed into a pellet using applied pressure with a hydraulic laboratory press with a 6.4 mm inner diameter dry pressing die (both supplied by MTI Corporation, Richmond, CA). Spectra were taken from randomly selected sites across the pellet surface. All samples were analyzed by a 514 nm Ar⁺ laser with a 3000 l/mm grating projected through 50x objective lens with a 1.5 cm focal length. The laser was oriented 90° with respect to the sample. The laser power settings ranged from 5 – 50%. Spectra were collected from scans held at 120s. Each spectrum was accumulated from 3 scans.

3.5.5 Combustion Infrared (IR) Spectrometry

Combustion IR spectroscopy (Evans Analytical Group, Liverpool, NY, using Instrumental Gas Analysis (IGA)) was conducted for total carbon concentration in the sol-gel derived freestanding glass before and after TGA exposure. The retained carbon in the sample was oxidized in an oxygen plasma (temperature > 2000°C), where evolved CO and CO₂ gases were detected by infrared detectors. The carbon concentration was quantified to ppm concentration from a minimum 10 mg sample weight.

3.5.6 Inductively Coupled Plasma – Optical Emission Spectrometry

3.5.6.1 Fiber digestion procedure

Inductively coupled plasma – optical emission spectrometry (ICP-OES) was used to measure the concentration of Si, B, and Ti digested from Sylramic and Sylramic *iBN* fibers prior to oxidation and from their corresponding thermally grown oxides after oxidation. The unoxidized fibers were analyzed to determine their stability to the

digestion solutions. The digested sol-gel derived glass coatings and oxides from glass coated Sylramic fibers after oxidation were also analyzed by ICP-OES. Hydrofluoric (HF) acid solutions are known silica glass etchants⁹² and have been used to dissolve thermally grown oxides from SiC oxidation³⁵. HF and/ or combined HF and nitric (HNO₃) acid solutions are known etchants for borosilicate glasses^{93, 94}. An oxidized or unoxidized lanyard weighing between 8 – 18 mg was digested in a 15 mL polypropylene centrifuge tube (VWR International, Radnor, PA) for 48 – 72h in a 40°C water bath with periodic sonication. Lanyards were digested in a 2: 1 volumetric ratio of deionized H₂O to a 5: 1 acid solution of HF(48% TraceMetal™ grade, Thermo Fisher Scientific, Inc., Waltham, MA): HNO₃ (67 – 70% TraceMetal™ grade, Thermo Fisher Scientific, Inc., Waltham, MA). The lanyards were left to digest under stagnant ambient conditions for 3 – 4 more days. The tubes were manually shaken and inverted several times. The liquid digestion product was then decanted off for analysis. The wet fibers were dried in ambient fume hood conditions for several days. Once dry, they were imaged in the SEM and fiber diameter measurements were made for fiber recession quantification.

3.5.6.2 High purity CVD-SiC and silicon coupon digestion procedures

The digested sol-gel derived glass coatings and oxides from oxidized glass coated CVD-SiC and Si coupons were analyzed by ICP-OES. Unoxidized coupons were included to determine coupon stability in the acid digestion solution. The unoxidized or oxidized coupons were digested in 7 mL solutions consisting of a 2: 1 volumetric ratio of deionized H₂O to HF for 48 – 72h in a 40°C water bath with periodic sonication. The coupons were left to digest under stagnant ambient conditions for 3 – 4 more days, during

which the tubes were manually shaken and inverted several times. The liquid digestion product was then decanted off for analysis.

3.5.6.3 Sol-gel derived freestanding gel and glass digestion procedure

The bulk Si and B concentrations were determined from the dried gels and converted glasses before and after TGA exposure. Samples weighing 70 – 110 mg were first dissolved in a 2:1 ratio of HF to deionized DI H₂O for several days with periodic sonication in a 40°C water bath. The concentrated digestion solutions were diluted to 500 ppm for analysis.

3.5.6.4 ICP-OES analysis procedure

An ICP-OES Thermo Scientific (Thermo Fisher Scientific, Inc. Waltham, MA) iCap 6200 Duo ICP spectrometer was used for all measurements. The instrument was operated at 1150 W RF power with 1.0 L/min auxiliary gas flow. Three repeats per sample were measured in AutoView Plasma View with 10 s integration times for both axial and radial views. The emission lines (nm) for each element are itemized in Table 4:

Table 4: ICP-OES emission lines used for detecting B, Si, and Ti from digestion solutions

Element	Emission Line (nm)
B	208.8 (I)
	249.6 (I)
	249.7 (I)
Si	185.0 (I)
	221.6 (I)
	250.6 (I)
	251.6 (I)
	288.1 (I)
Ti	308.8 (II)
	323.4 (II)

A 10 ppm (in mg/ L units) solution of Indium (In) was used as the internal standard. All Si, B, and Ti emission lines were referenced to the In 230.6 (II) nm line. A calibration curve was constructed from ICP-OES results for 0.1 ppm, 1 ppm, 10 ppm, 100 ppm, and 300 ppm Si, B, and Ti solutions prepared just prior to analysis. All internal standard and calibration solutions were prepared from 1000 ppm ICP standards (Inorganic Adventures Christiansburg, VA). The results for each wavelength per element were then averaged and converted into mole percent (mol%) concentrations.

3.5.7 X-ray Photoelectron Spectroscopy (XPS)

The surface B concentration was quantified from freestanding glasses as a function of sputter depth after high temperature exposure in the TGA instrument at 800 and 1200°C for 100 h in dry O₂. Glasses were sent to Case Western for analyses conducted in a PHI Versaprobe XPS.

3.5.8 FactSage thermochemical software

FactSage thermochemical software databases were utilized to access several phase diagrams and thermodynamic data. Prediction of products and phase were conducted by equilibrium calculations in a variety of time, temperature, and gas environment conditions.

3.5.9 Image J software for image processing and analysis

Statistical analysis of micrographs and elemental EDS maps was conducted with Image J software for particle size and area fraction analysis of phases present in a material's microstructure.

4 **Task 1: Boron nitride effects on the high temperature oxidation of silicon carbide fibers**

High temperature oxidation studies were conducted on silicon carbide fibers to elucidate the mechanisms that cause acceleration of silicon carbide oxidation kinetics by the presence of a BN surface layer. Oxidation of Sylramic *iBN* SiC fibers with a BN layer and Sylramic SiC fibers without a BN layer was conducted by thermogravimetric analysis in dry O₂ for times up to 100 h at temperatures ranging from 800 – 1300°C. The oxidized fibers were characterized for weight change, oxide thickness, and fiber recession. The boron concentrations in the oxides were quantified by Inductively Coupled Plasma-Optical Emission Spectrometry and correlated with the weight change behavior, oxide thickness, and fiber recession of the oxidized fibers. Sylramic fibers followed the Deal and Grove oxidation kinetic model. A transient period of accelerated oxidation kinetics was observed with Sylramic *iBN* fibers. Oxides formed from Sylramic *iBN* fibers were typically higher in boron concentration. The higher boron concentrations led to initial rapid oxidation rates of Sylramic *iBN* fibers that were 3 – 10 times faster than observed for pure SiC. Slower oxidation rates followed as the oxide surface became increasingly enriched with SiO₂ due to boria volatilization. Excessive SiC oxidation, thought to result from high oxide boria concentrations, was not supported by the Sylramic *iBN* oxide thickness measurements. Further, the Sylramic *iBN* fiber recession was not increased by the transient period of accelerated oxidation. Observation of BN effects on SiC fiber oxidation kinetics was limited by exposure conditions that assisted boria volatilization from the oxide surface.

4.1 *Objectives of Task 1*

A quantitative relationship between the thermally grown borosilicate glass composition and the time, temperature, and gas environment under which it formed has not been previously determined. Further, a correlation between the accelerated SiC oxidation kinetics and the boron concentration in the thermally grown borosilicate glass has not been formulated. Consequently, the objectives of this study are twofold. The first objective is to systematically determine the oxide compositions from the oxidation of B-bearing SiC fibers under varying temperature and time regimes in a dry O₂ environment. The second objective is to elucidate the effects of the oxide boron concentration on the SiC fiber oxidation mechanisms.

4.2 *Experimental re-cap*

Two types of SiC fibers were investigated: Sylramic and Sylramic *iBN*. Prior to oxidation, the Sylramic fiber was desized. The Sylramic *iBN* fiber was used as-received. The unoxidized fibers were characterized for fiber diameter, microstructure, composition, and phase utilizing SEM/ EDS and XRD characterization techniques. The fibers were prepared for oxidation testing by being twisted into lanyards from 10 cm fiber lengths cut from the spool. A representative macroimage of the Sylramic *iBN* lanyard suspended in the TGA is shown in Figure 19. Details on the fibers, desizing procedure, and the TGA instrument were provided earlier in the Experimental section. Benchtop lanyard weights were recorded before and after oxidation. Exposures were conducted for 1 – 100 h at 800 – 1300°C in dry O₂. The lanyard weight was continuously recorded as a function of time in dry O₂ exposures. The lanyards reached the set temperature ten minutes into test, which was chosen as the start point for plotting the weight change profiles. Buoyancy

effects, which occur earlier in the ten-minute heat-up stage, were eliminated. The final TGA weight was set equal to the benchtop balance weight of the oxidized lanyard. The difference between the oxidized lanyard final TGA weight and benchtop balance weight, due to balance signal drift, was linearized with time and subtracted from the TGA data.

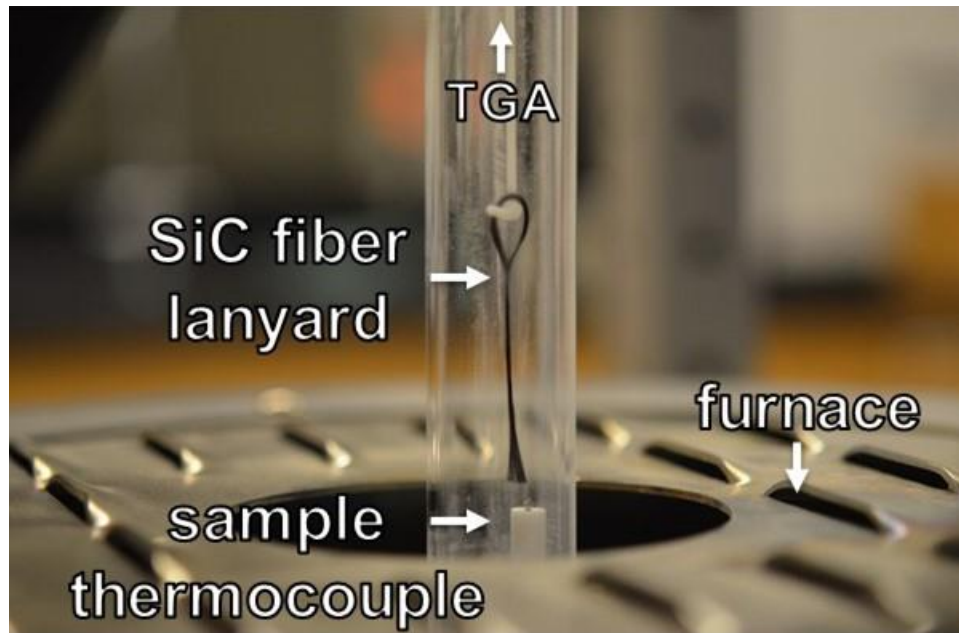


Figure 19: Sylramic iBN lanyard suspended in the TGA apparatus with the furnace in the lowered position. The sample thermocouple is located below the lanyard. The furnace is raised to initiate oxidation exposure.

The oxide microstructures were imaged by SEM with secondary electrons. Oxide thickness measurements were conducted on oxidized fiber cross-sections fractured from the lanyards. A minimum of 25 oxide cross-sections were measured with the SEM software measurement tool. The standard error on the mean oxide thickness was calculated with a 95% confidence interval. The oxidized lanyards were then digested in HF-HNO₃ solutions as described in the Experimental section. The oxide compositions were determined by ICP-OES from analysis of the digested oxide solutions. The digested fibers were dried, then imaged by SEM for with secondary electrons. The fiber recession

was calculated from measuring digested fiber diameters from a minimum of 25 fiber cross-sections, also with the SEM software measurement tool.

4.3 Results

4.3.1 Characterization of fibers prior to oxidation

The Sylramic *iBN* and Sylramic fiber surfaces were imaged by SEM with secondary electrons, as shown Figure 20 A and B, respectively. The microstructure of the BN layer (Figure 20 A) is comprised of roughly uniform, nanometer-sized spherical grains. The microstructure of the Sylramic fiber includes SiC grains intercepted with dark and bright intercalates, representative of B_4C and TiB_2 constituents, as labeled in Figure 20 B.

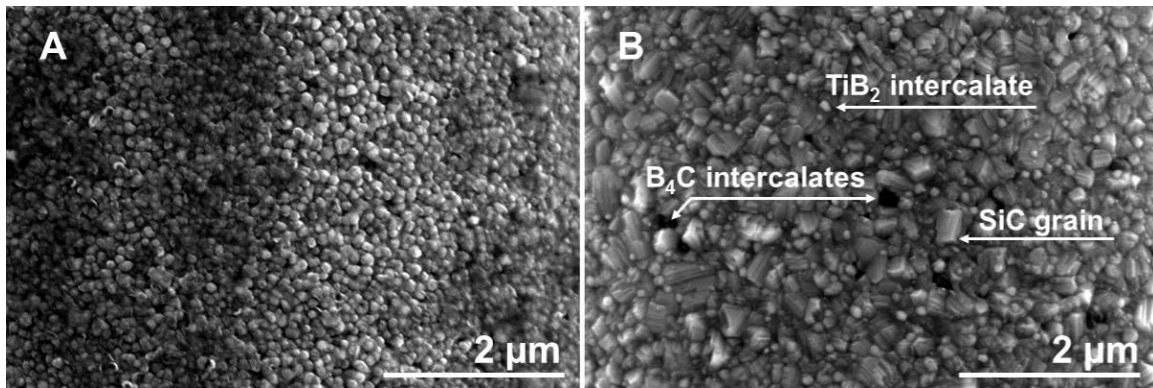


Figure 20: Secondary electron micrographs of A) Sylramic *iBN* and B) Sylramic fibers surfaces.

The Sylramic *iBN* fiber cross-section was imaged by SEM with backscattered electrons. A micrograph of the Sylramic *iBN* fiber cross-section is shown in Figure 21. The BN layer, highlighted by the arrows shows a thickness of ~ 150 nm. The cross represents a point in the BN layer that was analyzed by EDS. The inset in Figure 21 shows the X-ray spectrum resulting from signals collected at the cross. The spectrum shows that oxygen is present in the BN layer. The presence of oxygen in the BN layer is ascribed to boric acid impurity in the BN layer⁹⁵. The BN layer, which is unstable to

water vapor⁹⁶ even in ambient conditions⁹⁷, could have reacted with some moisture from the environment that was present in the desiccator. Presence of Si and C are attributed to signals coming from the fiber beneath the BN layer. Some of the C can also be attributed to contamination from the chamber.

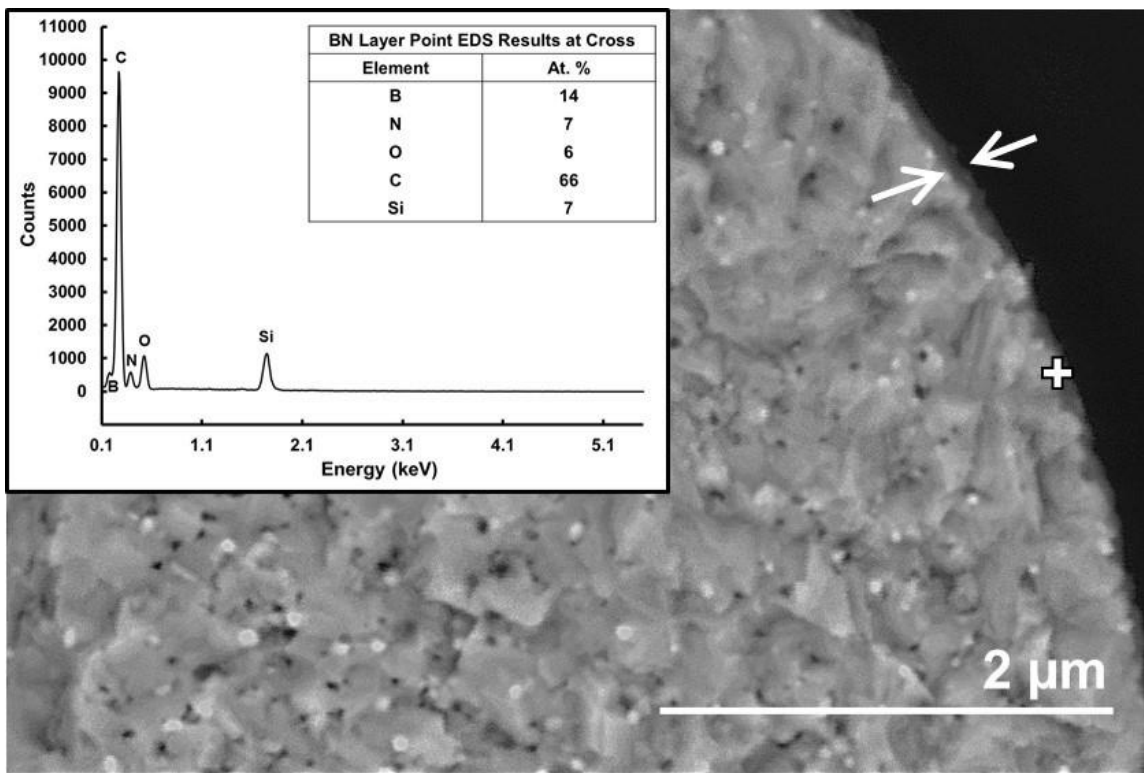


Figure 21: Backscatter electron image of Sylramic iBN cross-section illustrating the BN layer (between arrows). The cross represents point EDS sampling of the BN coating.

Elemental B, N, and O maps (Figure 22) were constructed from the EDS analysis of the Sylramic iBN fiber cross-section in Figure 21, highlighting the BN layer on the fiber surface.

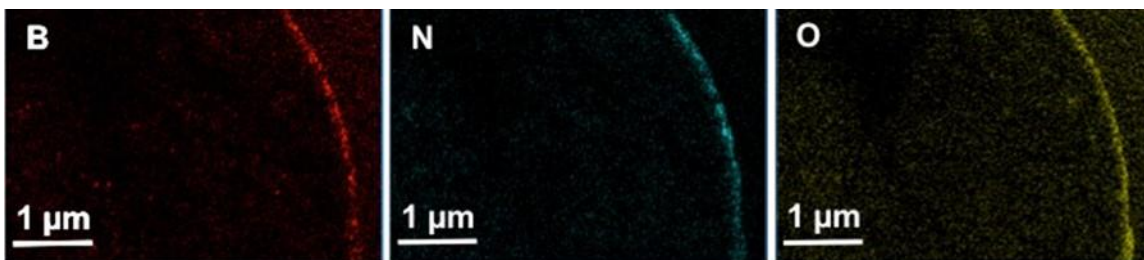


Figure 22: Elemental EDS maps of the Sylramic iBN fiber cross-section imaged from backscattered electrons.

The fiber diameters were measured from fiber cross-sections. The average fiber diameters were $9.6 \pm 0.3 \mu\text{m}$ for Sylramic and $10.4 \pm 0.5 \mu\text{m}$ for Sylramic *iBN*. Powder XRD results identified cubic β -SiC and hexagonal TiB_2 crystalline phases for both fiber types, in accord with Lipowitz et al.³⁴ and Dong et al.⁸⁷

4.3.2 Oxidation results

The results from the oxidation studies are subdivided by temperature-dependence and time-dependence for clarity. The results are described in the following sections.

4.3.2.1 Temperature-dependent oxidation results

4.3.2.1.1 Weight change profiles

Representative Sylramic fiber TGA traces were plotted as specific weight change versus time from isothermal oxidation exposures at temperatures ranging from 800 – 1300°C, as shown in Figure 23. The weight gain was linear for exposures from 900 – 1000°C, signifying that the fiber oxidation kinetics were surface – reaction controlled²³. The fibers lost weight during 800°C exposures, ascribed to oxidation of the free carbon content in the fibers⁸⁷. Linear reaction rate constants (k_1), given by the slopes of the linear weight gain, are reported in Table 5. The weight change profiles exhibited parabolic oxidation kinetics for exposures $\geq 1100^\circ\text{C}$, consistent with diffusion controlled oxidation kinetics²³. Although the Sylramic fibers generally followed the Deal and Grove oxidation kinetic model²², the deviations in the weight change profiles were attributed to oxidation effects from the B_4C and TiB_2 constituents.

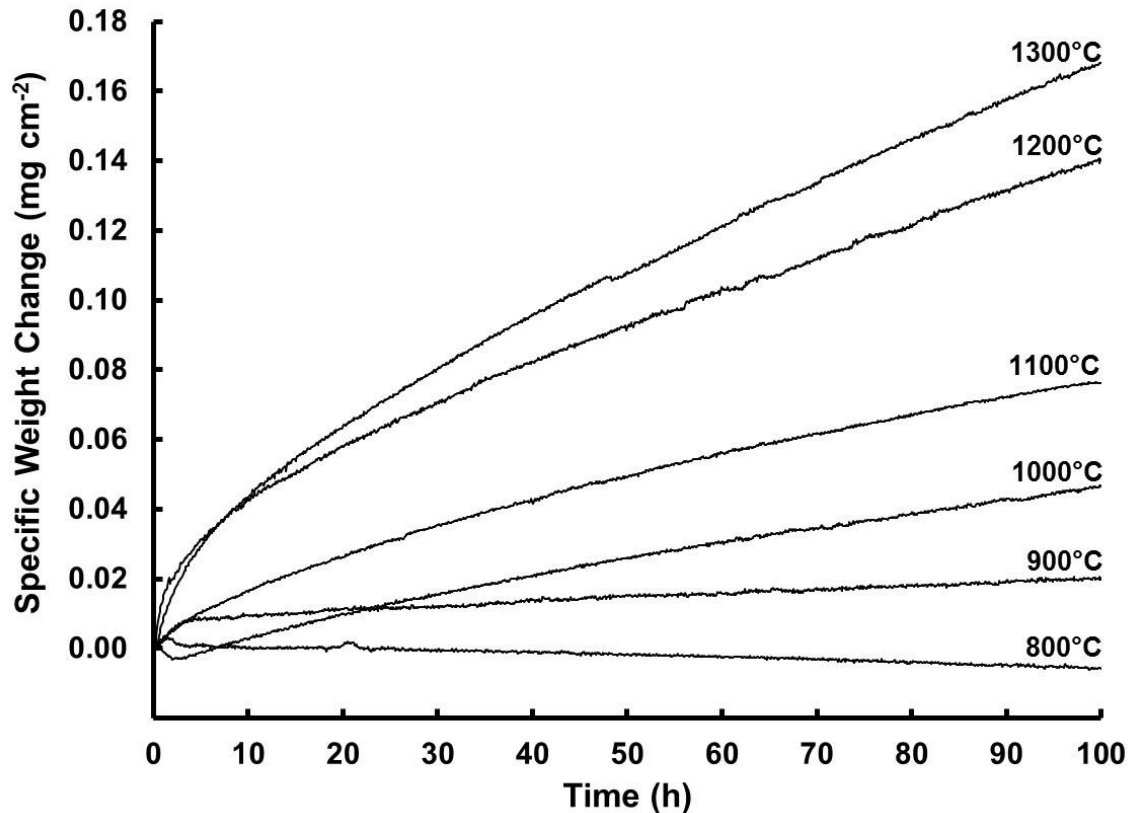


Figure 23: TGA specific weight change results as a function of time for Sylramic fibers exposed to 1 atm of dry O_2 for 100 h under isothermal temperatures ranging from 800 – 1300°C.

The weight change profiles from Sylramic *iBN* fibers oxidized under the same conditions are shown in Figure 24. Transient periods of rapid weight gain (highlighted by the dashed rectangle) occurred at all temperatures except 1300°C. The transient period was followed by weight loss for exposures $\leq 900^\circ\text{C}$, or weight gain for exposures $\geq 1000^\circ\text{C}$. Transient periods of rapid weight gain were not always reproducible. Sometimes linear weight gain was observed at 1000°C and parabolic weight gain was observed at 1100°C (neither shown here). Parabolic oxidation behavior was always observed at 1300°C.

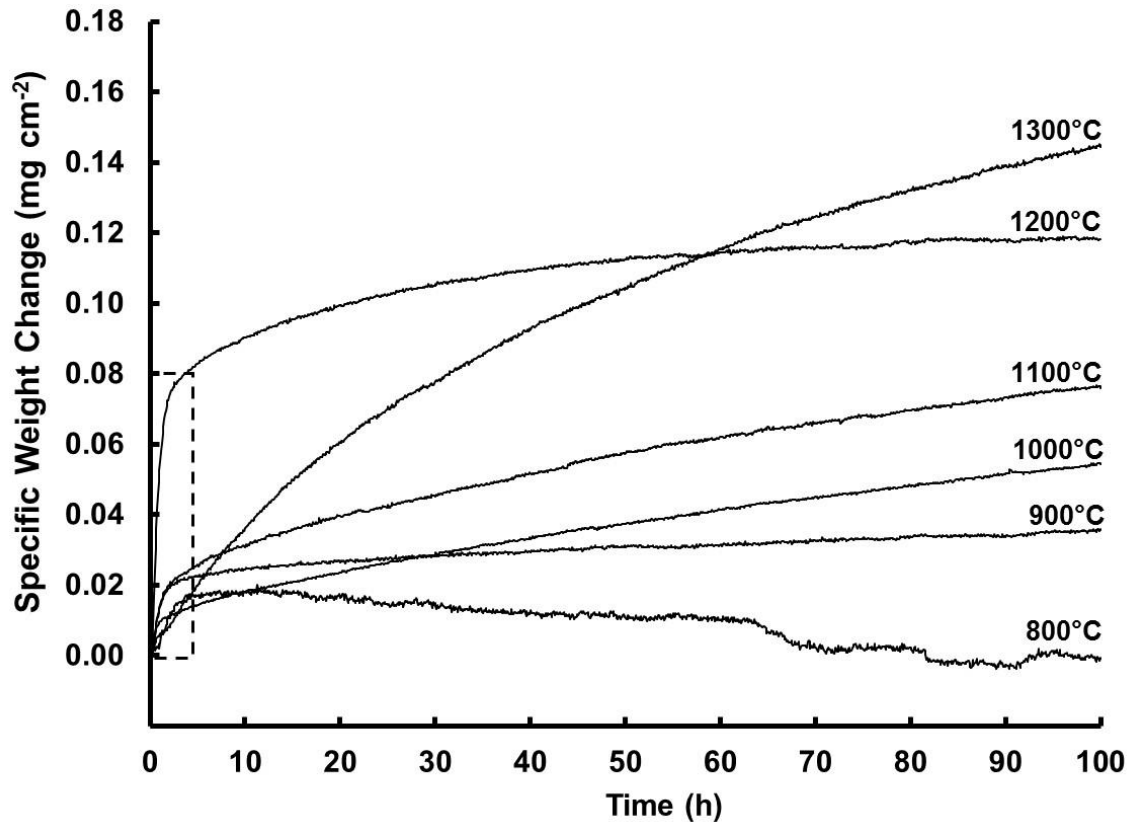


Figure 24: TGA specific weight change results as a function of time for Sylramic *iBN* fibers exposed to 1 atm of dry O_2 for 100 h under isothermal temperatures ranging from 800 – 1300°C.

The Sylramic fiber parabolic weight gain profiles were plotted versus root time in Figure 25 A. The linear fits, shown by dashed lines, approximate a linear dependence consistent with parabolic oxidation. Sylramic *iBN* fiber specific weight changes from the same oxidation conditions were plotted versus root time in Figure 25 B. The linear dependence is approximated only for the weight change data recorded from the 1300°C exposure. Linear dependence was established after the initial transient for the weight change data recorded from the 1100 and 1200°C exposures. The Sylramic and Sylramic *iBN* parabolic rate constants, k_p , were calculated from the squared slopes of linear fits. These are reported in Table 5. The number of repeat exposures at each temperature is given in parentheses. The Sylramic rate constants calculated from TGA results in this

study are in fair agreement (within a factor of five) with rate constants reported in literature for other β -SiC, also reported in Table 5.

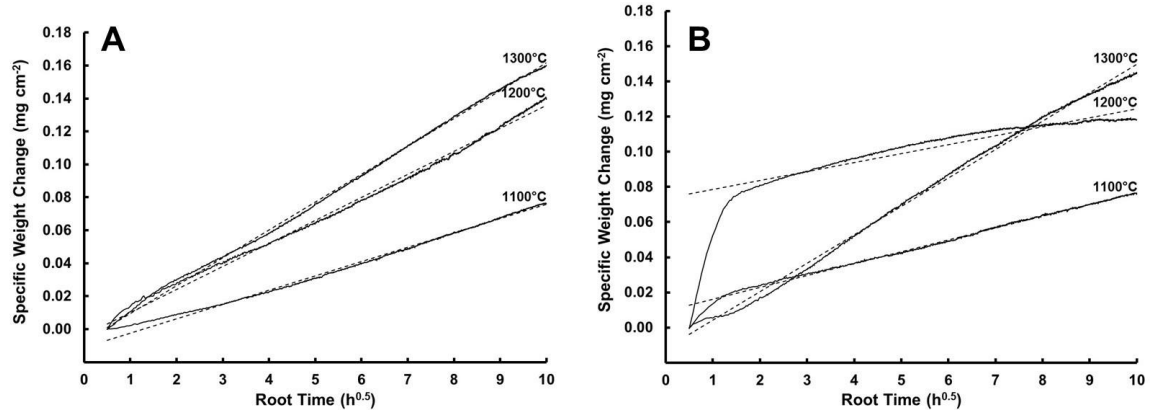


Figure 25: TGA specific weight change results as a function of the square root of time for fibers exposed to 1 atm of dry O₂ for 100 h under isothermal temperatures ranging from 1100 – 1300 °C. A) Sylramic and B) Sylramic iBN. Linear fits shown by dashed lines.

Table 5: Compiled linear (k_l) and parabolic (k_p) oxidation rate constants determined from TGA data, oxide thickness and fiber recession measurements. Asterisks refer to the Sylramic iBN TGA traces where an initial transient was observed. The corresponding Sylramic iBN rate constants were calculated from the slopes of the linear dependence established after the transient.

Temperature (°C)	SiC Material	Reference	TGA Results		Oxide Thickness		Fiber Recession	
			k_l (mgcm ⁻² h ⁻¹)	k_p (mg ² cm ⁻⁴ h ⁻¹)	k_l (μm h ⁻¹)	k_p (μm ² h ⁻¹)	k_l (μm h ⁻¹)	k_p (μm ² h ⁻¹)
800	Sylramic	This Study	-5.0x10 ⁻⁵ ± 2.8x10 ⁻⁵ (2)		(0)	1.8x10 ⁻³	2.5x10 ⁻³ ± 3.1x10 ⁻³ (4)	
	CVD-SiC	21						
900	Sylramic	This Study	1.0x10 ⁻⁴ (1)		2.3x10 ⁻³ ± 7.2x10 ⁻⁴ (2)		2.7x10 ⁻³ ± 1.5x10 ⁻³ (3)	
	*Sylramic iBN CVD-SiC	This Study 21	3.0x10 ⁻⁴ (1)		8.6x10 ⁻³			
1000	Sylramic	This Study	4.5x10 ⁻⁴ ± 7.1x10 ⁻⁵ (2)		8.1x10 ⁻³ ± 5.4x10 ⁻³ (2)		9.3x10 ⁻³ ± 1.5x10 ⁻³ (2)	
	Sylramic iBN	This Study	4.0x10 ⁻⁴ (1)					
	*Sylramic iBN CVD-SiC	This Study 21	4.0x10 ⁻⁴ (1)		2.8x10 ⁻²			
1100	Sylramic	This Study		4.2x10 ⁻⁵ ± 3.8x10 ⁻⁵ (3)		2.5x10 ⁻² ± 1.8x10 ⁻² (3)		1.7x10 ⁻² ± 3.6x10 ⁻³ (2)
	Sylramic iBN	This Study		1.1x10 ⁻⁴ (1)				
	*Sylramic iBN CVD-SiC	This Study 21		1.2x10 ⁻⁴ ± 6.6x10 ⁻⁵ (2)		1.1x10 ⁻³		
1200	Sylramic	This Study		2.7x10 ⁻⁴ ± 1.0x10 ⁻⁴ (1)		8.3x10 ⁻² ± 1.7x10 ⁻² (2)		5.1x10 ⁻² ± 4.9x10 ⁻³ (2)
	*Sylramic iBN Sylramic CVD-SiC	This Study 34 17		2.6x10 ⁻⁵ (1)		2.9x10 ⁻² 1.8x10 ⁻²		
1300	Sylramic	This Study		3.0x10 ⁻⁴ ± 2.5x10 ⁻⁵ (2)		1.3x10 ⁻¹ ± 2.2x10 ⁻² (3)		5.1x10 ⁻² (1)
	Sylramic iBN	This Study		2.6x10 ⁻⁴ (1)		7.6x10 ⁻² ± 9.8x10 ⁻³ (3)		
	CVD-SiC	17		2.3x10 ⁻⁴		3.8x10 ⁻²		

The linear and parabolic oxidation rate constants, k_l and k_p , calculated from the Sylramic fiber weight change data were plotted on a log₁₀ scale versus inverse temperature, as shown in Figure 26. The data points at each temperature were from repeat exposures. The temperature dependence of the linear and parabolic oxidation regimes were approximated by linear fits. The parabolic rate constants calculated from exposures at 1100°C show a large scatter about the linear fit. The Sylramic fiber oxidation kinetics

may be governed by both surface-reaction limited and diffusion controlled regimes that are in competition at 1100°C, which may have arisen from oxidation of the TiB₂ and B₄C constituents affecting the fiber oxidation behavior. The scatter at the other temperatures is less. In general, these results show that the Sylramic fiber oxidation kinetics were governed by known oxidation models for SiC. The effects of the free carbon oxidation on the fiber weight loss at during 800°C exposures were demonstrated. The effects from the TiB₂ and B₄C constituents on the SiC oxidation behavior must be also considered.

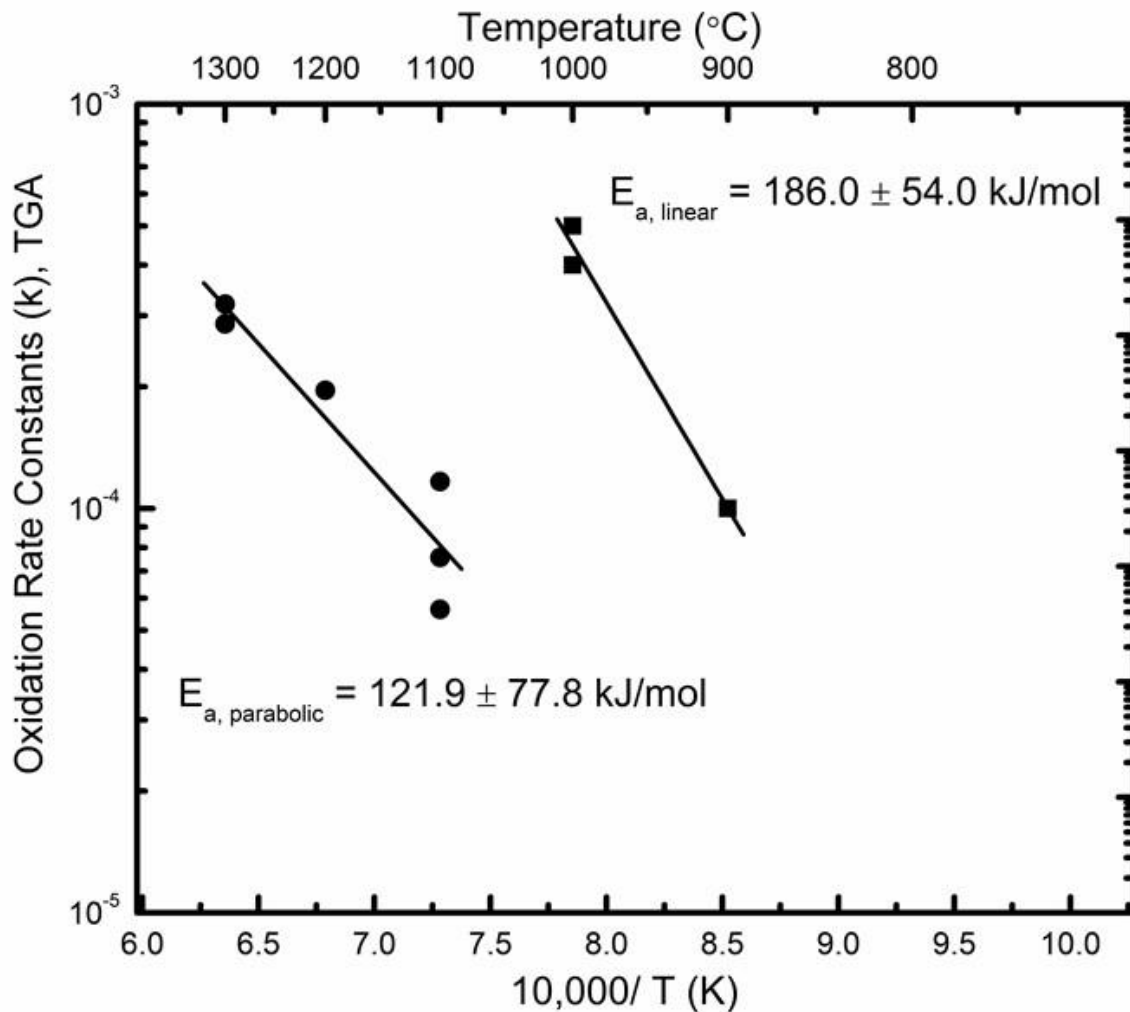


Figure 26: Plot of Sylramic oxidation rate constants versus inverse temperature for linear ($\text{mg cm}^{-2} \text{h}^{-1}$, squares) and parabolic ($\text{mg}^2 \text{cm}^{-4} \text{h}^{-1}$, circles) oxidation mechanisms determined from TGA weight change data following isothermal oxidation for 100 h in dry O_2 at 900 – 1300°C.

The linear and parabolic oxidation activation energies (E_a) were calculated from the slopes of the linear fits from TGA weight change profiles. These results are reported in Table 6 with their standard errors. The results from oxide thickness, described further in the following section, are shown in comparison with literature results from oxidation studies of the following stoichiometric β -SiC materials: bulk CVD-SiC,¹⁷ C-terminated ($\bar{1}\bar{1}\bar{1}$) CVD-SiC,²¹ and HiNicalonTM-Type S fibers^{87, 98}. The variance on the activation energy values from literature was not reported.

Table 6: Compiled reaction limited and diffusion limited activation energies for oxidation of Sylramic fibers compared to literature values for related SiC materials

Specimen	Reaction limited oxidation mechanism		Diffusion limited oxidation mechanism	
	Source	E_a (kJ/ mol)	Source	E_a (kJ/ mol)
Sylramic – this work	TGA wt. change	186 ± 54.0	TGA wt. change	122 ± 77.8
Sylramic – this work	Oxide thickness	146 ± 194	Oxide thickness	156 ± 87.7
Sylramic – this work	Fiber recession	42.9 ± 145		113 ± 115
($\bar{1}\bar{1}\bar{1}$) CVD-SiC ⁴¹	Oxide thickness	170	Oxide thickness	94.3
Bulk CVD-SiC ⁴³	-	-	Oxide thickness	118
Silicon ²²	-	-	Oxide thickness	119
HiNicalon TM -Type S ⁹⁸	Oxide thickness	138	Oxide thickness	248
Vitreous SiO ₂ ²⁵	-	-	Molecular diffusion	113

4.3.2.1.2 Oxide thickness

Oxidation of the Sylramic and Sylramic *iBN* fibers resulted in the formation of a thermally grown borosilicate glass from the combined SiC, TiB₂⁹⁹, B₄C⁴, and BN oxidation reactions. Micrographs of oxidized fiber cross-sections are shown in Figure 27 for Sylramic (top row, A – B) and Sylramic *iBN* (bottom row, C – D) following 100 h exposures at 900 and 1300°C. The oxide thickness increased with increased temperature, in accord with weight change results.

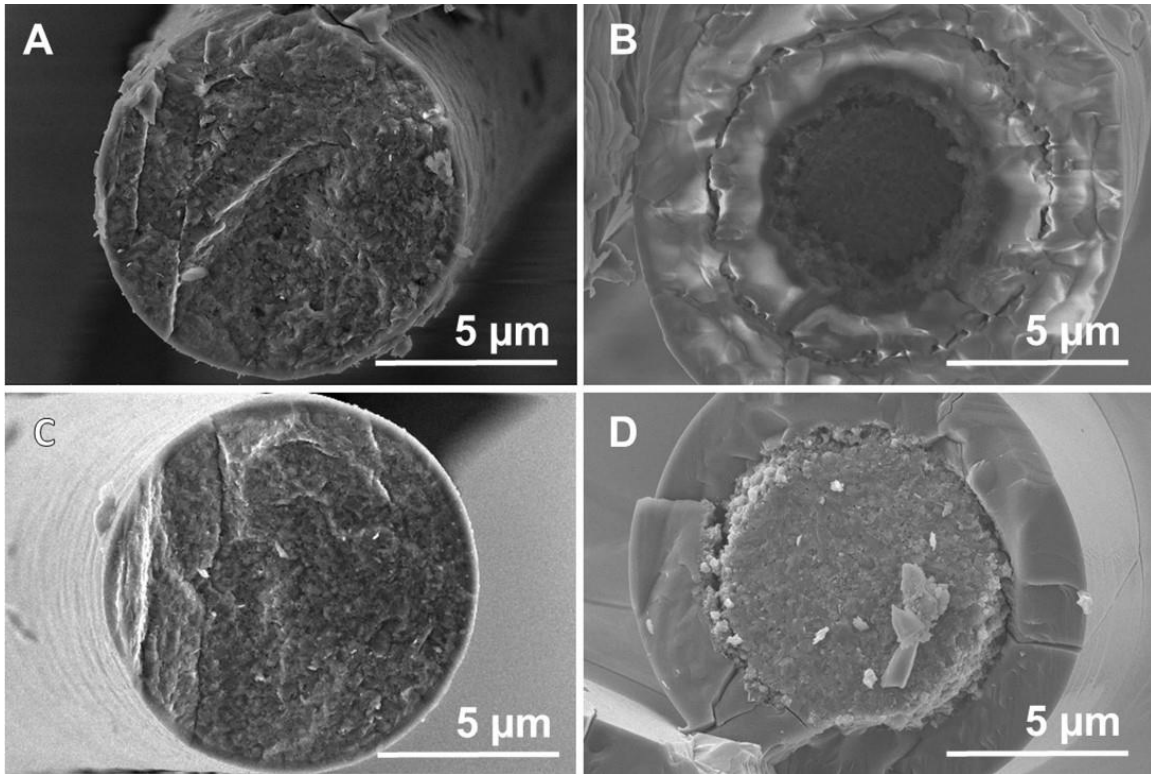


Figure 27: Micrographs of oxidized fiber cross-sections after 100 h exposures in dry O₂. Top row: Sylramic fiber cross-sections - A) 900 °C, B) 1300 °C. Bottom row: Sylramic iBN fiber cross-sections - C) 900 °C, D) 1300 °C. Oxidized fiber cross-sections were imaged by SEM with secondary electrons.

Oxide thicknesses were measured from the oxide edge to the fiber surface. Sylramic *iBN* and Sylramic mean oxide thickness measurements, averaged over at least 48 – 72 fibers from 2 – 3 repeat exposures at each temperature, are plotted in Figure 28. The oxide thicknesses after 800°C exposures could not be accurately measured due to the thin oxide formed and the fiber roughness. Sylramic *iBN* oxide thicknesses were statistically insignificant from Sylramic oxide thicknesses following 900 – 1100°C exposures. Sylramic oxide thicknesses exceeded Sylramic *iBN* oxide thicknesses following 1200 – 1300°C exposures.

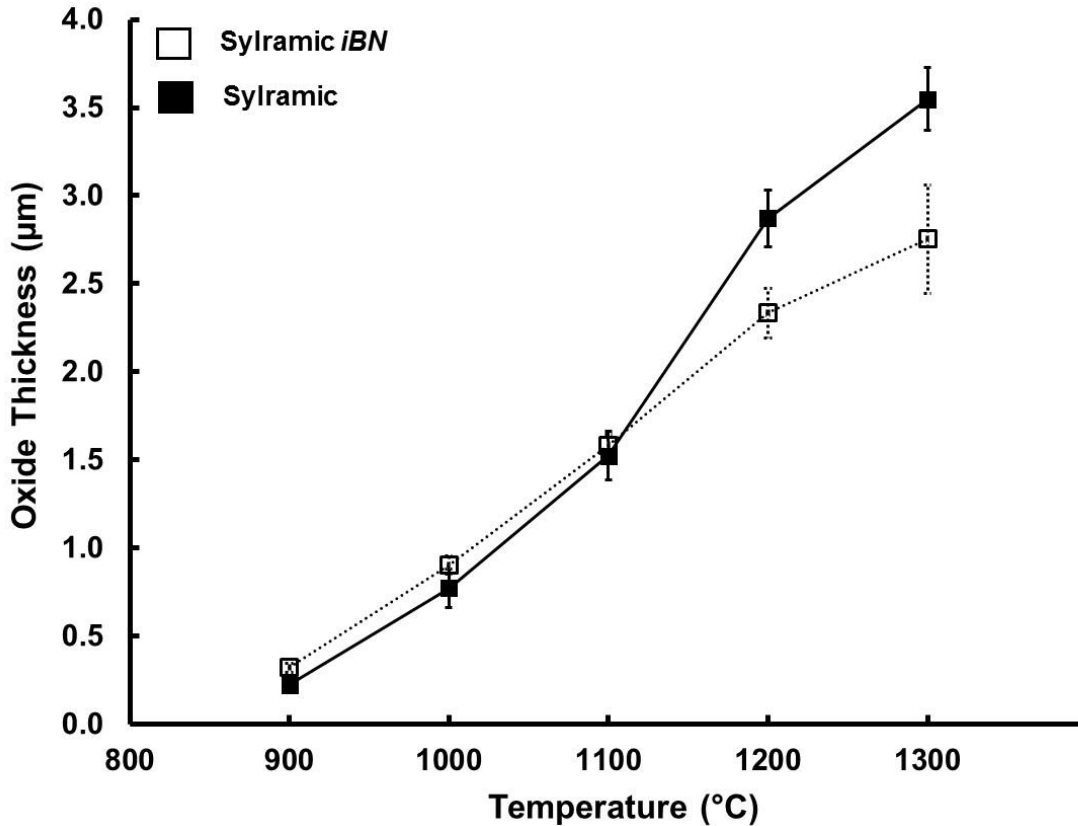


Figure 28: Oxide thickness measurements as a function of temperature for Sylramic iBN (open squares) and Sylramic (filled squares) oxidized fibers exposed for 100 h in dry O₂ under isothermal conditions ranging from 900 – 1300 °C.

Sylramic fibers exhibited linear TGA weight change at $\leq 1000^{\circ}\text{C}$ exposures, from which oxide growth at these exposures was assumed to be governed by linear oxidation kinetics based on TGA results. The linear rate constants, k_1 , were calculated from these measured oxide thicknesses per unit time,³⁰ reported as $\mu\text{m}/\text{h}$ in Table 5. Parabolic oxide growth was assumed from parabolic TGA weight change at $\geq 1100^{\circ}\text{C}$. The Sylramic fiber parabolic oxidation rate constants were calculated from the squared oxide thicknesses per unit time,³⁰ reported as $\mu\text{m}^2/\text{h}$ in Table 5. Literature results from the dry oxidation of CVD-SiC coupons were compared^{17, 21}. Results from Lipowitz et al. on the dry air oxidation of Sylramic fibers were also included in Table 5. The rate constant reported by Lipowitz et al.³⁴ from oxidation exposures in air was extrapolated in this work to a value

$2.9 \times 10^{-2} \mu\text{m}^2/\text{h}$ by multiplying by a factor of $1 \text{ atm} / 0.2 \text{ atm}^{35}$ to account for the higher O_2 partial pressure used in this study. The reasonable agreement between the Lipowitz study and this study was within a factor of three.

The temperature dependence of the Sylramic rate constants determined from oxide thicknesses are shown plotted in Figure 29. The scatter about the linear fits were greater for the rate constants calculated from the oxide thickness than they were for those calculated from weight change, particularly at the 1000 and 1100°C intermediate temperatures. The scatter at these temperatures corresponds with the transition from linear oxidation kinetics at 1000°C to parabolic oxidation kinetics at 1100°C observed by the weight change profiles shown in Figure 26. The scatter in the linear oxidation kinetic region (900 and 1000°C) is too great for the activation energy to be meaningful. There are a few reasons to explain the large degree of scatter. First, it is distributed only over two temperatures. Second, it may be supporting evidence for competing oxidation mechanisms taking place at these intermediate temperatures, in particular at 1000 and 1100°C. Third, the temperature dependence of the O_2 solubility, which is unknown for borosilicate glasses, may be stronger in thermally grown borosilicate glasses than it is for thermally grown silica glasses. If so, then the temperature dependence of the O_2 solubility will have a greater effect on both surface-reaction and diffusion controlled oxidation regimes in SiC systems that contain B-based constituents and oxidize to form thermally grown borosilicate glasses.

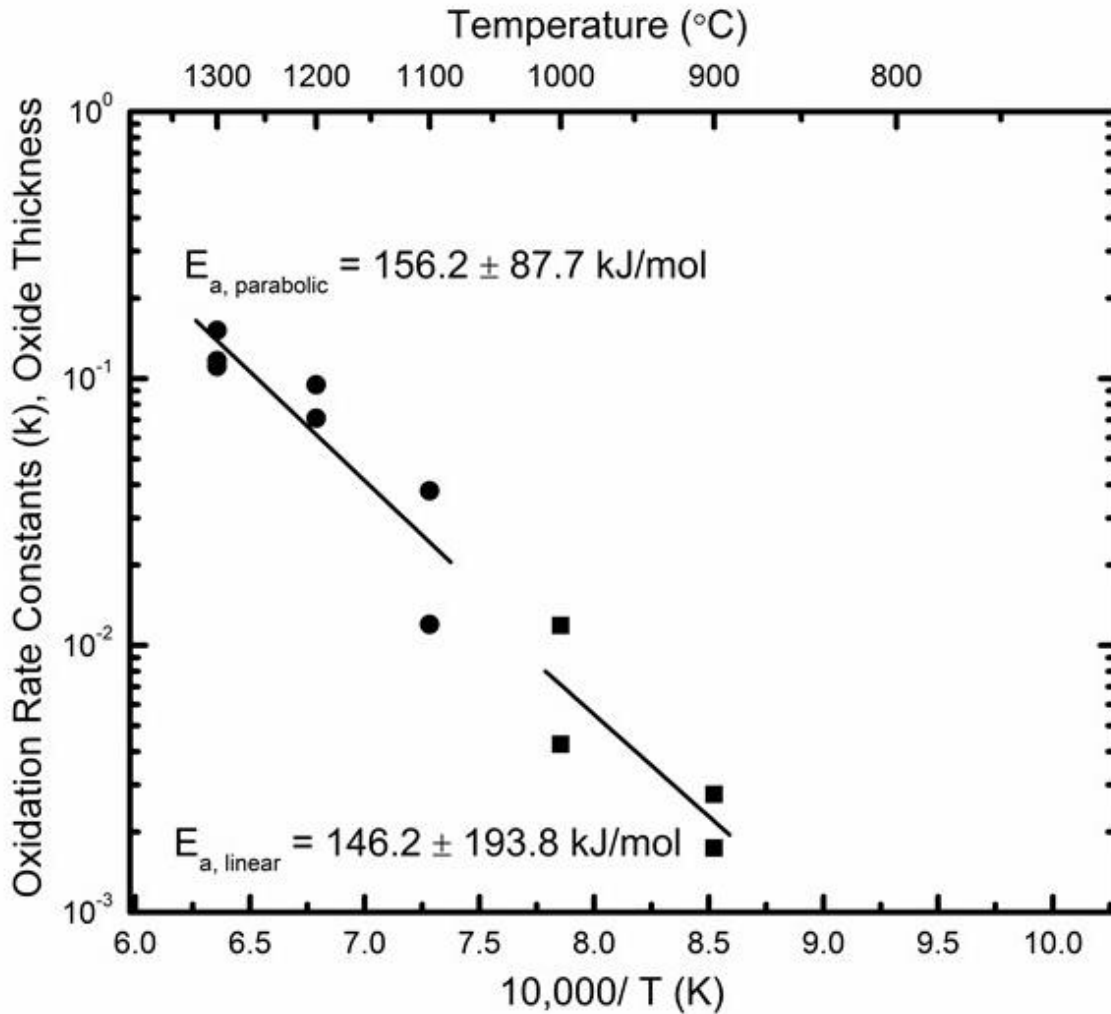


Figure 29: Plot of Syramic oxidation rate constants versus inverse temperature for linear ($\mu\text{m h}^{-1}$, squares) and parabolic ($\mu\text{m}^2 \text{h}^{-1}$, circles) oxidation mechanisms determined from oxide thickness measurements.

The activation energies, E_a , for linear and parabolic oxidation mechanisms are reported in Table 6. The E_a calculated from TGA data and oxide thicknesses in this work are in reasonable agreement with literature except for the results reported for the parabolic oxidation of Hi-Nicalon™ Type S fibers, which have a significantly higher reported E_a . The standard error is attributed to the scatter observed at intermediate temperatures, 1000 – 1100°C, due to competing oxidation mechanisms. The results in this study are consistent with molecular O_2 diffusion through the borosilicate controlling the oxidation rate.

4.3.2.1.3 Fiber recession

Sylramic and Sylramic *iBN* fiber recession evidence is shown by micrographs of fiber cross-sections shown in Figure 30 observed from digested fibers.

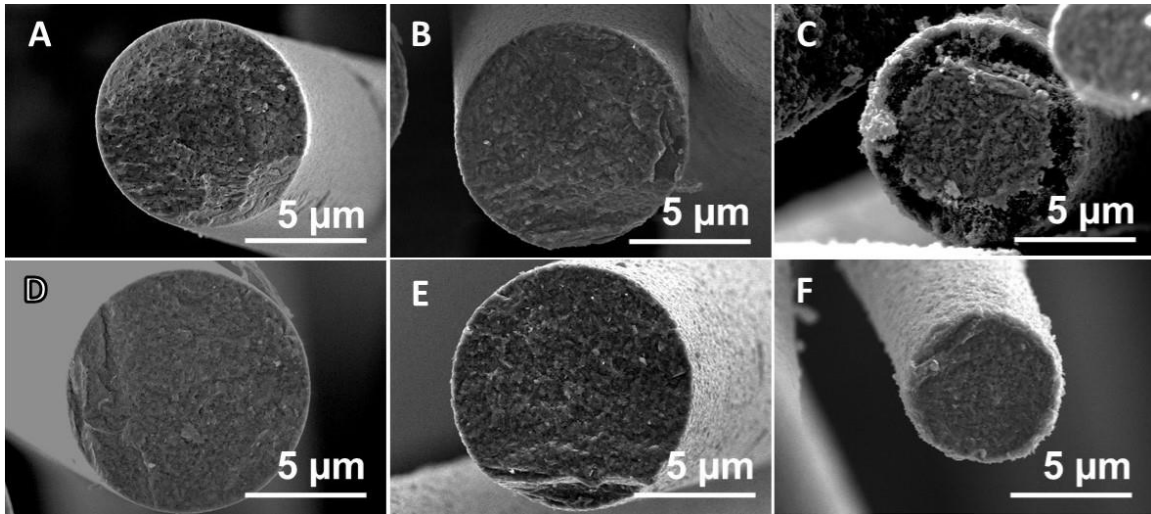


Figure 30: Secondary electron micrographs of fiber cross-sections after digestion. Top row: Sylramic fiber cross-sections A) Unoxidized fiber, and after oxidation for 100 h in dry O₂ at B) 900 °C, C) 1300 °C. Bottom row: Sylramic *iBN* fiber cross-sections D) Unoxidized fiber, and after oxidation for 100 h in dry O₂ at E) 900 °C, F) 1300 °C.

Mean Sylramic *iBN* and Sylramic fiber diameters were averaged over at least 24 – 96 fibers for 2 – 4 repeat exposures at each oxidation temperature. The plotted results are shown in Figure 31. The percent fiber recession was not statistically different between the fiber types. For example, the percent fiber recession after oxidation at 1300 °C was 23% for both fiber types.

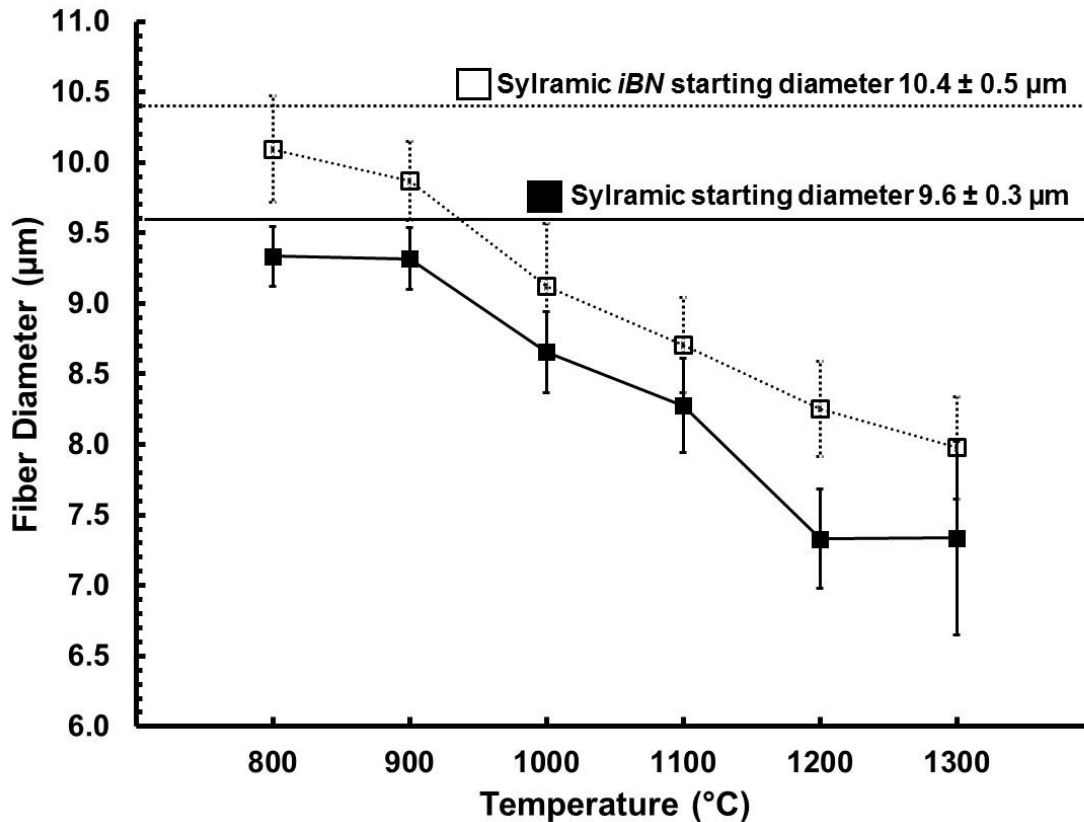


Figure 31: Mean fiber diameters for Sylramic iBN (open squares) and Sylramic (filled squares) following digestion after exposures for 100 h in isothermal dry O₂ exposures ranging from 800 – 1300 °C.

The temperature dependence of the Sylramic rate constants was determined from fiber recession measurements, assuming linear oxidation kinetics for exposures $\leq 1000^\circ\text{C}$ and parabolic oxidation kinetics for exposures $\geq 1100^\circ\text{C}$. The rate constants are shown plotted in Figure 32. The activation energies, E_a , for linear and parabolic oxidation kinetics were included in Table 6. The variance in the starting fiber diameters is reflected in the high degree of scatter about the linear fits, especially for exposures $\leq 1000^\circ\text{C}$, resulting in a low E_a with large uncertainty in the linear regime. The scatter is too high, resulting in E_a that are meaningless, due to the error in the starting diameters that propagated into fiber recession measurements.

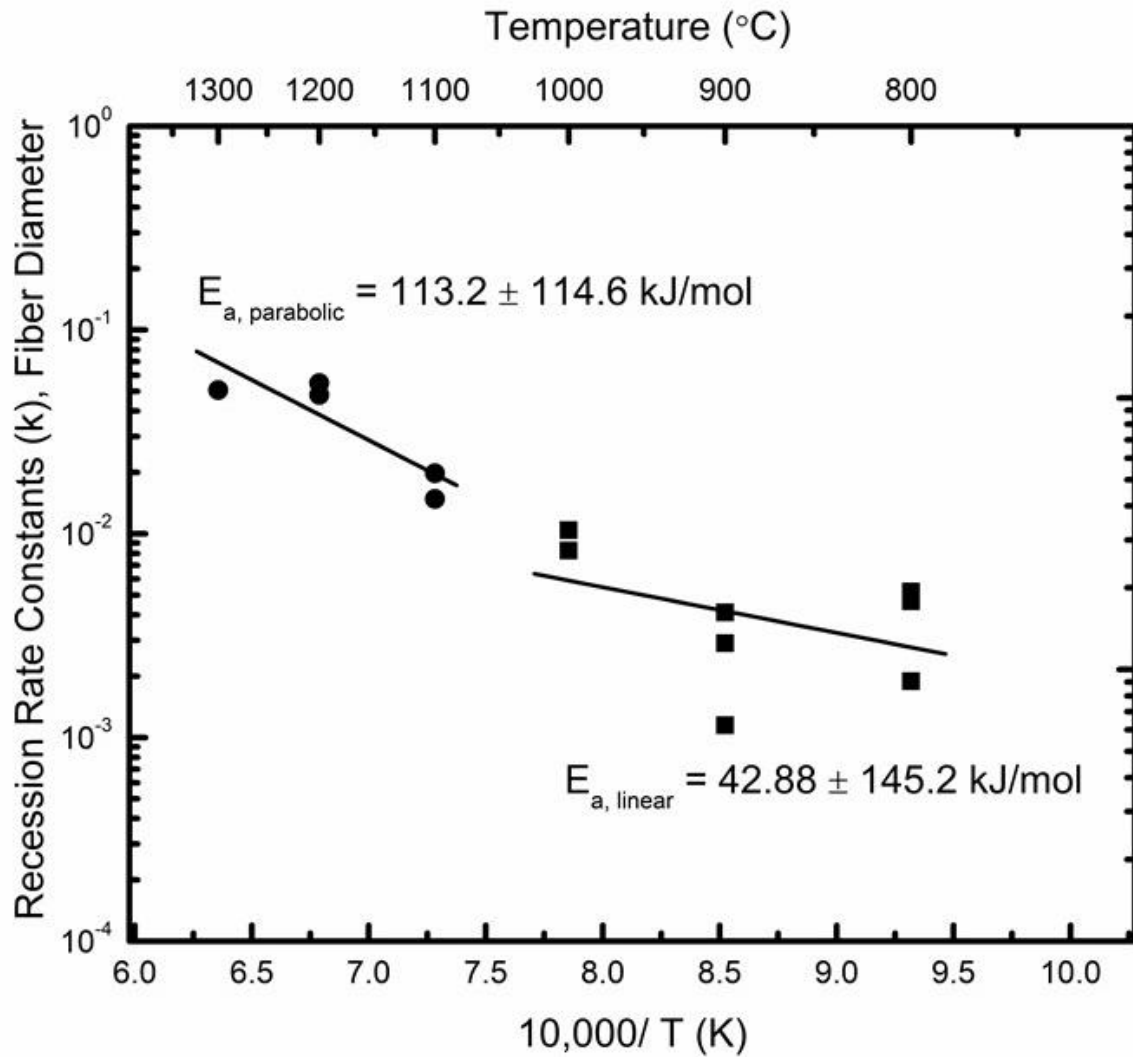


Figure 32: Plot of Syramic fiber recession rate constants versus inverse temperature for linear ($\mu\text{m h}^{-1}$, squares) and parabolic ($\mu\text{m}^2 \text{h}^{-1}$, circles) oxidation mechanisms determined from fiber diameter measurements.

4.3.2.1.4 Oxide composition, ICP-OES

The unoxidized Syramic *iBN* fibers were stable in the digestion solutions. The total Si and B concentrations from unoxidized Syramic *iBN* fiber digestion solutions were < 1 ppm. In comparison, the Si and B concentrations leached from unoxidized Syramic fiber digestions were 2.2 ± 1.9 ppm and 1.1 ± 1.2 ppm, respectively. The combined Si and B concentrations from oxidized Syramic fiber digestion solutions were as low as 20 ppm. Therefore, the average leached Si from the baseline unoxidized fibers

was subtracted from the ICP-OES results of the digested oxidized Sylramic fibers to increase the accuracy of Si and B determined from the composition of SiO₂ and B₂O₃ in the dissolved oxides with minimal contributions of leached Si from the fiber itself.

The Sylramic and Sylramic *iBN* oxide B concentrations (balance Si) averaged over 2 – 4 repeat exposures at each temperature are shown plotted in Figure 33. The analysis error of individual element wavelengths was $< \pm 1 - 2$ ppm. The B concentration in Sylramic *iBN* oxides ranged from 27 – 12 mol% from oxidation at 800 – 900°C and 10 – 6 mol% from oxidation at 1100 – 1300°C, indicating a strong temperature dependence. The Sylramic *iBN* oxide B concentrations exceeded the Sylramic oxide B concentration for all exposures $\leq 1200^\circ\text{C}$. The oxide B concentration for the Sylramic fibers oxidized at 800°C averaged 13 mol%, but was otherwise independent of temperature. Sylramic and Sylramic *iBN* oxide B concentrations converged at 1300°C.

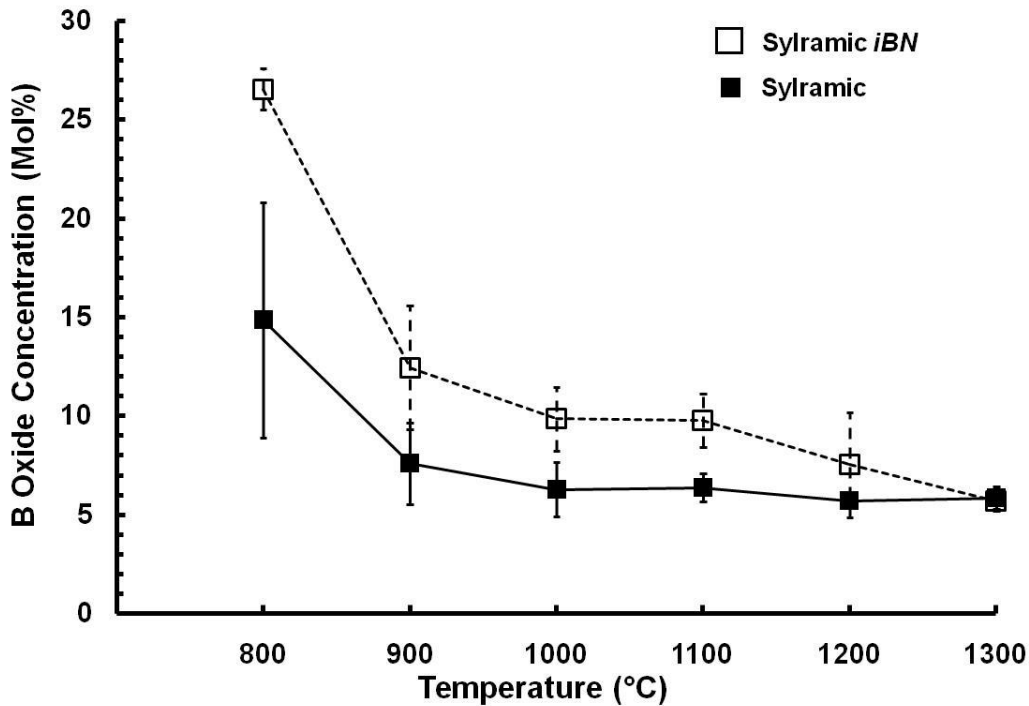


Figure 33: ICP-OES results for average B concentration in digested oxides from fibers as a function of temperature after 100 h isothermal exposures in dry O₂. Sylramic *iBN* – open squares; Sylramic – filled squares.

4.3.2.2 Time-dependent oxidation results

4.3.2.2.1 Oxide thickness

The oxide thicknesses for time-dependent oxidation tests of Sylramic *iBN* at 900, 1200, and 1300°C are plotted in Figure 34 A. The 900°C oxide thicknesses, measurable after 9 h of oxidation, did not notably increase with time. This rapid oxide growth during the initial 9 h interval supports TGA results displaying rapid transient oxidation kinetics. The oxide thickness was $0.23 \pm 0.01 \mu\text{m}$ from exposures at 900°C for 9 h. For comparison, it would take 50 h to grow an oxide thickness of 0.23 μm on stoichiometric β -SiC, based on Deal and Grove's linear-parabolic model using the k_1 and k_p values reported by Ramberg et al. for C-terminated ($\bar{1}\bar{1}\bar{1}$) CVD-SiC oxidized in these same conditions²¹. The 1 h exposures at 1200 and 1300°C resulted in equivalent oxide thicknesses of 0.4 μm , shown superimposed in Figure 34 A. Calculated oxide thicknesses from the k_p reported by Ogbuji and Opila for the dry oxidation of CVD-SiC¹⁷ are included for comparison with the 1200°C Sylramic *iBN* oxide thicknesses in this work. Using the 1200°C k_p for CVD-SiC reported by Ogbuji and Opila¹⁷, it would take 9.9 h to grow an equivalent SiO₂ oxide thickness. This order of magnitude increase in SiC oxidation kinetics is in line with others^{23, 39, 41} who also observed orders of magnitude increases in the oxidation kinetics of Si-based materials due to the presence of B₂O₃. Oxide thicknesses that developed from the dry O₂ exposures at 1200 and 1300°C were plotted versus root time for in Figure 34 B. The good linear fits (dotted lines) suggest the oxides grew by parabolic oxidation kinetics¹⁷. The forced linear fit for the 1200°C results shows parabolic oxidation kinetics were more rapid at 1 h than the parabolic oxidation rate observed at longer times.

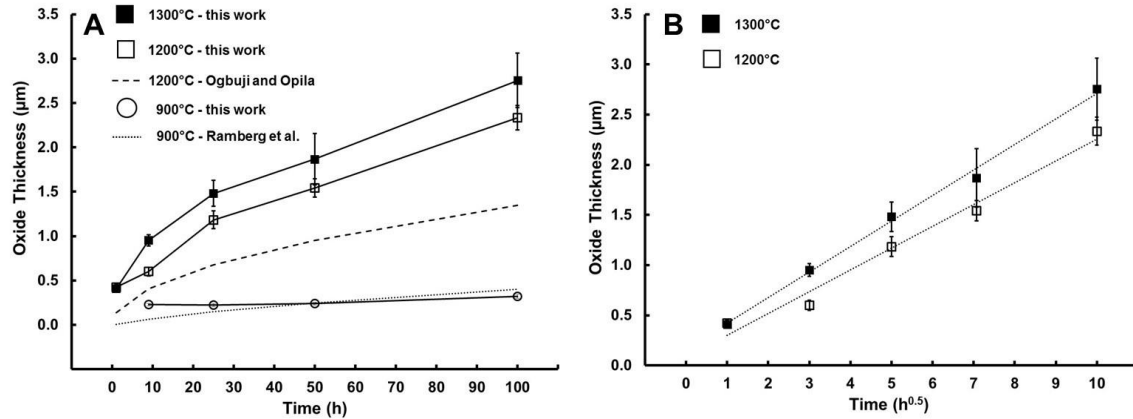


Figure 34: Sylramic iBN oxide thickness measurements: 1300 °C represented by filled squares, 1200 °C represented by open squares, and 900 °C represented by open circles. A) Sylramic iBN oxide thickness plotted versus time for 900, 1200, and 1300 °C exposures in dry O₂. Calculated oxide thicknesses from the parabolic rate constant reported by Ogbuji and Opila for the dry O₂ oxidation of CVD-SiC at 1200 °C¹⁷ represented by the dashed line. Calculated oxide thicknesses from the linear and parabolic rate constants are reported by Ramberg et al. for the dry O₂ oxidation of (111)CVD-SiC at 900 °C²¹ are represented by the dotted line. B) Oxide thickness versus the square root of time for 1200 and 1300 °C exposures. Note the symbols for oxide thicknesses following 1 h 1200 and 1300 °C exposures are superimposed.

4.3.2.2.2 Oxide composition

The Sylramic iBN oxide B concentrations from ICP-OES analysis of digested oxides following time-dependent exposures at 900, 1200, and 1300 °C are plotted in Figure 35. The analysis error of individual element wavelengths was $< \pm 1 - 2$ ppm. The B concentration decreased sharply with time following 900 °C exposures, whereas it was comparatively constant following 1200 and 1300 °C exposures. The oxides formed from 900 °C exposures at 1 h were too thin to be distinguished from the fiber surface roughness and could not be measured. But, the oxide B concentration was the highest from the 1 h exposure. The oxide B concentration declined steeply with increasing exposure times at 900 °C without marked increases in oxide thickness. These two results in combination show that reduction in oxide B concentration with increased exposure time was due to boria volatilization and not to increases in the oxide SiO₂ concentration from fiber oxidation.

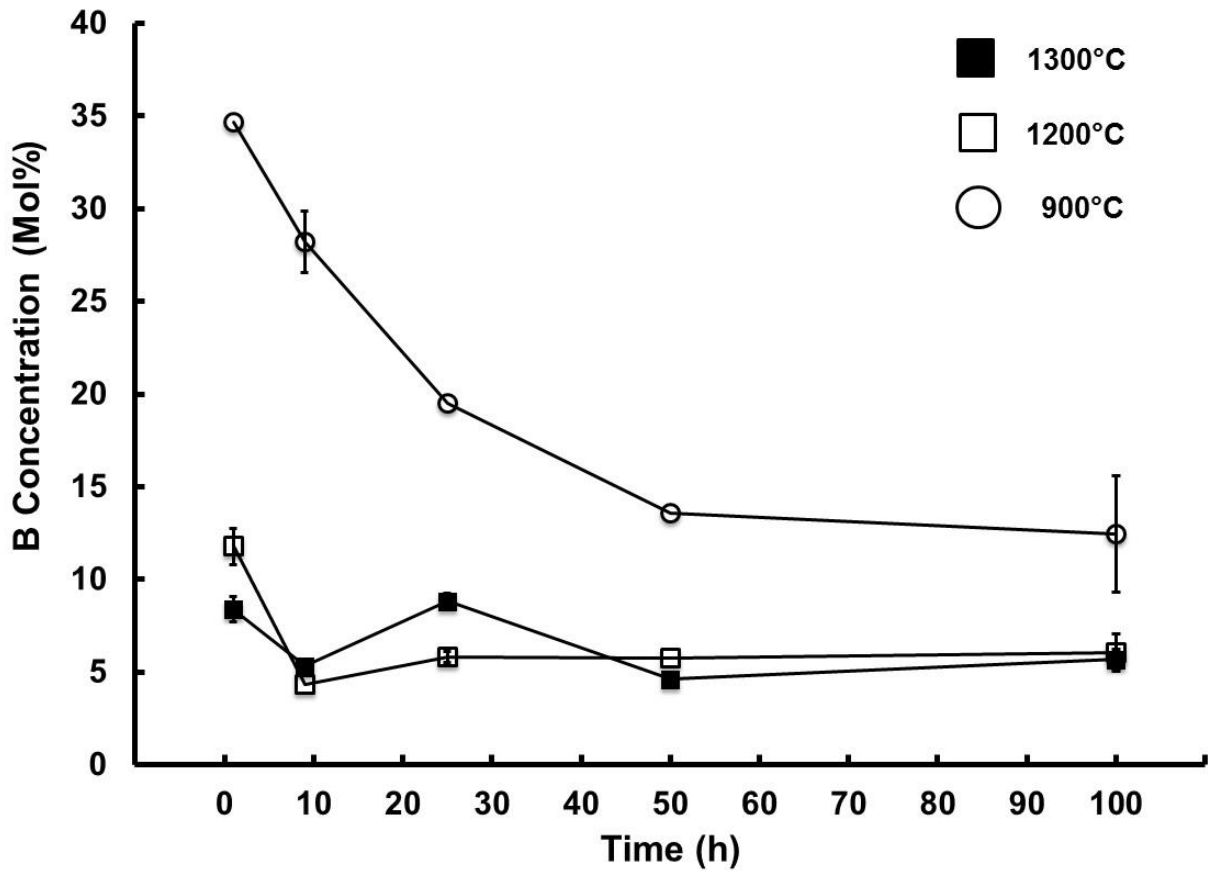


Figure 35: ICP-OES results for Sylramic iBN oxide B concentration as a function of oxidation time at three different temperatures in dry O₂: 900, 1200, and 1300°C.

4.4 Discussion

4.4.1 Effects of the oxide boron concentration on oxygen transport

Oxidation of Sylramic iBN fibers below 1300°C at short times yielded oxides with the high boron concentrations that approached 35 mol%. It was during these short periods of oxidation that rapid weight gain and oxide growth were observed. These results are evidence that oxidation of the BN layer led to high concentrations of boria in the thermally grown borosilicate glass that corresponded with more rapid SiC oxidation in comparison with what has been previously observed by others for pure SiC^{17, 21} for early times of exposure.

In this study, the O₂ diffusion through a thermally grown borosilicate glass is related to its structure as follows. Boria undergoes significant structural modifications with heating^{49, 50, 52, 54}. The vitreous boria structure is composed of B₃O₆ boroxol ring units interconnected by planar BO₃ triangles^{47, 48}. Raman spectroscopic investigations by Hassan et al. found that heating vitreous boria above its melt temperature (~ 450°C) causes the boroxol rings to open into BO₃ triangles that connect into chainlike segments⁵⁴. The boroxol ring decomposition increases with temperature, and the boria structure becomes increasingly chainlike⁵⁴. The decomposition of the boroxol rings into BO₃ triangles was also observed to occur when binary borosilicate glasses were heated above the boria melt temperature⁶⁶. The decomposition of the boroxol rings is accompanied by increases in bonds between the boria and silica units, referred to as Si-O-B bonds⁶⁶. The silica structure is chemically altered by Si-O-B bond formation that results from the boria structural changes induced by heating⁶⁶. It is hypothesized in this study that the breakup of the silica structure via Si-O-B bonds increases the O₂ transport in silica. It is proposed that higher boria concentrations in the thermally grown borosilicate glass 1) increases O₂ transport because the O₂ diffusion is much faster in molten boria⁶³ than in silica²⁵, and 2) further breakup the silica structure via increased Si-O-B formation.

4.4.2 Boria volatility

The oxide boron concentration in oxidized Sylramic *iBN* fibers was found to decrease as the exposure time increased without further increases to the oxide growth (i.e., time-dependent oxidation studies at 900°C). The boria concentration in Sylramic *iBN* oxides was strongly dependent on the exposure temperature, whereas the boria

concentration in Sylramic fibers was constant by comparison. These results are evidence for boria volatilization from Sylramic *iBN* oxides that were enriched with boria by oxidation of the BN layer. The highest boria concentration detected from Sylramic *iBN* oxides was 24 mol% (35 mol% boron), balance silica, obtained from fibers exposed for 1 h at 900°C.

The boria volatilization was assessed with FactSage calculations (FactSage version 7.0)¹⁰⁰. The B₂O₃ (g) partial pressures from pure liquid B₂O₃ and in a thermally grown borosilicate glass with a 24 mol% concentration of B₂O₃ were determined in two environments: dry O₂, and in an impurity level (10 molar ppm) of H₂O vapor, balance O₂. The FactPS and FactOxid databases were used. The pure liquid B₂O₃ activity was fixed to a 0.24 mol fraction in order to have consistency with the B₂O₃ concentration in the Sylramic *iBN* thermally grown borosilicate glass following oxidation for 1 h at 900°C (24 mol% B₂O₃ and 76 mol% SiO₂). The H₂O vapor activity was also fixed to 10 molar ppm, to simulate H₂O impurity levels in the O₂ gas stream having dewpoints < -56°C, achievable with the type 3A molecular sieves used in this study to purify the TGA O₂ environment. The log₁₀ partial pressures of the vapor species plotted in Figure 36 show that the vapor species from B₂O₃-SiO₂ and pure B₂O₃ get closer as temperature increases. The B₂O₃ (g) partial pressures in dry O₂ showed a strong temperature dependence, consistent with ICP-OES results for Sylramic *iBN* oxide B concentration. However, the partial pressures do not predict the rapid Sylramic *iBN* oxide B loss that was observed. The HBO₂ partial pressures have both temperature dependence and vapor pressures that would predict B₂O₃ loss due to volatilization demonstrated by ICP-OES results. Conversely, the H₃BO₃ partial pressures were the lowest and are temperature

independent. The rapid reductions of boria concentration in the thermally grown borosilicate glass likely resulted from formation of volatile HBO₂ species due to the high sensitivity of B₂O₃ to even impurity levels of H₂O vapor.

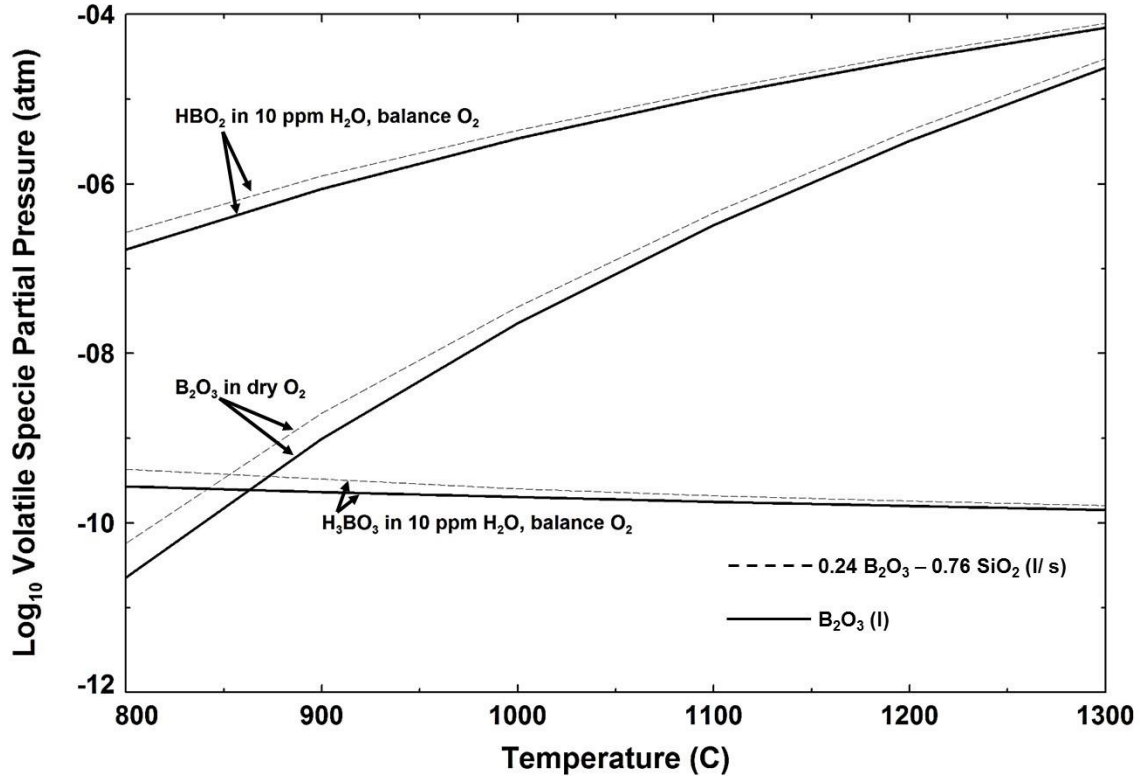


Figure 36: FactSage calculated partial pressure temperature dependence for predominant volatile species from vaporization and volatilization reactions of a 24 mol% B₂O₃ borosilicate glass composition (dashed line) and pure liquid B₂O₃ (solid line) in 10 ppm water vapor, balance O₂, and in dry O₂.

As a result, the rapid Sylramic *iBN* weight gains observed for all dry O₂ exposures below 1300°C were transient. Further, the rapid weight gains did not result in statistically greater Sylramic *iBN* oxide thicknesses in comparison with Sylramic oxides. In fact, the Sylramic *iBN* oxides thicknesses were lower at exposures $\geq 1200^\circ\text{C}$ even though the Sylramic and Sylramic *iBN* oxide B concentrations were similar. These results are attributed to the combination of the rapid Sylramic *iBN* fiber oxidation and boria volatility as follows. At early times of exposure (< 1 h), the high concentrations of B in Sylramic *iBN* oxides (i) accelerated SiC fiber oxidation kinetics, which were ii) rapidly

sealed by the thermally grown borosilicate glass attributed to significant reductions in SiO_2 viscosity by B_2O_3 incorporation, followed by (iii) a concomitant reduction in surface B concentration due to B_2O_3 vaporization, resulting in (iv) a SiO_2 -rich oxide surface that slowed inward O_2 diffusion, and (v) limited further oxide growth at earlier times than in the absence of B_2O_3 . Consequently, the transient period of rapid Sylramic *iBN* oxidation did not result in increased fiber recession.

4.4.3 Implications for ceramic matrix composites

The BN interphase oxidizes at a lower temperature and at a faster rate than SiC^{40} in environments where the O_2 partial pressure is high enough to enable the oxidation of BN and $\text{SiC}^{12, 40, 101}$. The BN layer will be consumed at a faster rate than the SiC fiber, resulting in greater production of B_2O_3 with respect to SiO_2 . The Sylramic *iBN* oxidation results from this study showed that the boria-rich thermally grown borosilicate glass produced from oxidation of the BN layer resulted in a transient period of rapid SiC fiber weight gain. The accelerated SiC fiber oxidation kinetics were limited by boria volatilization from the oxide surface. The amount of B_2O_3 that can be produced is limited by the BN thickness, which is significantly less than the thickness of the fiber or adjacent SiC matrix. Significant SiC fiber and matrix oxidation was observed by others^{3, 15}, in spite of the limited amount of B_2O_3 that can be produced from oxidation of the BN interphase. These findings indicate that excessive SiC oxidation can occur in conditions where boria volatilization is restricted, such as in microcracks present in the SiC matrix that are allow for rapid O_2 ingress. The excessive borosilicate glass that developed also suggests that boria is reactive with the adjacent SiC fibers and matrix, which is possibly a separate mechanism that accelerates SiC oxidation kinetics.

4.5 *Conclusions*

The transient period of rapid oxidation kinetics observed in Sylramic *iBN* TGA traces at $< 1300^{\circ}\text{C}$ was attributed to the oxidation of the BN layer that contributed to B concentrations in the Sylramic *iBN* oxides that ranged from 7 – 35 mol%. These Sylramic *iBN* oxide B concentrations are believed to have led to the higher oxide thicknesses following short exposures < 9 h for temperatures $\leq 1200^{\circ}\text{C}$. Longer times and higher temperature exposures led to boria volatilization, which in turn reduced boria effects in accelerating Sylramic *iBN* fiber oxidation kinetics, resulting in no observable differences between Sylramic and Sylramic *iBN* fiber recession. The rapid sealing of Sylramic *iBN* fibers combined with rapid boria vaporization at exposure temperatures $\geq 1200^{\circ}\text{C}$ restricted oxide growth. Significant Sylramic *iBN* fiber degradation is predicted in conditions that would limit B_2O_3 vaporization from the thermally grown borosilicate glass surface.

4.6 *Recommendations for future work*

High temperature oxidation studies on Sylramic *iBN* fibers in an O_2 environment in which boria volatility is limited are recommended to allow further study in the role of B in accelerating SiC oxidation kinetics.

5 Task 2: Effects of boron, pressure, and temperature on the oxidation behavior of reaction-bonded SiC coupons

Reaction-bonded SiC (RB-SiC) ceramics were used as model materials to understand the role of boron concentration on the RB-SiC oxidation behavior. Boron (B) was processed into RB-SiC coupons, comprised of silicon carbide (SiC) particles embedded in a silicon (Si) melt-infiltrated matrix. The oxidation behavior of a baseline (0 wt.% B) was compared to the oxidation behavior of RB-SiC coupons containing 0.5 and 4 wt.% B exposed to 900 and 1200°C dry O₂ environments. The effects of pressure on the oxidation kinetics were also investigated. The presence of B accelerated the RB-SiC oxidation kinetics. Extensive subsurface oxidation was also observed adjacent to a B phase present beneath the oxide. Elevated O₂ pressure also accelerated oxide growth. The combined effects of B and elevated O₂ pressure led to increased thermochemical degradation. The oxides devitrified due to trace aluminum and calcium present in the as-received coupons. These findings demonstrate that B incorporation into SiC-based matrices in ceramic matrix composite (CMC) architectures will degrade the CMC oxidation resistance. Oxidation from trace aluminum and calcium will have further deleterious effects on CMC oxidation behavior.

5.1 Objectives of Task 2

The objectives of this task are twofold. First, the effects of boron (B) RB-SiC oxidation kinetics were sought. Exposures were conducted at low and high temperature to determine if oxidation mechanisms changed with temperature. In a real combustion environment, the materials are exposed to high pressures (~ 30 atm) in addition to high temperatures. The parabolic oxidation kinetics of silicon are linearly increased with

increased O₂ pressure²⁶, similar results are expected for SiC. The second objective was to determine the effects of elevated O₂ pressure on RB-SiC oxidation kinetics. The combined effects of B concentration, temperature, and pressure on RB-SiC oxidation behavior were evaluated. The implications of the findings on CMC thermochemical degradation were presented.

5.2 *Experimental recap*

The RB-SiC coupons were characterized prior to oxidation to establish microstructure, composition, and phase content. Isothermal oxidation exposures were carried out in dry O₂ environments at 900 and 1200°C. The exposures were carried out in two different types of furnaces: 1) the thermogravimetric analysis (TGA) instrument at the University of Virginia (UVA), equipped with a thermobalance to measure weight change as a function of time under isothermal conditions at 1 atm; and 2) a custom-built furnace at Oak Ridge National Lab (ORNL) which can operate at elevated pressures. The furnace at ORNL, often called the Keiser rig, will be referred to as the high pressure rig (HPR) hereafter. Exposures in the high pressure rig were conducted at 1 atm and at 4.4 atm O₂. All exposures were carried out for 100 h. The oxidation behavior of RB-SiC coupons containing 0, 0.5, and 4 wt.% B concentration levels were compared. Weight changes were evaluated. The oxides were investigated for macrostructure, microstructure, composition, and phase using a variety of analytical techniques summarized in Table 7. The microstructures were imaged in SEM with backscattered electrons. FactSage thermochemical software was utilized to further the understanding of phases and compounds energetically favored to form based on results from elemental and diffraction analyses of the oxide microstructures. Image J image processing software was utilized for

statistical quantification of phase distribution.

Table 7: Consolidated list of characterization techniques utilized in Task 2

Evaluation	Property	Technique
Weight change	<ul style="list-style-type: none"> • Oxidation and volatilization reactions 	<ul style="list-style-type: none"> • Benchtop weight change (TGA and HPR) • TGA weight change profiles
Macrostructure	<ul style="list-style-type: none"> • Oxide and substrate topography 	<ul style="list-style-type: none"> • Optical macrographs • Optical profilometry
Microstructure	<ul style="list-style-type: none"> • Phase identification and distribution 	<ul style="list-style-type: none"> • SEM/ EDS • Image J analysis
Crystal structure	<ul style="list-style-type: none"> • Polymorphic and allotropic crystal structure determination 	<ul style="list-style-type: none"> • XRD
Composition	<ul style="list-style-type: none"> • Composition of segregated phases • Bulk composition 	<ul style="list-style-type: none"> • SEM/ EDS • ICP-OES
Oxide thickness	<ul style="list-style-type: none"> • Oxide growth 	<ul style="list-style-type: none"> • Cross-sectional measurement of oxide thicknesses using the SEM software measurement too

Oxide thickness measurements were conducted on oxidized coupons that were cut in half lengthwise, potted in epoxy, and polished to a mirror finish with 1 μm diamond suspension. A total of 31 – 41 measurements were made distanced 0.5 mm apart on both sides of the coupon length. The standard error on the mean oxide thickness was calculated with a 95% confidence interval. Further details on the oxidation equipment and characterization techniques were provided earlier in the Experimental section.

5.3 *Results*

5.3.1 Coupon characterization prior to oxidation exposure

5.3.1.1 Macrostructure

The unoxidized RB-SiC coupons had the same appearance to the eye regardless of boron content. A representative macrograph of an unoxidized coupon is shown in Figure 37.



Figure 37: Representative macrograph of unoxidized RB-SiC coupons.

5.3.1.2 Microstructure

The coupon microstructures were imaged in SEM with backscattered electrons. A comparison of microstructures from coupons containing 0, 0.5, and 4 wt.% B is shown by the micrographs in Figure 38 A – C, respectively. Microstructural features common to all coupons included: 1) a phase of grey “islands”, 2) a lighter grey continuous phase, and 3) randomly distributed small black specks. A large black phase is present only in B-containing coupons, as shown in Figure 38 B and C. A fifth dark grey phase appeared in the coupon containing 4 wt.% B, as shown in Figure 38 C. Energy dispersive X-ray spectroscopy (EDS) was utilized to identify the phase compositions.

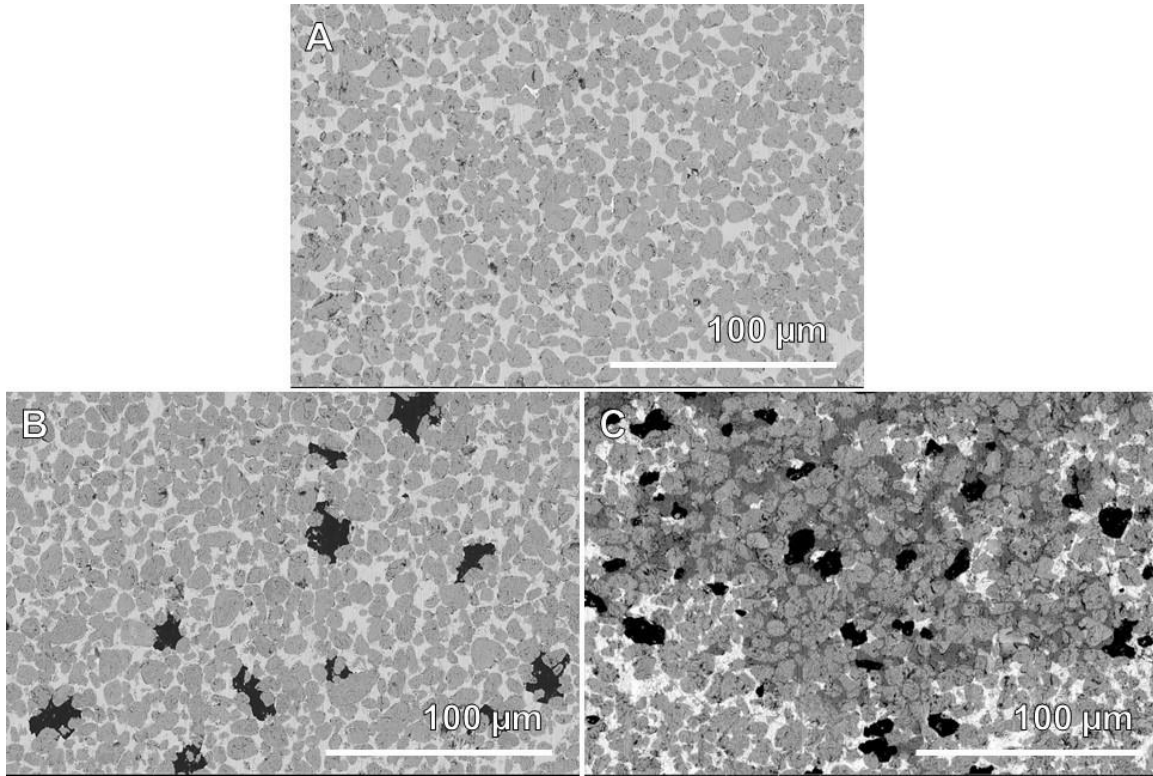


Figure 38: Plan-view micrographs of RB-SiC coupons. A) 0 wt.% B, B) 0.5 wt.% B, and C) 4 wt.% B.

5.3.1.2.1 Phase analysis by EDS: elemental maps

EDS analysis of the baseline (0 wt.% B) coupon microstructure, Figure 38 A, provided elemental maps of the phases present in all coupons (i.e., grey “islands”, light grey continuous phase, and small black specks). Carbon (C), silicon (Si), and aluminum (Al) were identified, as shown by the elemental maps in Figure 39. The C map, which corresponds with the grey “islands”, represents SiC particles. The bright spots in the C map are residual carbon that had not reacted during coupon processing¹⁰². The Si map represents two phases: 1) the bright green areas in the Si map, which correspond with the light grey continuous phase, represents the melt infiltrated Si matrix; and 2) the dark green areas that overlap with the C map are again the SiC phase. The Al map, which corresponds with the small black specks, was identified as an Al constituent.

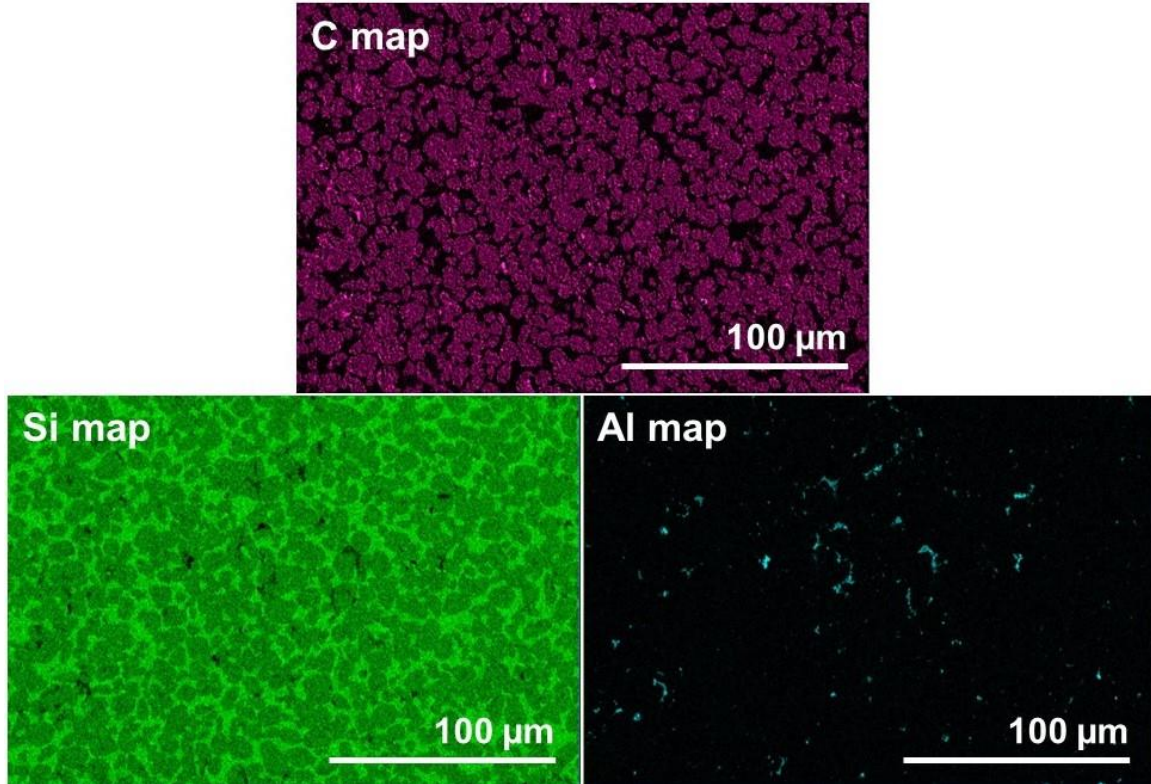


Figure 39: Elemental EDS maps of C, Si, and Al taken from the baseline 0 wt.% B coupon microstructure

EDS maps of the 0.5 and 4 wt.% B coupon microstructures are shown in Figure 40 and 41. The large black phases present in these microstructures (Figure 38 B and C) are B, as shown by the B elemental maps in Figure 40 and Figure 41. The Al maps shown in Figure 40 and Figure 41 show Al was present in two phases: 1) as a pure Al phase represented by the small bright specks, and 2) in the B phase. The Si maps in Figure 40 and 41 show that the B phase was segregated from the Si and SiC phases. Elemental C maps were also included in Figure 40 and 41. The low intensity regions in the C maps correspond to areas containing the B phase.

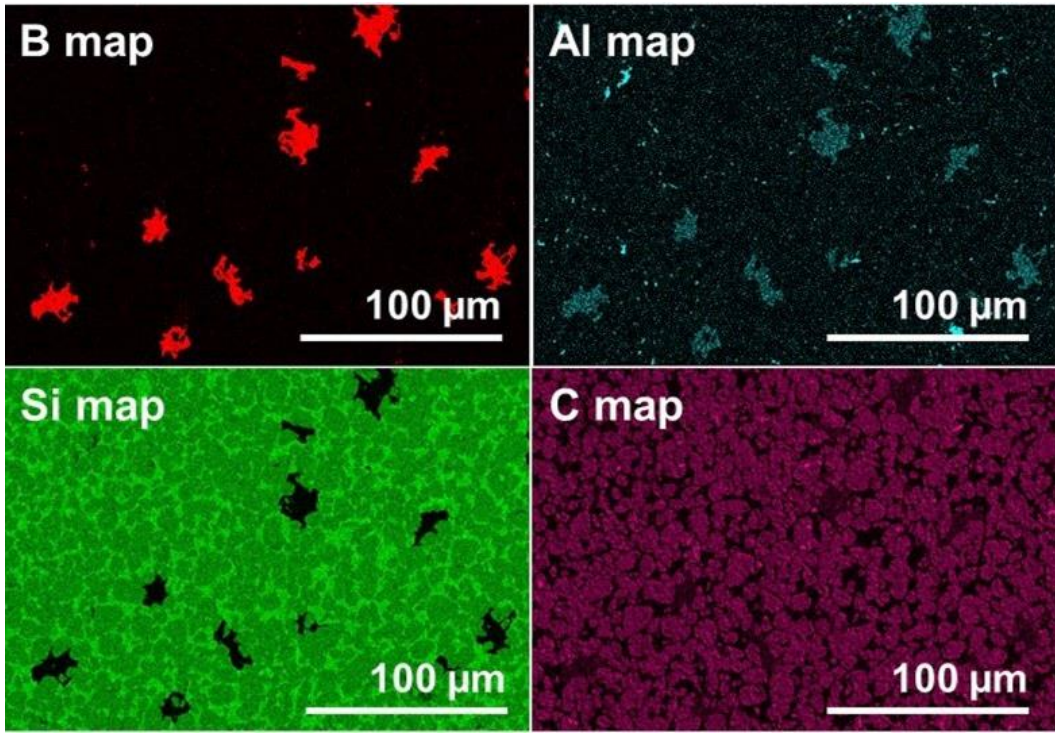


Figure 40: EDS elemental maps taken in plan view from 0.5 wt.% B RB-SiC coupon.

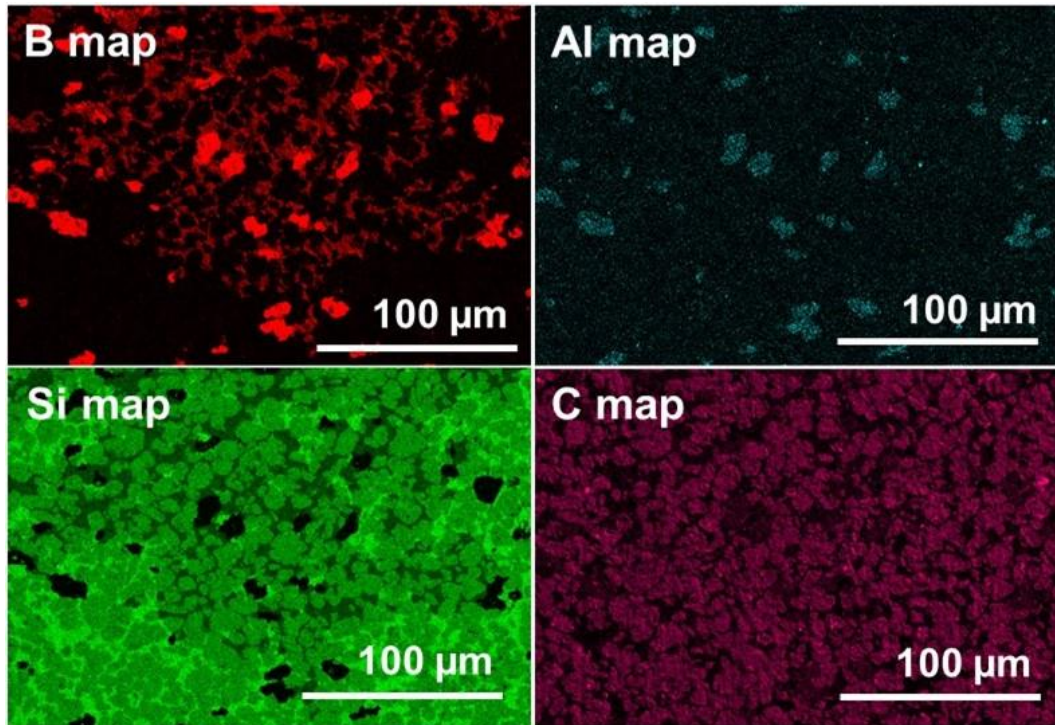


Figure 41: EDS elemental maps taken in plan view from 4 wt.% B RB-SiC coupon.

5.3.1.2.2 Phase analysis by EDS: point ID

The presence of the Al phase, and its presence in the B phase in particular, was unexpected. Point 1 in Figure 42 left was analyzed by point EDS to identify its composition. The top spectrum in Figure 42 right, is the result from the EDS analysis of Point 1. The spectrum shows that the B-rich phase also contained C, O, Al and Si. The Si signal likely arose from the surrounding Si and SiC matrix since the B and Si EDS maps show that these phases are segregated. The presence of C may be indicative of a B-C compound, but contamination from the SEM chamber may also have contributed to the C concentration. The presence of O may have resulted from surface contamination or some oxidation of the coupon during processing. The combination of B and Al suggests the presence of a B-rich – Al compound.

The dark grey phase present in the 4 wt.% B coupon microstructure (Figure 38 C) was also investigated by point EDS. Point 2 in Figure 42 left represents the area in the dark grey phase that was analyzed. The results from point 2 are provided by the bottom spectrum in Figure 42. The spectrum shows that the dark grey phase was comprised of Ca, in addition to B, C, O, and Si. As with Al, the presence of Ca was also unexpected. For a better understanding of the EDS results, the possibility of compound formation from reactions between B, Al, Ca, Si, and C was determined by utilizing the compound data stored in FactSage databases that are accessed through the Databases module, described next.

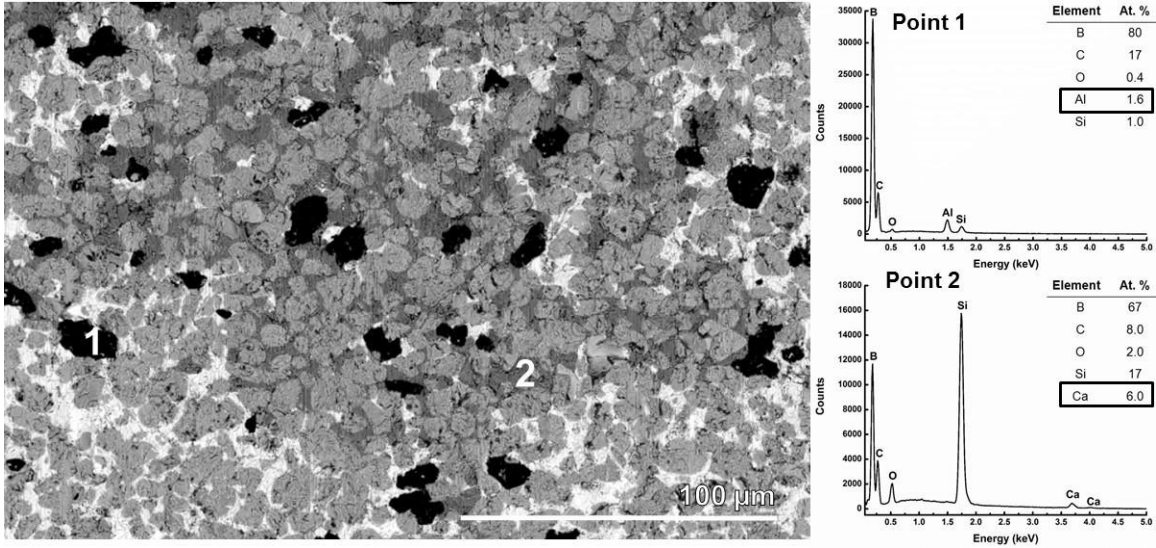


Figure 42: Left) Point ID EDS analysis of the black (Point 1) and dark grey (Point 2) phases present in the micrograph taken from the 4 wt.% B-containing RB-SiC coupon. Top right) spectrum corresponding with the point ID analysis of Point 1. Bottom right) spectrum corresponding with the point ID analysis of Point 2.

5.3.1.3 FactSage prediction of compounds formed from B, Al, Ca, Si, and C

The FactSage phase diagram database was utilized to look up binary and ternary phase diagrams of systems Al-B, Ca-B, Ca-Si, B-C, and Ca-B-Si. First, binary phase diagrams for systems Al-B, Ca-B, Ca-Si, and B-C are shown in Figure 43. The EDS compositions from Points 1 and 2 spectra in Figure 42 were used to identify the appropriate phase regions in the phase diagrams. For instance, the Al-B phase diagram shows the co-existence of B with an AlB_{12} compound. Other compounds predicted from the phase diagrams are CaB_6 , CaSi_2 , and B_4C . A Ca-Si-B compound was not predicted.

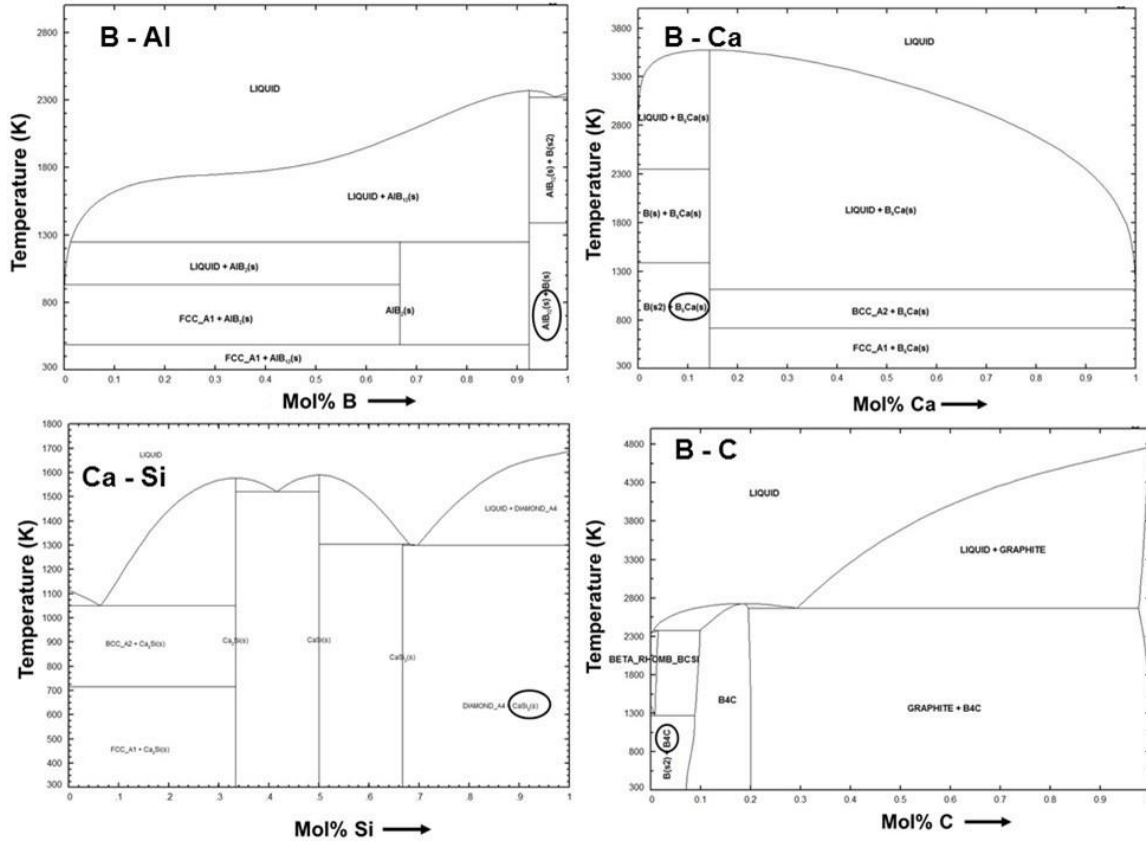


Figure 43: Binary phase diagrams of systems B-Al, B-Ca, and Ca-Si, and B-C¹⁰⁰.

Standard state free energies of formation of AlB_{12} , B_4C , CaB_6 , and CaSi_2 compounds were looked up in the FactSage Databases module and were listed in Table 8. The negative free energies indicate that all compounds may form; however B_4C is the least energetically favored compound. The greater negative free energy of formation for CaSi_2 relative to CaB_6 suggests Ca is more likely to bond with Si than with B. Any effects from the Al and Ca on the RB-SiC oxidation behavior are unknown. Therefore, it was important to 1) identify their presence, and 2) understand their phase identity and distribution in the coupon microstructures.

Table 8: FactSage data for compounds consistent with EDS Points 1 and 2 in Figure 42 left

EDS Point ID	Compounds predicted to form	Gibbs Free Energy (kJ/mol) of formation at 298 K, 1 atm
1	AlB ₁₂	-236
	B ₄ C	- 70.8
2	B ₆ Ca	-188
	CaSi ₂	-233

5.3.1.4 B Phase area fraction

The B phase fraction and distribution are hypothesized to impact the RB-SiC oxidation behavior. Image J analysis of the B elemental maps from the B-containing RB-SiC coupons quantified the area fraction that the B phase occupied as a function of B concentration. Particle size analysis of the B phase taken from B elemental maps shown earlier in Figure 40 and 41 are provided in Figure 44 A and B, respectively. The B area fraction quantified from the particle size analysis was 4% in the 0.5 wt.% B coupon and 15% in the 4 wt.% B, indicating that the B area fraction increased with increasing B concentration. The greater number of particles in the 4 wt.% B coupon indicates that the distribution of the B phase increased with increased B concentration. The effect of this B content and distribution on the RB-SiC oxidation behavior is investigated in this study.

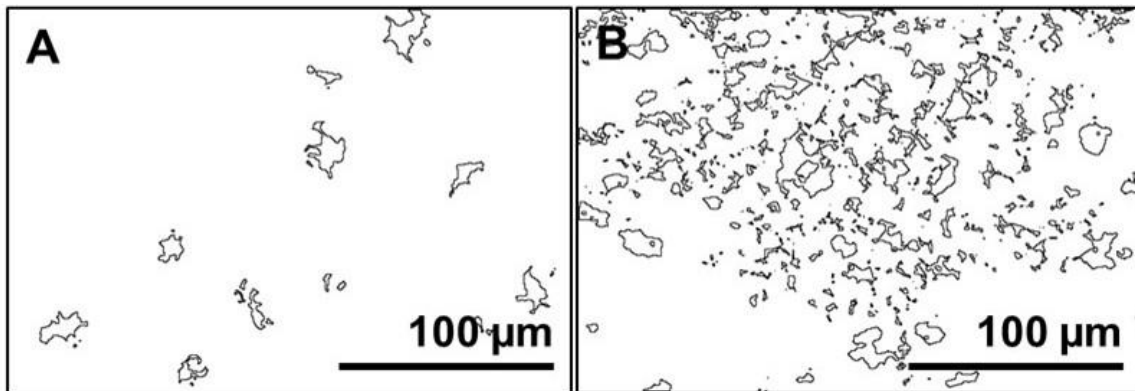


Figure 44: Quantification of B area fraction by Image J particle size analysis of B elemental maps. A) Particle outlines of the B phase of the B elemental EDS map taken from the RB-SiC coupon containing 0.5 wt.% B (Figure 40) Particle outlines of the B phase of the B elemental EDS map taken from the RB-SiC coupon containing 4 wt.% B (Figure 41).

5.3.2 Crystal structure

The crystal structures of the phases in the RB-SiC coupons were identified by XRD. The diffraction patterns of the RB-SiC coupons containing 0, 0.5, and 4 wt.% B are shown in the stacked plots in Figure 45. Peaks for the diamond cubic Si and hexagonal SiC polymorph are present in every pattern. Peaks representing B, Al and Ca, or any possible crystalline compounds thereof, were not present in the diffraction patterns, likely due to their concentrations being below the instrument's sensitivity limits.

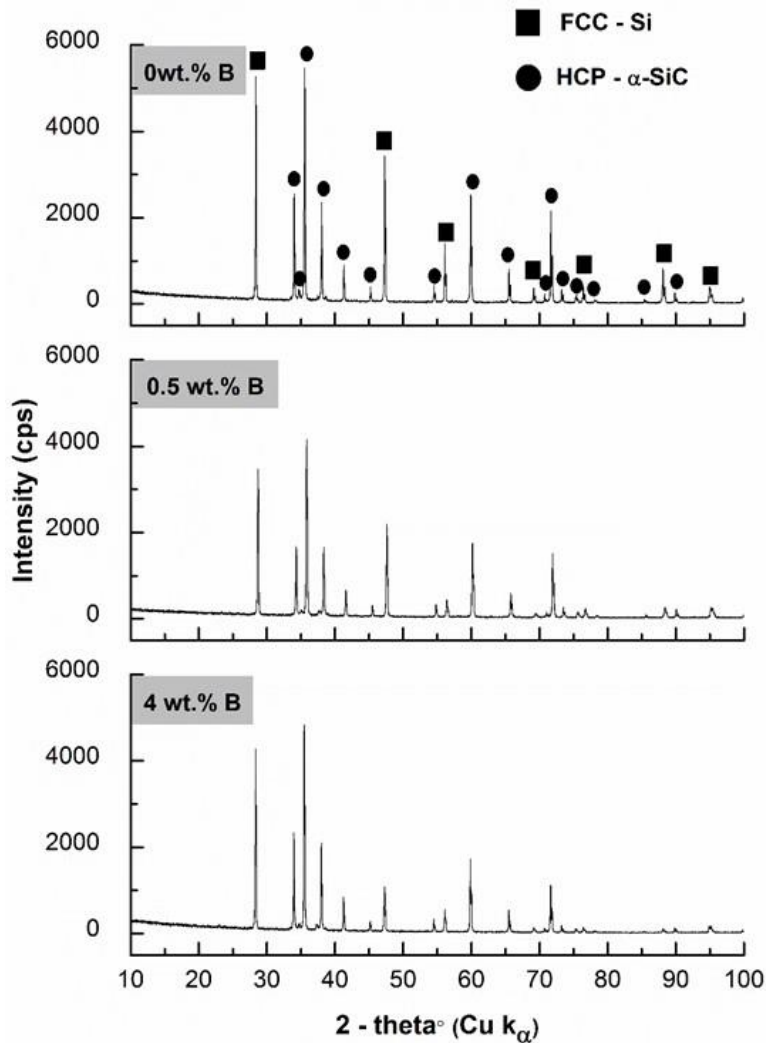


Figure 45: XRD analysis of RB-SiC coupons. From top-to-bottom: Diffraction patterns from RB-SiC coupons containing 0, 0.5, and 4 wt.% B.

5.3.3 Oxidation exposures

The weight change profiles obtained from isothermal oxidation of RB-SiC coupons in the TGA were provided first. Oxidation mechanisms were identified. The benchtop weight change results from the exposures in TGA and the high pressure rig were then compared.

5.3.3.1 Weight change profiles

Plots of the weight change profiles from TGA exposures of 0, 0.5, and 4 wt.% B coupons at 900°C for 100 h in 1 atm dry O₂ are shown in Figure 46 as specific weight change versus time. It is apparent from the individual plots that the coupon composition affected the weight change behavior. For instance, the weight change from oxidation of the baseline (0 wt.% B) RB-SiC coupon was rapid up to the first ~ 8 h of exposure, followed by weight loss for the remainder of the exposure. The weight change profile from oxidation of the 0.5 wt.% RB-SiC coupon was roughly linear with a slight change in slope occurring at ~ 50 h of exposure. Oxidation of the 4 wt.% RB-SiC coupon exhibited a sharp weight increase during the first few hours of exposure, followed by a rapid weight loss up to 10 h of exposure. The weight gain was then roughly linear for the remainder of the exposure. The fluctuations in the weight change profiles are a demonstration of competing oxidation mechanisms that took place during exposure.

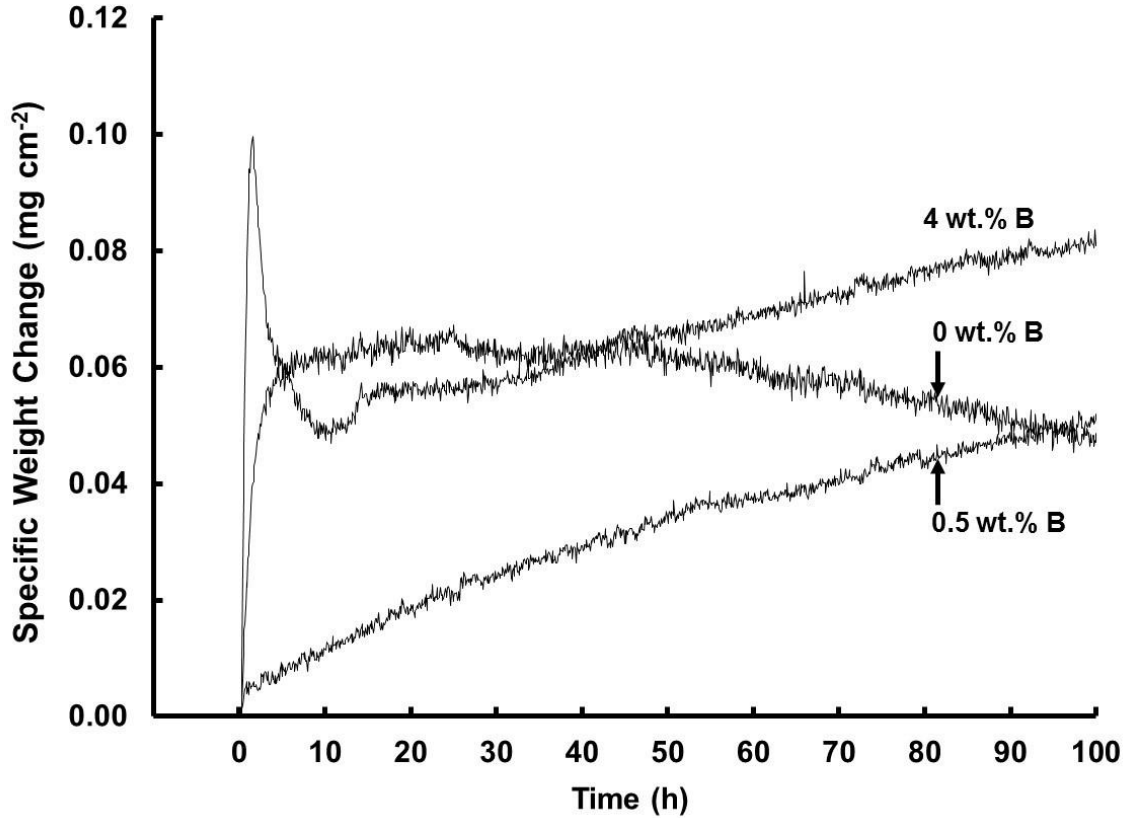


Figure 46: TGA weight profiles of RB-SiC coupons containing 0, 0.5, and 4 wt.% B from exposures at 900°C for 100 h in 1 atm dry O₂.

Plots of the weight change profiles from TGA exposures of 0, 0.5, and 4 wt.% B coupons at 1200°C for 100 h in 1 atm dry O₂ are shown as specific weight change versus time in Figure 47 A, and as specific weight versus the square root time in Figure 47 B. The weight change profiles in Figure 47 A suggest that parabolic oxidation kinetics were followed. The linear behavior observed when the specific weight change was plotted versus root time in Figure 47 B is further evidence that the oxidation mechanism was controlled by diffusion²³. The parabolic rate constants, k_p , were calculated from the squared slopes of the linear fits (Figure 47 B dotted lines) to the specific weight change plotted versus root time. The 4wt.% B k_p was 4.3 times greater than the baseline k_p . The results indicate that the RB-SiC coupons oxidized faster when B was present. Although the linear fit R^2 values were > 0.991 for all fits, the linear approximation fits poorly to the

baseline transient period of rapid weight gain. Further, the linear fit to the 4 wt.% B RB-SiC weight change deviates at ~ 38 h, where there was a slight change in slope. The ratio of the slope from the first 38 h of test to the slope from the remaining 62 h of test is 1.8, meaning that the parabolic kinetic rate constant decreased by approximately a factor of three with the change in slope.

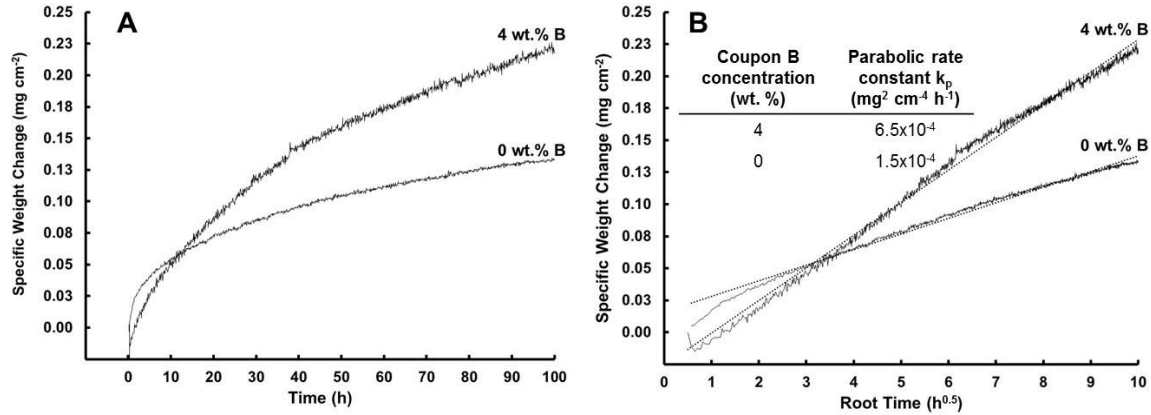


Figure 47: TGA weight profiles of RB-SiC coupons containing 0 and 4 wt.% B from exposures at 1200 °C for 100 h in 1 atm dry O₂. A) Plots of specific weight change versus time. B) Plots of specific weight change versus root time. Forced linear fits are denoted by dotted lines. TGA weight change profiles of RB-SiC coupons containing 0.5 wt.% B are unavailable for exposures at 1200 °C.

5.3.3.2 Benchtop weight change

Benchtop weight changes, determined after both TGA and high pressure rig exposures, were normalized to the coupon surface areas. The specific weight changes from TGA exposures were plotted versus temperature in Figure 48 A. The 0 wt.% B and 0.5 wt.% B coupons had similar weight gains, whereas the weight gain was greater for 4 wt.% B coupons following both 900 and 1200 °C TGA exposures. The specific weight changes from high pressure rig exposures were plotted versus pressure in Figure 48 B. Results from 900 and 1200 °C were presented together. The solid lines from 900 °C exposures and the dashed lines from 1200 °C exposures are to guide the eye only. The 900 °C trends show that the 0 wt.% B coupon weight gain was independent of pressure,

whereas the B-containing coupon weight gains increased with 1) increased pressure and 2) increased B concentration. The coupons weight gains between TGA and high pressure rig exposures at 1 atm were similar in magnitude. The boron effects on the RB-SiC weight gain were most evident from coupons containing 4 wt.% B. Coupon weight gains from 1200°C high pressure rig exposures increased with increased pressure and B concentration, as shown in Figure 48 B (lines are to guide the eye).

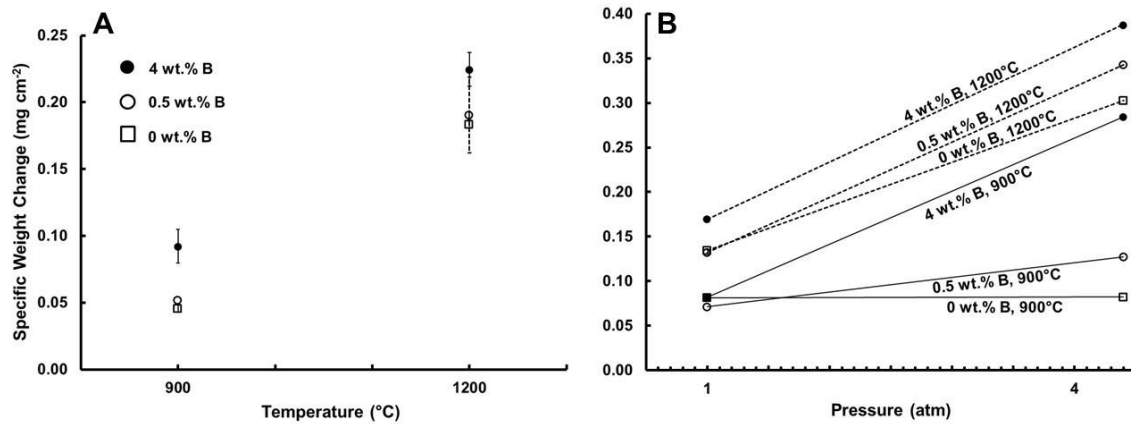


Figure 48: Specific weight change from benchtop weight measurements following TGA and high pressure rig exposures of RB-SiC coupons containing 0, 0.5, and 4 wt.% B. A) Specific weight change from 900 and 1200 °C TGA exposures for 100 h in 1 atm dry O₂. B) Specific weight from 900 (solid lines) and 1200 °C (dashed lines) high pressure rig exposures in 1 and 4.4 atm dry O₂. Lines are to guide the eye.

5.3.4 Characterization of oxidized RB-SiC coupons

5.3.4.1 Oxide macrostructure

Oxidation of B-containing coupons resulted in oxides with visibly rough topographical features. Optical macrographs of 4 wt.% B coupon surfaces before and after TGA and high pressure rig oxidation exposures at 1200°C are shown in Figure 49 A – D. In contrast with the smooth unoxidized coupon surface shown in Figure 49 A, globules were present in the oxidized coupon surfaces (Figure 49 B and C, outlined by dashed circles), or the oxide had a frosty appearance (Figure 49 D).

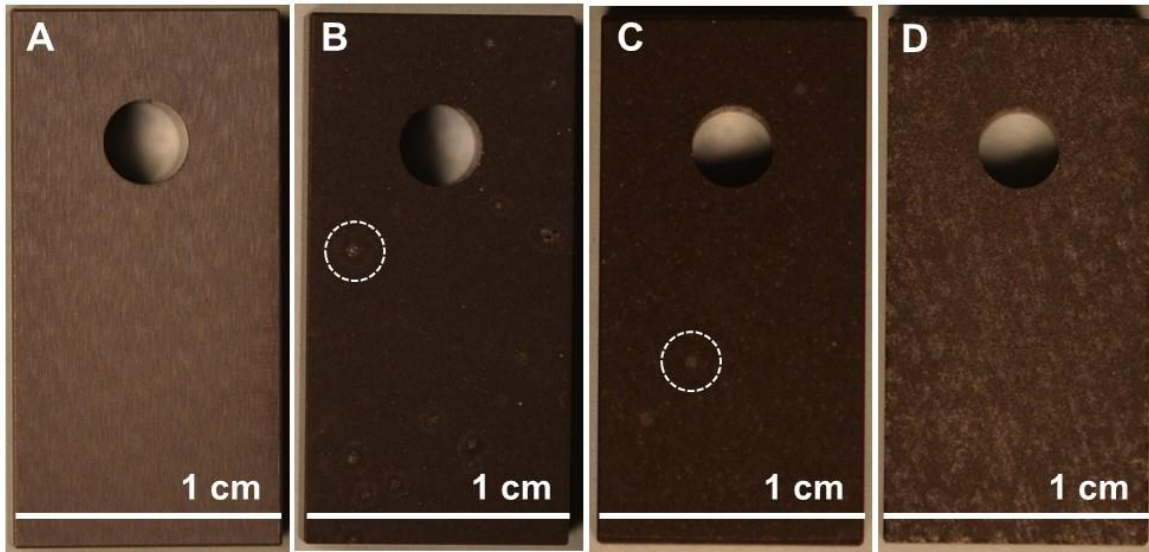


Figure 49: Optical macrographs of RB-SiC coupons containing 4 wt.% B. A) Unoxidized coupon, B) Oxidized coupon following the 1200 °C TGA exposure, C) Oxidized coupon following 1200 °C high pressure rig exposure at 1 atm dry O₂, and D) Oxidized coupon following 1200 °C high pressure rig exposure in 4.4 atm dry O₂.

The oxide surface roughness was quantified with optical profilometry. The surface roughness of an unoxidized coupon and oxidized coupons following 1200 °C exposures in the TGA or high pressure rig are compared in Figure 50 A – C, respectively. A 350 x 250 μm² area was analyzed. The colors of the analyzed areas correlate with surface roughness heights shown in the scale bars to the right of the analyzed areas. The unoxidized coupon surface roughness predominantly ranges from 3.5 – 4.5 μm, as shown in Figure 50 A. The surface roughness of the oxidized coupon following TGA exposures showed peak-to-valley differences that approached 20 μm in the dominant surface roughness range of 10 – 30 μm, as shown in Figure 50 B. Oxidation at elevated pressure resulted in comparatively lower oxide surface roughness that ranged from 10 – 20 μm, as shown in Figure 50 C.

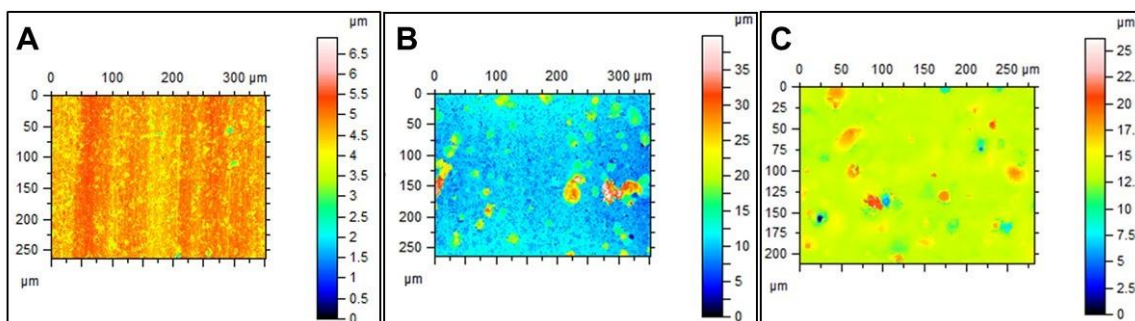


Figure 50: Optical profilometry of the surface roughness of RB-SiC coupons containing 4 wt.% B. A) Unoxidized coupon, B) Oxidized coupon following the TGA exposure at 1200 °C in 1 atm dry O₂, and C) Oxidized coupon following the high pressure rig exposure at 1200 °C in 4.4 atm dry O₂. (Courtesy of Madeline Morales)

5.3.4.2 Oxide microstructure

The oxide microstructures were extensively characterized with SEM/ EDS. The following sections describe these results. The oxide microstructures were imaged in the SEM in plan view with backscattered electrons. Images were taken from 3 – 5 areas on each coupon. The surface microstructures were greatly affected by the oxidation of B. Additional effects from oxidation of the Al and Ca constituents on the microstructure were also found. For clarity, the characterization results of the oxide microstructures are subdivided into two sections. The oxide microstructures that developed from TGA exposures are described first, followed by a description of the oxide microstructures that formed by high pressure rig exposures. In both of these sections, the effects of B precede the effects of Al and Ca on the oxide microstructures.

5.3.4.2.1 Oxide microstructures formed from TGA exposures at 900 °C

5.3.4.2.1.1 B effects on oxide microstructure

Micrographs of oxides formed on RB-SiC containing 0, 0.5, and 4 wt.% B following oxidation in the TGA at 900 °C are compared in Figure 51 A – C, respectively. Each micrograph shows extensive oxidation occurred at the interface between the SiC islands and the Si matrix. There were additional dome-shaped features present on

oxidized B-containing coupons, as shown in Figure 51 B and C. A comparison of Figure 51 B and C shows that these domes occurred at a higher frequency and qualitatively covered a greater surface area on the 4 wt.% B coupon. Points 1 and 2 in Figure 51 B and point 3 in Figure 51 C were investigated with EDS for composition. The EDS results are described next.

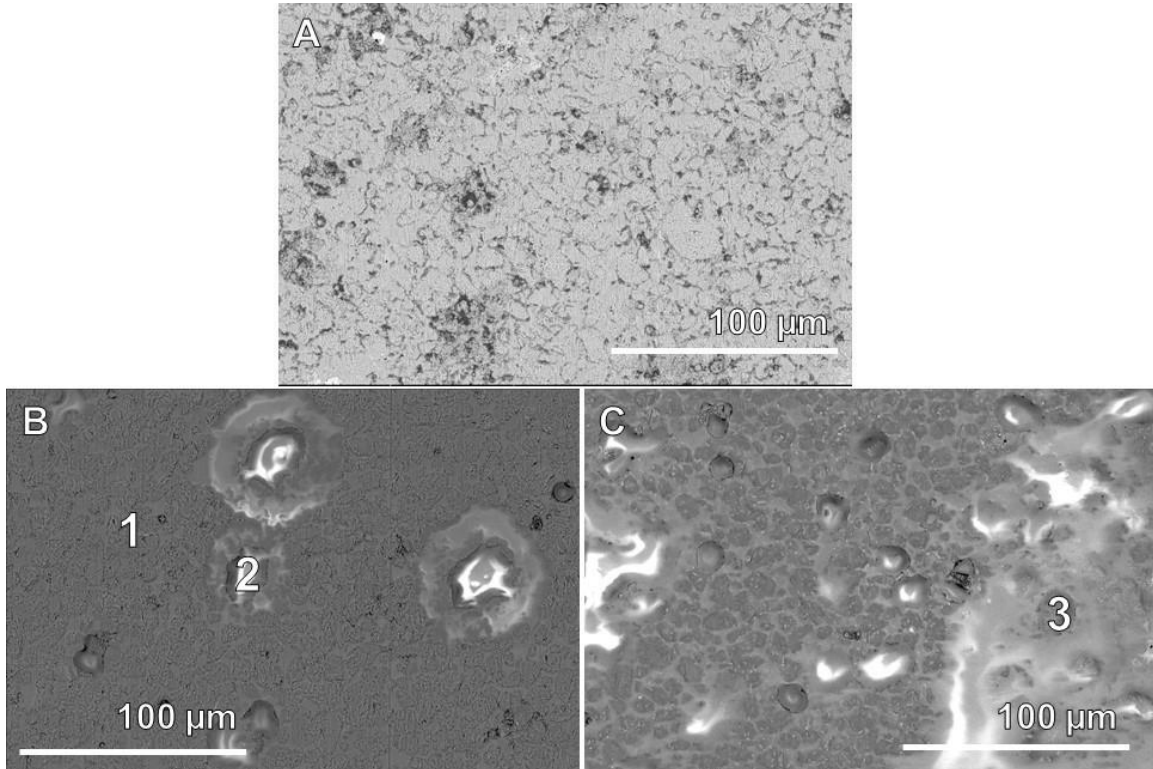


Figure 51: Plan-view micrographs of oxidized RB-SiC coupons following TGA exposures at 900 °C for 100 h in 1 atm dry O₂. A) 0 wt.% B baseline coupon, B) 0.5 wt.% B coupon, and C) 4 wt.% B coupon. Labels 1- 3 correspond with areas analyzed by EDS.

The spectra and elemental compositions corresponding with points 1 – 3 are provided sequentially in Figure 52. The compositional results were included in each spectrum for qualitative comparison of localized oxide compositions. For instance, the high O concentrations indicate that surfaces being analyzed were oxides. The top spectrum is the result from analysis of Point 1, an area on the oxidized coupon sampled away from a dome (Figure 51 B). It is mainly comprised of Si, which is attributed to the

formation of silica. The middle and bottom spectra in Figure 52 are results obtained from analysis of points 2 and 3, which were sampled from the domes shown in Figure 51 B and C, respectively. The domes are comprised mostly of B, which is attributed to the formation of boria-rich borosilicate glass. Note that the frequency of the borosilicate domes are greater in the oxide formed on the 4 wt.% B due to the increase in B phase distribution with increased B concentration. It is unlikely that the oxide structure contains C bonds. The C concentration is attributed to surface contamination.

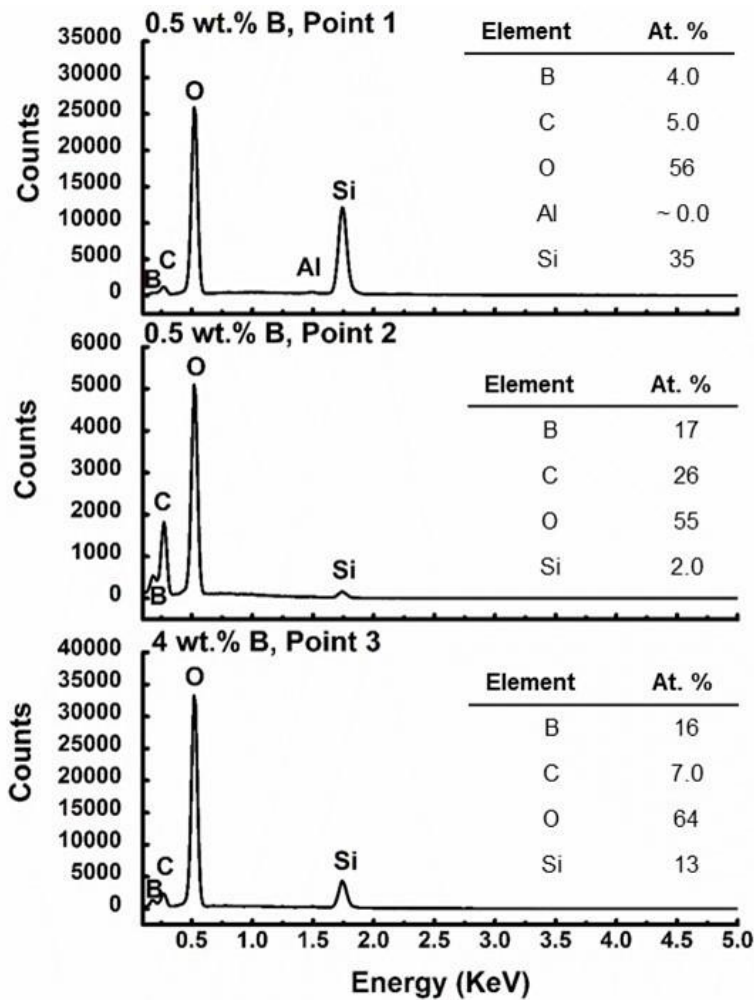


Figure 52: Point EDS spectra and elemental compositions from 0.5 and 4 wt.% B coupon surfaces oxidized in the TGA instrument at 900°C for 100 h in 1 atm dry O₂. Point 1 (top spectrum) and Point 2 (middle spectrum) collected from the 0.5 wt.% B coupon, as shown in Figure 51 B. Point 3 (bottom spectrum) collected from the 4 wt.% B coupons, as shown in Figure 51 C.

Elemental EDS maps were also constructed from the microstructures shown in Figure 51 B and C. A comparison of B and Si maps obtained from map analysis of these microstructures are provided in Figure 53. The B and Si maps in the left column were obtained from analysis of the oxidized 0.5 wt.% B coupon, and the corresponding maps in the right column were obtained from analysis of the oxidized 4 wt.% B coupon. Elemental O maps were excluded, as O was uniformly present across the entire oxidized surface. The boria-rich oxide regions were difficult to resolve from B maps alone, as shown in Figure 53 top row, but were well-defined in the Si maps shown in Figure 53 bottom row. Formation of the boria globules is attributed to the oxidation of the B phase. The dome shapes of the boria globules is postulated to have arisen from immiscibility with SiO₂^{46, 103}, or from wetting^{60, 104} and viscosity^{42, 55} limitations.

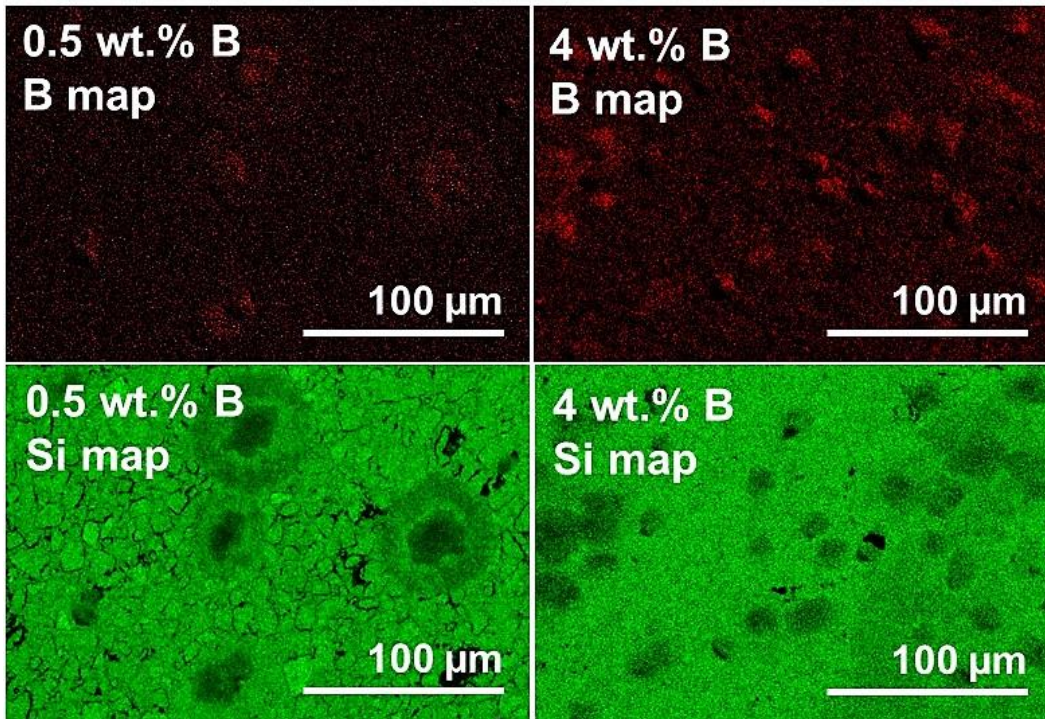


Figure 53: Elemental EDS maps of B and Si taken of oxides formed on RB-SiC coupons containing 0.5 and 4 wt.% B after oxidation in the TGA instrument at 900 °C for 100 h in 1 atm dry O₂, shown Figure 51 B and C. Left column) B map (top) and Si map (bottom) from the 0.5 wt.% B coupon oxidized surface, and Right column) B map (top) and Si map (bottom) from the 4 wt.% B coupon oxidized surface.

5.3.4.2.1.2 Al effects on oxide microstructure

Elemental Al EDS maps constructed from the microstructures shown in Figure 51A – C are shown in Figure 54 A – C. The maps in Figure A and B indicate that Al diffused to the surface through the Si and SiC interfaces where it oxidized to form alumina (Al_2O_3). There was no evidence of Al present in the borosilicate domes formed on 0.5 and 4 wt.% coupons, as shown in Figure 54 B and C, respectively. The presence of Al appeared more diffusively distributed on the oxidized 4 wt.% B coupon (Figure 54 C). The presence of Al on oxidized baseline and 0.5 wt.% B coupons (Figure 54 A and B, respectively) was more localized.

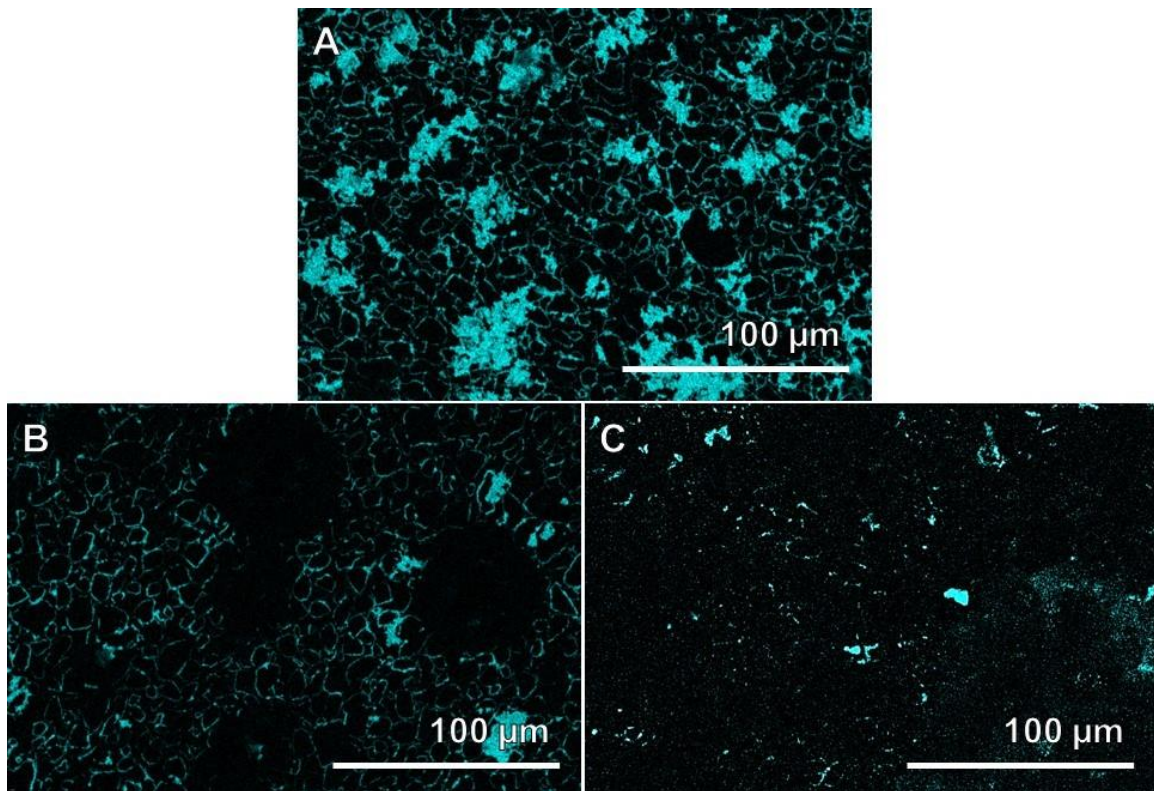


Figure 54: Elemental EDS maps of Al taken of oxides formed on RB-SiC coupons containing 0, 0.5 and 4 wt.% B oxidized in the TGA instrument at 900°C for 100 h in 1 atm dry O_2 , shown in Figure 51 A, B, and C, respectively. A) 0 wt.% B baseline coupon, B) 0.5 wt.% B coupon, and C) 4 wt.% B coupon.

5.3.4.2.1.3 Ca effects on oxide microstructure

The micrographs shown below in Figure 55 A – C were taken from different areas

on the baseline and B-containing coupons shown previously in Figure 51 A – C. These oxide microstructures differ by the appearance of a sharp light grey phase that was sometimes prone to cracking and pitting, as shown in Figure 55 B and C. Points 1 and 2 in Figure 55 A, and points 3 and 4 in Figure 55 B and C, respectively, were investigated with EDS for composition. The results are provided below.

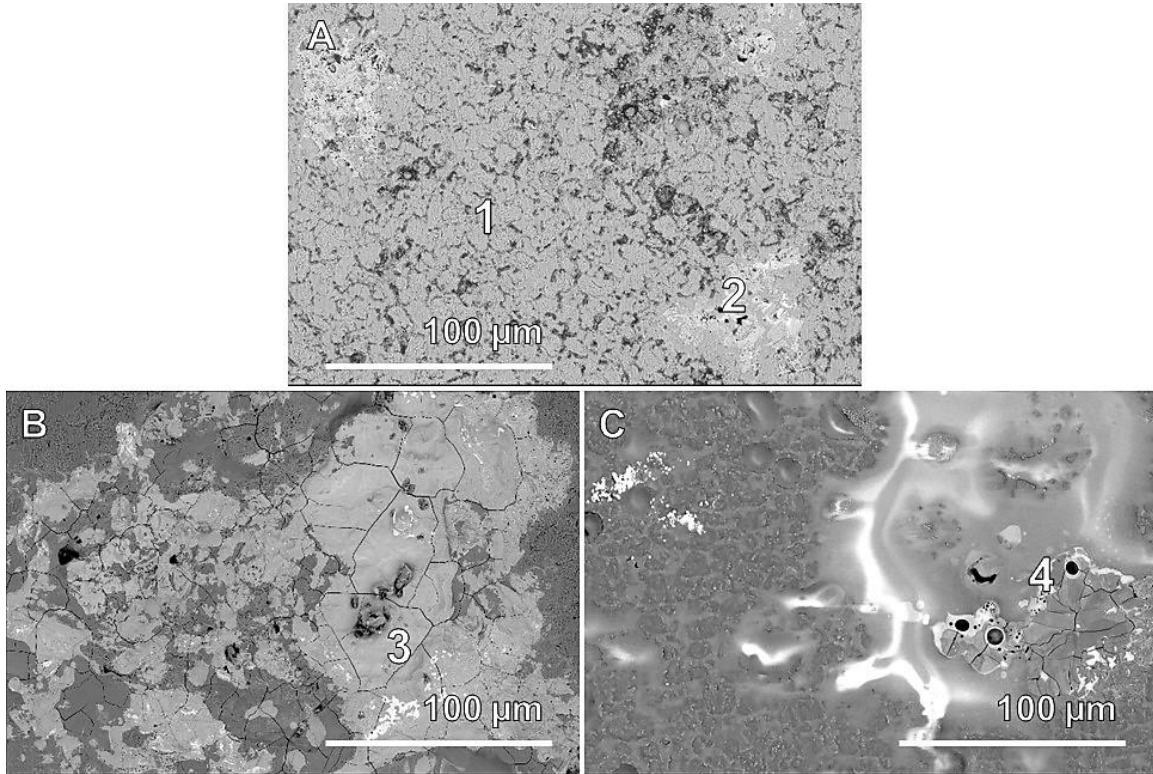


Figure 55: Plan-view micrographs of oxidized RB-SiC coupons following TGA exposures at 900 °C for 100 h in 1 atm dry O₂ showing a bright oxide phase prone to cracking and pitting. A) 0 wt.% B baseline coupon, B) 0.5 wt.% B coupon, and C) 4 wt.% B coupon. Labels 1- 4 correspond with areas analyzed by Point ID EDS.

The top left spectrum in Figure 56 is the result from analysis of Point 1, an area on the oxidized baseline coupon sampled away from the light grey phase (Figure 55 A). The dominant peaks are Si and O, which are attributed to the formation of silica. The top right spectrum in Figure 56 was obtained from analysis of Point 2 sampled from the grey phase in Figure 55 A. Here, Ca and Al were present with Si and O. The middle and bottom spectra in Figure 56 are results obtained from analysis of points 3 and 4, which

were sampled from the borosilicate domes shown in Figure 55 B and C, respectively.

Both spectra show peaks for B, Ca, O, Al, and Si.

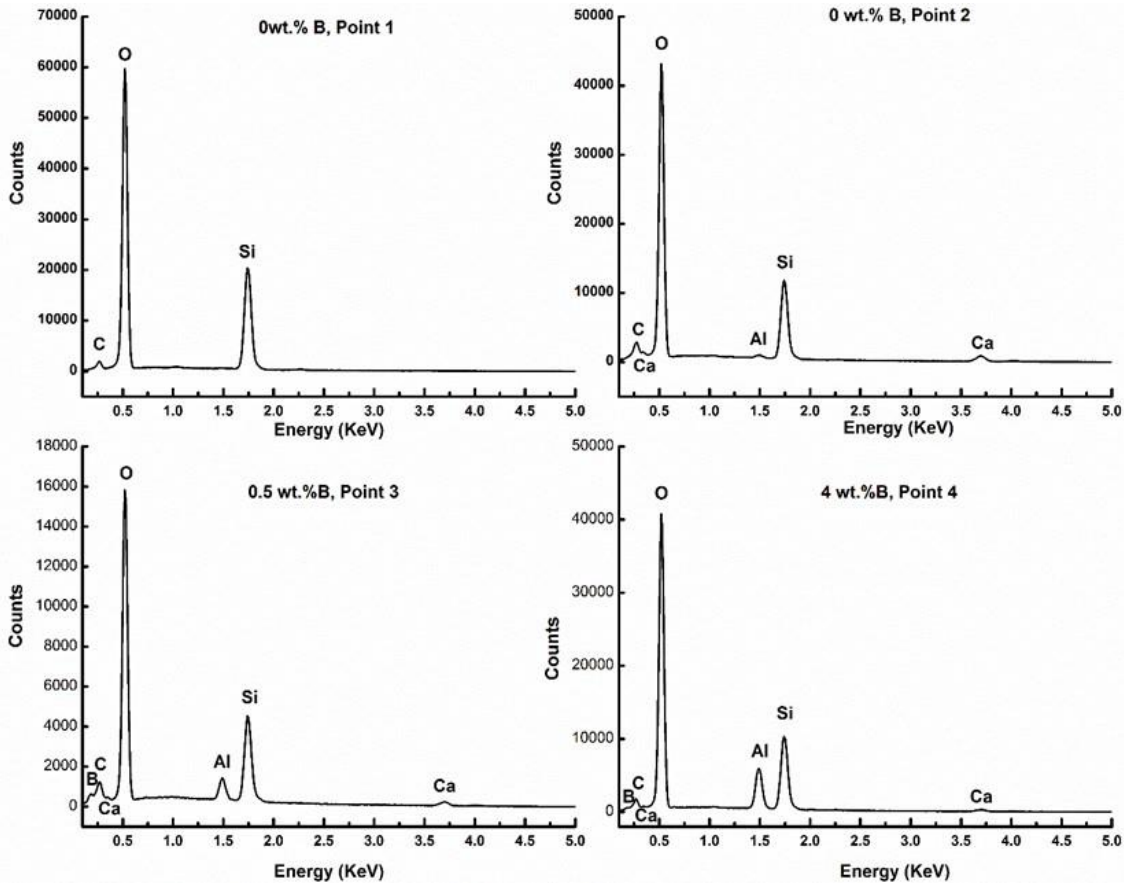


Figure 56: Point EDS spectra and elemental compositions from 0.5 and 4 wt.% B coupon surfaces oxidized in the TGA instrument at 900 °C for 100 h in 1 atm dry O₂. Point 1 (top left) and Point 2 (top right) collected from the 0 wt.% B coupon; Point 3 (bottom left) collected from the 0.5 wt.% B coupon; and Point 4 (bottom right) collected from the 4 wt.% B coupon, as shown by labels 1 – 4 in Figure 55.

Compositions from the point EDS spectra shown in Figure 56 were listed in Table 9. The Ca concentrations are considerably high. These results show that Al and Ca introduced defects, like cracks and pits, in the oxide microstructure, which are fast diffusion pathways for O₂ ingress.

Table 9: Point EDS elemental compositions from 0.5 and 4 wt.% B coupon surfaces oxidized in the TGA instrument at 900°C for 100 h in 1 atm dry O₂. Point 1 (top left) and Point 2 (top right) collected from the 0 wt.% B coupon; Point 3 (bottom left) collected from the 0.5 wt.% B coupon; and Point 4 (bottom right) collected from the 4 wt.% B coupon, as shown by labels 1 – 4 in Figure 55.

Element	Elemental Concentrations (At. %)			
	0 wt.%B, Point 1	0 wt.% B, Point 2	0.5 wt.% B, Point 3	4 wt.% B, Point 4
B	0.0	0.0	7.0	4.0
C	3.0	2.0	3.0	2.0
Ca	0.0	21	14	8.0
O	64	58	59	58
Al	0.0	1.0	3.0	8.0
Si	33	18	14	20

5.3.4.2.2 Oxide microstructures formed from TGA exposures at 1200°C

Micrographs of oxides formed on RB-SiC containing 0, 0.5, and 4 wt.% B following oxidation in the TGA at 1200°C are compared in Figure 57 A – C, respectively. The 0 wt.% B coupon was extensively oxidized at the Si-SiC interface (Figure 57 A). Oxides formed on the B-containing coupons were populated with cracks and bubbles (Figure 57 B and C). Results from point EDS analysis (not shown here) of the oxidized B-containing coupons detected Si and O, but not B. The presence of cracks in silica signals that the oxide had devitrified, forming cristobalite which can nucleate at 1200°C with the presence of impurities¹⁰⁵.

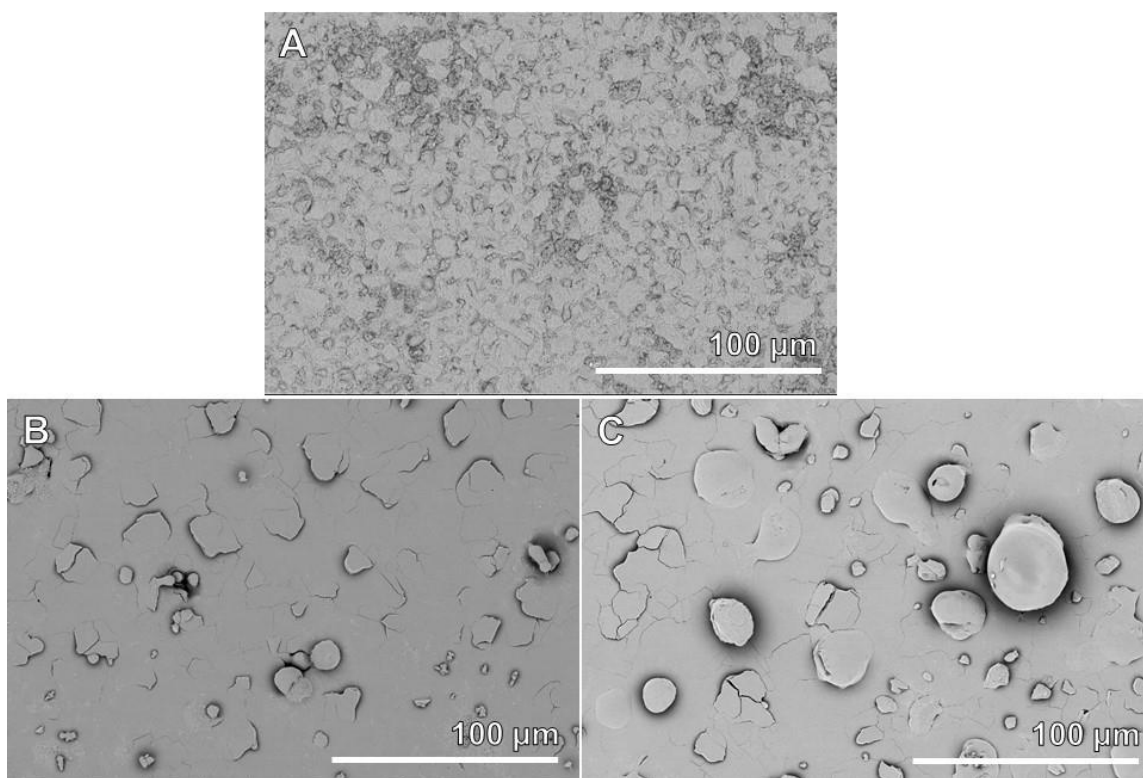


Figure 57: Plan-view micrographs of oxidized RB-SiC coupons following TGA exposures at 1200°C for 100 h in 1 atm dry O₂. A) 0 wt.% B baseline coupon, B) 0.5 wt.% B coupon, and C) 4 wt.% B coupon.

5.3.4.2.3 Oxide microstructures formed from high pressure rig exposures

Micrographs of oxides formed on RB-SiC containing 0, 0.5, and 4 wt.% B following oxidation in the high pressure rig at 900°C in 1 and 4.4 atm dry O₂ are compared in Figure 58. The oxide microstructures resulting from oxidation in 1 atm dry O₂ (Figure 58 top row) share the same features that were present in oxide microstructures formed on coupons oxidized in the TGA at 900°C, shown previously in Figure 51. These features include extensive oxidation at the interface between the SiC islands and the Si matrix, and the presence of domes in oxides formed on B-containing coupons. The oxide microstructures that developed during 900°C exposures in 4.4 atm dry O₂ were different from those that developed from 1 atm exposures. For instance, the oxide formed on the baseline coupon was cracked, as shown in Figure 58 D. The domes formed on the B-

containing coupons were comparatively broader and flatter, as shown in Figure 58 E and F, respectively. Results from point EDS analysis (not shown here) of the oxidized B-containing coupons detected did detect B at the oxide surfaces, even in the flat regions shown in Figure 58 F.

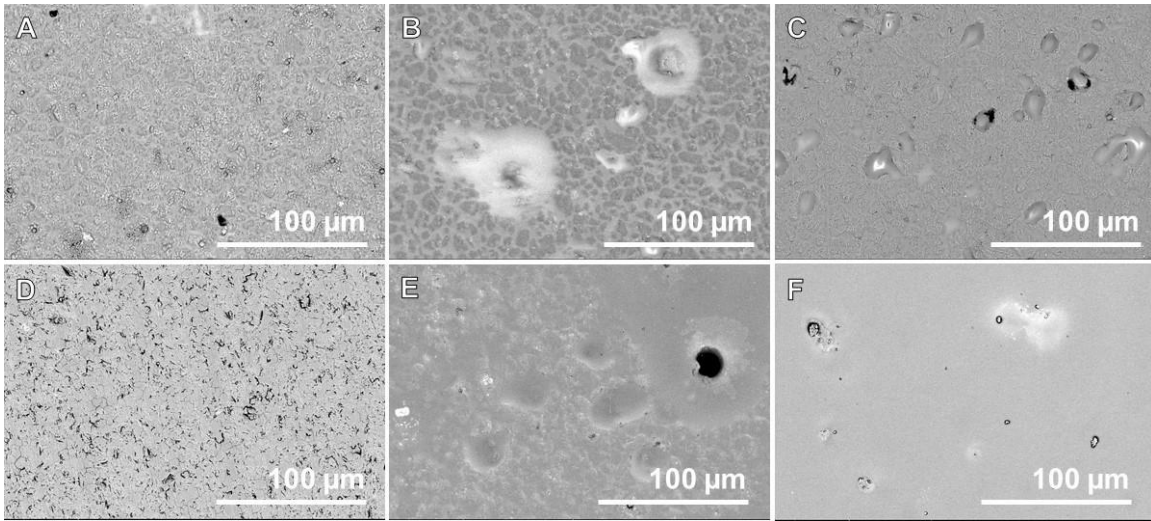


Figure 58: Plan-view micrographs of oxidized RB-SiC coupons following high pressure rig exposures at 900 °C for 100 h. Top row: A) 0 wt.% B baseline coupon, B) 0.5 wt.% B coupon, and C) 4 wt.% B coupon exposed in 1 atm dry O₂. Bottom row: D) 0 wt.% B baseline coupon, E) 0.5 wt.% B coupon, and F) 4 wt.% B coupon exposed in 4.4 atm dry O₂.

Micrographs of oxides formed on RB-SiC containing 0, 0.5, and 4 wt.% B following oxidation in the high pressure rig at 1200 °C in 1 and 4.4 atm dry O₂ are compared in Figure 59. The oxides were extensively cracked, as were the oxides formed from 1200 °C TGA exposures, shown previously in Figure 57. Point EDS did not detect B at the oxide surfaces (results not shown here).

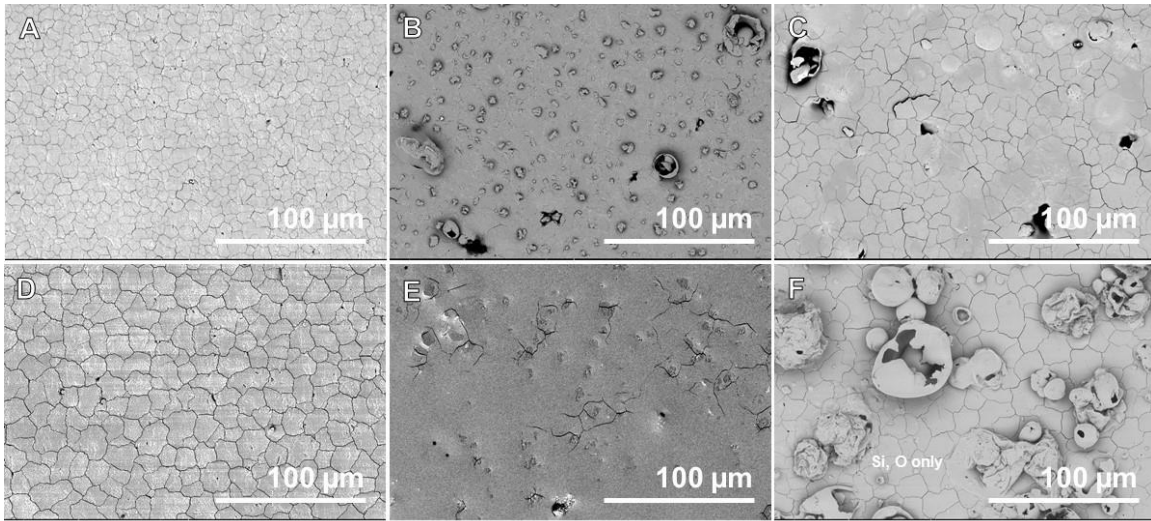


Figure 59: Plan-view micrographs of oxidized RB-SiC coupons following high pressure rig exposures at 1200 °C for 100 h. Top row: A) 0 wt.% B baseline coupon, B) 0.5 wt.% B coupon, and C) 4 wt.% B coupon exposed in 1 atm dry O₂. Bottom row: D) 0 wt.% B baseline coupon, E) 0.5 wt.% B coupon, and F) 4 wt.% B coupon exposed in 4.4 atm dry O₂.

5.3.4.3 Predicting oxide formation from FactSage¹⁰⁰ equilibrium calculations

FactSage calculations were conducted to further the understanding of phases formed in the oxide microstructures observed by SEM/ EDS. Equimolar reactant concentrations of Si, SiC, B and O₂ were used as inputs. Reactant concentrations of Al and Ca were limited to < 0.1 moles to reflect the concentrations of Al and Ca detected by EDS in the unoxidized coupons (Figure 54). Calculations were done for temperatures of 900 and 1200 °C. The pressure was set to 1 atm. The FactPS and FTOxide databases were selected. Only products with activities of one were considered. A liquid glass comprised of SiO₂, B₂O₃, Al₂O₃, and CaO was predicted to form at both temperatures from the oxidation of Si and SiC, B, Al, and Ca, respectively. The crystalline tridymite and cristobalite polymorphs of SiO₂ were also predicted to form. Calcium silicate CaSiO₃ and calcium aluminosilicates CaAl₂Si₂O₈ were also likely products. Non-oxide products predicted to form were SiB₆ and B₄C. The oxide products predicted by FactSage agree with SEM/ EDS analysis of the oxide microstructures. The non-oxide products predicted

by FactSage were not detected by EDS analysis due to surface oxidation. The oxidized coupons were also analyzed by XRD to determine if the crystalline oxides predicted by FactSage were present in the oxides. The XRD results are described next.

5.3.4.4 Oxide crystal structure

The coupons oxidized at 900°C in both TGA and high pressure rig environments were too thin for detection. The signals from the oxides formed from 1200°C exposures, however, were discernible from the signals given by substrate. The normalized XRD patterns from the coupons oxidized in the 1200°C environments are given in Figure 60. Results from high pressure rig exposures are labeled as HPR. The pattern from the unoxidized 0 wt.% B coupon was included as a reference against which the peaks from the oxides could be distinguished. Peaks representing cristobalite were identified with HiScore software. The positions of the cristobalite peaks are shown boxed out in Figure 60. A low intensity peak highlighted by the quotation mark was present only in the oxide formed on the 0 wt.% B coupon during high pressure rig exposures in 4.4 atm dry O₂. This peak was identified as Na₂CaSiO₄. The presence of sodium, Na, in the oxide is thought to have come from furnace contamination. The coupons were loaded onto alumina tubes, which contain impurity levels of Na, which is highly reactive with SiO₂ oxides¹⁰⁶.

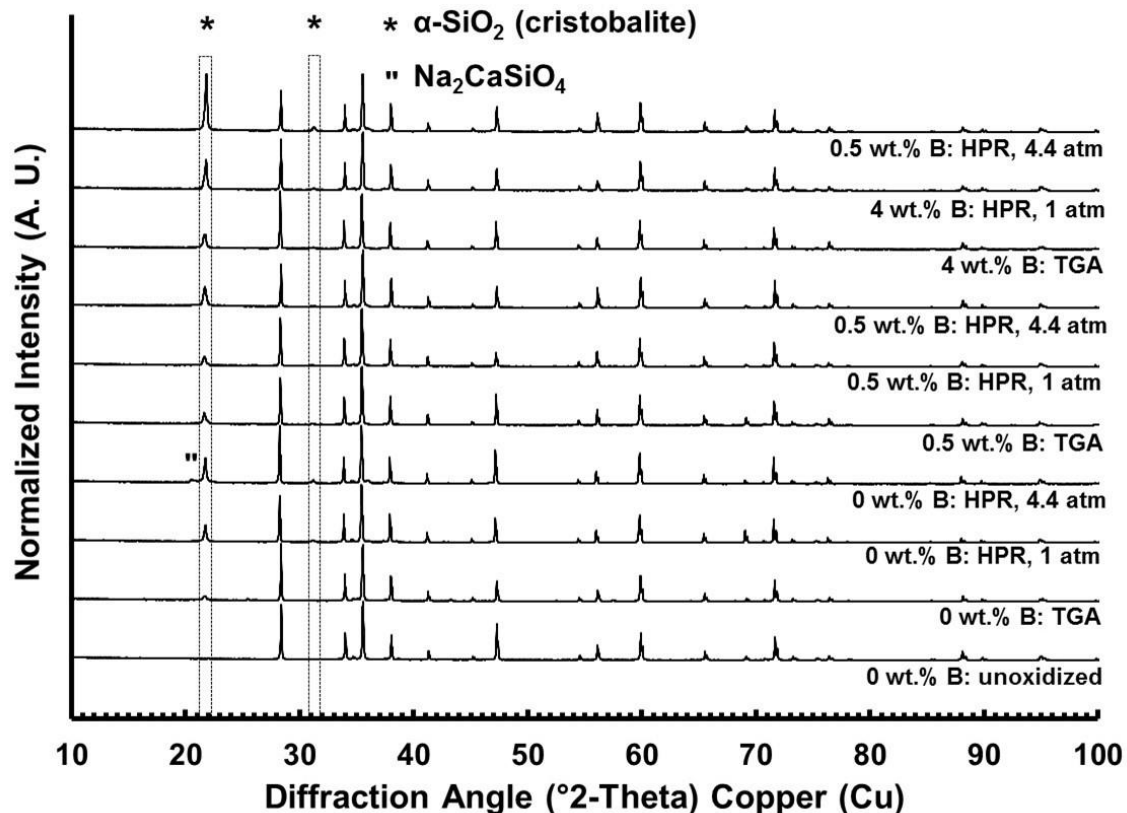


Figure 60: X-ray diffraction patterns collected from 0, 0.5, and 4 wt.% B coupons oxidized at 1200°C for 100 h in dry O₂ in the TGA and in the high pressure rig in 1 and 4.4 atm dry O₂. The diffraction pattern from the unoxidized 0 wt.% B coupon is included for comparison with patterns from oxidized coupons.

5.3.4.5 Oxide thickness

Oxide thicknesses from coupon cross-sections following TGA and high pressure rig exposures at 1200°C were observed by SEM and measured with the SEM software measurement tool. Micrographs of oxide cross-sections were taken while oxide thicknesses were measured. The oxide thicknesses were measured from the oxide outer edge to the oxide-substrate interface. A range of 31 – 41 measurements were made because the oxide edges were often undulated, as shown in Figure 61 A. Areas where the oxides were porous or broken were not measured. The oxide thickness near the domes formed on 0.5 and 4 wt. % B coupons, as shown in Figure 61 B and C, respectively, was measured and averaged separately. Oxides were sometimes present under pits, as shown

in Figure 61 D. Oxide thicknesses in the pits were not measured.

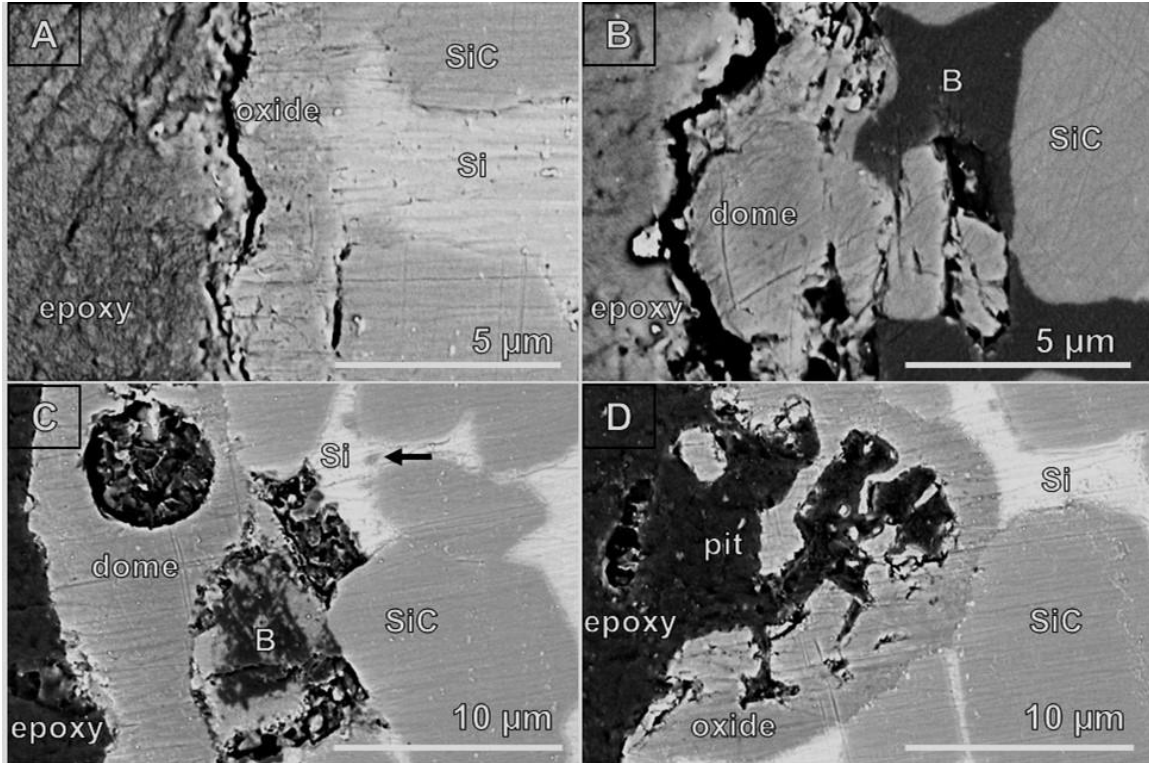


Figure 61: Oxide cross-section BEI of oxidized RB-SiC coupons following TGA exposures at 1200 °C for 100 h in 1 atm dry O₂. A) 0 wt.% B baseline coupon, B) 0.5 wt.% B coupon showing oxide dome-shape, C) 4 wt.% B coupon showing oxide dome-shape, and D) 4 wt.% B coupon showing oxide pit.

The cross-section of the dome in Figure 61 C has heterogeneous features, such as a hole and degradation around the B phase. Small spots were also present in the Si phase, highlighted by the arrow. These heterogeneities in the oxide cross-section were probed by EDS. The Si, B, Al, and O elemental maps from the EDS analysis are provided in Figure 62. The maps indicate that the oxide was comprised of two distinct phases, silica and alumina. The combined Al and O maps also show that the spots in the Si phase (Figure 61 C, arrow) are comprised of alumina, Al₂O₃. This finding indicates that Al preferentially oxidized within the substrate interior where the O₂ partial pressure was lower than at the gas-oxide interface. The low O intensity adjacent to the B phase suggests that degradation was due to some B oxidation.

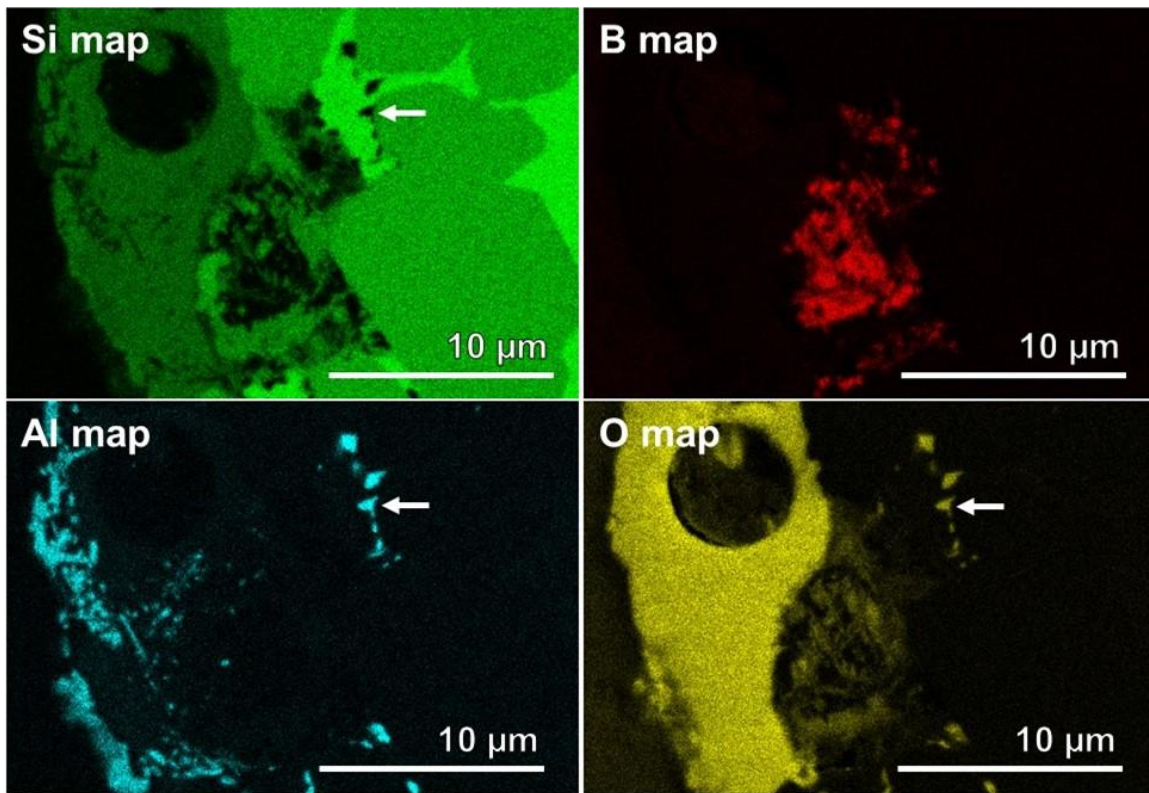


Figure 62: Elemental EDS maps of dome-shaped oxide cross-section from an oxidized 4 wt.% B coupon following TGA exposure at 1200°C for 100 h in 1 atm dry O₂.

5.3.4.5.1 Oxide thickness measurements

The mean oxide thickness measurements from TGA and high pressure rig exposures at 1200°C in 1 atm dry O₂ are provided in Table 10. The average heights measured from the domes in oxides formed on the B-containing coupons are also included Table 10 with standard deviations. Dome heights were measured when present at the 0.5 mm distances where oxide thickness measurements were made along the coupon long edge. The results show that the oxide thicknesses from TGA and high pressure rig exposures are in good agreement, within a factor of 1 – 1.3. The pressure effects on oxide growth were also evaluated from oxide thickness measurements on the oxidized coupon cross-sections, provided in Table 10.

Table 10: Mean oxide thicknesses measured from coupon cross-sections oxidized at 1200°C for 100 h in 1 and 4.4 atm dry O₂. Average dome heights measured from oxides formed on B-containing coupons were also included – parentheses represent the number of domes measured.

Oxidation furnace	Baseline	0.5 wt.% B		4 wt.% B	
	Oxide Thickness (μm)	Oxide Thickness (μm)	Dome height (μm)	Oxide Thickness (μm)	Dome height (μm)
TGA 1 atm	1.5 ± 0.3	2.0 ± 0.1	4.7 (1)	2.0 ± 0.3	8.2 ± 2.4 (9)
High pressure rig 1 atm	1.5 ± 0.1	1.6 ± 0.1	6.1 ± 3.5 (4)	2.0 ± 0.2	10 ± 4.8 (6)
High pressure rig 4.4 atm	2.8 ± 0.1	1.6 ± 0.1	5.7 ± 5.0 (4)	3.8 ± 0.4	9.6 ± 1.1 (6)

The mean oxide thickness measurements from high pressure rig exposures at 1200°C in 1 and 4.4 atm dry O₂ provided in Table 10 were also plotted, as shown in Figure 63 (lines are to guide the eye), to highlight the pressure effects on the oxide growth. Oxide thicknesses were greatest for coupons containing 4 wt.% B. Further, the oxide growth increased with increased pressure, with the exception of the oxidized 0.5 wt.% B coupon, which did not exhibit a pressure dependence. However, its weight gain increased with increased pressure (Figure 48 – lines are to guide the eye). Further inspection of the oxidized 0.5 wt.% B coupon cross-sections revealed that oxidation occurred further into the substrate interior, which contributed to the weight gain, but not to the oxide thickness measured at the coupon edge. These results are described in the next section.

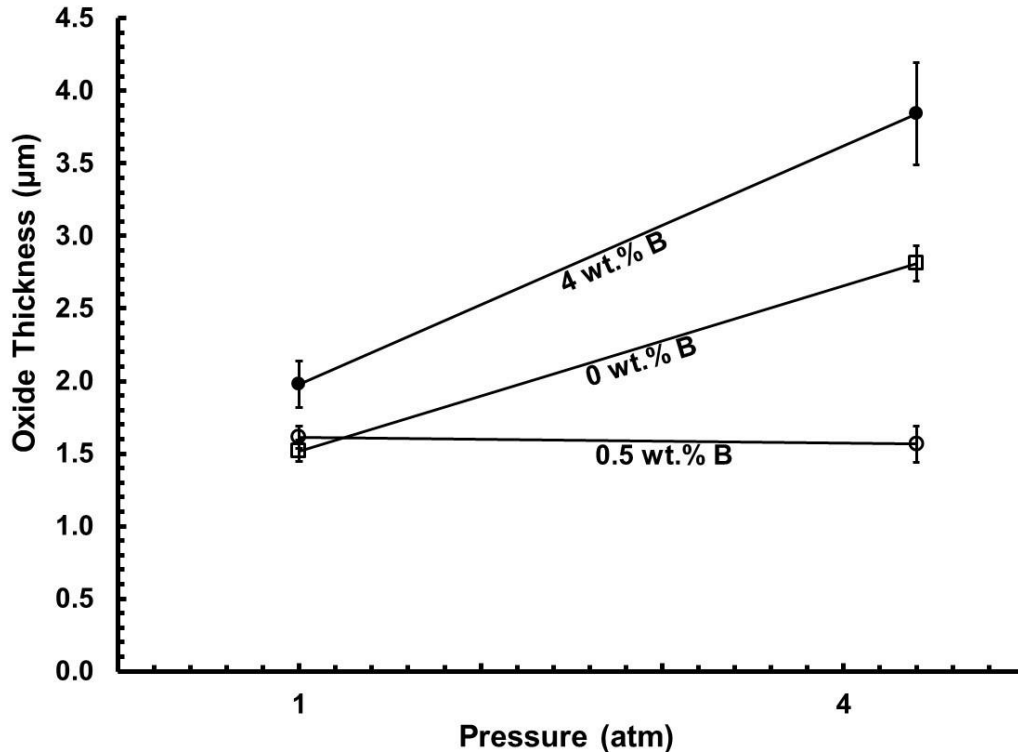


Figure 63: Oxide thickness measurements of RB-SiC coupons containing 0, 0.5, and 4 wt.% B following high pressure rig exposures at 1200°C for 100 h in 1 and 4.4 atm dry O₂. Lines are to guide the eye.

5.3.4.6 Subsurface oxidation

The 0.5 wt.% B coupon oxidized in the substrate interior during high pressure rig exposures at 1200°C in 4.4 atm dry O₂. A representative micrograph exemplifying internal oxidation is shown by the backscattered electron image in Figure 64, top left. The cross-section was analyzed with EDS with the O, Si, and Al maps also shown in Figure 64. Particular emphasis was placed on the location of oxygen. The O map shows the presence of an oxide at the coupon edge, but also surrounding the B phase located in the coupon interior beneath the oxide. The O and Si maps indicate that the oxide surrounding the B phase is SiO₂. The oxide surrounding the B phase extended into the coupon by ~ 5 µm and is defined at the oxide/ substrate by the oxide substrate equilibrium. Further into the substrate, the O and Al maps show the innermost oxide to be alumina, Al₂O₃.

Subsurface oxidation was not observed in the absence of a B phase near the coupon surface.

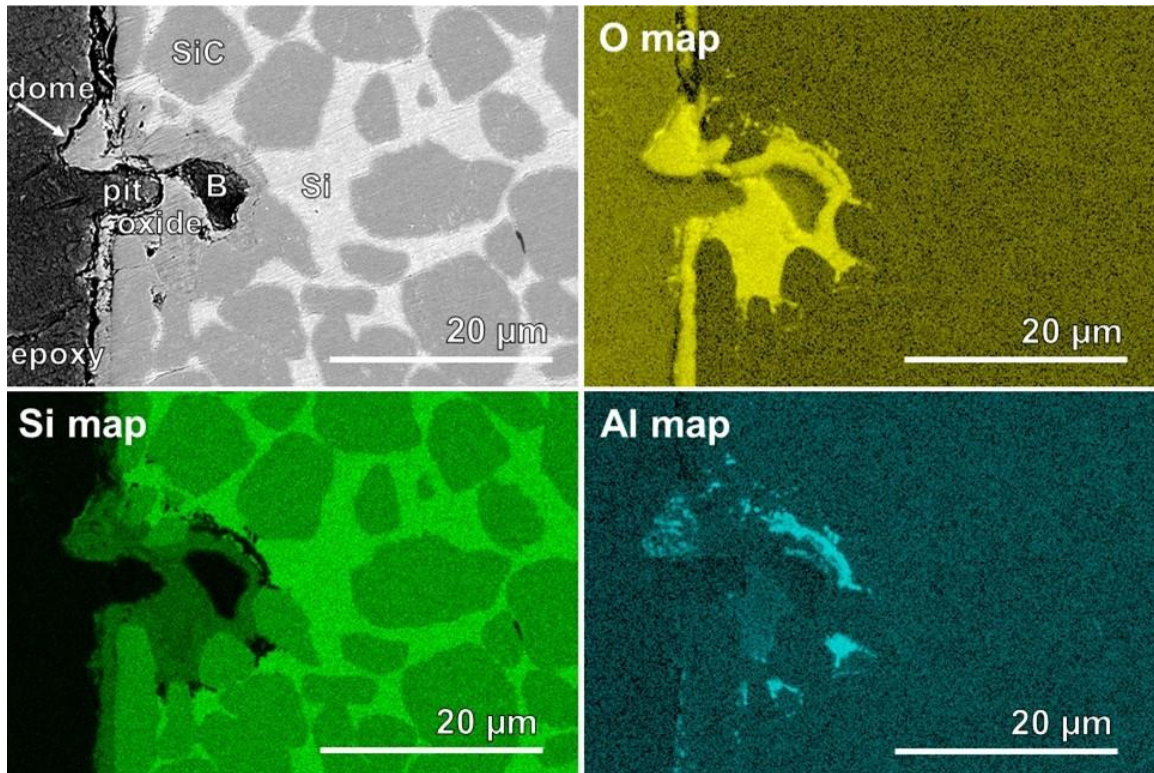


Figure 64: Micrograph (top left) taken from an oxidized 0.5 wt.% B coupon cross-section representing subsurface oxidation. The coupon was oxidized at 1200°C for 100 h in 4.4 atm dry O₂. The micrograph is shown with corresponding maps collected from EDS analysis of the microstructure.

5.3.4.7 Parabolic oxidation kinetics

The parabolic oxidation rate constants, k_p , were calculated from the average oxide thickness measurements taken at each pressure. Parabolic oxidation kinetics were assumed based on the parabolic weight change behavior given by the TGA weight change profiles shown earlier in Figure 47. The oxide thicknesses were squared, then divided by the total exposure time, to calculate the rate of parabolic oxide growth³⁰. The k_p for Si and SiC are linearly proportional with pressure^{24, 26}. Ratios of the 4.4 atm and 1 atm k_p were calculated. These results are provided in Table 11. The results show that oxide growth was faster in coupons that contained B by a factor of ~ 1.8. The results also

show that pressure increased growth rates, with the exception of the 0.5 wt.% B coupon, which was susceptible to oxidation beneath the surface as described in the previous section. Although the rate constants calculated from the baseline and 4 wt.% B coupon oxide thicknesses increased with pressure, they increased by factors less than 4.4. The oxides that also formed from the oxidation of the Al constituents were attributed to reducing the pressure effects on the RB-SiC oxidation kinetics because the Al parabolic oxidation rate constant has a pressure dependence less than unity, $P_{O_2}^{1/6}$,¹⁰⁷ whereas the Si parabolic rate constant has a linear pressure dependence, $P_{O_2}^1$.²⁶

Table 11: Parabolic rate constants calculated from oxide thickness

Coupon	Parabolic rate constant ($\mu\text{m}^2 \text{h}^{-1}$)			Ratio of $k_p^{4.4 \text{ atm}}$: $k_p^{1 \text{ atm}}$ from high pressure rig exposures
	TGA	High pressure rig		
	1 atm	1 atm	4.4 atm	
Baseline	2.1×10^{-2}	2.3×10^{-2}	7.9×10^{-2}	3.4
0.5 wt.% B	3.8×10^{-2}	2.6×10^{-2}	2.4×10^{-2}	0.9
4 wt.% B	3.8×10^{-2}	3.9×10^{-2}	1.5×10^{-1}	3.8

5.3.4.8 Bulk oxide compositional analysis by ICP-OES

The stability of the unoxidized 0 wt.% B RB-SiC to the digestion solutions was determined prior to digesting the oxides on oxidized coupons. Unoxidized coupons were digested in water and in 25 vol.% hydrofluoric acid solutions. Since the pre-characterization results of the as-received coupons found the presence of Al and Ca, the digestion solutions were analyzed for these elements in addition to Si. The ICP-OES analysis found no presence of these elements in the water digestion solution, but over 100 ppm Si was detected in the hydrofluoric acid solution. The amount of Si that leached from the unoxidized coupon is enough to overestimate the amount of Si that would be detected from digestion of the oxides. Hydrofluoric acid digestion solutions are known silica and borosilicate glass etchants⁹⁴, often used to remove the SiO_2 scale from oxidized

silicon⁹² and oxidized SiC³⁵. The detection of Si from the acid digestion of the unoxidized RB-SiC coupons in this work is hypothesized to have come from a native SiO₂ present on the as-received coupons, which could have formed during processing. The native oxide must have been very thin since there were no microstructural changes observed by SEM on the unoxidized coupon before and after acid digestion. The instability of the substrate itself to the acid digestion solution limits sensitive ICP-OES analysis to water digestions only.

5.4 Discussion

5.4.1 Boron effects on RB-SiC oxidation kinetics in 1 atm O₂ environments

In the absence of B, Ca, and Al found present in the as-received material, the RB-SiC will oxidize to form vitreous SiO₂ at the temperatures conducted in this study^{108, 109}. Oxidation of the 0 wt.% B coupon in this study led to the formation of complex oxide microstructures comprised of three separate phases: SiO₂, Al₂O₃ and a calcium aluminosilicate. Oxidation of the B-containing coupons also led to the formation of a complex oxide with the additional incorporation of boria. In 1 atm O₂, all RB-SiC constituents were expected to oxidize, based on Ellingham diagrams for oxides formed from the oxidation of Ca, Al, Si, and B in O₂¹¹⁰, highlighted by the arrows in Figure 65. The relative stability of these oxides differ, where those with a negative free energy of reaction are more energetically favored to form at a single temperature. Since the Ca oxidation reaction has the most negative free energy at all temperatures of interest, given a limited amount of oxygen, it will oxidize preferentially, whereas B will oxidize last. The implication is that these competing oxidation reactions affect the O₂ transport through the silica scale.

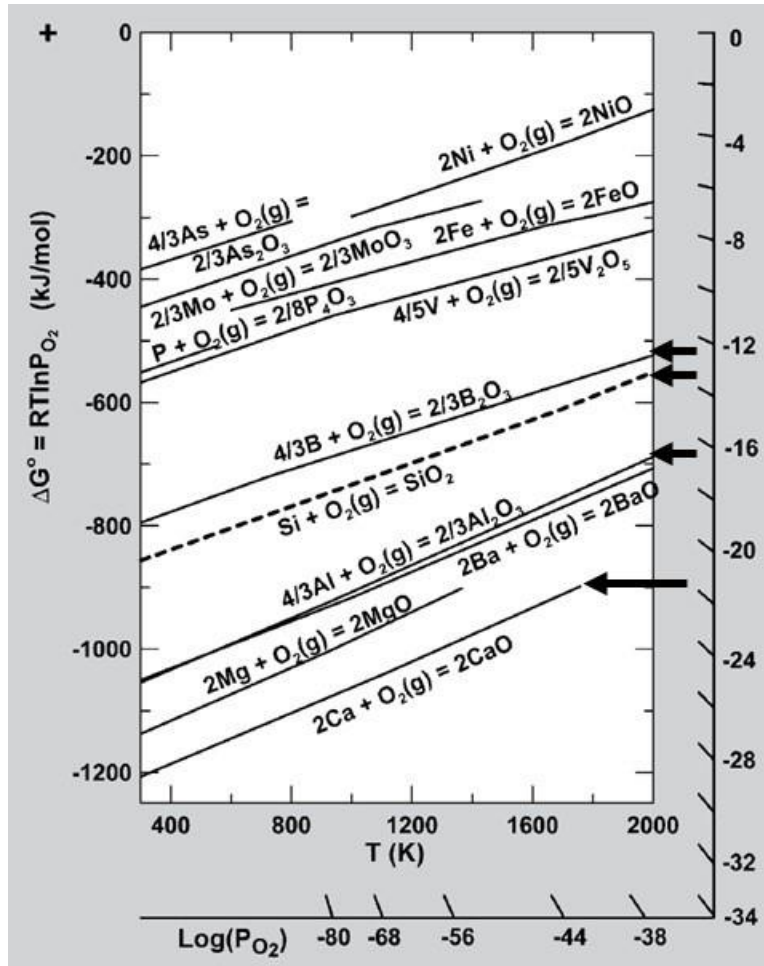


Figure 65: Ellingham diagram from Lynch¹¹⁰. Oxide reactions relevant to this study are highlighted by arrows.

It was not possible to elucidate the oxidation mechanisms from the TGA weight change at 900°C due to similar amounts of oxide formation by competing reactions. At 1200°C, however, the oxidation kinetics of Si and SiC increase^{21, 22}. The transient oxidation kinetics¹¹¹ exhibited by the 1200°C TGA weight change profile for the 0 wt.% B coupon arose from the oxidation of the available Ca and Al at the surface of the coupon, followed by oxidation of Si and SiC major phases that dominated the overall oxidation behavior of the coupon. Devitrification of the oxides during 1200°C exposures was nucleated by the Ca and Al contaminants¹⁰⁵. Ternary glass mixtures of CaO-SiO₂-B₂O₃ are known to fully crystallize into CaB₂O₄ and CaSiO₃ phases at 900°C¹¹²; although

the XRD analysis in this study did not support the formation of these phases.

The oxidation kinetics of the B-containing coupons were faster than the oxidation kinetics of the 0 wt.% B coupons because of the increased oxygen transport through a thermally grown borosilicate glass^{41, 60}. Evidence for accelerated oxidation kinetics in the B-containing coupons was demonstrated by increased weight gain, oxide microstructure, and thicker oxides. Although the weight gains between the baseline and 0.5 wt.% B coupons were similar, the differences in their oxide microstructure reveal the effects of B on the RB-SiC oxidation kinetics. The domes present on the oxidized B-containing coupon surfaces following 900°C exposures formed from rapid oxidation of the B phase because molecular O₂ transport is faster in boria⁶³ than it is in silica²⁵. The domes were a boria-rich thermally grown borosilicate glass, as identified by EDS analysis. The dome-shape resulting from the poor wettability of borosilicate glasses on SiC substrates⁶⁰. The weight gain of the 0.5 wt.% B coupons was suppressed by boria volatilization reactions that are significant at 900°C and above¹⁴.

The oxide thicknesses of the B-containing coupons were not significantly greater than the 0 wt.% B oxide thicknesses following 1200°C exposures. However, the average height of borosilicate domes, 4 and 8 μm for 0.5 and 4 wt.% B coupons, respectively, were 3 – 5 times greater than the average 0 wt.% B oxide thickness (Table 4). These domes were shown to form where the B phase was located near the substrate surface (Figure 64). The factor of 4 increase in the oxidation kinetics of the B-containing coupons calculated by TGA weight change is much greater than the 1.8 increase in oxidation kinetics calculated by oxide thickness. As mentioned earlier, the dome heights were not averaged into oxide thicknesses measured from B-containing coupons. The

discrepancy between oxidation rate increases calculated by weight change versus oxide thickness would be reduced by averaging the dome heights and oxide thicknesses together. When the dome heights are included in oxide thickness measurements, the oxidation kinetics of the 4 wt.% B-containing coupons are greater than that of the 0 wt.% B coupon by factors up to 4.5, in accord with oxidation kinetics determined from TGA weight change.

5.4.2 Pressure effects on RB-SiC oxidation kinetics

The coupons increased in benchtop weight gain as pressure was increased. The oxidation mechanisms from 900°C exposures could not be determined from TGA data due to competing oxidation reactions, which individually have different O₂ pressure dependencies. The mechanisms from oxide thickness measurements would likewise be indeterminate. Oxide thicknesses measured from coupons oxidized at 1200°C did not always reflect the increases in weight gain, which demonstrated that parabolic oxidation kinetics were followed. The oxide thickness of the 0.5 wt.% B coupon was constant with pressure although there was a threefold increase in weight. The weight gain was supported by subsurface oxidation that occurred on B phases located near the substrate surface. The presence of an alumina phase at a depth of 10 μm below the coupon surface is evidence that O₂ was transported deep into the coupon through the subsurface oxide. Thus, excessive oxide formation occurred due to the presence of B, even far within the substrate. These results are further evidence that O₂ transport is fast in a borosilicate glass.

Subsurface oxidation did not occur in the 4 wt.% B coupons exposed to the 4.4 atm dry O₂ at 1200°C. The B area fraction was shown to increase with B concentration,

which also increased distribution of the B phase. The oxide formed on the 4 wt.% B coupon was continuous due to the closer proximity of the B intercalates. The oxide growth rates of both 0 and 4 wt.% B coupons increased by nearly a factor of four with a 4.4 increase in pressure. The parabolic oxidation rate constants were not linearly proportional with pressure, as otherwise expected of Si and SiC materials^{24, 26}. The proportionality was less than unity due to the oxidation of the trace Al. Because the presence of CaO in the oxides was infrequent, and is not considered to have contributed to the RB-SiC oxidation kinetics, even though the oxides were prone to crack and pit where CaO was located.

5.4.3 Implications of B effects on CMC matrix material oxidation resistance

Acceleration of RB-SiC oxidation kinetics due to the presence of B demonstrate that B incorporation into SiC-based matrix materials for CMC applications would have deleterious effects on the CMC oxidation resistance. Excessive oxide formation was observed in this study to occur at low temperatures (900°C) as evidenced by the formation of borosilicate domes over the oxidized B phase. Excessive CMC matrix oxidation may fuse the fibers to the oxidized matrix, thereby significantly reducing the fracture toughness of the composite²⁰. Subsurface oxidation was also shown in this work to occur in the vicinity of the B phase near the substrate surface at temperatures and pressures relevant to combustion environments. The potential for subsurface oxidation to occur in the CMC matrix would compromise the benefits of self-healed cracks at the composite surface that arrest oxidant ingress⁵⁷⁻⁶⁰.

5.5 *Conclusions*

The RB-SiC oxidation kinetics increased with increased temperature, pressure, and B concentration. Oxidation of the 0.5 and 4 wt.% B coupons at 900°C in 1 and 4.4 atm O₂ resulted in excessive borosilicate glass formation that was present as localized borosilicate glass domes. The frequency of the borosilicate glass domes was greater on the oxidized 4 wt.% B coupon because of the increased distribution of the B phase. The higher distribution of the B phase in the 4 wt.% B coupon was advantageous for forming a continuous oxide during exposures at 1200°C, even if much thicker oxides formed relative to the 0 wt.% B coupons oxidized in the same conditions. In contrast, oxidation of the 0.5 wt.% B coupon in elevated O₂ at 1200°C resulted in subsurface oxidation in the vicinity of the B phase. The results showed that the B phase was not located at the surface, but was in close proximity to substrate surface, which led to subsurface oxidation that extended 10µm deep into the substrate. The subsurface oxidation is more deleterious because it results in increased substrate recession. Although the RB-SiC oxidation kinetics were faster in the presence of B, the increased B phase distribution resulting from higher B concentrations is preferable for the formation of a continuous oxide that is thought to restrict subsurface oxidation.

5.6 *Recommendations for future work*

The B effects on RB-SiC oxidation were activated at both the low 900°C and high 1200°C temperature regimes, although the oxidation behavior at these two temperature extremes were considerably different. Results from mid-range temperature exposures at 1050°C (in progress at ORNL) may enable the development of a relationship that bridges the low and high temperature oxidation mechanisms. Weight gains from 900°C exposures

in 4.4 atm dry O₂ suggest measurable oxide thicknesses may have formed and should be investigated. Evidence for B₂O₃ volatility was provided by point EDS analysis of borosilicate oxides formed from 1200°C exposures. A surface sensitive technique, such as XPS combined with depth profiling, would be useful in determining the boron concentration gradient in the borosilicate oxide. This technique would also overcome the limitations of ICP-OES analysis of oxide composition due to the substrate reactivity with the hydrofluoric acid solutions.

6 **Task 3: Optimization of sol-gel synthesis, coating application, and freestanding glass fabrication**

Borosilicate glass coatings with well-defined B concentration were synthesized and applied onto Si-based substrates for the purpose of elucidating the effects of the known boria glass concentration on SiC oxidation kinetics. Extensive characterization of the sol-gel derived borosilicate glasses was carried out to: 1) optimize the synthesis procedure to maximize B retention, produce thin, adherent, and crack-free films on CVD-SiC coupons, Si coupons, and SiC fibers, and to cast durable monolithic freestanding glass structures; 2) determine and maximize the B incorporation in the glass structure; and 3) determine C content, distribution, and bonding in the sol-gel derived glasses.

6.1 *Objectives of Task 3*

The stability of the B concentration was determined from systematic quantification of B concentration in each gel-to-glass conversion step. The effect of the drying conditions on maximizing the B retention in coatings versus freestanding glasses was investigated. This effort not only probed the role of solvent concentration on B loss, but also introduced batch volume scale up as an additional factor leading to boron loss. The role of the heat treatment gas environment on B bonding in the glass network is described. Lastly, pertinent questions on retained C incorporation in the glass structure in the presence of B were put forth.

6.2 *Experimental procedure, recap*

Silica, borosilicate, and boria glasses were synthesized from tetraethyl orthosilicate (TEOS), trimethoxyboroxine (TMBX), and (2-aminopropyl)triethoxysilane (APTES) (Sigma-Aldrich St. Louis, MO) and used as-received. A short list of select

formulations relevant to this task is provided here in Table 12. Additional synthesis details were provided in the Experimental section.

Table 12: Select sol-gel synthesis formulations conducted in Task 3

Descriptor	Formulation (F)	Mol% TEOS; APTES	Mol Silane/TMBX	Mol Si/ B	Nominal Mol% B	Mol H ₂ O/ TEOS	Catalyst	Solvent (Vol%)	Batch Temperature (°C)
Silica-only	1	99; 1.0	---	---	---	2.7	0.06N HNO ₃	70-90	22
	2	94.5; 5.5	---	---	---	2.7	1N HCl	90	22
Borosicate 52 - 65 mol% B; TMBX pre-cursors	4	78; 22	2.8	0.9	52	1.5	0.03N HNO ₃	30-70	22
	5	76; 24	2.5	0.8	55	1.5	0.03N HNO ₃	70-90	22
	6	85; 15	2.2	0.6	62	1.5	1N HCl	90	40
	7	75; 25	1.5	0.5	67	1.5	1N HCl	90	40
Borosicate 67 - 75 mol% B; TMBX pre-cursor	8	75; 25	1.5	0.5	67	1.5	0.03N HNO ₃	90	40
	9	75; 25	1.5	0.5	67	1.5	1N HNO ₃	92.5	40
	10	75; 25	1.0	0.3	75	1.5	3N HCl	90-95	40-60
Borosicate 67 - 75 mol% B; Boria pre-cursor	11	75; 25	1.0	0.5	67	1.5	1 N HCl	90	40
	12	75; 25	1.0	0.3	75	1.5	3 N HCl	90 - 95	60
Boria >98 mol% B; TMBX pre-cursor	13	75; 25	0.06	0.02	98	1.5	1 N HCl	70	40

6.3 *Results*

The solvent loading had the largest impact on the optimization of the sol gel synthesis. Its main effects are individually described below.

6.3.1 Gelation

The range of solvent loading ranged from 30 – 95 vol%, and was ultimately fixed to 90 or 95 vol%. The APTES concentration in silica formulations ranged from 1 – 5.5 mol% depending on batch volume. For small volumes (< 60 mL), a 1 mol% APTES concentration in silica formulations (F 1) resulted in gelation one hour after synthesis, providing sufficient time for coating substrates and casting molds for monolithic glass structures. A higher APTES concentration of 5.5 mol% was needed to enable sol gelation for larger batch size silica formulations (> 60 mL). Scale-up of both solvent concentration and batch volume did not affect gelation of borosiloxane formulations (remaining formulations in Table 1), allowing for the APTES concentration to be maintained at a 3:1 mole ratio of TEOS: APTES.

6.3.2 Maximizing B retention

The sol-gels were characterized by ICP-OES for B concentration as a function of solvent concentration, drying, and glass conversion parameters. In Table 13, the B concentration was quantified by ICP-OES in dried gels with mid-range B concentrations (F 4) as: 1) dried gel coatings scraped off SiC substrates and 2) freestanding dried gels. The comparison shows higher B concentrations in the films than in the freestanding dried gels, which were slower to dry than the films. The results also indicate that actual B concentrations are lower than the nominal B concentration, signifying B loss between the syntheses and drying stages.

Table 13: ICP-OES results of B concentrations in thin gel films and freestanding glasses, nominally 52 mol%

Formulation (F)	Thin Film Gels		Freestanding Gels
	Solvent (vol%)	B (mol%)	B (mol%)
Mid-range B (F 4)	30	41.6	33.2
Nominal 52 Mol% B	50	41.6	30.0
	70	-	30.8

The B concentrations of freestanding gels in the mid-range for B concentration (F 4 – 6) were analyzed by ICP-OES before and after conversion to glasses. Nominal B concentrations versus the actual B concentrations are compared in Table 14 as a function of solvent concentration, glass conversion maximum heat treatment temperature (described as maximum heat treatment temperature in Table 14), and batch volume scale up. The results show a clear trend in increased B loss with increased solvent loading. The gel B loss was also shown to increase with increased batch volume (F 6). As solvent concentrations were increased, higher maximum heat treatment temperatures were shown to increase glass B concentrations. Converted glass B concentrations approached gel concentrations by 800°C maximum heat treatment temperature, but fell below nominal B concentrations.

Table 14: ICP-OES results of actual B concentration as a function of maximum heat treatment temperature in converted glasses

Formulation (F)	Nominal B (mol%)	Solvent (vol%)	Actual B (mol%) in Gels	Actual B (mol%) in Glasses for Maximum heat treatment temperature				
				400°C	500°C	600°C	700°C	800°C
4	52	30	42	-	-	-	-	-
		50	30	27	-	-	-	-
		70	31	22	-	-	-	-
5	55	70	29	-	20	-	24	-
		80	27	-	-	-	27	-
		90	24	-	12	-	20	-
6	62	90	18	-	-	11	-	-
		90 scale-up	20	-	-	13	11	17

6.3.3 Optimization of the gel-to-glass conversion

6.3.3.1 Heat treatment optimization for borosilicate glasses

Weight change during glass conversion for high range B concentration (F 7) glasses were measured in the TGA instrument as a function of time and temperature. TGA weight change results of three different time-temperature profiles differing by maximum heat treatment temperature are plotted in Figure 66. The top plot (black) shows continuous weight loss during the 1h isothermal hold at 400°C, with increasing weight loss up to the 600°C maximum heat treatment temperature, during which the weight became constant. Significant weight loss ensued throughout each 400°C isothermal hold, indicating that this temperature is too low for complete organic volatilization during glass conversion. Water, siloxane oligomers, and gaseous hydrocarbons were likely evolving^{73, 113}. The slowing and eventual stagnation of weight change in the temperature range of 500 – 600°C indicates that the maximum heat treatment temperature range was optimized

for this formulations. All ensuing borosilicate formulations (F 7 – F 12) were heat treated with an 8 h isothermal hold at 400°C followed by a 4 h isothermal hold at a 550°C maximum heat treatment temperature, then cooled to room temperature.

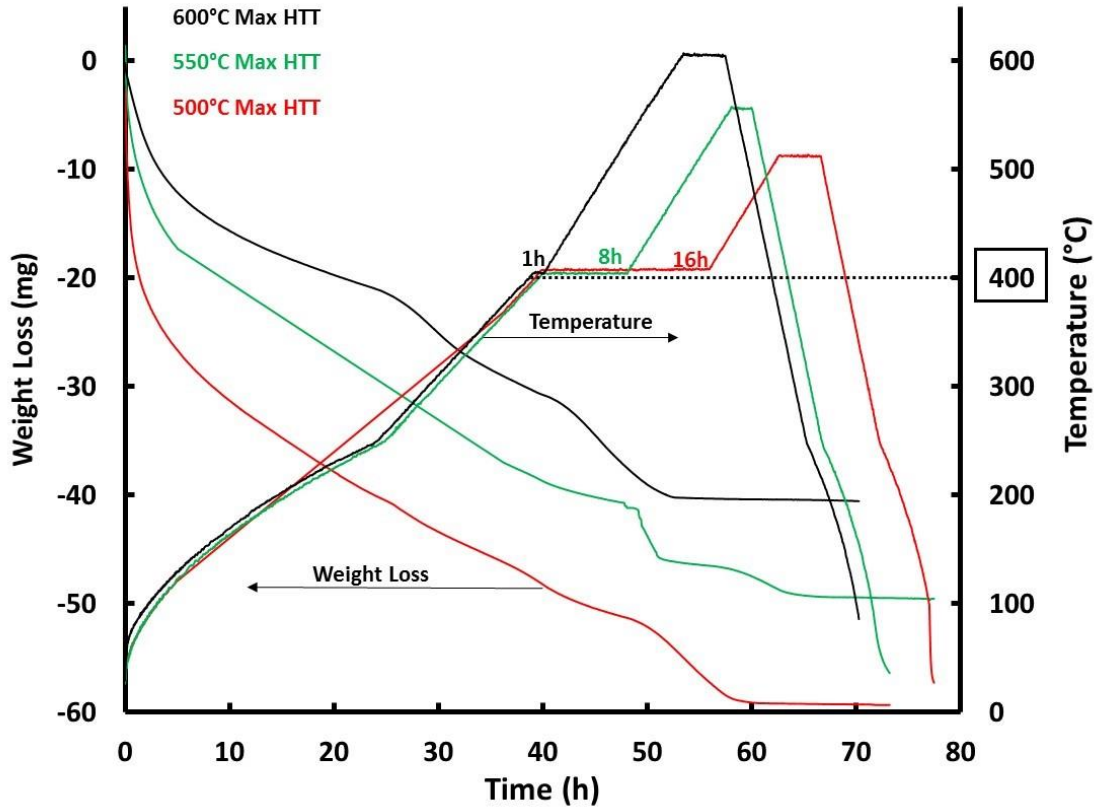


Figure 66: Heat treatment in the TGA instrument used to establish the gel-to-gel conversion heat treatment- weight loss results as a function of time and temperature for borosilicate (F 7) gel-to-glass conversion: Black) Top plot showing hold time of 1 h at 400 °C with maximum temperature of 600 °C); Green) Middle plot showing hold time of 8 h at 400 °C with maximum temperature of 550 °C; and Red) Bottom plot showing hold time of 16 h at 400 °C with maximum temperature of 500 °C.

6.3.3.2 Heat treatment optimization for borica glasses

The maximum heat treatment temperature that could be applied during the gel-to-glass conversion of the borica synthesis (F 13) was constrained by the low 450°C borica melt temperature. Borica becomes a fluid liquid at 500°C¹¹⁴. Another complication with borica is that it's hygroscopic and readily reacts with water to form boric acid¹¹⁵. Boric acid transforms to borica by dehydration at temperatures above 150°C¹¹⁴.

Two heat treatment procedures were conducted in the gel-to-conversion of the boria coatings to address both of these issues. The first heat treatment was conducted after the coatings were dried in the desiccator. The maximum heat treatment temperature used in the first heat treatment was 400°C. The maximum heat treatment temperature was held for 4 h in the dry Ar/ H₂ environment. The coated substrates were heat treated in a horizontal tube furnace. The heat treated coated substrates were stored in the desiccator. The second heat treatment was conducted immediately prior to oxidation in the TGA apparatus. The coated substrates were suspended in the TGA instrument in the dry Ar/ H₂ gas flowing at 100 sccm. The TGA furnace was heated to 500°C. The heat treatment was conducted for 1 h. The majority of the weight loss occurred in the first 10 minutes at 500°C. The weight leveled off during the remainder of the heat treatment. The coated coupons were then removed from the TGA apparatus and were weighed on the benchtop balance after cooling to room temperature. The coatings typically lost 1.5 – 1.9 mg from the second heat treatment. The coated substrates were then immediately re-loaded in the TGA instrument. The gas was switched to dry O₂ and the oxidation test was initiated. The oxidation of the boria coated coupons is described later in Task 5.

6.3.3.3 Boron concentration reproducibility and stability

Earlier it was shown that solvent concentration, drying, and batch volume were synthesis variables that contributed to B loss. Following optimization of the heat treatment time-temperature profile shown in Figure 65 for formulations with high nominal B concentrations (i.e., F 7), additional heat treatment variables such as the maximum heat treatment temperature and gas environment were investigated as factors that might affect the freestanding glass B concentration reproducibility. The B stability in

the freestanding glasses synthesized from TMBX and B₂O₃ precursors were also compared.

6.3.3.4 Boron concentration reproducibility

Several glass conversion variations were performed on the high-B gel formulation (F 7, nominal 67 mol% B concentration) to test for reproducibility of B retention in freestanding glasses. The gel and glass B concentrations determined by ICP-OES are provided in Table 15. Trials 1-3 represent three repeats of the F 7 synthesis. Trial 4 was a scaled up repeat of F 7. The B concentrations were also determined for glasses converted by heat treatments ranging from 400-600°C maximum heat treatment temperature (labeled as maximum HTT in Table 15), conducted in two different pieces of equipment: the TGA instrument and the horizontal tube furnace (labeled as HTF in Table 15). The effect of the heat treatment gas environment, 100% Ar or Ar/ H₂, on the glass B concentration was also assessed.

The gel B concentrations, left portion of Table 15, show good agreement between repeats 1-3 and with the scaled up version (Trial 4). Moreover, the small range in B concentration in glasses, right portion of Table 15, indicate a minimal effect of heat treatment temperature and gas environment on B retention. The lower B concentration in Trial 4 glass again shows greater B loss as batch volumes were increased. These results indicate that synthesis parameters were not optimized for larger batch volumes. Glass B concentrations up to 41 mol% were achieved, and concentrations of 31-35 mol% were attained with the most frequency. Assuming that B is molecularly bonded as boria, these results (28 mol% boria) approach the upper limit of 30 mol% boria reported in Schlichting's⁴¹ study.

Table 15: ICP-OES results testing for B reproducibility in borosilicate (F 7) gels and freestanding glasses

Trial	Actual B (mol%) in Gels	B Loss (mol%) in Gels	Maximum HTT (°C)	Apparatus	Gas Stream	Actual B (mol%) in Glasses	Additional B Loss (mol%)
1	37	46	400	TGA	Ar	31	15
					Ar/H ₂	33	11
				HTF	Ar	33	11
2	45	33	400	TGA	Ar/H ₂	35	23
			450	HTF	Ar	40	10
			500	TGA	Ar/H ₂	33	27
			550	TGA	Ar/H ₂	35	22
3	45	33	550	HTF	Ar/H ₂	41	3.3
4-scale up	38	44	550	HTF	Ar/H ₂	24	26
1	37	46	600	TGA	Ar	34	8
					Ar/H ₂	33	11
				HTF	Ar	34	9
2	45	33	600	HTF	Ar	36	6

6.3.3.5 Boron concentration stability

A comparison between the freestanding glass B concentrations from formulations F 9 – 10 synthesized from the TMBX precursor and freestanding B concentrations from formulations F 11 – F 12 synthesized from the B₂O₃ precursor following heat treatment in Ar/ H₂ at a 550°C max heat treatment temperature is provided in Table 16. All formulations were synthesized in large batch volumes (> 60 mL). The concentration of retained B ranged from 23 – 26 mol%. B retention was the same for syntheses formulated with TMBX or B₂O₃. The increased B loss due to increased solvent concentration was offset by increasing the ratio of the B-precursor in the formulation, as evident by the

retained B concentrations in F 10.

Table 16: ICP-OES results comparing B concentrations in freestanding glasses synthesized from TMBX and B₂O₃precursors

Formulation (F)	Nominal B concentration (mol%)	Solvent concentration (vol%)	Actual glass B concentration (mol%)
9	67	92.5	23
10	75	95.0	26
11	67	90.0	26
12	75	95.0	44

6.3.4 Glass structure molecular bonding, Fourier transform infrared spectroscopy

The Fourier transformed infrared (FTIR) spectra in Figure 67 show the progression of gel-to-glass conversion as a function of max heat treatment temperature (labeled as max HTT in Figure 67) and gas composition of a high-range B formulation synthesized with the TMBX precursor (F 7).

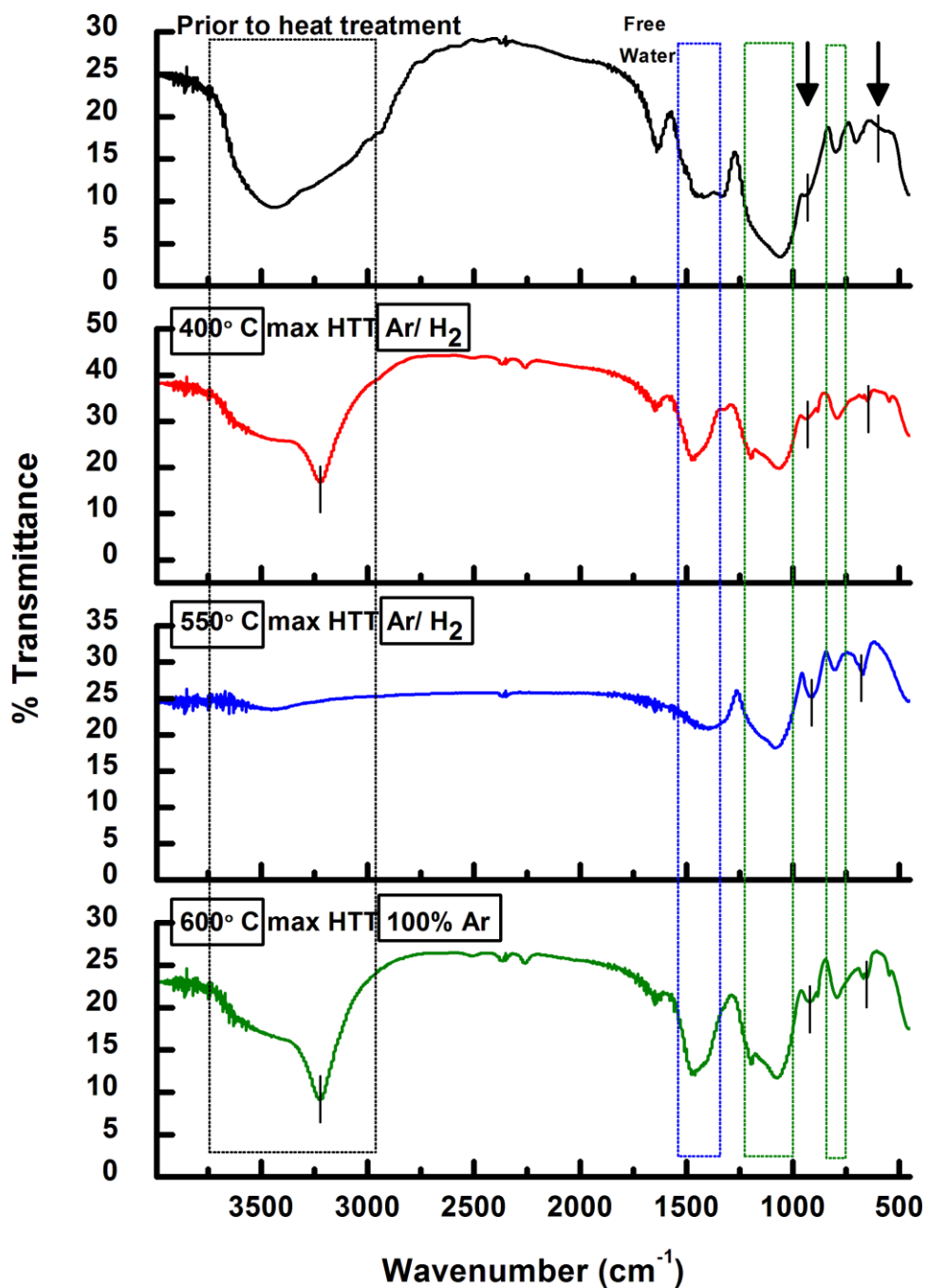


Figure 67: Evolution of borosilicate (F 7) gel-to-glass bonding: FTIR spectra as a function of maximum heat treatment temperature (max HTT) and gas environment.

1. Black Box) Bonding to –OH. The top spectrum was collected from the oven dried gel prior to glass conversion and shows a broad band at about 3448 cm^{-1} , attributed to Si-O-H ($3700 - 3200\text{ cm}^{-1}$)¹¹⁶ and B-O-H bond overlap ($3300 - 3200\text{ cm}^{-1}$)¹¹⁶.

Following conversion at 400°C maximum heat treatment temperature, the broad Si-O-H,

B-O-H band seen in the starting gel narrowed in width at about 3222 cm^{-1} in the B-O-H bonding range¹¹⁶. Interestingly, when the gels were converted in the Ar/ H₂ gas composition, this band disappeared at 550°C maximum heat treatment temperature, but remained present for the glass converted in 100% Ar at 600°C maximum heat treatment temperature, along with the peak assigned to water at $\sim 1635\text{ cm}^{-1}$ ⁷³. A shoulder at 1196 cm^{-1} and a low intensity peak at 548 cm^{-1} were distinguishable in both 400°C and 600°C maximum heat treatment temperature spectra. These bands are tentatively ascribed to boric acid, also observed in borosiloxane gel spectra from a prior work by Pena-Alonso and Soraru¹¹⁷. These bands were absent in their glass after 1000°C pyrolysis¹¹⁷. In this study, the heat treatment temperature of 400°C or the Ar gas environment at 600°C may be insufficient to destabilize B(OH)₃, especially in the presence of water.

2. Blue Box) Borate Bonds. A broad band in approximately the 1400 cm^{-1} vicinity is present for all spectra, typically referred to as the B-O stretching band^{68, 117}, perhaps in part contributed by non-bridging B-O bonds^{71, 73}. For the 400°C maximum heat treatment temperature and the glass converted in Ar at 600°C maximum heat treatment temperature, this band may coincide with B-C bonds, in which asymmetric CH₃ deformation peaks arise in the $1460 - 1405\text{ cm}^{-1}$ region, and symmetric CH₃ deformation peaks arise in the $1330 - 1280\text{ cm}^{-1}$ region for B-CH₃ functional groups¹¹⁶. The peak at 704 cm^{-1} , only present in the gel and disappears with heat treatment, is another peak ascribed to B-CH₃ bonds from a symmetric C-B-C stretch¹¹⁶. At 550°C maximum heat treatment temperature, this band shifts to lower wavenumbers⁷³. For the gel converted in the 100% Ar gas environment, this band narrows, but remains fixed in position. Absence of a 720 cm^{-1} B-O-B deformation vibration is consistent with Villegas and Navarro⁷³, indicating

that the bending B-O-B vibration arising from a B₂O₃ network¹¹⁸ is not present in these sol-gel derived borosilicate glasses.

3. Green Boxes) Silicate Bonds. The Si-O band at 1200-1000 cm⁻¹⁶⁸ is present and intense for every spectrum. The low intensity shoulder at 1196 cm⁻¹ could also be assigned to Si-O-CH₂-, which is predicted to appear in the 1190 – 1140 cm⁻¹ region¹¹⁶; however it has also been attributed to asymmetric stretching of Si-O⁷¹, or to boric acid¹¹⁷, as described above. The vibration appearing at ~800 cm⁻¹ has been attributed to SiO₄ tetrahedron rings⁷³ and to O-Si-O bending^{71, 118} and lies within the spectral region for Si-O/ Si-C overlap¹¹⁹.

4. Black Arrows) Borosilicate Bonding. Another important trend shown in the spectra is exhibited by the decreasing intensity of the Si-O-H and B-O-H bands (black box) at 3700 – 3200 cm⁻¹, which corresponded with increasing intensity of the Si-O-B peaks^{71, 73} (arrows) at 930-915 cm^{-169, 120} and ~ 670 cm^{-1 69, 70, 120}. This trend occurs more strongly as a function of gas composition (i.e., Ar/ H₂ mixture vs. Ar) than as a function of maximum heat treatment temperature. The disappearance of the B-O-H band for the 550°C maximum heat treatment temperature highlights full integration of B into Si-O-B bonds⁷³.

The FTIR analysis on a freestanding glass formulated from the B₂O₃ precursor (F 11) was conducted following heat treatment in Ar/ H₂ at a 550°C maximum heat treatment temperature. Borosilicate bonds were present in the spectrum (not shown here) indicating that bridged Si-O-B bonds were present in the glass. Free water was detected as well as hydroxyl bonds, Si-OH and B-OH, indicating that the glass had not fully condensed following this heat treatment procedure that was optimized for glasses

synthesized from the TMBX precursor.

6.3.5 XRD phase characterization of glasses following heat treatment

Diffraction patterns shown in Figure 68 were collected on converted glasses to determine if B-OH bonding present in the FTIR spectra represents a crystalline boric acid phase in the glass. Glass powders from the high-B formulation F 7 previously converted at maximum heat treatment temperature of 400, 550, and 600°C in both Ar/ H₂ and 100% Ar gas streams were analyzed. In all spectra, a broad peak at $2\theta \sim 22^\circ$ is present and attributed to amorphous silica⁷⁰. Additional peaks at $2\theta = 28^\circ$ and $2\theta = 15^\circ$ were sought, but not present. Lack of these peaks, indicative of a crystalline B(OH)₃ phase⁷⁶, suggests that B-OH bonding was fully incorporated in the amorphous glass structure.

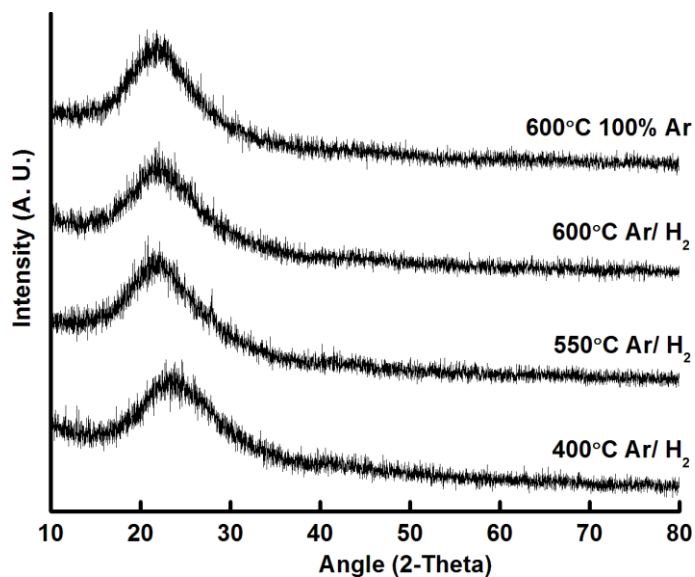


Figure 68: XRD results of converted glass powders from high-B (F 6) formulations: Top) maximum HTT of 600 °C in Ar gas stream, Middle-Top) maximum heat treatment temperature of 600 °C in Ar/ H₂ gas stream, Middle-Bottom) maximum heat treatment temperature of 550 °C in Ar/ H₂ gas stream, and Bottom) maximum heat treatment temperature of 400 °C in Ar/ H₂ gas stream.

6.3.6 Carbon incorporation in glass structure

Carbon retention was visually evident from darkened freestanding glasses following conversion. Combustion IR was conducted on borosilicate formulation F 8 that

was converted in Ar/ H₂ at 550°C maximum heat treatment temperature. The quantified carbon concentration was 5 wt.%. Further investigation of the carbon structure within the glass was conducted by Raman spectroscopy. Another glass from the same synthesis (F 8) was pulverized and pressed into a pellet as shown in Figure 69.

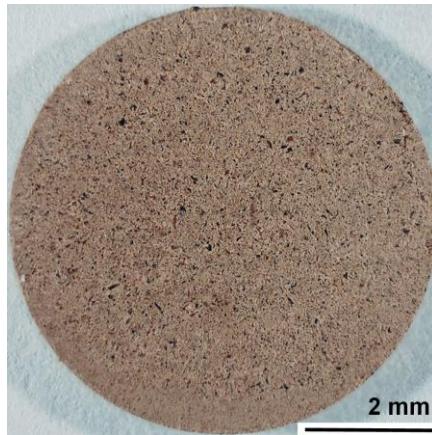


Figure 69: Optical image of high-B glass (F 8) cold pressed into a pellet.

Dark intercalates from the pellet were investigated under the Raman 514 nm laser using the 3000 mm/ 1 grating. A representative Raman spectrum of a dark intercalate in Figure 70 shows evidence of a free carbon phase in the glass by the broad peaks at ~ 1350 cm^{-1} and 1600cm^{-1} ¹⁷⁵ and are attributed to disordered graphite¹²¹.

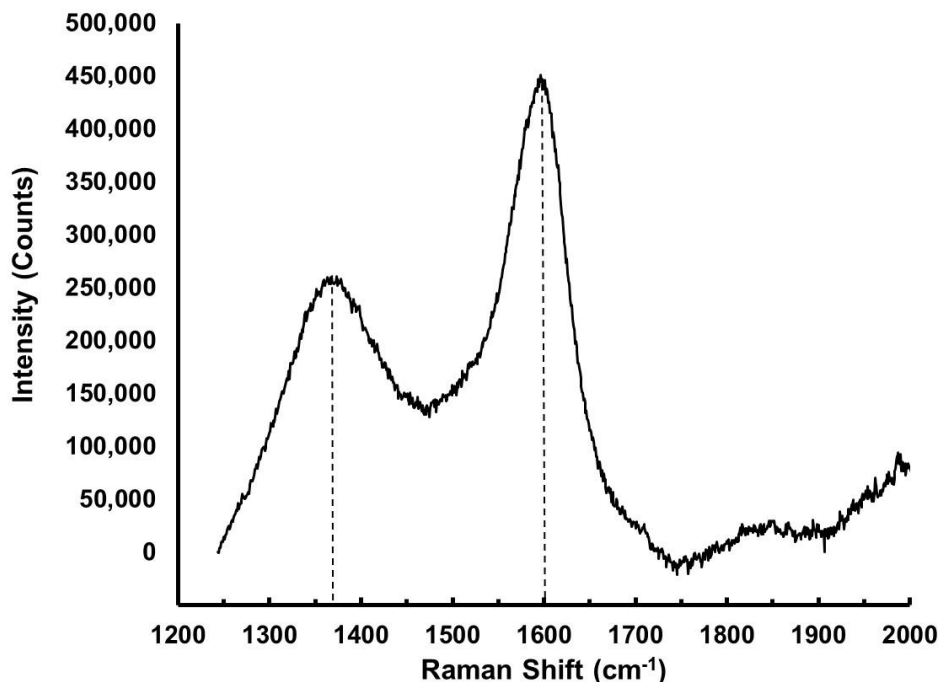


Figure 70: Raman spectrum of a dark intercalate from the borosilicate formulation F 8 glass pellet.

6.3.7 Substrate coating optimization for thin silica and borosilicate films

Despite increasing B loss that occurred in borosilicate glass formulations as the solvent concentration was increased, increasing the solvent concentration to 90 – 95 vol% was necessary to achieve the desired film thickness and surface coverage on SiC substrates for thin films < 1 μm . At 90 vol% solvent concentration, the coupons and fibers were coated with a single dip coat. At 95 vol%, the coupons and fibers were dip-coated three times.

6.3.7.1 SiC substrates

A comparison of coated CVD-SiC coupons showing differences in coating features resulting from synthesis variables such as solvent concentration and precursor chemistry is given in Figure 71. The silica coating (F 2), shown in Figure 71 A, produced by single dip coat in the sol synthesized at 90 vol% solvent concentration was cracked, exposing the underlying substrate. Cracks in TMBX synthesized coatings (F 10) were

minimized by increasing the solvent concentration to 95 vol% and by increasing the number of dip coats to three, as shown in Figure 71 B. Coupon pre-oxidation did not improve coating quality (Figure 71 C). Coatings synthesized with the boria precursor and 95 vol% solvent concentration (F 12) were applied by three dips coats showed very good surface coverage and negligible cracking, as shown in Figure 71 D.

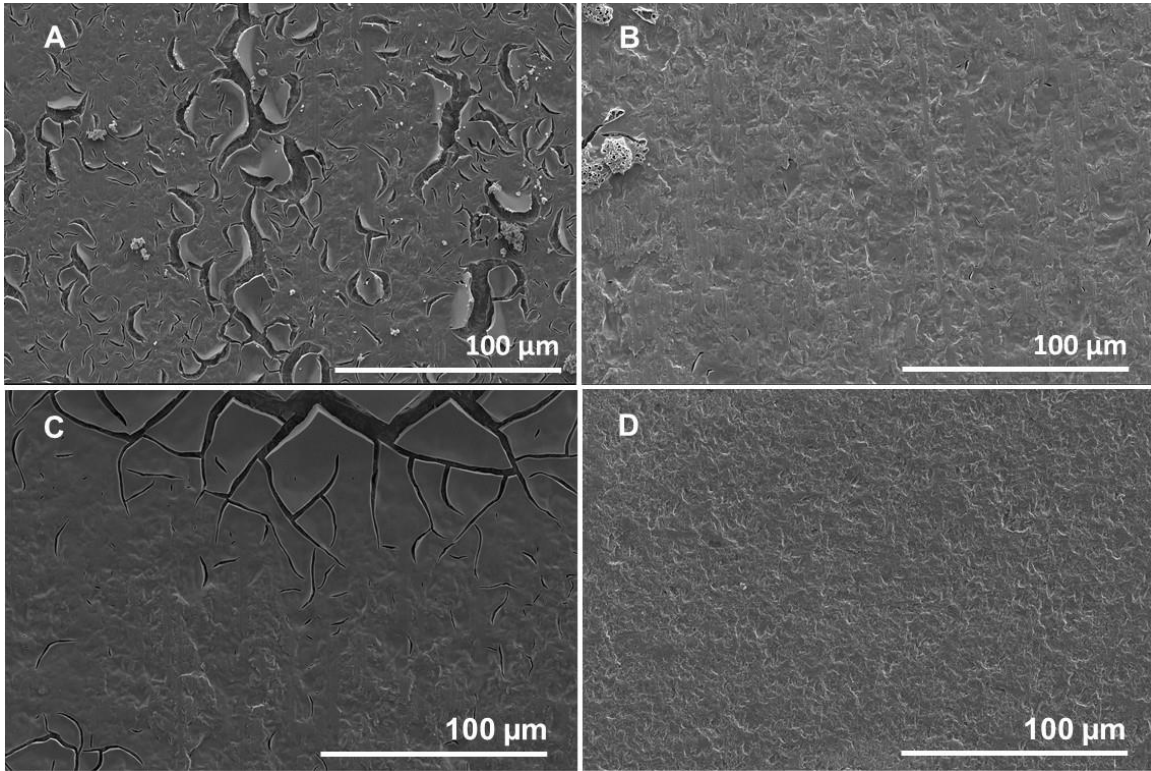


Figure 71: Micrographs of silica and borosilicate coated coupons. A) Silica (F 2) coating surface synthesized with 90 vol% solvent concentration applied without prior pre-oxidation, B) Borosilicate (F 10) coating surface synthesized with TMBX precursor and 95 vol% solvent concentration applied without prior pre-oxidation, C) Borosilicate (F 10) coating surface synthesized with TMBX and 95 vol% solvent concentration applied by three dip coats following pre-oxidation for 5 min at 1000 °C, and D) Borosilicate (F 12) coating surface synthesized with the B_2O_3 precursor and 95 vol% solvent concentration applied without prior pre-oxidation. Coupons were imaged in plan view by SEM with secondary electrons.

6.3.7.2 Si substrates

The same coating procedures taken to optimize the coating of CVD-SiC coupons were used to coat Si coupons. Crack-free coatings with good surface coverage as shown previously in Figure 71 D were not achieved. Figure 72 shows the cracked appearance of a borosilicate glass coating synthesized from the B_2O_3 precursor with a 95 vol% solvent

concentration (F 12).

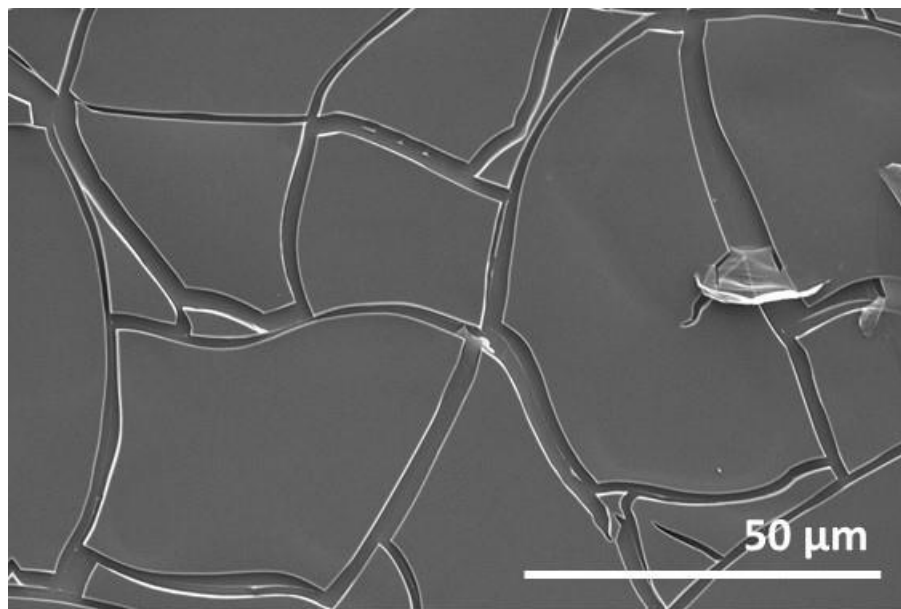


Figure 72: Micrograph of a borosilicate coating synthesized with the B_2O_3 precursor and 95 vol% solvent concentration (F 12) applied by three successive dip coats onto a Si coupon. Coupon was imaged in plan view by SEM with secondary electrons.

6.3.7.3 SiC fiber substrates

Micrographs of coated Sylramic fiber cross-sections following heat treatment are shown in Figure 73. Effects of the solvent concentration and precursor chemistry are apparent. For example, silica glass coatings (F 2) synthesized with 90 vol% solvent concentration and applied with a single vacuum immersion onto Sylramic fibers resulted in a smooth film with good surface coverage and film thickness of $0.7\ \mu\text{m}$, as shown in Figure 73 A. Well-defined borosilicate coatings with a film thickness of $0.9\ \mu\text{m}$ were achieved when synthesized with TMBX precursor and a 90 vol% solvent concentration (F 7), as shown in Figure 73 B. However, undesirable coating features shown in Figure 73 C resulted, such as poor adhesion, when the solvent concentration in coatings synthesized with TMBX precursor was increased to 95 vol%, despite increasing the number of dips coats to three. Undesirable coating features shown in Figure 73 D also

resulted from borosilicate coatings synthesized by the B_2O_3 precursor with a 90 vol% solvent concentration, indicating that the precursor chemistry also contributes to coating quality.

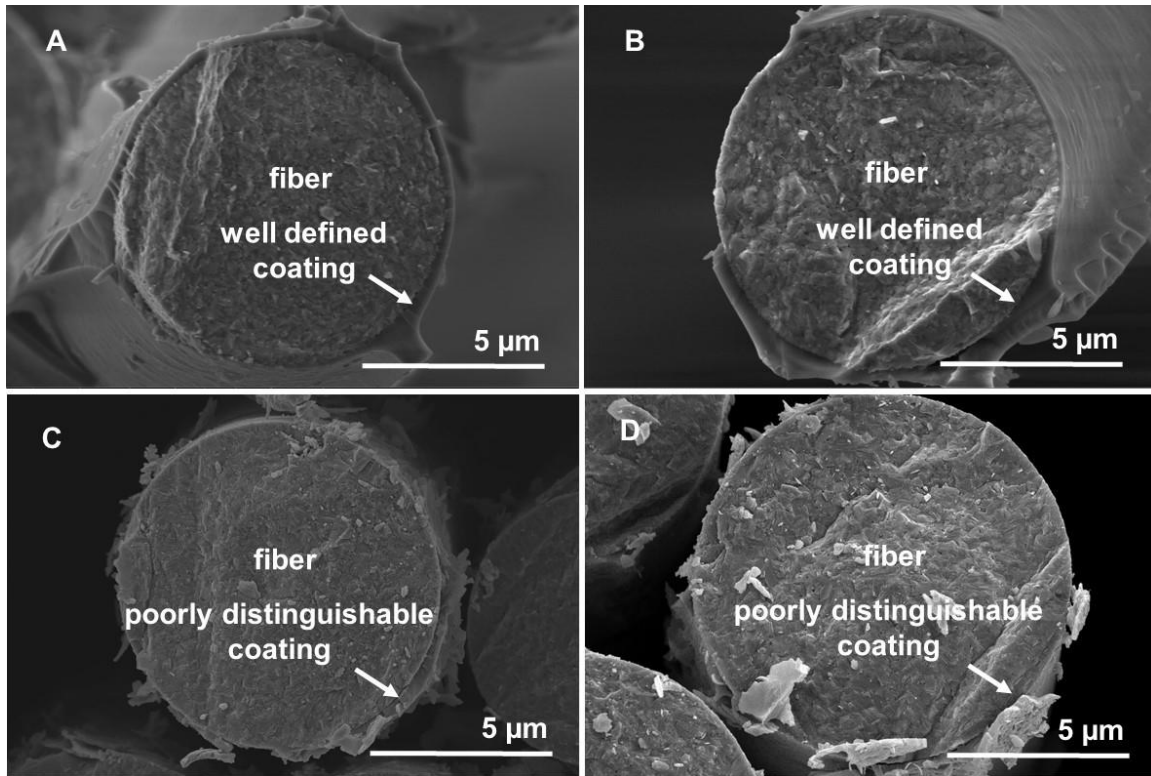


Figure 73: Micrographs of glass coated Sylramic fiber cross-sections. A) Silica (F 2) coating synthesized with 90 vol% solvent concentration applied by a single immersion, B) Borosilicate (F 7) coating synthesized with 90 vol% solvent concentration applied by a single immersion, C) Borosilicate (F 7) coating synthesized with 95 vol% solvent concentration applied by three consecutive immersions, and D) Borosilicate (F 12) coating synthesized with 90 vol% solvent concentration applied by a single immersion. Cross-sectioned fibers were imaged by SEM with secondary electrons.

Borosilicate coatings synthesized from the TMBX precursor with a 95 vol.% solvent concentration vacuum coated onto Sylramic and Sylramic *iBN* fibers that were previously pre-oxidized gave poor to fair results. Micrographs of coated fiber lengths that were not previously pre-oxidized coated fibers are compared with coated fiber lengths previously pre-oxidized in Figure 74. Coatings applied onto Sylramic fibers showed improved surface coverage with pre-oxidation, as evident in Figure 74 A and B. The coating quality on Sylramic *iBN* fibers was not improved with pre-oxidation, as shown in

Figure 74 C and D.

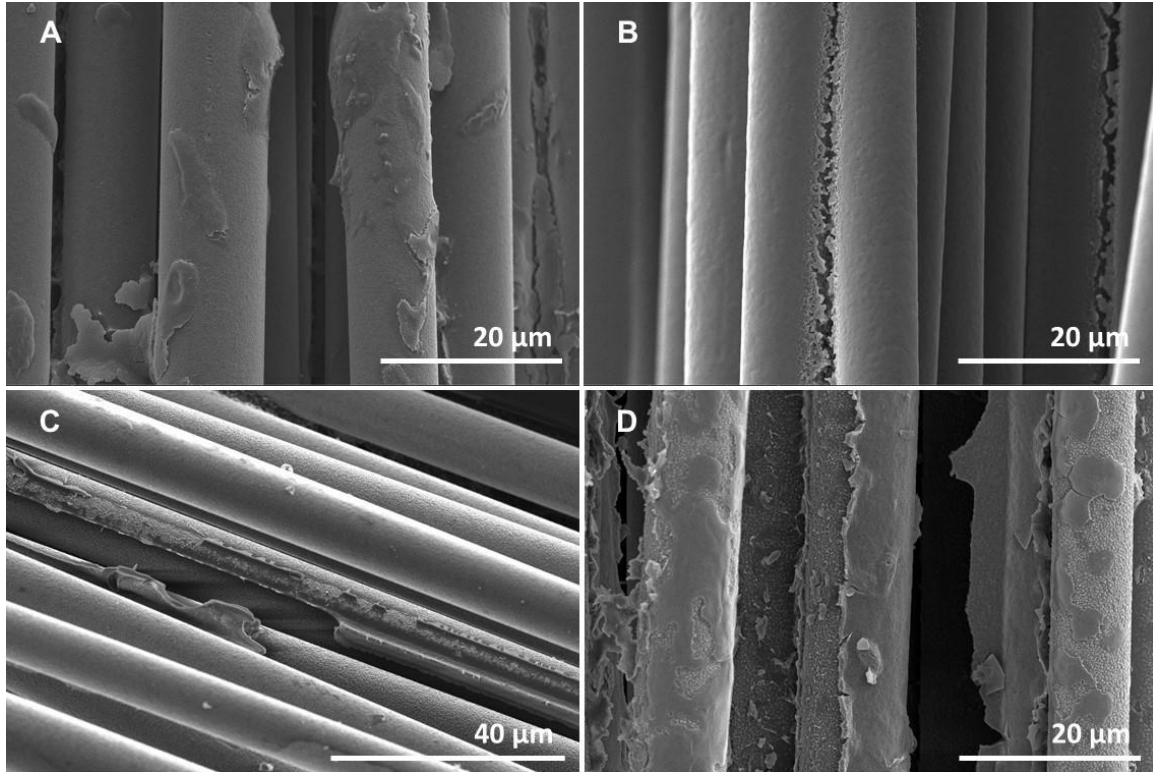


Figure 74: Micrographs of fiber lengths showing the comparison of fiber pre-oxidation effects on improving coating surface coverage. Coatings were synthesized with TMBX precursor and a 95 vol% solvent concentration that were vacuum coated three times in succession. A) Sylramic fiber not per-oxidized prior to being coated, B) Sylramic fibers pre-oxidized for 5 min at 1000 °C prior to being coated, C) Sylramic iBN fibers not per-oxidized prior to being coated, and D) Sylramic iBN fibers pre-oxidized for 5 min at 1000 °C prior to being coated. Fiber surfaces were imaged by SEM with secondary electrons.

In sum, silica and borosilicate coatings synthesized with 95 vol% solvent concentration provided optimal coatings on SiC coupons dip-coated three times. These same coating procedures resulted in cracked coatings when applied onto Si coupons. Silica and borosilicate coatings synthesized from the TMBX precursor with a 90 vol% solvent concentration applied by single vacuum immersion provided optimal coatings on Sylramic fibers. Corresponding borosilicate fiber coatings synthesized from the B_2O_3 precursor were inferior to coatings synthesized with the TMBX precursor. Many attempts taken to optimize the coating procedure for coating Sylramic *iBN* fibers were unsuccessful. These results in combination show that although extensive efforts were

made to individualize the coating procedure for each type of substrate, optimal coatings were not always achieved.

6.3.7.4 Substrate coating optimization for thick borosilicate and boria films

Thick applications of borosilicate and boria glass coatings were investigated for two reasons. The thick borosilicate glass coatings were investigated to replicate the thick (10 μm) sol-gel derived borosilicate glass coatings that were applied onto silicon substrates in Schlichting's study⁴¹. Boria coatings were intentionally applied in thick layers because a substantial amount of the coating is predicted to volatilize during exposures in the high temperature oxidation environment, supported by Reactions 6 – 8¹⁶ shown earlier. Borosilicate coatings synthesized from formulation F 9 with the TMBX precursor at a 92.7 vol% solvent concentration were applied by three consecutive dip coats. Boria coatings synthesized from formulation F 13 with the TMBX precursor at a 70 vol% solvent concentration were applied by seven consecutive dip coats. The coated substrates were imaged in plan view by SEM with secondary and backscattered electrons. Micrographs of the borosilicate and boria coated coupons following heat treatment are shown in Figure 75 A and B, respectively. The borosilicate coating is heavily cracked and delaminated from the substrate at the cracks. In contrast, the boria coating has considerably less cracks by comparison and is adhered to the substrate. The small pits that are present in the boria coatings are attributed to burst bubbles from the release of water vapor from boric acid dehydration¹¹⁴ during the heat treatment.

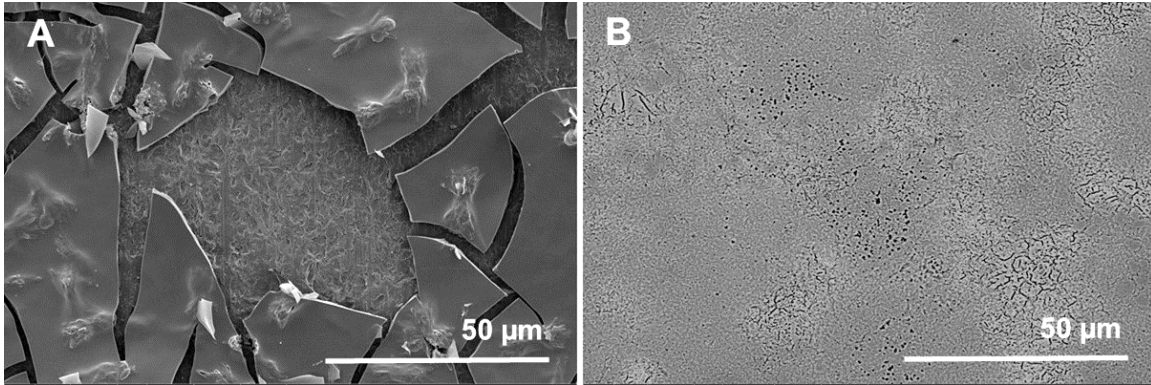


Figure 75: A) Micrograph of a borosilicate coating synthesized with the TMBX precursor and 92.7 vol% solvent concentration (F 9) applied by three successive dip coats onto a CVD-SiC coupon. Coupon was imaged in plan view by SEM with secondary electrons. B) Micrograph of a boria coating synthesized with the TMBX precursor and 70 vol% solvent concentration (F 13) applied by seven successive dip coats onto a CVD-SiC coupon. Coupon was imaged in plan view by SEM with backscattered electrons.

6.3.8 Optimization of freestanding glass fabrication

While the high solvent amount enabled the application of thin glass coatings, it complicated the structural integrity of drying gels. Gels that dried in ambient lab environment were fragile and prone to cracking (Figure 76 A). Therefore, the drying process prior to conversion was optimized by leaving the sols to gel and age in the ambient lab environment followed by drying in a convection oven as previously described. This process provided the structural integrity needed in the gels (Figure 76 B), to achieve minimally cracked freestanding glasses (Figure 76 C).

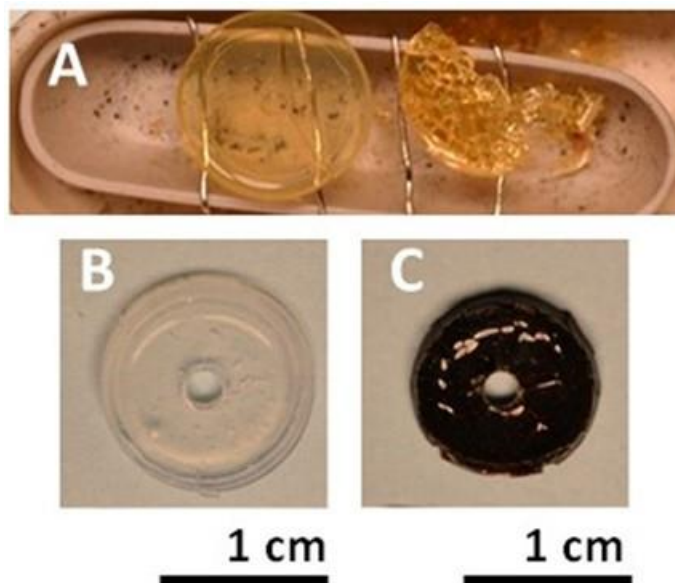


Figure 76: Examples of ambient dried versus oven dried gels synthesized from borosilicate formulation (F 5). A) Ambient dried gels post conversion, B) Oven dried gel prior to conversion and C) The same oven dried gel converted to a glass.

6.4 Discussion

Following several iterations to optimize the sol-gel synthesis procedure and careful characterization of the glasses and coatings, three main findings were uncovered:

- 1) B concentration was a function of solvent concentration, gel drying rate, maximum heat treatment temperature and batch volume. B concentration stability was found to be largely independent of convection oven drying, furnace equipment, and gas environment. Borosilicate bond formation increased with increased maximum heat treatment temperature and Ar/ H₂ gas environment;
- 2) carbon was retained after glass conversion and is present as a free C phase, and
- 3) coating film thicknesses less than 1 μm, necessary to achieve adherent films on coupons and fibers, required high solvent concentrations, which compromised freestanding glass durability unless dried in an oven prior to conversion. These findings are discussed in more detail below.

6.4.1 Boron retention and borosilicate bond formation

The amount of B retained was always less than the nominal values for the B concentration. B loss was shown to increase in two instances: 1) increased solvent concentration and 2) increased batch volume. Further B loss was shown to occur after glass conversion. The majority of the loss occurred in the gelation stage (30 – 70%), followed by an additional B loss of 3 – 40% after glass conversion. These results indicate that B species are unstable in the sol-gel procedure, supported by several previous works^{68–70, 72, 90, 120}. The source of B instability in the gel stage is explained by many factors. First, unreacted precursors can evaporate out of the gel⁶⁹. During drying, formation of a white powdery precipitate was observed, presumably boric acid, which burned off during heat treatment⁶⁹, leading to lower B concentrations in the glass than in the gel. Second, since ethanol is a product of the synthesis, increasing additions of ethanol for the purpose of improved substrate coating may have pushed the hydrolysis reaction to favor reactants⁷², leading to less B incorporation with increasing solvent content. Third, the greater B loss with larger batch sizes, needed for simultaneous coating application and FSG fabrication, could be due to excessive reaction time after the introduction of the B precursor. As water is increasingly produced by condensation reactions¹²⁰, a lengthy reaction time creates an opportunity for water to hydrolyze borosilicate bonds. Additionally, increasing the catalyst pH in future scale up syntheses could possibly hinder the hydrolysis of borosiloxane bonds⁷⁰. This work demonstrates that further optimization of synthesis parameters is needed to improve B retention in larger batch volumes.

Synthesis and heat treatment variables that did affect the retained B concentration

were identified from small batch volume syntheses. For one, greater B concentration was shown to occur in thin film gels than in corresponding freestanding gels (Table 13). This result is explained by the film's faster drying rate, in which borosilicate bond formation was promoted and borosilicate bond hydrolysis was suppressed because of the rapid evaporation of water from the drying gel¹²⁰. B concentration in converted glasses was shown to increase towards gel concentrations with increasing maximum heat treatment temperature (Table 14), indicating that maximizing B retention in the converted glass was temperature dependent because different organic species evolve at different temperatures¹¹³. B concentration was shown to be stable once synthesis chemistry, batch volume, and maximum heat treatment temperature were determined and invariable to furnace equipment or the Ar, Ar/ H₂ gas environment (Table 15). As shown in Table 16, B loss could be mitigated in formulations with the highest solvent concentration (F 10 and 12) by formulating with an increased ratio of B precursor.

The FTIR results indicated that the B concentration is reflective of various B molecular species (namely, B-OH, B-O, and Si-O-B), which disallows for the assumption that the B concentration is only a measure of boria. These results showcase the complexity of the sol-gel derived borosilicate glass structure, which varies as a function of glass conversion conditions, primarily maximum heat treatment temperature and gas environment. As shown in Figure 66, the gas environment played a larger role in Si-O-B formation than temperature at maximum heat treatment temperature > 500°C maximum heat treatment temperature, and Ar/ H₂ gas was shown to increase Si-O-B formation with a commensurate reduction in B-OH, specifically for formulation F 7. To our knowledge, this finding has not been reported elsewhere, and it is unclear why increased Si-O-B

formation takes place in the presence of H₂, since the purpose of H₂ is to convert carbon to methane⁸¹ for minimization of carbon retention. A working hypothesis to explain these findings is that carbon removal by H₂ discouraged chemical interactions between carbon and B in the glass network. Prior work by Gervais, et al.⁷⁶ credited B-C bond formation in the glass structure with increasing pyrolysis temperature (1000°C) in Ar at the expense of borosilicate bonds, thus providing evidence that temperature-dependent interactions between carbon and B are strong and real. The incorporation of H₂ with Ar in this study may have freed up B species from reaction with carbon, which in turn enhanced B incorporation into the silica network, as supported by the FTIR results.

The presence of OH and water bonding in a freestanding glass following the optimized heat treatment profile (Figure 66) is attributed to increased solvent concentration from 90 vol% to 92.5 vol% in the case of F 10 synthesized with TMBX. The presence of OH and water bonds in the FTIR analysis of the boria-synthesized borosilicate glass (F 11) synthesized with a 90 vol% solvent concentration was attributed to the high water sensitivity of boria, which may have greater capacity than the TMBX precursor to remain hydrolyzed after the heat treatment.

6.4.2 Carbon incorporation in the glass structure

The black color of the freestanding glasses shows that carbon was incorporated in the glass structure following conversion to glass even in the presence of H₂. A free carbon phase was confirmed by Raman analysis. The issue of carbon retention is important to address since its oxidation is expected in the high-temperature oxidizing environment^{77, 80, 82} that glass coatings will be exposed to during SiC oxidation testing. This expected weight loss must be understood for deconvolution of weight change in

oxidation studies. In addition, substantial carbon incorporation in the glass network may affect oxidant transport rates through the glass^{77, 83} and might impede observation of boron effects on SiC oxidation. The incorporation of the carbon phase in the glass network is unknown. Models of nano-scale carbon walls bonded to the silica network were proposed¹²². Simulations of the sol-gel derived silica glasses, often referred to as silicon oxycarbide glasses, show that the only energetically favorable incorporation of the free carbon phase is in sheets or slabs that are not bonded to the silica structure^{85, 123}.

An equally important concern is the interaction of carbon with the glass network during oxidation testing. Prior work by Pena-Alonso et al. has also shown that formation of nanocrystalline SiC and thicker carbon phases were promoted in silicon-boronoxycarbide glasses as a function of temperature at 1200 – 1500°C in Ar gas environments⁷⁵. The significance of the temperature range in their study is that it includes temperatures of interest for the oxidation studies that were conducted on SiC substrates coated with sol-gel derived glass layers described later in Task 5. Although these temperature-dependent reactions that led to the formation of nanocrystalline phases involving carbon took place in an inert environment, it is conceivable that they can form in an oxygenated environment despite competing carbon oxidation reactions. The oxygen transport might be additionally altered by the potential formation of these phases. Further understanding of carbon incorporation in the glass network in the presence of B is as a function of both high temperature (> 1000°C) and oxygenated (1 atm) gas environment for long times (100h) is needed.

6.5 *Conclusions*

The sol gel process was optimized for applying thin (< 1 μm thick) adherent

borosilicate glass coatings on SiC substrates and for casting freestanding borosilicate glass disks of high structural integrity. This optimization necessitated use of solvent concentrations up to 90 – 95 vol%, which resulted in substantial B loss. Additional B loss occurred during heat treatment in the gel-to-glass conversion. Larger batch volumes had greater B loss than smaller batch volumes for the same synthesis process, likely resulting from longer reaction times used for larger batch volumes that could have provoked borosiloxane bond hydrolysis. It was also shown that higher levels of B retention occurred in thin gel films than in bulk gels, attributed to a more rapid water removal rate in drying films. Increased maximum heat treatment temperature also increased B retention, but the stability of the B concentration was largely unaffected by the heat treatment furnace or gas environment. In addition to contributing processing factors that affected the glass B concentration and its stability, further insight into effects on B bonding in the glass network by the heat treatment gas environment was also provided in this work. FTIR spectra provided evidence that an Ar/ H₂ gas environment leads to enhanced Si-O-B formation relative to heat treatments in Ar, attributed to removal of carbon by H₂. Carbon incorporation in the glass, both in the glass network and in free form, was elucidated by a combination of FTIR, Combustion IR analysis, and Raman spectroscopy. However, the understanding of the carbon reactivity, bonding, and phase in high temperature oxidizing gas environments is tenuous. Sol-gel derived borosilicate glasses with well-defined composition, bonding, and phase applied onto SiC substrates were oxidized to enhance the understanding of B on oxygen transport in borosilicate glasses, described in more detail in Task 4.

6.6 *Recommendations for future work*

The sol-gel chemistry is sensitive to slight changes in variables. The heat treatment conditions for each sol-gel formulation must be individually optimized to maximize removal of organics, water, and carbon. Parameters that were optimized for one type of formulation cannot be assumed to carry over into another type of formulation, even if the formulations are closely similar, such as small increases in solvent concentration or replacing one precursor with another. Both of these changes can change the synthesis reactions, and this is determined by molecular bonding analysis with FTIR and Raman spectroscopy.

Task 4: High temperature stability of sol-gel derived borosilicate glasses in dry O₂

This task sought to understand the behavior of sol-gel derived freestanding glasses in the high temperature dry O₂ environment. Freestanding silica and borosilicate glasses were exposed to high temperature dry O₂ environments at 800 and 1200°C for 100 h. The freestanding glasses were characterized for weight change, composition, and molecular bonding. The retained carbon had fully oxidized from the silica glasses during dry O₂ exposures at 1200°C, but 1.5 wt.% of the carbon was retained in the borosilicate glasses exposed to the same conditions. Further, boria had volatilized from the borosilicate glass surface. The boria volatilization led to boria depletion that was 0.3 μm in depth. The borosilicate glasses changed shape from melting in the high temperature environments.

The changes to freestanding glasses resulting from the high temperature exposures in the dry O₂ environment are expected to also occur in the sol-gel derived glass coatings. Firstly, the boria depletion from a sol-gel derived borosilicate glass coating may affect O₂ transport due to silica surface enrichment from boria volatilization. The effects of the borosilicate coating on accelerating the SiC substrate oxidation may not be observed. Secondly, the presence of carbon in the borosilicate glasses following exposures to the high temperature dry O₂ environment is evidence for strong carbon-boron interactions, which may limit the ability of the sol-gel derived borosilicate glasses to structurally model thermally grown borosilicate oxides. Lastly, the borosilicate glass melting can result in beading and dewetting of the glass coating from the SiC substrate. Identification of these issues with sol-gel derived borosilicate glasses beforehand will

help in the interpretation of results from the oxidation of SiC substrates coated with sol-gel derived glass layers.

7.1 *Objectives of Task 4*

The objective of this task was determine the behavior of the sol-gel derived freestanding glasses exposed to high temperature dry O₂ environments. Carbon oxidation and boria volatility were investigated. The effects of the retained carbon on O₂ transport through the glass were evaluated. Further, the effects of carbon retention on the ability of sol-gel derived borosilicate glass coatings to model thermally grown borosilicate oxides was discussed. Implications of the boria volatilization from borosilicate glass coatings on the ability to observe boria effects on SiC oxidation were presented.

7.2 *Experimental recap*

Tetraethyl orthosilicate (TEOS) and (2-aminopropyl)triethoxysilane (APTES) were used as the silicon (Si) precursor for synthesis of silica and borosilicate freestanding glasses. Two boron (B) precursors were investigated for synthesis of borosilicate freestanding glasses: 1) trimethoxyboroxine, which will be called TMBX hereafter, and 2) boria powder. The silica and borosilicate gels were converted to glasses by different heat treatment conditions. The silica gels were heat treated in an Ar/ H₂ environment at a 1000°C maximum heat treatment temperature and 450 – 550°C for borosilicate gels heat treated in pure Ar or Ar/ H₂ environments. The list of silica and borosilicate formulations and their heat treatment conditions are provided in Table 17. Freestanding glasses from the boria formulation, F 13, were not investigated because they would melt significantly at the 800 and 1200°C temperature exposures conducted in this task. Additional synthesis details were provided earlier in the Experimental section.

Table 17: Select sol-gel synthesis formulations conducted in Task 4

Formulation (F)	Mol% TEOS; APTES	Mol Silane/ TMBX or Boria	Mol Si/ B	Nominal Mol% B	Mol H ₂ O/ TEOS	Catalyst	Solvent (Vol%)	Batch Temperature (°C)	Heat Treatment Conditions	
Silica-only	2	94.5; 5.5	---	---	---	2.7	1N HCl	22	90	Ar/ H ₂ ; 1000°C maximum heat treatment temperature
	7	75; 25	1.5	0.5	67	1.5	1N HCl	40	90	Ar; 450°C maximum heat treatment temperature
Borosilicate:TMBX precursor	8	75; 25	1.5	0.5	67	1.5	0.03N HNO ₃	40	90	Ar/ H ₂ ; 550°C maximum heat treatment temperature
	9	75; 25	1.5	0.5	67	1.5	1N HNO ₃	40	92.5	Ar/ H ₂ ; 550°C maximum heat treatment temperature
Borosilicate: Boria precursor	11	75; 25	1.0	0.5	67	1.5	1N HCl	40	90	Ar/ H ₂ ; 550°C maximum heat treatment temperature

Exposures of the converted glasses to the high temperature dry O₂ environment were conducted in the TGA instrument for 100 h under isothermal conditions at 800 or 1200°C. The freestanding glass weights were recorded as a function of time during TGA exposures. Further details on the TGA instrument were provided in the Experimental section. Several post-exposure characterization methods were carried out to investigate changes in composition and molecular bonding induced by the exposure temperature and TGA environment, resulting from carbon oxidation and boria volatilization in particular. These characterization methods included combustion IR and Raman spectroscopy, ICP-OES, surface depth profiling by XPS, and FTIR spectroscopy. These methods are listed in Table 18. Further details on the characterization methods can be found in the

Experimental section.

Table 18: Characterization methods carried out on individual freestanding glasses from isothermal exposures to the high temperature dry O₂ environment conducted at 800 and 1200°C for 100 h

FSG	Characterization methods to test for FSG stability in the TGA environment					
	Weight change	Combustion IR	Raman spectroscopy	ICP-OES	XPS	FTIR
Silica F 2	X	X	X			
TMBX-synthesized glass F 7				X	X	X
TMBX-synthesized glass F 8		X	X	X		X
TMBX-synthesized glass F 9	X			X		X
Boria-synthesized glass F 11	X			X		X

7.3 Results

The results of the freestanding glass exposures to the high temperature dry O₂ environment are divided into two sections. The first section describes the weight results from exposures to the dry O₂ environment at 800 and 1200°C for 100 h. The second section covers the results from characterization of the freestanding glasses following exposures to the TGA environment.

7.3.1 Weight change profiles from 800°C exposures in dry O₂ for 100 h

The weight change profiles recorded during freestanding glass exposures at 800°C for 100 h in dry O₂ are provided in Figure 77. The O₂ linear gas velocity at 800°C was 1.6 cm s⁻¹. The TMBX- and boria-synthesized borosilicate freestanding glasses (F 9 and F 11, respectively) both lost substantial weight during exposure, as shown in Figure 77. The weight change results of the silica glass (F 2), which had much less weight loss by comparison, is shown by plot in the inset in Figure 77. Benchtop weight change measurements showed that the silica freestanding glass specific weight change was - 0.04 mg/ cm². The TMBX (F 9)- and boria (F 11)-synthesized borosilicate glass specific weight changes were - 8.5 mg/ cm² and - 9.0 mg/ cm², respectively.

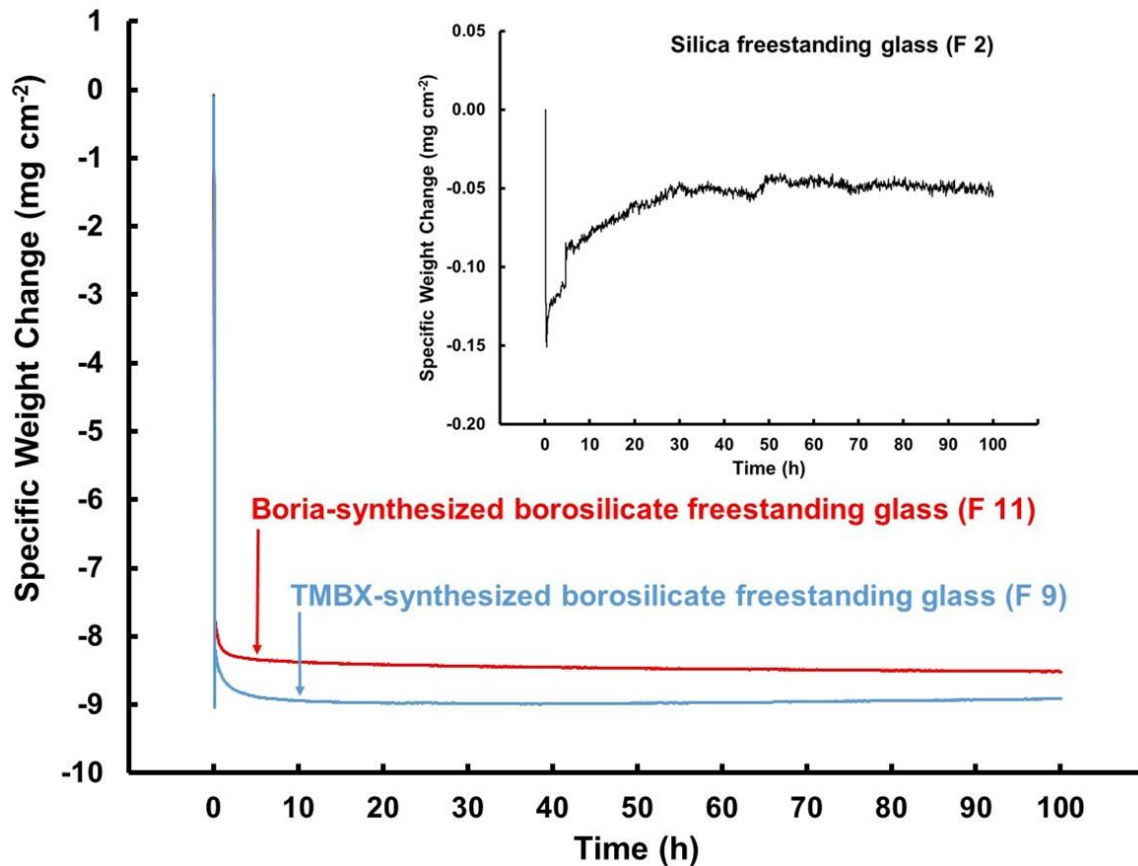


Figure 77: Plots of the freestanding glass specific weight change versus time from TGA exposures at 800°C for 100 h in dry O₂.

Macrographs were taken of the freestanding glasses after the 800°C exposures in dry O₂ for 100 h. A comparison of the silica and boria-synthesized freestanding glass visual appearances taken before and after exposure are shown in Figure 78. The appearance of the silica freestanding glass remained the same, whereas the borosilicate freestanding glass had a bubbly surface, a dark core, and had changed in shape. The bubbles resulted from entrapped gases from volatilization reactions, possibly carbon oxidation and boria volatilization. The dark color present in both glasses indicates that the carbon was not fully oxidized. The TMBX-synthesized borosilicate glasses (F 7 – F 9, not shown here) were also dark and had changed shape during exposure to the same conditions. The morphological changes were due to some melting from the high

temperature exposure resulting from the reduction in viscosity that occurs with boron incorporation into the silica glass structure^{42, 46, 55}.

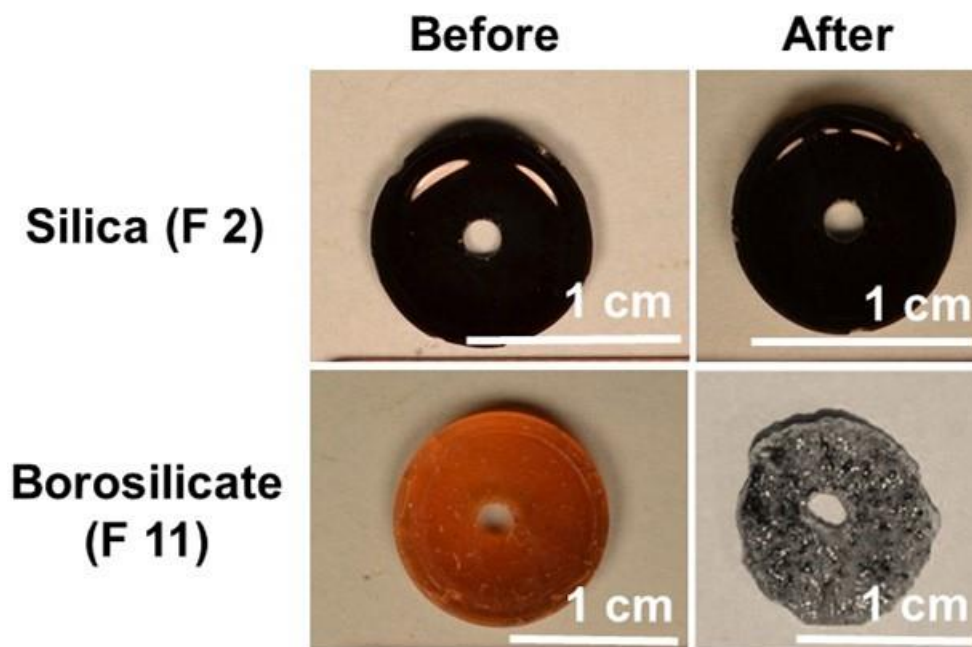


Figure 78: Macrographs of silica and borosilicate freestanding glasses taken before and after TGA exposures at 800°C for 100 h in dry O₂.

7.3.2 Weight change profiles from 1200°C exposures in dry O₂ for 100 h

The weight change profiles recorded during freestanding glass exposures at 1200°C for 100 h in dry O₂ are provided in Figure 79. The O₂ linear gas velocity at 1200°C was 2.2 cm s⁻¹. The TMBX- and boria-synthesized borosilicate freestanding glasses (F 9 and F 11, respectively) lost more weight in the 1200°C environment than they had in the 800°C environment. The silica freestanding glass (F 2) gradually lost more weight than it had during the 800°C exposure, as shown by the plot inset in Figure 78. The specific weight changes determined from benchtop weight measurements were:- 0.6 mg/ cm² for the silica freestanding glass (F 2), -19 mg/ cm² for the TMBX-

synthesized borosilicate freestanding glass (F 9), and -15 mg/cm^2 for the boria-synthesized borosilicate freestanding glass (F 11).

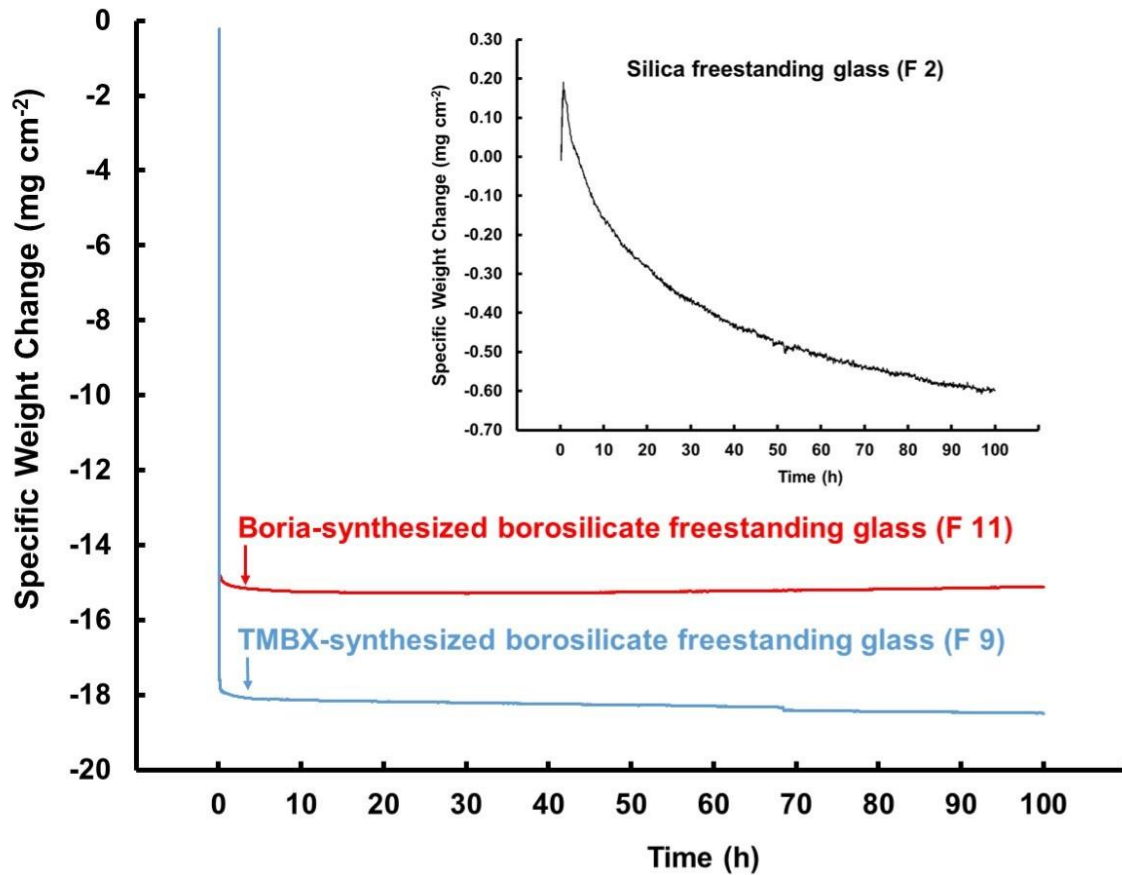


Figure 79: Plots of the freestanding glass specific weight change versus time from TGA exposures at 1200°C for 100 h in dry O_2 .

The freestanding glasses were visibly changed from TGA exposures at 1200°C . Macrographs of the silica (F 2) and boria-synthesized borosilicate (F 11) freestanding glasses taken before and after the 1200°C exposures are shown in Figure 80. The silica glass was bloated and white after exposure from carbon oxidation. The borosilicate glass was also bloated, but remained dark after exposure, indicating that carbon does not oxidize as readily from the borosilicate glass as it does from the silica glass. The shape of the borosilicate glass changed due to melting. The TMBX-synthesized borosilicate glasses (F 7 – F 9, not shown here) were also bloated, dark, and misshapen from exposure

in the same conditions. The freestanding glasses were characterized for composition and molecular bonding following exposures to the high temperature dry O₂ environment to identify the volatile species that contributed to the weight loss.

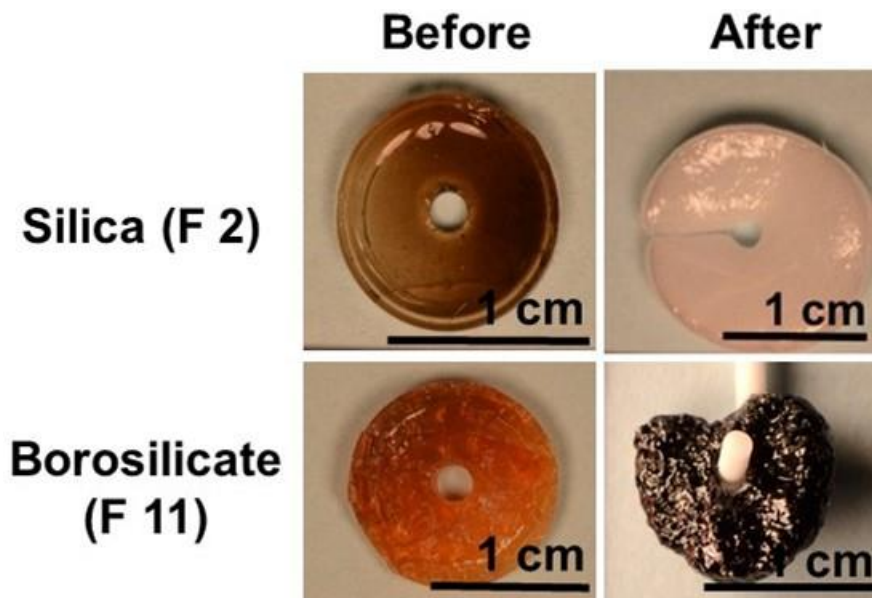


Figure 80: Macrographs of silica and borosilicate freestanding glasses taken before and after TGA exposures at 1200 °C for 100 h in dry O₂.

7.3.3 Post exposure characterization of freestanding glasses

The freestanding glasses were characterized for composition and molecular bonding after exposures to the high temperature dry O₂ environment. The results of the compositional and structural changes are individually described for carbon and boron in the following sections.

7.3.3.1 Carbon concentration and molecular bonding

Carbon oxidation from the silica and borosilicate freestanding glasses exposed to the high temperature dry O₂ environment at 1200 °C for 100 h was determined by Combustion IR. The carbon concentration in the silica (F2)- and TMBX-synthesized borosilicate (F 8) glasses that were exposed to the dry O₂ environment were compared to glasses that were not exposed to the same environment, but were cast from the same sol-

gel synthesis. The carbon concentration from these glasses is listed in Table 19. The results show that carbon had fully oxidized from the silica glass. In contrast, a considerable concentration of carbon (1.5 wt.%) was retained in the borosilicate glass following TGA exposure. These results suggest that interactions between boron and carbon prevented the carbon from fully oxidizing from the glass.

Table 19: Combustion IR results of the carbon concentration in silica- (F 2) and TMBX-synthesized borosilicate (F 8) freestanding glasses following TGA exposures at 1200°C for 100 h in dry O₂. The carbon concentrations were compared to glasses that were not exposed to the TGA environment, but were cast from the same sol-gel synthesis.

FSG	C Concentration (wt. %)	
	No TGA exposure	After TGA exposure
Silica (F 2)	1.9	0.01
Borosilicate (F 8)	5.0	1.5

The TMBX-synthesized borosilicate glass (F 8) was characterized by Raman spectroscopy to determine the carbon incorporation in the glass structure following exposures to the high temperature environment at 1200°C for 100 h in dry O₂. Raman spectra were collected from ~ 3 randomly selected areas. A representative Raman spectrum from one of these areas is shown in Figure 81. The spectrum shows that free carbon was present in the glass, represented by D and G peaks located at ~1350 cm⁻¹ and 1600 cm⁻¹ positions^{75, 84}. Carbon was not detected from analysis of the silica freestanding glass (F 2) following exposure to the same conditions.

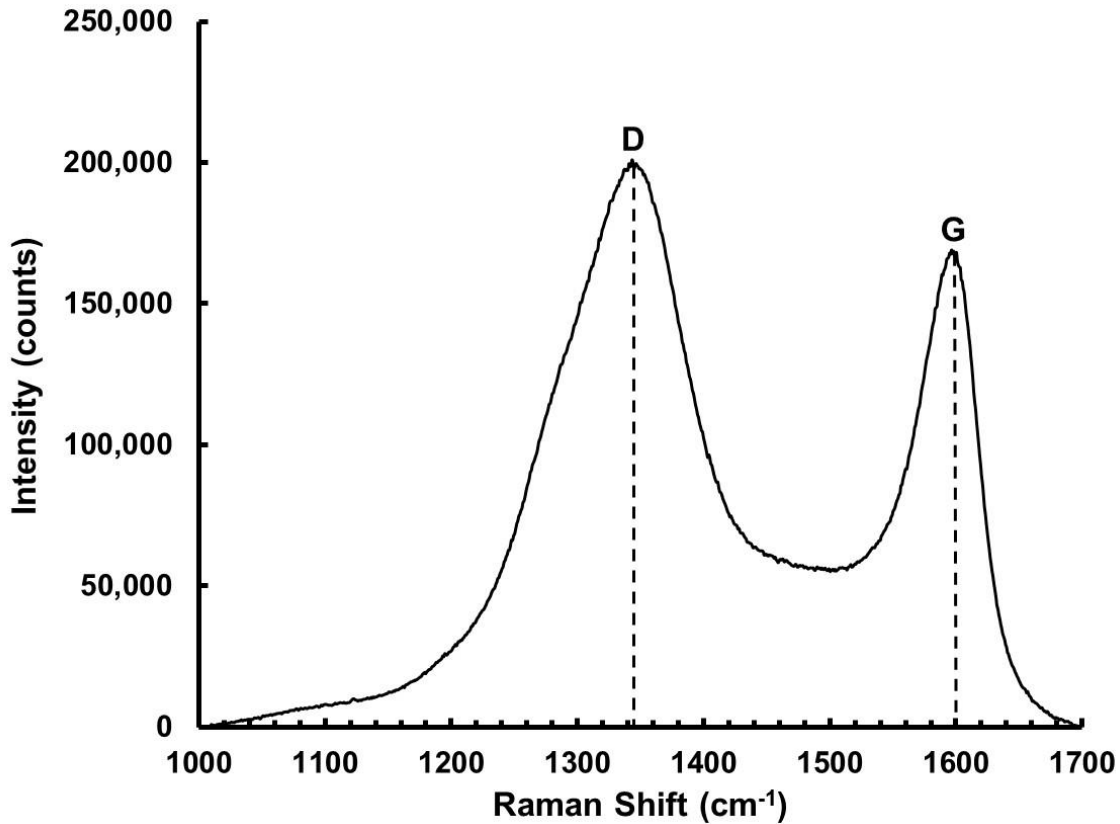


Figure 81: Raman spectrum from analysis of the TMBX-synthesized borosilicate glass (F 8 following TGA exposures for 100 h at 1200 °C in dry O₂).

7.3.3.2 Boron concentration and molecular bonding

The borosilicate freestanding glasses were investigated for boron volatility by investigating the bulk and surface boron compositions of the glasses following high temperatures exposures in dry O₂. The boron compositions in the exposed glasses were compared with boron compositions in glasses that were not exposed to the high temperature dry O₂ environment, but were cast from the same sol-gel synthesis. These results are described in the following sections.

7.3.3.3 Bulk boron concentration: ICP-OES results

The bulk boron concentrations in the TMBX (F 9 – F 10)- and boria (F 12)-synthesized borosilicate freestanding glasses were determined by ICP-OES analysis of glasses digested in HF solutions. The ICP-OES results for the borosilicate glasses

following high temperature dry O₂ exposures at 800 and 1200°C for 100 h are listed in Table 20. The bulk boron concentrations in the exposed glasses were compared to the bulk boron concentrations to glasses that were not exposed to the high temperature dry O₂ environment, but were cast from the same sol-gel synthesis.

The results of the bulk boron concentrations were mixed. The boron concentrations in TMBX-synthesized glasses synthesized with 90 vol.% solvent (F 7 and F 8) were unchanged with exposure relative to the concentrations observed after the 800°C exposure and to glasses from these syntheses that were not exposed. The boron was stable in these formulations. The boron concentration increased in glasses synthesized with higher solvent concentrations (F 9, synthesized with 92.5 vol.% solvent) with exposure. These results indicate that some organics, specifically the silicon precursor and/ or silicon hydroxide, SiOH, had not fully volatilized from the glasses during heat treatment as a consequence of higher solvent concentrations. They were then evolved during TGA exposure. The boron concentration in the boria-synthesized glass (F 11, synthesized with 90 vol.% solvent) increased with exposure at 800°C, again ascribed to evolution of weakly integrated Si-species during TGA exposure. The boron concentration then decreased with exposure at 1200°C, indicating that the boria precursor was not strongly bonded to the glass structure, and had volatilized at the higher exposure temperature.

Table 20: Borosilicate FSG B concentration prior to and after TGA exposure at 800 and 1200 °C for 100 h in dry O₂ determined by ICP-OES

Borosilicate FSG formulation	B concentration (mol%)		
	Not exposed	After 800°C exposure	After 1200°C exposure
F 7	40	--	40
F 8	45	--	41
F 9	23	37	38
F 11	26	38	30

7.3.3.4 Surface boron concentration: surface depth profiling results by XPS

A TMBX-synthesized borosilicate freestanding glass (F 7) was characterized for boria volatility with surface depth profiling analysis with XPS following TGA exposure at 1200°C for 100 h in dry O₂. The concentrations of O, Si, and B from the XPS analysis were plotted as a function of sputter depth, as shown in Figure 82 A. The O and Si concentrations are constant, whereas the B concentration increases with sputter depth. The B concentration gradient is shown superimposed in Figure 82 B. Although the ICP-OES results indicated that the bulk B concentration in this glass was stable to the TGA environment (F 7 in Table 20), the XPS results are evidence that boria volatilized from the glass surface during exposure. Depletion of B extended 0.3 μm into the glass.

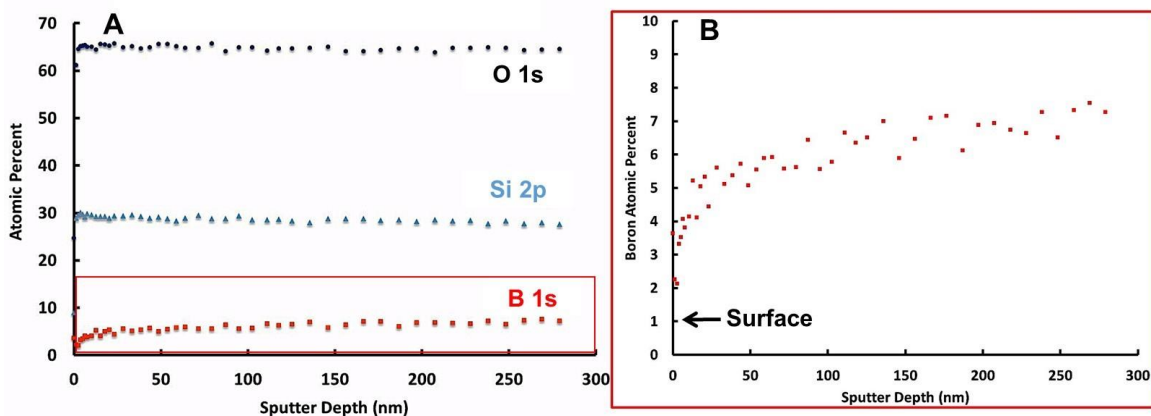


Figure 82: Surface composition of O, Si, and B determined from surface depth profiling of a TMBX-synthesized borosilicate freestanding glass (F 7) by XPS following TGA exposure at 1200°C for 100 h in dry O₂. A) Surface concentrations of O, Si, and B (at. %) as a function of surface depth. B) Surface concentration of boron as a function of sputter depth shown superimposed to highlight the boron concentration gradient, which extends more than 0.3 μm into the glass surface.

7.3.3.5 Boron molecular bonding

The structural variations of the TMBX (F 7 – F 9)- and boria (F11)-synthesized borosilicate freestanding glasses due to high temperature exposures at 800 and 1200°C for 100 h in dry O₂ were investigated with FTIR spectroscopy. The FTIR spectra of the

converted glasses (converted by heat treatment, but not exposed to the TGA environment) are shown by the in Figure 83 A. Two main regions of molecular bonding are highlighted: 1) bands that represent hydroxyl (-OH) bonds in the 4000 – 1600 cm^{-1} wavenumber region, including water, and 2) peaks that represent borosilicate bonds (Si-O-B) at 930 and 670 cm^{-1} positions, highlighted by the arrows. The breadth and intensities of these peaks do not differ significantly for the formulation variants. The borosilicate glasses have similar structures. The FTIR spectra of the borosilicate glasses after high temperature exposure in dry O_2 are shown in Figure 83 B. The spectra from borosilicate glasses (F 9 and F 11) exposed to the TGA environment at 800°C are on top. The remaining spectra were collected from borosilicate glasses (F 7 – F9, F 11) exposed to the TGA environment at 1200°C. Note that the intensities for peaks assigned to –OH bonds diminished substantially, signifying that the glasses were condensed during TGA exposure. Water and –OH species were evolved. Further, the intensities for peaks assigned to borosilicate bonds had increased with TGA exposure, signifying that bonding between Si-O-Si and B-O-B units were enhanced by the evolution of water⁷² and increases in temperature⁶⁶. The sol-gel derived borosilicate glasses molecular structure was increasingly like the structure of a binary borosilicate glass with the combination of carbon oxidation and condensations reactions that occurred with the high temperatures exposures in dry O_2 .

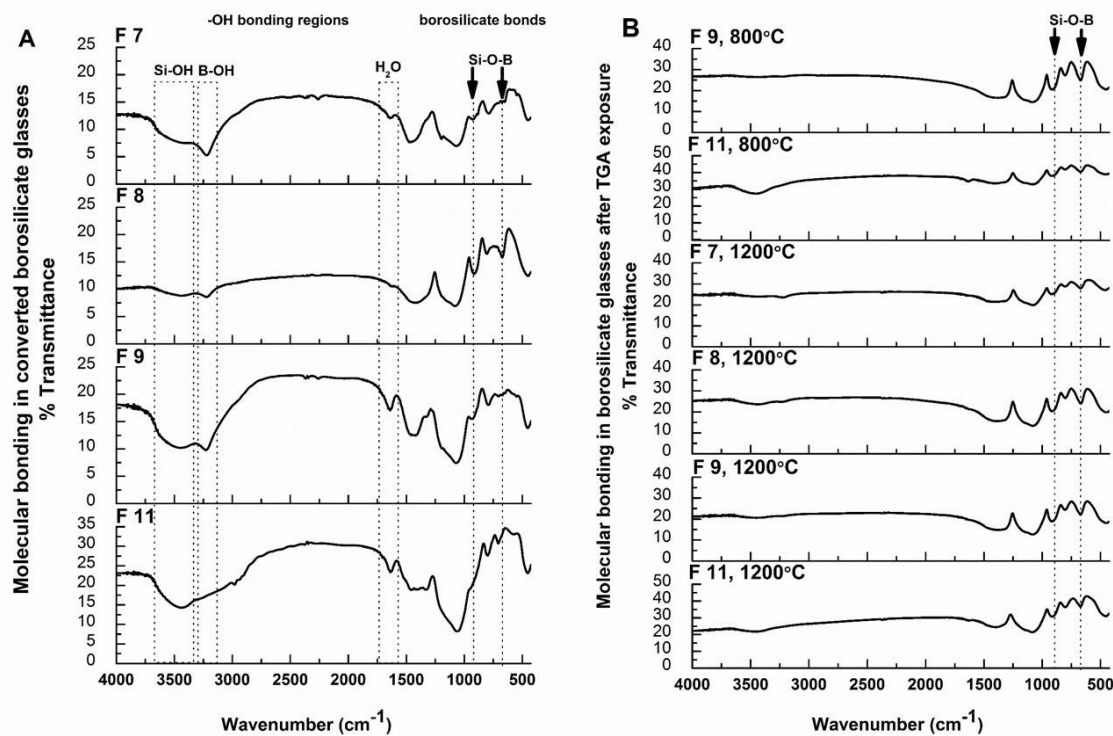


Figure 83: FTIR spectra from borosilicate freestanding glasses synthesized from the TMBX precursor (F 7 – F 9) and from the boria precursor (F 11). A) Stacked spectra from converted freestanding glasses. B) Stacked spectra of the freestanding glasses after dry O₂ exposures at 800 °C (F 9 and F 11, top two spectra, respectively) and after dry O₂ exposures at 1200 °C (F 7 – F 9 and F 11, bottom four spectra) for 100 h.

7.3.4 Summary of volatilization reactions that occurred in the sol-gel derived freestanding glasses from exposures to the TGA environment

The weight change profiles showed that the freestanding glass lost weight during exposure to the high temperature dry O₂ environment. The weight change profiles also showed that the weight loss increased with increased exposure temperature, verified by benchtop weight change measurements. Further, the borosilicate glasses changed shape due to some melting in the high temperature environment. Results from characterization of the borosilicate glasses after TGA exposure determined that the weight loss was due to a combination of 1) carbon oxidation, 2) boria volatility, and 3) condensation reactions from hydroxylated species that were retained in the converted glasses. The

characterization results also provided two important insights into the borosilicate glass structure. The first being that the carbon had not fully oxidized from the borosilicate glasses, even with exposures as high as 1200°C. The second being that the boron depletion in borosilicate glasses extended 0.3 μm deep into the surface. The implications of weight loss, partial carbon oxidation, boria volatility, and viscosity and melting on the behavior of sol-derived borosilicate glass coatings applied onto SiC substrates during oxidation tests are individually discussed in the following sections.

7.4 *Discussion*

7.4.1 Weight loss

The weight loss observed from the high temperature exposures of the sol-gel derived freestanding glasses in dry O₂ are expected to occur during oxidation testing of SiC substrates coated with sol-gel derived borosilicate glass layers for the purpose of observing boria effects on SiC oxidation kinetics. The expected weight loss from the glass coatings during oxidation testing is problematic for two reasons. One, the oxidation mechanisms of the coated substrates will not be able to be determined from weight change behavior alone³². Two, observation of boria effects on accelerating the SiC oxidation kinetics will be suppressed by the volatilization reactions occurring in borosilicate glass coating. These implications on interpreting the oxidation behavior of borosilicate glass coated SiC substrates caused by the coating volatilization reactions will be overcome by investigating the oxides microstructures following TGA exposures of the glass coated SiC substrates.

7.4.1.1 Carbon oxidation

Although the carbon oxidation that resulted from the high temperature exposures

of the freestanding glasses to dry O₂ was substantial, some of the carbon was still present in the borosilicate glasses, even after exposures at 1200°C for 100 h. The Raman results showed that free carbon was present in the borosilicate glasses after dry O₂ exposures. The structure of the free carbon phase in sol-gel derived glasses is under debate^{85, 122, 123}. For instance, several models were investigated by Kroll to determine the most energetically favorable incorporation of the free carbon phase in silicon oxycarbide glasses (such as the silica glasses synthesized in this study by a sol-gel method)⁸⁵. In his study, the free carbon phase is favored to exist fully segregated from the glass phase without any chemical bonding between the free carbon and the glass. It was shown here that the carbon phase in the silica glasses oxidized from 1200°C exposures in dry O₂.

In contrast, the carbon phase in the borosilicate glasses never fully oxidized, even after heat treatment in the presence of H₂ and TGA exposures as high as 1200°C in dry O₂. The retention of some free carbon in the borosilicate glasses after exposure to the TGA environment is ascribed to strong interactions between boron and carbon^{75, 124, 125}. Raman investigations by Kaur et al. determined that boron is incorporated into the free carbon phase during heat treatment of glasses synthesized by a sol-gel method¹²⁴. Boron incorporation into the free carbon phase was not resolved by the Raman spectra obtained from glasses in this study. The mechanisms that shield carbon from oxidation by the presence of boron are not understood. Further, the interactions of boron with the free carbon phase that hinder it from oxidizing during dry O₂ exposure must be considered as they relate to O₂ transport through sol-gel derived glass coatings. The transport mechanism of O₂ through silica and boria is governed by molecular O₂ permeation through the interstitials in the amorphous glass network^{25, 63, 126}. The segregated carbon

phase in a sol-gel derived glass may alter the transport mechanism of O₂. The carbon concentration in the sol-gel derived borosilicate glasses synthesized in this study is ~ 22 mol% prior to dry O₂ exposure. Although the carbon concentration was reduced to 1.5 wt.% from oxidation during TGA exposure, the effect of the retained carbon on O₂ transport rates through the glass is uncertain. At these low concentrations, the O₂ transport rates may not be affected by the free carbon phase. However, the presence of the free carbon phase was a limiting factor in synthesizing coatings that can be used models for thermally grown borosilicate oxides because a carbon-free binary borosilicate glass network could not be synthesized.

7.4.1.2 Boria volatility

Boria volatility was shown to occur in the borosilicate glass surface from exposure to the TGA environment. The boron depleted zone was ~ 0.3 μm. The depth of the boron concentration gradient was minor relative to the 1 – 2 mm thickness of the borosilicate glass. However, for a glass coating applied onto a SiC substrate with a thickness of ≤ 1 μm, this boron depleted zone would be significant as it relates to O₂ transport rates through the borosilicate glass coating. The O₂ diffusion through molten boria is orders of magnitude faster than in silica^{21, 25, 63}, which is why boria is thought to accelerate the SiC oxidation kinetics^{3, 60}. The boria concentration that triggers rapid oxidation of SiC is not presently known. The effect of boria volatility on the glass coating is that it 1) reduces the coating boron concentration, and 2) enriches the glass coating surface with silica, which will slow the O₂ diffusion through the glass coating. Further, oxidation of the SiC substrate enriches the borosilicate glass coating with silica at the coating-substrate interface. The combination of boria volatility and SiC oxidation may

impede the using borosilicate glass coatings to understand the effects of boria on SiC oxidation kinetics. As will be described later in Task 5, both thin ($\leq 1 \mu\text{m}$) and thick ($>1 \mu\text{m}$) borosilicate glass coatings were applied on SiC substrates in anticipation of boria volatility and silica enrichment of the coatings during high temperature oxidation testing.

7.4.2 Viscosity and melting

The silica freestanding glasses were bloated from dry O_2 exposures, namely at 1200°C , but the borosilicate underwent considerable morphological changes from both 800 and 1200°C TGA exposures. These changes are attributed to the effects of the low boria melt temperature⁴⁶ on lowering the viscosity of silica, which reduces significantly with increases in temperature⁵⁵. The sol-gel derived borosilicate glass coatings may likewise become molten during oxidation testing, which may result in beading and dewetting from the SiC substrate⁶⁰. The dewetting would lead to uneven surface coverage of the coating on the substrate, which may affect oxidation of substrate at different locations on its surface.

7.5 Conclusions

The freestanding glasses lost weight from exposure to the high temperature dry O_2 environment due to carbon oxidation and boria volatilization. Some carbon was retained in the borosilicate freestanding glasses after TGA exposure. Oxidation of the carbon and boria volatilization from borosilicate glass coatings will affect interpretation of glass coated SiC substrate oxidation mechanisms from weight change behavior. The transport of O_2 through a boria-depleted glass coating surface will likely be slower due to silica enrichment, which may affect the ability to observe boria effects on SiC oxidation kinetics with sol-gel derived borosilicate glass coatings. The C-B interactions affect the

glass structure because some of the B that would otherwise be distributed in B-O-B and Si-O-B bonds is tied up with carbon. The role of retained carbon and the effects of the C-B interactions on O₂ transport through the sol-gel derived borosilicate glass is not presently understood.

7.6 *Recommendations for future work*

Minimization of the retained C concentration by modifying the heat treatment parameters during gel-to-glass conversion will support efforts to model the borosilicate TGO with sol-gel derived borosilicate glasses.

8 Task 5: Oxidation of SiC substrates coated with borosilicate sol-gel derived glass layers

This task sought to understand the role of boron concentration in borosilicate oxides on the silicon carbide oxidation kinetics. An approach from a previous study by Schlichting was used⁴¹. Schlichting observed silicon oxidation kinetics to be greatly accelerated by coating silicon substrates with sol-gel derived borosilicate glass layers⁴¹. Sol-gel derived glass coatings with well-defined boron concentration were synthesized in this study and applied onto silicon carbide coupons and fibers. The sol-gel derived glass coatings were also applied onto silicon substrates in an effort to reproduce Schlichting's results. The oxidation behavior of coupons coated with three different coating compositions were compared against uncoated coupons. The coating compositions differed by the level of boron concentration. Three boron concentration ranges investigated were: 0, 24 – 55, and > 95 mol %, referred to as silica, borosilicate, and boron coatings, respectively.

Silica and borosilicate coatings were applied onto unoxidized coupons. Boron coatings were applied onto unoxidized coupons as well as onto coupons that already had a thermally grown oxide present from a pre-oxidation procedure. The effect of the boron coating to modify the structure of the existing thermally grown oxide and change the silicon carbide oxidation kinetics was investigated. Isothermal oxidation tests were conducted by thermogravimetric analysis at 800 and 1200°C for 100 h. The boron coatings accelerated the silicon carbide oxidation kinetics hypothesized to be due to boron fluxing of SiC by factors 13 – 811, dependent on the substrate pre-oxidation, at

temperatures as low as 800°C. Implications of boria fluxing of SiC on CMC degradation mechanisms were presented.

The borosilicate glass coatings had no notable effect on the SiC oxidation. The boron concentration was rapidly depleted from borosilicate coatings due to volatilization reactions, which limited the observation of boria effects on the SiC oxidation kinetics. Oxidation mechanisms could not be extracted from thermogravimetric analysis of borosilicate glass coated coupons due to a combination of boria volatility and oxidation of retained carbon. Other issues encountered with sol-gel derived glass coatings were poor wettability and cracking. Oxides produced from the oxidation of borosilicate-coated fibers and uncoated fibers were different in composition, thickness, and molecular bonding. While these issues might be limits on using sol-gel derived borosilicate glasses to model thermally grown borosilicate oxides, the sol-gel derived glasses provided a means to investigate the interactions of boria with SiC and with a thermally grown silica glass that cannot be investigated with thermally grown borosilicate glasses alone.

8.1 Objectives

The objectives in this task were threefold. The first objective was to determine the boron concentration in the sol-gel derived glass coatings that triggers rapid SiC oxidation kinetics. Insights into the boria effects on SiC oxidation were sought. The second objective was to reproduce the effects that borosilicate glass coatings had on the accelerated oxidation kinetics of silicon substrates as observed by Schlichting⁴¹ with borosilicate glass coated SiC substrates. Limitations in using Schlichting's approach were identified. The third objective was to determine if the sol-gel derived glass coatings are good models for thermally grown oxides.

8.2 *Experimental recap*

8.2.1 Sol-gel synthesis

The sol-gel syntheses were carried out with tetraethoxysilane (TEOS) and 3-aminopropyltriethoxysilane (APTES) silicon precursors (Sigma-Aldrich, St. Louis, MN), used as received. Three different glass compositions were synthesized. The first contained no boron (B), referred to as silica coatings hereafter. The second composition was formulated for a nominal 67 – 75 mol% B concentration range, hereafter referred to as borosilicate coatings. The borosilicate coatings were synthesized with two different B precursors. The first precursor was trimethoxyboroxine (TMBX, Sigma-Aldrich St. Louis, MO). The second precursor was boria powder (Sigma-Aldrich St. Louis, MO). Although boria is an uncommon B precursor, it was investigated here to reproduce Schlichting's synthesis as closely as possible⁴¹. The third composition was formulated for a nominal B concentration > 95 mol%. This composition will be referred to as a boria coating because of its high B concentration, and to distinguish it from the borosilicate coatings, which have lower B concentrations by comparison. The boria coatings were synthesized with the TMBX precursor. Coating application was optimized by reducing sol viscosities with 200 proof ethanol (Sigma-Aldrich St. Louis, MO). Detailed descriptions of the synthesis, coating, and heat treatment procedures can be found in the Experimental section and in Task 3. The list of formulations that were synthesized in Task 5 is provided in Table 21.

Table 21: Sol-gel synthesis formulations

Descriptor	Formulation (F)	Mol% TEOS; APTES	Mol Silane/B-precursor	Mol Si/ B	Nominal Mol% B	Mol H ₂ O/ TEOS	Catalyst	Solvent (Vol%)	Batch Temperature (°C)
Silica	3	92.5; 7.5	--	--	0	2.7	1 N HCl	95	22
Borosilicate: TMBX precursor	9	75; 25	1.5	0.5	67	1.5	1N HNO ₃	92.5	40
	10	75; 25	1.0	0.3	75	1.5	3N HCl	90-95	40-60
Borosilicate: B ₂ O ₃ precursor	12	75; 25	1.0	0.3	75	1.5	3N HCl	90 – 95	40-60
Boria: TMBX precursor	13	75; 25	0.06	0.02	98	1.5	1 N HCl	70	40

8.2.2 Substrates and coating application

Three different types of substrates were coated. The first substrate was a chemical vapor deposited – SiC (CVD-SiC) that is >99.9995% pure and pore-free (Coorstek Advanced Carbides, Golden, CO). The CVD-SiC substrates were machined by Bomas (Bomas Machine Specialties, Inc., Somerville, MA) into coupons (1cm x 2.54cm x 0.375 cm with a 0.375 cm hole for coupon suspension from the microbalance for thermogravimetric analysis). The second type of substrate was a 1 cm x 1 cm x 0.2 cm <100> oriented Si coupon from a scored 15 cm diameter Si wafer (Ted Pella, Inc., Redding, CA). A 0.32 cm hole was drilled into each Si coupon with an ultrasonic cutter using SiC grit (Gatan, Pleasanton, CA). The third type of substrate was Sylramic™ SiC fibers, also used earlier in Task 1. The CVD-SiC and Si coupons were sequentially cleaned in soapy deionized water, pure deionized water, 200 proof ethanol, and acetone for 2 minutes in a bath sonicator prior to coating. The uncoated substrates were weighed with a Mettler-Toledo MS105DU analytical balance (Mettler-Toledo, LLC, Columbus, OH).

Coatings were applied by a dip-coat method. A detailed description of the coating procedure can be found in the Experimental section. The coating thickness was built up by reducing the solvent concentration and/ or by increasing the number of dip coats to produce thin, thick, and very thick coatings. Thin coatings are representative of thermally grown oxides at early stages of oxidation ($< 1 \mu\text{m}$). Thick borosilicate coatings were also applied to reproduce the $10 \mu\text{m}$ coating thicknesses applied onto Si substrates in Schlichting's study⁴¹. Very thick boria coatings ($10 - 30 \mu\text{m}$) were also investigated because rapid volatilization of boria is a concern⁶⁰. Boria volatilization limits the observation of boria effects on SiC oxidation kinetics, as discussed earlier in Task 1.

The coated substrates were weighed on the benchtop balance after heat treatment for gel-to-glass conversion. The coating weights were calculated from the difference of the coated substrate weight to the bare substrate weight. The coating thicknesses were calculated from the coating weights and the respective substrate surface areas. The amorphous silica density, 2.2 g cm^{-3} , was assumed for both silica and borosilicate coatings. The density of boria, 2.46 g cm^{-3} , was assumed for boria coatings. Silica and borosilicate coatings were applied onto unoxidized substrates. Boria coatings were applied onto unoxidized and CVD-SiC coupons pre-oxidized in dry O_2 to produce a thermally grown oxide prior to coating application as described in Table 22, which also lists the coating formulations and the substrates onto which they were applied. The number of dip coats was designated as it relates to the coating thicknesses that were sought. Calculated coating thicknesses $\leq 1 \mu\text{m}$ were designated as thin, whereas coating thicknesses $> 1 \mu\text{m}$ were designated as thick. Actual coating thicknesses could not be

measured due to the fragility of the coatings, which broke off the substrate during attempts to grind off the coatings on one edge to expose the coating cross-sections.

Table 22: Substrates and coatings investigated in Task 5

Substrate	Coating formulation	Coating solvent concentration (vol.%)	Number of dip coats	Coating weight (mg)	Calculated coating thickness (μm)
Unoxidized CVD-SiC	Thin Silica coating, F 3	95	3	0.2 – 0.3	0.1 – 0.2
	Thin boria-synthesized borosilicate coating, F12	95	3	0.2 – 0.9	0.1 – 0.6
	Thin TMBX-synthesized borosilicate coating, F 10	95	3	1 – 1.3	0.6 – 0.8
	Thick TMBX-synthesized borosilicate, F 9	92.5	3	2.7 – 3.1	1.6 – 1.9
Unoxidized CVD-SiC			7	26.6	14.4
CVD-SiC pre-oxidized at 1000°C for 1 h	Thick boria coating, F 13	70	7	27.3	14.8
CVD-SiC pre-oxidized at 800°C for 100 h			7	24.3	13.2
Unoxidized silicon	Thin boria-synthesized borosilicate coating, F12	95	3	0.2 – 0.3	0.5 - 0.6
Unoxidized Sylramic SiC fibers	Thin silica coating, F 3	90	1	0.3 – 0.6	N/A
	Thin boria-synthesized borosilicate coating, F12	90	1	1.2 – 2.5	N/A

The oxidation rate constant data from Ramberg et al. was used to calculate the oxide thickness on the pre-oxidized CVD-SiC coupons²¹. The calculated oxide thicknesses were 0.07 μm for the coupon pre-oxidized at 1000°C for 1 h, and 0.3 μm for the coupon pre-oxidized at 800°C for 100 h.

8.2.3 Oxidation exposures

Thermogravimetric analyses (TGA) were conducted in the custom built TGA apparatus^{7, 127} described in detail in the Experimental section. All oxidation tests were conducted in 1 atm oxygen dry O₂. The exposures were conducted for 100 h under isothermal conditions at 800 and 1200°C. The 800°C exposures were within the range of temperatures reported in Schlichting's study⁴¹. The 1200°C exposures were representative of more typical aircraft engine combustion temperatures. Repeat exposures were conducted on silica and borosilicate coated substrates at both temperatures. Boria coated coupons were exposed once at 800°C only. Each specimen was weighed on the benchtop before and after oxidation.

8.2.4 Characterization techniques

The effects of the coatings on the oxidation behavior of the CVD-SiC coupons and SiC fibers were compared by weight change, oxide thickness, and oxide microstructure. Weight changes were evaluated with TGA weight change profiles and benchtop weight measurements. The oxidized coupon cross-sections were imaged with SEM and oxide thickness measurements were made with the SEM software measurement tool. The oxide thicknesses were measured along the coupon length in cross-section where the oxide on the long edge of the coupon was previously ground off with diamond paper. A total of 35 – 45 oxide thicknesses were measured along the cross-sectioned coupon length 0.5 – 1 mm apart. Oxidized SiC fibers were fractured to expose fiber cross-sections, which were also imaged with SEM. Oxide thicknesses were measured from a minimum of 25 oxidized fiber cross-sections. The standard error on the mean oxide thickness was calculated on a 95% confidence interval. The oxides were

investigated for microstructure, composition, and phase using a variety of analytical techniques consolidated in Table 23. The microstructures were imaged in SEM with secondary and backscattered electrons. The bulk coating and oxide compositions were analyzed by ICP-OES from deionized water and/ or HF acid digestions. The oxidized coupons and fibers coated with silica or borosilicate glass layers were digested in HF solutions only. The oxidized coupons coated with boria glass layers were digested in a two-step procedure: 1) digestion in deionized water, followed by 2) digestion in HF solutions. The oxidized substrates were digested for 24 – 48 h. The digested oxides were decanted into another tube and analyzed by ICP-OES. Further details on the characterization techniques can be found in the Experimental section. FactSage software was used for calculating equilibrium reactions of SiC and O₂ in the presence of boria.

Table 23: Consolidated list of characterization techniques utilized in Task 5

Evaluation	Property	Technique
Weight change	<ul style="list-style-type: none"> • Oxidation and volatilization reactions 	<ul style="list-style-type: none"> • Benchtop weight change • TGA weight change profiles
Microstructure	<ul style="list-style-type: none"> • Oxide imaging 	<ul style="list-style-type: none"> • SEM/ EDS
Oxide thickness	<ul style="list-style-type: none"> • Oxide growth 	<ul style="list-style-type: none"> • Cross-sectional measurement of oxide thicknesses using the SEM software measurement tool
Oxide Composition	<ul style="list-style-type: none"> • Oxide composition 	<ul style="list-style-type: none"> • SEM/ EDS • ICP-OES

8.3 *Results*

For clarity, the results from the oxidation studies are organized by substrate. The effects of the coating boria concentration on the oxidation kinetics of the CVD-SiC substrate are reported first. The results from reproducing Schlichting’s observations on the accelerated oxidation of Si substrates coated with borosilicate glass layers are described next. Results from the oxidation behavior of glass coated and uncoated SiC fibers are described last. The similarities and differences between the sol-gel derived

borosilicate glass coatings and the thermally grown borosilicate are identified. Glass coatings refer to coatings synthesized by the sol-gel method. Unoxidized substrates refer to substrates that were not coated and were included as a baseline against which the effects of the coatings on the substrate oxidation behavior could be assessed.

8.3.1 Effects of borosilicate glass composition on CVD-SiC oxidation kinetics

The results from the effects of the B concentration in the sol-gel derived coatings on the CVD-SiC oxidation kinetics are organized with TGA weight change results first, starting from exposures at 800°C, followed by exposures at 1200°C. The benchtop weight change results from 800 and 1200°C exposures are reported next. Results from investigating the oxide microstructures, thicknesses, crystal structure, and compositions from the 800 and 1200°C exposures are covered last.

8.3.1.1 Weight change profiles from 800°C exposures

As a baseline reference, the uncoated CVD-SiC coupon weight change profiles will be referred to as bare SiC. The plots of the coated coupons would ordinarily be offset in weight change and time based on the time it would take for a thermally grown oxide to grow to a thickness equivalent to the coating thickness. However, in these conditions, the thermally grown oxide thickness of the uncoated coupon oxidized for 100 h at 800°C in dry O₂ was calculated to be 0.3 μm (based on the rate constant data from Ramberg on the dry O₂ oxidation of CVD-SiC at 800°C²¹). Since it would take more than 100 h to grow a thermally grown oxide equivalent to the glass coating thicknesses (Table 20), the plots of the coated coupon weight change profiles were not offset.

The weight change profiles from the oxidation of the silica and borosilicate glass coated coupons are provided in Figure 84 A and B, respectively. The weight change

profiles were all practically constant, indicating that the SiC substrate oxidation kinetics were slow, as expected for pure SiC exposed at 800°C^{15,58}. More importantly, the presence of a borosilicate glass coating had no effect on accelerating the SiC oxidation kinetics. The accelerated oxidation kinetics that Schlichting observed with borosilicate glass coated silicon coupons⁴¹ were not reproduced in this study with SiC coupons.

The weight change profiles from the oxidation of boron coated coupons are provided in Figure 84C. All weight change profiles exhibited rapidly increasing weight gain in the first 10 h of exposure. The slowing weight gain transitioned to weight loss at roughly 40 h of exposure. The thermally grown oxides present on pre-oxidized coupons were not barriers to the significant weight gain observed during the first half of the exposure, nor was the thickness of the 14 μm boron coating. More importantly, the boron coatings promoted oxidation. Very high coating B concentrations were needed to trigger rapid oxidation of SiC.

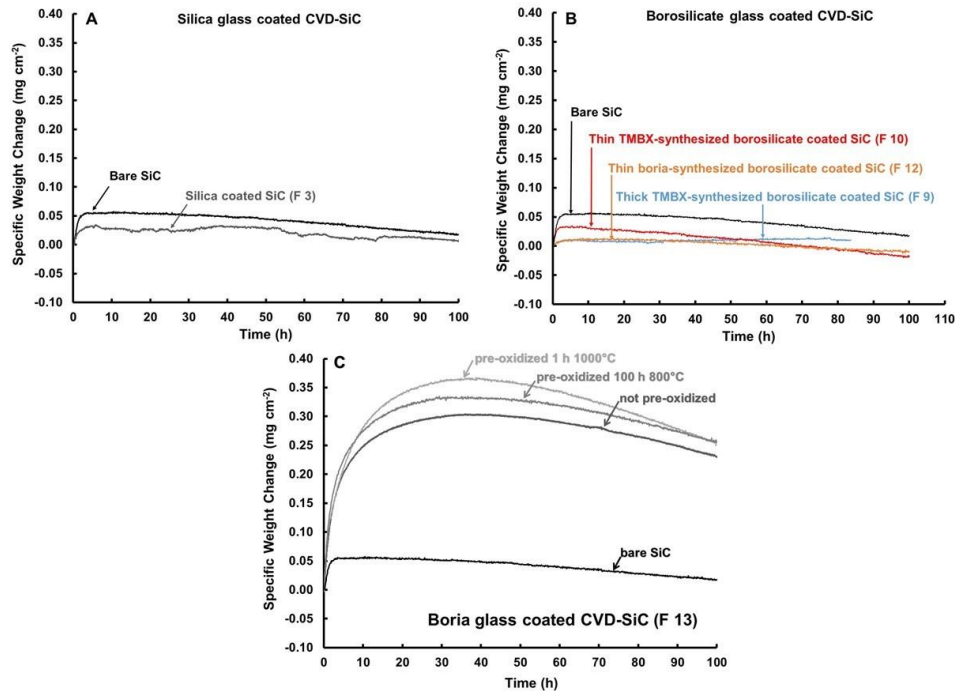


Figure 84: Weight change profiles plotted as specific weight change versus time recorded from TGA exposures at 800°C for 100 h in dry O₂. A) Weight change profiles from uncoated and silica coated CVD-SiC coupons. B) Weight change profiles from uncoated and borosilicate glass coated CVD-SiC coupons. C) Weight change profiles of uncoated and boria glass CVD-SiC coated coupons. Two of the boria glass coated coupons were pre-oxidized in dry O₂ prior to coating application. The pre-oxidation conditions are individually described in the plots.

8.3.1.2 Weight change profiles from 1200°C exposures

The oxidation kinetics of the CVD-SiC coupons were not accelerated when coated with borosilicate glass layers (F 9, F 10, F 12) during oxidation at 800°C for 100 h in dry O₂. Borosilicate glass coated CVD-SiC coupons were oxidized at 1200°C to determine if the effects of the borosilicate glass coatings on SiC oxidation kinetics could be observed at higher exposure temperatures. Boria glass coated coupons were not oxidized at 1200°C out of concern that the coating would melt or volatilize before effects on the SiC oxidation kinetics could be observed.

The weight change profiles from the oxidation of the silica and TMBX-synthesized borosilicate glass coated CVD-SiC coupons at 1200°C for 100 h in dry O₂ are provided in Figure 85. The thin silica- (F 3) and thin borosilicate (F 10) glass coated

coupons weight results were offset by the time it would take a thermally grown oxide to grow an thickness equivalent to the coating thicknesses under these oxidation conditions. The weight change profile from the thick borosilicate glass coated coupon (F 9) was not offset because its coating is too thick for the time offset to occur within the 100 h test duration. The weight change profile from the uncoated coupon, referred to as bare SiC, was included as a baseline against which the coated coupon oxidation behavior could be compared. The weight change from the uncoated and silica coated coupons appear to follow parabolic oxidation kinetics. The borosilicate coated coupons gained weight during the first ~ 20 h of test, then gradually lost weight for the remainder of the exposure. The weight loss increased with increased coating thickness. Any effects of the borosilicate glass coated coupons on increased oxidation were not observed during these 1200°C exposures. Schlichting's approach⁴¹ could not be reproduced with borosilicate glass coated CVD-SiC coupons.

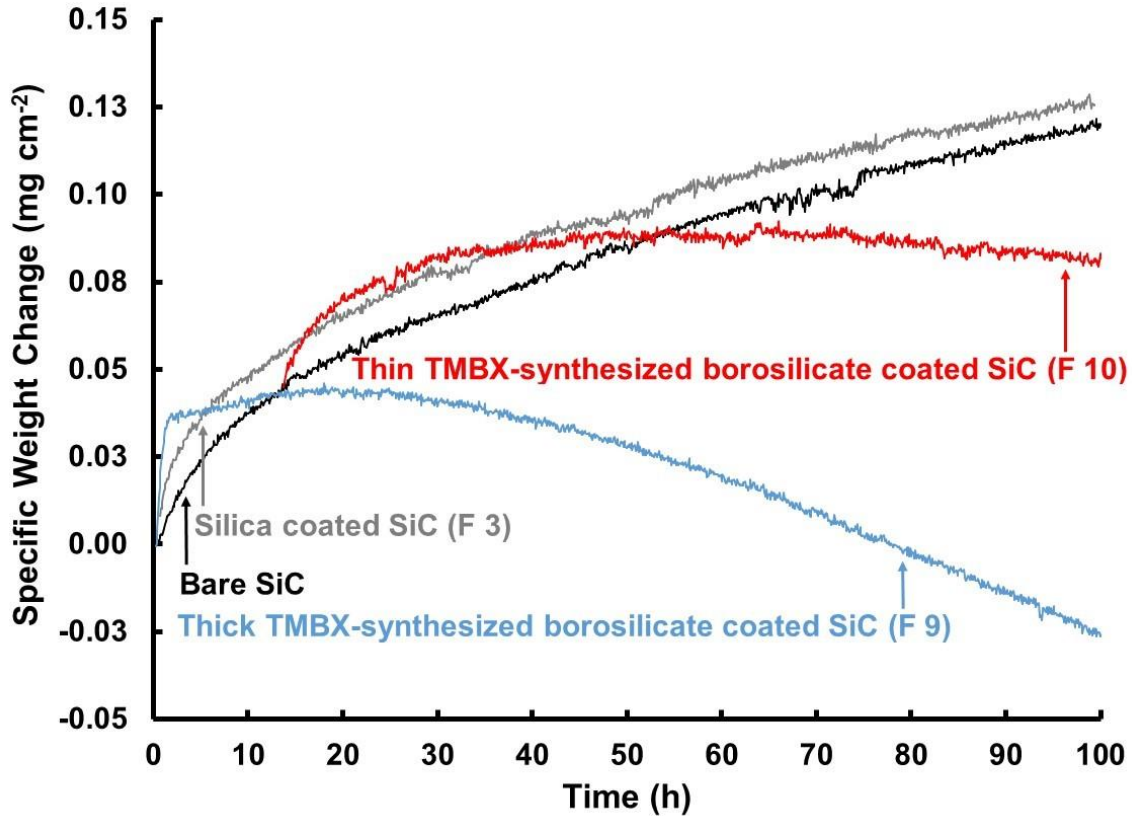


Figure 85: Weight change profiles from TGA exposures of uncoated, silica- (F 3) and TMBX-synthesized borosilicate (F 9 and F 10) glass coated CVD-SiC coupons oxidized at 1200°C for 100 h in dry O₂. Weight change profiles from thin boria-synthesized borosilicate glass coated CVD-SiC coupons are unavailable.

8.3.2 Benchtop specific weight change

The benchtop weight change measurements taken before and after uncoated and coated CVD-SiC coupons were oxidized are normalized to the coupon surface area. The specific weight change results were organized in Table 24 based on oxidation exposure temperature. The silica coated coupons were in very close agreement with the uncoated coupon. The thin borosilicate coated coupons (F 10, F 12) lost weight after oxidation at 800°C, and gained less weight than the uncoated and silica coated coupons after oxidation at 1200°C. The weight loss was even greater for the coupons coated with thick borosilicate glass layers (F 9). The boria coated coupons, oxidized at 800°C only, gained

a significant amount of weight, despite the application of very thick (~ 14 μm) borica coatings.

Table 24 : Specific weight change results from benchtop weight change measurements following TGA exposures at 800 and 1200 °C for 100 h in dry O₂

CVD-SiC coupon descriptor	Specific weight change (mg cm ⁻²)	
	800°C	1200°C
uncoated	0.01	0.12 ± 0.0004
Silica glass coating, F 3	0.008 ± 0.002	0.11 ± 0.01
Borica-synthesized borosilicate coating, F 12	-0.003 ± 0.008	0.09 ± 0.004
Thin TMBX-synthesized borosilicate glass coating, F 10	-0.03 ± 0.003	0.04 ± 0.01
Thick TMBX-synthesized borosilicate glass coating, F 9	-0.06	-0.03
Borica glass coating on unoxidized CVD-SiC	0.2	--
Borica glass coating on CVD-SiC pre-oxidized at 1000°C for 1 h	0.3	--
Borica glass coating on CVD-SiC pre-oxidized at 800°C for 100 h	0.3	--

8.3.3 Oxide microstructures

The microstructures of oxidized coated CVD-SiC coupons were observed by SEM in plan view. Uncoated coupons had featureless oxide microstructures; hence they were not shown here. Oxide microstructures that developed from the oxidation of coated coupons varied with both the exposure conditions and with the type of coating that was applied. For instance, cracks that were present on silica coated coupons (F 3) oxidized at 800°C had healed when oxidized at 1200°C, as shown in Figure 86 A and B, respectively.

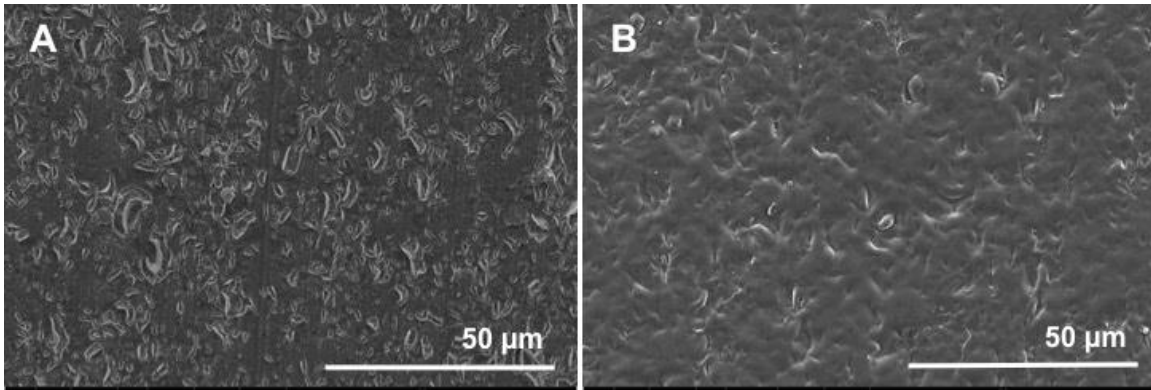


Figure 86: Micrographs of thin silica glass coated CVD-SiC coupons (F 3) oxidized for 100 h in dry O₂ at (A) 800 °C and (B) 1200 °C. Microstructures were observed by SEM in plan view with secondary electrons.

The precursor used in the synthesis of the borosilicate glass coatings affected the oxide microstructures that developed from the oxidation of thin borosilicate coated coupons. Micrographs of oxide microstructures from oxidized CVD-SiC coupons coated with the boria-synthesized borosilicate coating variant (F 12) are shown in Figure 87 A and B. The oxide formed from the 800 °C exposure was uniform and free of defects, as shown in Figure 87 A. In contrast, localized cracks developed in the oxide formed from the 1200 °C exposure, as shown in Figure 87 B.

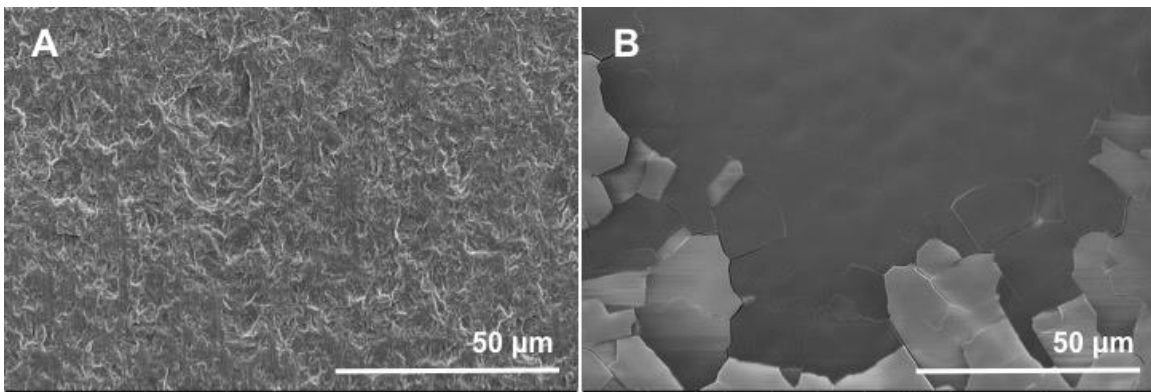


Figure 87: Micrographs of thin boria-synthesized borosilicate glass coated CVD-SiC coupons (F 12) oxidized for 100 h in dry O₂ at A) 800 °C and B) 1200 °C. Microstructures were observed by SEM in plan view with secondary electrons.

Micrographs of oxide microstructures from oxidized CVD-SiC coupons coated with the TMBX-synthesized borosilicate glass variant (F 10) are shown in Figure 88 A

and B. The unevenness in the oxide that developed during the 800°C exposure was not present in the defect-free oxide that developed during the 1200°C exposure, as shown in Figure 88 A and B, respectively.

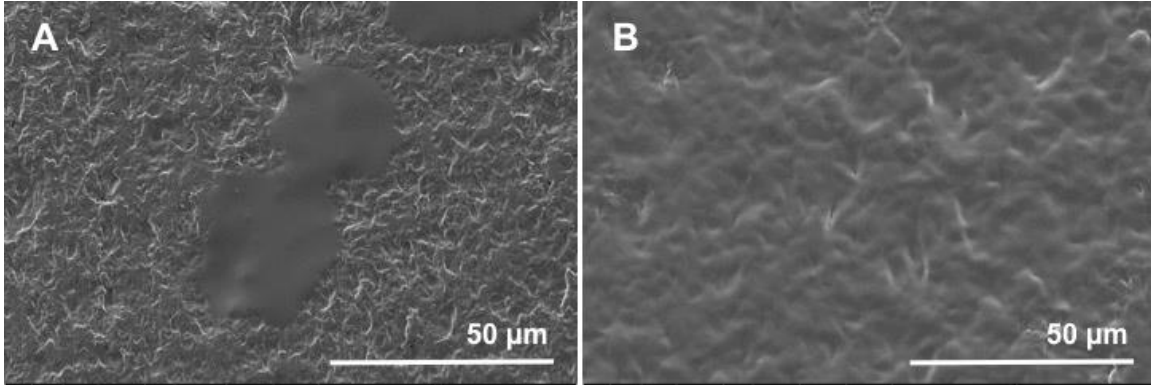


Figure 88: Micrographs of thin TMBX-synthesized borosilicate glass coated CVD-SiC coupons (F 10) oxidized for 100 h in dry O₂ at A) 800 °C and B) 1200 °C. Microstructures were observed by SEM in plan view with secondary electrons.

Oxidation of the CVD-SiC coupons coated with thick layers of the TMBX-synthesized borosilicate coating variant (F 9) resulted in oxides that dewetted from the substrate during exposures at 800°C, or cracked during exposures at 1200°C, as shown in Figure 89 A and B, respectively.

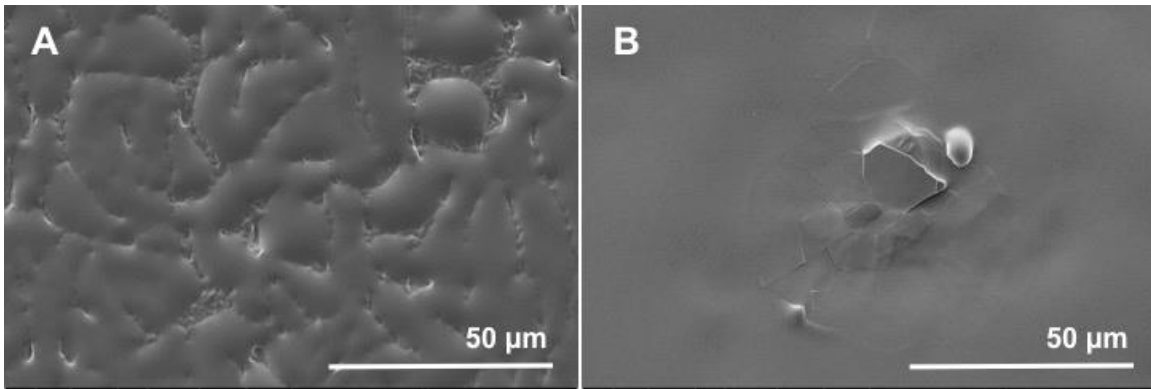


Figure 89: Micrographs of thick TMBX-synthesized borosilicate glass coated CVD-SiC coupons (F 10) oxidized for 100 h in dry O₂ at A) 800 °C and B) 1200 °C. Microstructures were observed by SEM in plan view with secondary electrons.

The oxide microstructures formed from the oxidation of boron coated CVD-SiC coupons are shown in Figure 90 A – C. The differences in the oxide microstructures are

ascribed to the CVD-SiC coupon pre-oxidation treatment that was conducted prior to coating application. For instance, oxidation of the boria glass coated coupon that was not previously pre-oxidized resulted in an oxide with fine and lacey microstructural features, as shown in Figure 90 A. Round protrusions were present in the oxide that had formed from the oxidation of the boria coated CVD-SiC coupon that was pre-oxidized at 1000°C for 1 h, as shown in Figure 90 B. Oxidation of the boria coated CVD-SiC coupon that was pre-oxidized at 800°C for 100 h resulted in an oxide microstructure that was cut by large sharp protrusions, as shown in Figure 90 C.

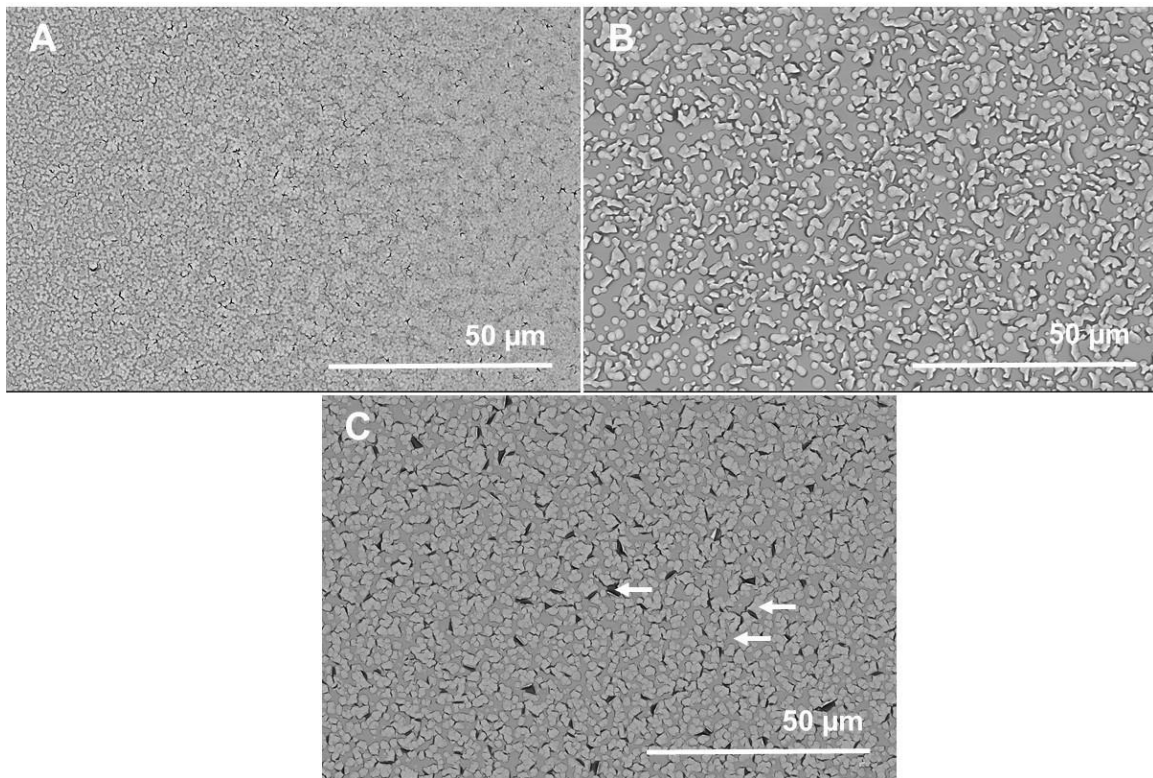


Figure 90: Micrographs of thick boria glass coated CVD-SiC coupons (F 13) oxidized for 100 h in dry O₂ at 800°C. A) Oxide microstructure of boria coated coupon not pre-oxidized prior to coating application. B) Oxide microstructure of a boria coated coupon pre-oxidized at 1000°C for 1 h prior to coating application. C) Oxide microstructure of a boria coated coupon pre-oxidized at 800°C for 100 h prior to coating application. Arrows represent spots where the oxide was analyzed by EDS. Microstructures were observed by SEM in plan view with backscattered electrons.

The localized composition of the various microstructural features observed in the oxides formed from the oxidation of the boria coated CVD-SiC coupons were further

investigated with point EDS analysis. The composition of the oxides was uniform (results not shown), indicating that the microstructural features did not develop because of compositional inhomogeneities. Only O, Si, and B were detected by EDS. The B concentration ranged from 10.6 – 12.8 at.% from point analysis of three different spots on the oxidized boron coated coupon that was pre-oxidized at 800°C for 100h. The spots that were analyzed are marked by arrows in Figure 90 C.

8.3.4 Oxide thickness

The oxidized bare and glass coated CVD-SiC coupon cross-sections were imaged by SEM following 800 and 1200°C exposures. The oxide thickness results from measurements conducted on the oxidized uncoated coupons and the silica and borosilicate coated coupons were compared first. The oxide thickness results from measurements conducted on the oxidized boron coated coupons were reported last.

8.3.4.1 Oxidized silica and borosilicate glass coated CVD-SiC coupons

The oxides resulting from 800°C TGA exposures of the uncoated and silica and borosilicate coated CVD-SiC coupons were too thin to be resolved by SEM observation, even with high magnification. The oxidized CVD-SiC coupons coated with borosilicate glass layers (borosilicate glass coating formulations F 9 – 10, F 12 – 13) did not show evidence of accelerated SiC oxidation kinetics due to the presence of B. The immeasurable oxide thickness was attributed to negligible substrate oxidation and to dewetting that occurred during oxidation of the thick borosilicate glass coated coupons (F 9) at 800°C, as was shown earlier in Figure 89 A.

The oxide growth that resulted from 1200°C TGA exposures of the uncoated and silica and borosilicate coated CVD-SiC coupons was measurable. Micrographs of

oxidized coupon cross-sections imaged from uncoated and coated coupons by SEM are compared in Figure 91. The oxide microstructures of thermally grown oxide (oxidized uncoated coupon, Figure 91 A) and the oxidized glass coated coupons (Figure 91 B – D) were indistinguishable. They were dense and adherent.

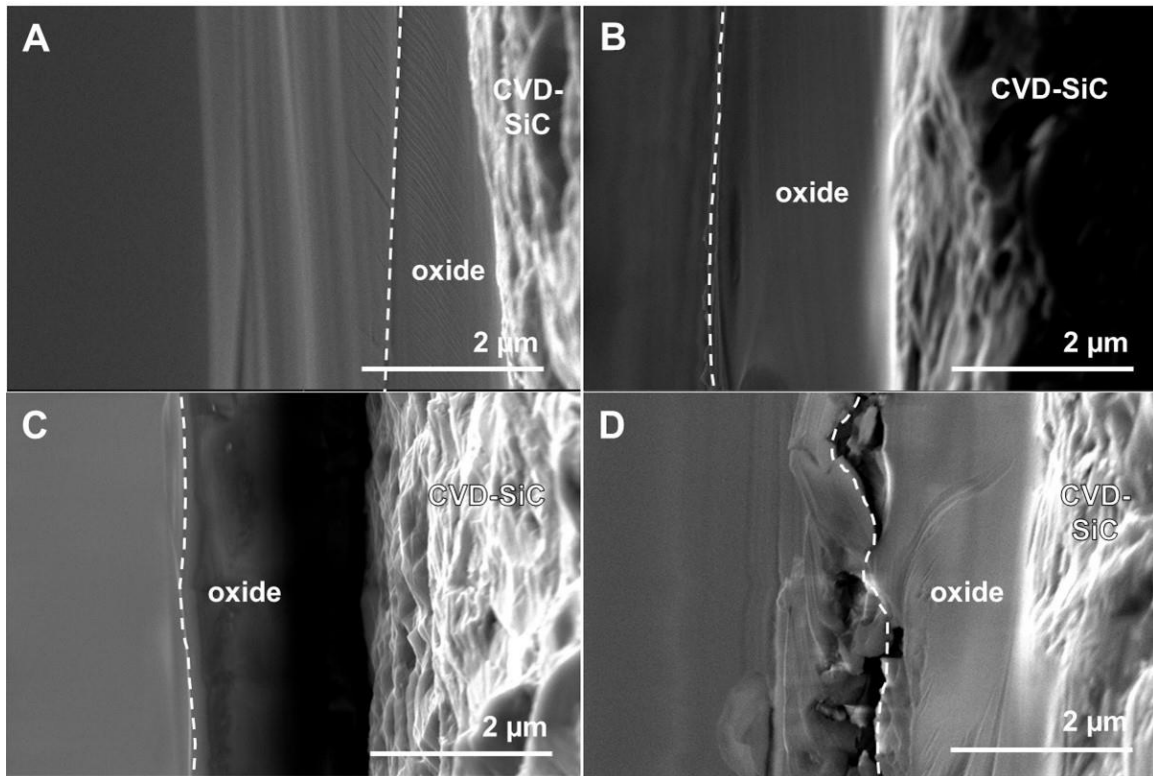


Figure 91: Micrographs of cross-sectioned uncoated and coated CVD-SiC coupons oxidized for 100 h in dry O₂ at 1200 °C. A) Uncoated coupon, B) thin silica glass coated coupon (F 3), C) thin boron-synthesized borosilicate glass coated coupon (F 12), and D) thick TMBX-synthesized borosilicate glass coated coupon (F 9). Cross-sections were observed by SEM with secondary electrons. Micrographs showing the oxidized cross-section of the thin TMBX-synthesized glass coated coupon (F 10) was not shown.

The mean oxide thicknesses measured from the uncoated and coated coupons oxidized at 1200 °C are reported with their respective standard errors in Table 25. The oxide thicknesses were averaged over 1 – 3 different specimens. At least 25 oxide thickness measurements were made. As shown in Table 25, the differences in oxide thicknesses were not statistically different, regardless of coating composition. The SiC oxidation kinetics were not accelerated by the presence of a borosilicate glass coating;

otherwise oxide thicknesses from borosilicate coated coupons would substantially exceed the oxide thickness of the uncoated coupon.

Table 25: Comparison of average oxide thicknesses measured from uncoated and silica- and borosilicate glass coated CVD-SiC coupons oxidized at 1200 °C for 100 h in dry O₂.

Coating formulation	Calculated coating thickness (μm) from Table 20	Repeats	Total number of measurements	Oxide thickness (μm)
Bare	--	3	149	1.7 ± 0.1
Silica glass coating F 3	0.1 – 0.2	2	50	1.7 ± 0.1
Boria-synthesized glass coating F 12	0.1 – 0.6	2	47	1.7 ± 0.1
Thin TMBX-synthesized glass coating F 10	0.6 – 0.8	2	50	1.6 ± 0.1
Thick TMBX-synthesized glass coating F 9	1.6 – 1.9	1	41	2.2 ± 0.4

8.3.4.2 Oxidized boria glass coated CVD-SiC coupons

The oxides resulting from 800°C TGA exposures of the boria glass coated CVD-SiC coupons were easily measurable by SEM observation at low magnification.

Micrographs of oxidized coupon cross-sections are compared in Figure 92 A – C. The oxides were adherent and durable, unlike the boria coatings that were easily damaged during polishing for the intended purpose of measuring the boria coating thickness prior to oxidation. The large sharp protrusions observed on the oxide surface of the boria coated coupon that was pre-oxidized at 800°C for 100 h, shown earlier in Figure 90 C, were also present in the oxide cross-section, as shown in Figure 92 C.

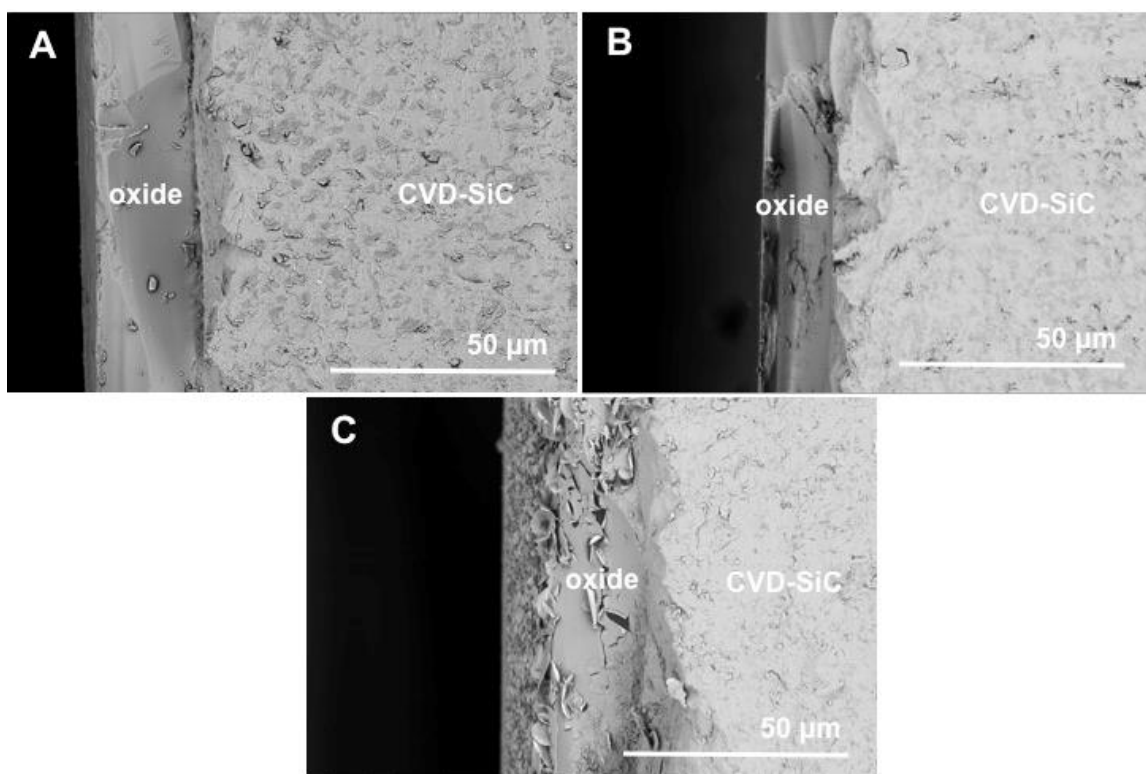


Figure 92: Micrographs of cross-sectioned boria coated CVD-SiC coupons (F 13) oxidized for 100 h in dry O_2 at $800^\circ C$. A) Coupon not pre-oxidized prior to coating application, B) coupon pre-oxidized at $1000^\circ C$ for 1 h prior to coating application, and C) coupon pre-oxidized at $800^\circ C$ for 100 h prior to coating application. Cross-sections were observed by SEM with backscattered electrons.

The oxide thicknesses measured from the boria coated coupons oxidized at $800^\circ C$ were measured from the oxide surface to the substrate interface. The mean oxide thickness was averaged over ~ 40 measurements. The boria coating thickness, calculated from the coating weight, was then subtracted from the mean oxide thickness. The difference between the mean oxide thickness and the calculated coating thickness is referred to as the actual oxide growth. The calculated thicknesses of the pre-oxidized coupon thermally grown oxides, $0.07 - 0.3 \mu m$, as calculated from the oxidation rate data provided by Ramberg²¹, were considered negligible and were accounted for in the oxide growth calculations. The mean oxide thicknesses and actual oxide growth are included together in Table 26. Oxidation of the boria coated coupon that was not pre-oxidized prior to coating application underwent the most significant amount of oxidation, having

an actual oxide growth of nearly 9 μm . The actual oxide growth was much lower for boria coated coupons that were pre-oxidized prior to coating application. Pre-oxidation was shown to substantially curb the SiC oxidation kinetics that were accelerated by the presence of a boria coating. These results were substantiated by the weight gain from oxidation of the boria coated pre-oxidized coupons. The specific weight change results from benchtop balance measurements are also included in Table 26. The weight gains were ~ 1.9 mg, which are far greater than the 0.1 mg weight gain of the uncoated coupon oxidized under these same conditions. The 1.9 mg weight gain was assigned to the weight of silica formed from oxidation of the boria glass coated CVD-SiC coupons. The silica oxide thickness calculated from the weight gain is 1.1 μm , which underestimates the actual oxide growths shown in Table 26 by factors of $\sim 1 - 8$. The actual oxide growths were underestimated by weight gain because the boria glass coating was volatilizing while the substrate was gaining weight due to oxidation.

Table 26: Average oxide thicknesses measured from boria glass coated CVD-SiC coupons oxidized at 800°C for 100 h in dry O₂

Oxidized boria coated coupons distinguished by pre-oxidation conditions	Calculated boria coating thickness (μm) (from Table 20)	Total number of oxide thickness measurements	Measured oxide thickness (μm)	Actual oxide growth (μm)	Specific weight change (mg cm^{-2})
Unoxidized	14.4	40	22.9 ± 0.76	8.54	0.24
1 h at 1000°C	14.8	39	16.2 ± 1.19	1.37	0.25
100 h at 800°C	13.2	40	16.3 ± 1.31	3.10	0.26

8.3.5 Bulk oxide composition

The bulk oxide compositions were analyzed by ICP-OES from water and/ or HF digestions of oxidized coupons. All silica- and borosilicate coated coupons were digested in HF solutions after oxidation at 800 and 1200°C. Uncoated, unoxidized coupons were included to determine if they were unstable to the HF solutions. No Si was detected,

signifying that the coupons themselves were stable to the HF solutions and did not contribute to values measured for the coated or oxidized coupons. The compositions of the sol-gel derived borosilicate glass coatings digested from unoxidized coupons are compared to the compositions of the oxides digested from borosilicate glass coated coupons following oxidation in Table 27. The results show that the B concentration generally decreased following oxidation. The lower oxide B concentrations following oxidation at 800°C are ascribed to B volatility in the high temperature environment and not to increase Si concentrations because the substrate oxidation at 800°C was negligible. The oxide B concentrations were even lower following oxidation at 1200°C, ascribed to a combination of high temperature B volatility and increased Si concentration in the oxides due to increased oxidation of the SiC substrate at the higher temperature exposures.

Table 27: ICP-OES results of the bulk B concentration in oxides digested from borosilicate glass coated CVD-SiC coupons oxidized for 100 h in dry O₂ at 800 and 1200 °C

Formulation	B concentration in sol-gel derived borosilicate glass coating digested from unoxidized coated coupons	B concentration in oxide following 100 h TGA exposures (mol%)	
		800°C (1 – 2 repeats)	1200°C (1 – 2 repeats)
Boria-synthesized glass coating F 12	31	9.2 ± 5.2	2.5 ± 2.1
Thin TMBX-synthesized glass coating F 10	24	27 ± 0.2	8.9 ± 8.2
Thick TMBX-synthesized glass coating F 9	55	36	unavailable

The oxidized boria coated coupons were digested in deionized water first since boria is highly soluble in water⁴². The oxides should also contain substantial amounts of SiO₂ because the boria coated coupons underwent significant oxidation at 800°C, as described in the previous section. The silica is also water soluble in borosilicate glasses at concentrations up to 35 mol%⁴². The silica water solubility drops off significantly when silica concentrations in the borosilicate glass exceed 40 mol%⁴². Therefore, the oxidized

boria coated coupons were digested in HF solutions following digestions in water. The oxide B concentration quantified by ICP-OES from water and HF digested oxides are given in Table 26. The molarity of the Si concentration from oxide digestions in the HF solution was provided to compare the oxide relative concentrations of Si. The B and Si concentrations from both water and HF digestions were then added together to calculate the total boria concentration.

The boria concentration in the boria coating prior to oxidation was 95 mol%. The boria concentration in the oxides ranged from 42 – 50 mol%, balance silica, as given in Table 28. The presence of Si in the HF solutions came from silica due to SiC oxidation. The concentration of Si was highest in the oxide digested from the boria coated coupon that was not pre-oxidized, which signifies this coupon oxidized the greatest, as indicated by the oxide thickness results shown in Table 26.

Table 28: ICP-OES results of the bulk B concentration in oxides digested from boria glass coated CVD-SiC coupons oxidized for 100 h in dry O₂ at 800 °C

Descriptor	B concentration in H ₂ O digestions (mol%)	B concentration in HF digestions (mol%)	Si molarity in HF digestions (mol/L)	Total B concentration from combined H ₂ O and HF digestions (mol%)	Calculated total boria concentration (mol%)
Boria glass coating B concentration	--	97	--	--	95
Oxide from boria glass coated CVD-SiC not pre-oxidized	76	< 1	4.3 x 10 ⁻³	59	42
Oxide from boria glass coated CVD-SiC pre-oxidized at 1000 °C for 1 h	75	< 1	1.8 x 10 ⁻³	67	50
Oxide from boria glass CVD-SiC pre-oxidized at 800 °C for 100 h	75	< 1	2.3 x 10 ⁻³	63	46

8.3.6 Efforts to reproduce Schlichting's experiments: oxidation of sol-gel derived borosilicate glass coated Si substrates

Earlier it was shown that accelerated oxidation of borosilicate glass coated CVD-SiC coupons was not observed. Attempts were made in this study to reproduce Schlichting's approach⁴¹ with Si coupons, but the coatings were significantly cracked despite methodical efforts made to optimize the coating application procedure (described in Task 3). The Si coupons were coated with the boron-synthesized borosilicate glass coating formulation F 12 to replicate Schlichting's borosilicate glass coating procedure as closely as possible. Representative weight change profiles from TGA exposures conducted on uncoated and boron-synthesized borosilicate glass coated Si coupons (F 12) at 800 and 1200°C for 100 h in dry O₂ are given in Figure 93, respectively. The borosilicate glass coated coupon weight change profiles were similar to the uncoated Si coupon at 800 and 1200°C.

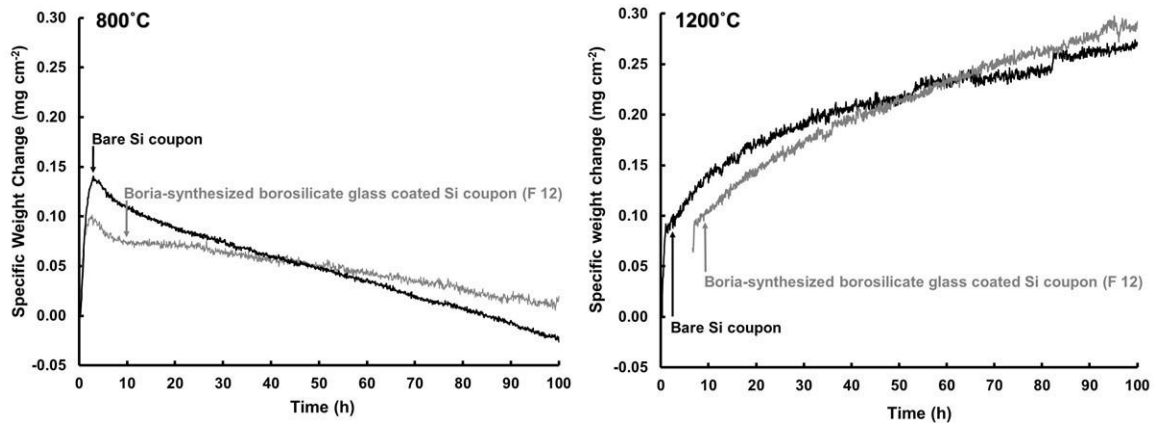


Figure 93: Weight change profiles from TGA exposures of uncoated and boron-synthesized borosilicate glass coated (F 12) Si coupons oxidized at 800 and 1200°C for 100 h in dry O₂. A) Weight change profiles from 800°C exposures plotted as specific weight change versus time. B) Weight change profiles from 1200°C exposures plotted as specific weight change versus time.

The TGA weight change results from the 1200°C exposures in Figure 93 were re-plotted as specific weight change versus the square root of time. The weight change,

shown plotted in Figure 94, is linear when plotted this way, indicating that the oxidation kinetics were diffusion controlled²². The parabolic rate constants, k_p , were calculated by squaring the slopes of the linear fits, which are shown by the dashed lines in Figure 94. There was less than a factor of two difference between the uncoated and borosilicate glass coated coupons, showing again that the borosilicate glass coatings did not accelerate the Si coupon oxidation kinetics. Given that boria effects were not observed on CVD-SiC coupons coated with borosilicate glass coated CVD-SiC layers (F 9, F 10, F 12), it is assumed that the boria effects would also not be observed on the borosilicate glass coated Si coupons even if the coatings had not cracked.

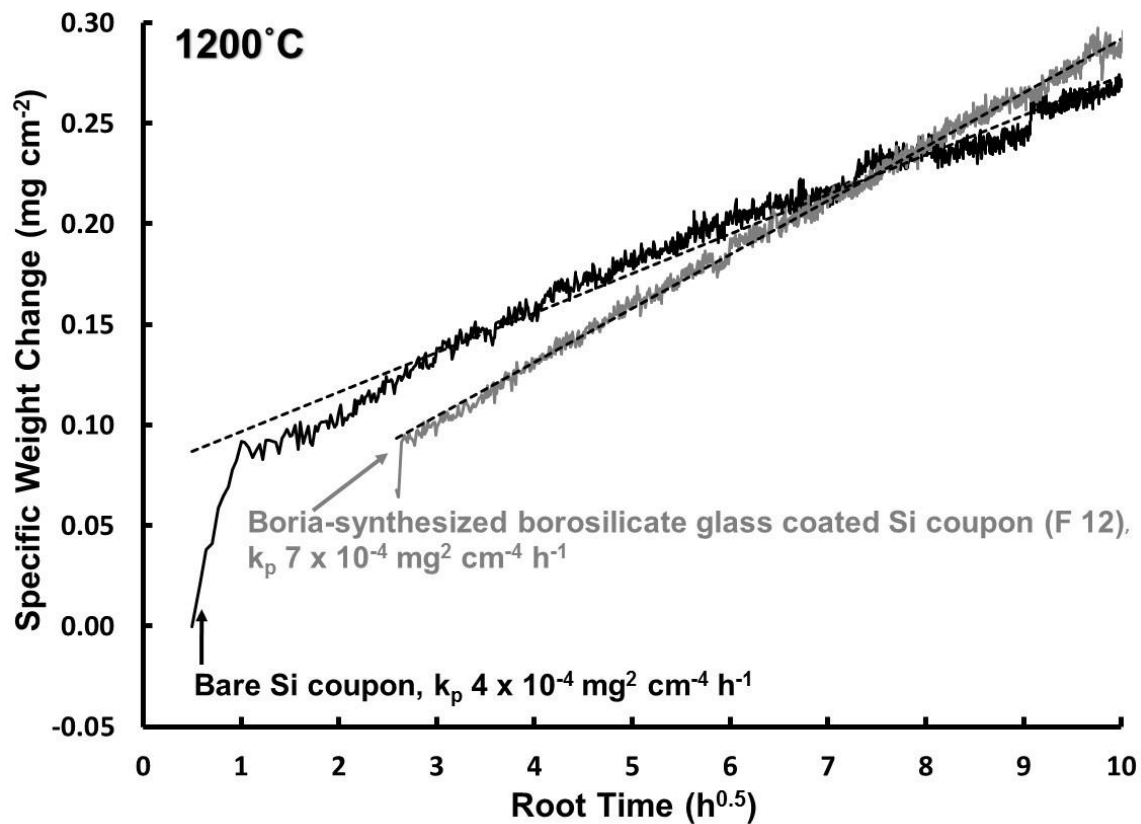


Figure 94: Weight change profiles from TGA exposures of uncoated and boria-synthesized borosilicate glass coated (F 13) Si coupons oxidized at 1200 °C for 100 h in dry O₂ plotted as specific versus the square root of time. Dashed lines denote linear fits to the plotted weight change data. Parabolic rate constants, k_p , were calculated from the squared slopes of the linear fits.

The surface microstructures formed after the oxidation of the boria-synthesized borosilicate glass coated CVD-SiC coupons (F 12) at 800 and 1200°C are shown in Figure 95 A and B, respectively. Significant oxide dewetting was observed. Oxide thickness measurements were not conducted because of the dewetting. The oxides were digested in HF solutions. The oxide B concentrations were determined with ICP-OES analysis. The oxide B concentration following the 800°C exposure was 7.7 ± 1 mol%, averaged over two repeat exposures. The oxide B concentration following the 1200°C exposure was only 0.2 ± 0.2 mol%, due to boria volatilization. The B concentration in the oxide formed from oxidation at 800°C was sufficient to accelerate the Si oxidation kinetics, based on Schlichting's results⁴¹. For instance, Schlichting reported a k_p value of $2 \text{ mg}^2 \text{ cm}^{-4} \text{ h}^{-1}$ after of Si coupons were coated with borosilicate glass coatings having a 1 mol% boria concentration oxidized for 20 h at 800°C, which is 3,000 times greater than the k_p calculated for the borosilicate glass coated coupon in this study after oxidation at 1200°C for 100 h. Schlichting's experiments could not be reproduced in this study.

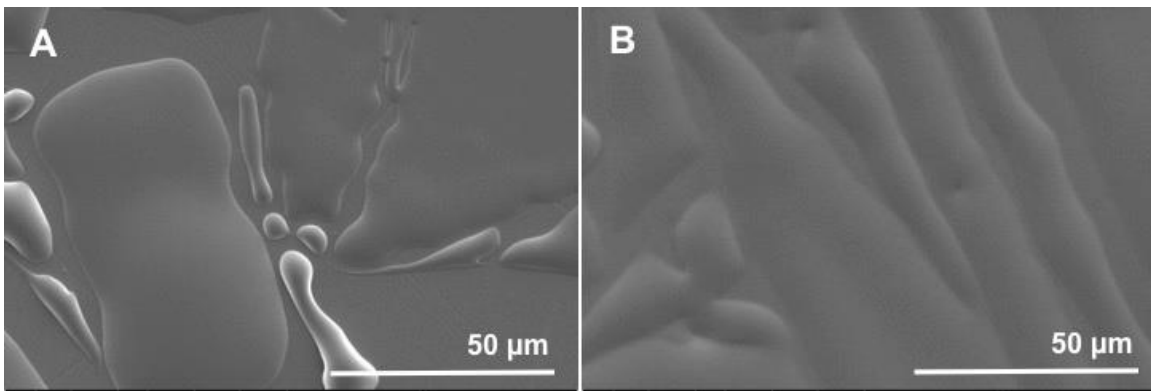


Figure 95: Micrographs of thin boria-synthesized borosilicate glass coated Si coupons (F 12) oxidized for 100 h in dry O₂ at (A) 800 °C and (B) 1200 °C. Microstructures were observed by SEM in plan view with secondary electrons.

8.3.7 Oxidation of sol-gel derived borosilicate glass coated Sylramic SiC fibers

This task sought to understand the acceleration of SiC using Schlichting's approach in applying sol-gel derived borosilicate glass coatings onto Sylramic SiC fibers.

The Sylramic SiC fibers form a thermally grown borosilicate oxide because the fibers contain TiB_2 and B_4C^{34} constituents that form boria when oxidized. In this task, the oxidation of the uncoated Sylramic fibers was compared with the oxidation the same fibers coated with silica (F 3) and coated with the boria-synthesized borosilicate glass layers (F 12). The oxides that formed after oxidation of uncoated and coated fibers were compared for thickness and composition. The ability of the borosilicate glass coating to model the thermally grown borosilicate oxide was investigated by comparing the molecular bonding in the borosilicate thermally grown oxide to the oxide formed from oxidation of the borosilicate coated fibers.

8.3.7.1 Weight change profiles from 800 and 1200°C exposures

Representative weight change profiles from TGA exposures conducted on uncoated, silica- (F 3), and boria-synthesized borosilicate glass coated Sylramic SiC fibers (F 12) at 800 and 1200°C for 100 h in dry O_2 are given in Figure 96 A and B, respectively. The weight change from oxidation of the uncoated and borosilicate glass coated fibers at 800°C (Figure 96 A) was the same, whereas the silica glass coated fibers lost weight initially. This was then followed by linear weight gain for the remainder of the exposure. The weight change behavior of the uncoated and silica glass coated fibers at 1200°C appear to follow parabolic oxidation kinetics, as shown in Figure 96 B. The weight change behavior of the borosilicate glass coated fibers, also plotted in Figure 96 B, was inconsistent and cannot be described by any known oxidation model for SiC.

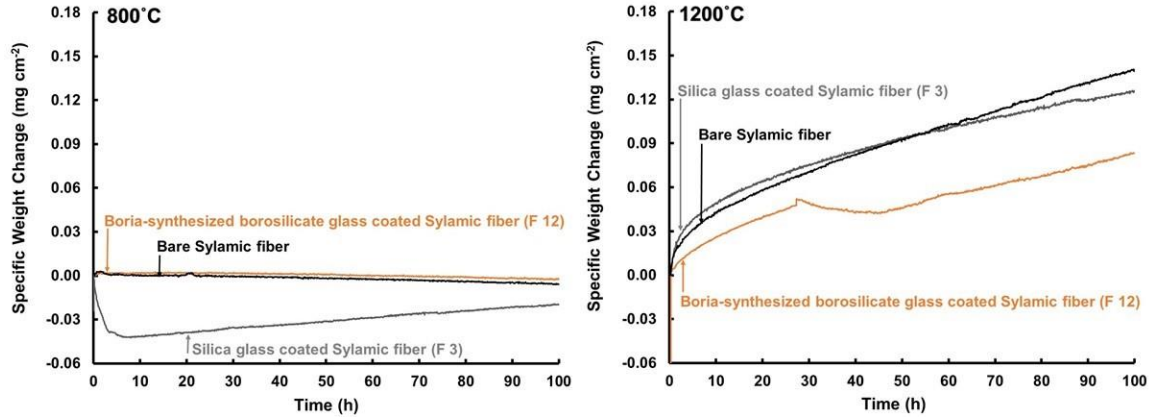


Figure 96: Weight change profiles from TGA exposures of uncoated and boria-synthesized borosilicate glass coated (F 13) Sylamic fibers oxidized at 800 and 1200 °C for 100 h in dry O₂. A) Weight change profiles from 800 °C exposures plotted as specific weight change versus time. B) Weight change profiles from 1200 °C exposures plotted as specific weight change versus time.

8.3.7.2 Oxide thickness

The oxidized fibers were cross-sectioned and the oxides were observed by SEM.

Oxide thicknesses were measured with the SEM software measurement tool.

Micrographs of cross-sections imaged from uncoated, silica-, and borosilicate glass coated fibers oxidized at 800 °C for 100 h in dry O₂ are shown in Figure 97 A – C, respectively. The oxides formed from oxidation of the uncoated and silica-coated fibers were too thin to measure. The oxidized borosilicate glass coated fibers fused together during oxidation at these same conditions. The fused oxides are ascribed to melting and flowing of the borosilicate glass coating during oxidation occurring with oxide growth. The fused oxides (Figure 97 C) were thicker than oxides formed on the uncoated and silica coated fibers (Figure A and B, respectively), which could have resulted from faster oxide growth due to the presence of the borosilicate glass coating. However, the oxide growth does not support the accelerated oxidation observed in Schlichting’s study on borosilicate glass coated Si coupons⁴¹.

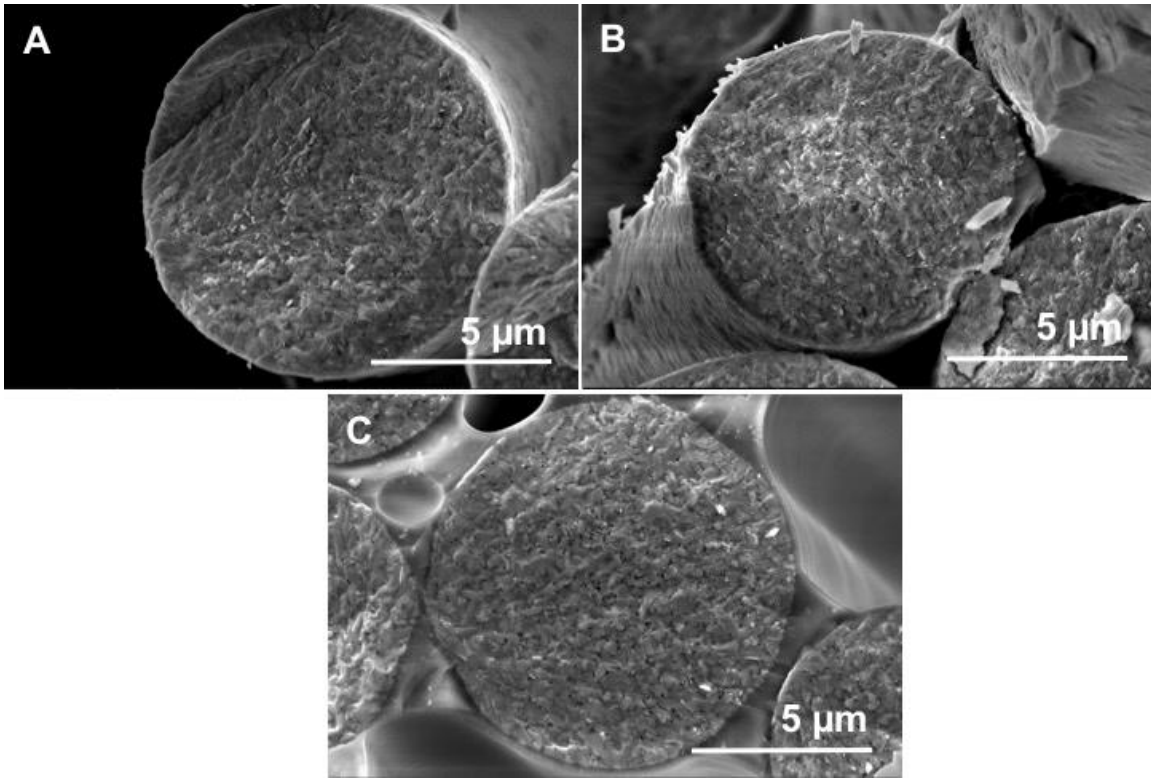


Figure 97: Micrographs of cross-sectioned uncoated and coated Syramic fibers oxidized for 100 h in dry O₂ at 800°C. A) Uncoated fibers, B) silica glass coated fibers (F 3), C) boria-synthesized borosilicate glass coated fibers (F 12). Microstructures were observed by SEM in plan view with secondary electrons.

Micrographs of cross-sections imaged from uncoated, silica-, and borosilicate glass coated fibers oxidized at 1200°C for 100 in dry O₂ are shown in Figure 98 A – C, respectively. All fibers were fused together by the oxides. The oxide thicknesses were measured from the oxide surface to the fiber surface. Oxide thicknesses between fused fibers were not included in the oxide thickness measurements.

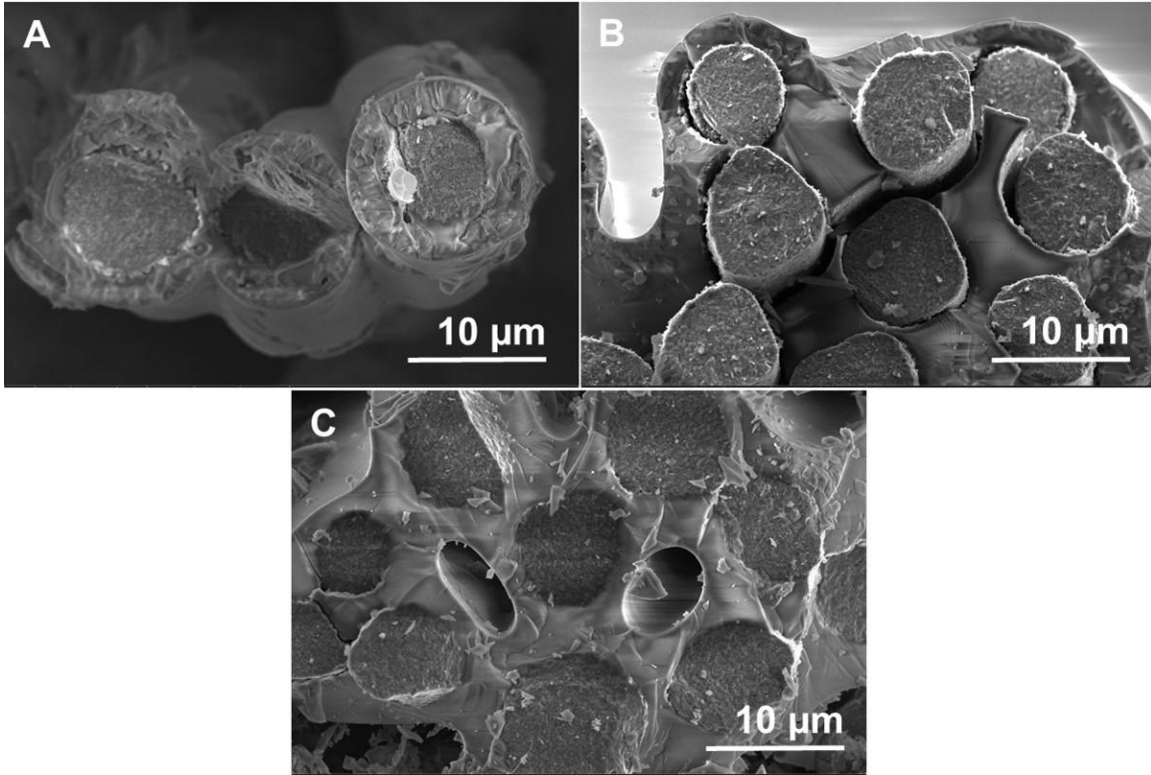


Figure 98: Micrographs of cross-sectioned uncoated and coated Syramic fibers oxidized for 100 h in dry O₂ at 1200°C. A) Uncoated fibers, B) silica glass coated fibers (F 3), C) boria-synthesized borosilicate glass coated fibers (F 12). The oxides fused the fibers together. Microstructures were observed by SEM in plan view with secondary electrons.

The oxide thicknesses were average over two repeat exposures from 47 – 50 measurements. The mean oxide thickness results are reported in Table 29 with their standard error on a 95% confidence interval. The oxide thickness formed from oxidation of the uncoated fibers was the greatest whereas the oxide thickness formed from oxidation of the borosilicate glass coated fibers was the lowest, although only moderately less than the uncoated fibers.

Table 29: Average oxide thicknesses measured from uncoated and glass coated Syramic fibers oxidized at 1200°C for 100 h in dry O₂

Coating formulation	Repeats	Total number of measurements	Oxide thickness (µm)
Bare	2	50	2.9 ± 0.17
Silica glass coating F 3	2	50	2.7 ± 0.31
Boria-synthesized glass coating F 12	2	47	2.3 ± 0.17

8.3.7.3 Borosilicate oxide molecular bonding

The oxides formed from oxidation of the uncoated and borosilicate glass coated Sylramic coupons at 1200°C for 100 h in dry O₂ were investigated for molecular bonding with Raman spectroscopy. The uncoated and coated fibers were analyzed prior to oxidation exposures. The Raman spectra from the analysis of the unoxidized, uncoated and coated fibers are shown in Figure 99 A and B respectively. The major peaks at ~ 790 and ~ 970 cm⁻¹ are attributed to vibrations from SiC⁸⁷. The borosilicate glass coating was identified by the peak at 890 cm⁻¹ shown by the spectrum in Figure 90 B, which is attributed to vibrations from Si-O-B bonds in the glass¹¹⁹. The peaks at ~ 1350 and 1600 cm⁻¹ are attributed to residual free carbon present in the fibers⁸⁷. The peak at 1080 cm⁻¹, present in the uncoated fiber spectrum shown in Figure 98 A, is tentatively ascribed to the B₄C constituent in Sylramic fibers⁸⁷.

The spectra from the oxides analyzed after oxidation at 1200°C are shown in Figure 99 C and D. The peaks from the oxidized, uncoated coupon, shown by the spectrum in Figure 99 C, are identified first. The first two peaks located at 101 and 225 cm⁻¹ are assigned to titanium dioxide, TiO₂, from the oxidation of the fiber TiB₂ constituent. The peaks at 407 and 435 cm⁻¹ are assigned to Si-O-Si, B-O-B, and Si-O-B bonds arising from the thermally grown borosilicate oxide⁶⁶. The peak at 610 cm⁻¹ is tentatively assigned to Si-O-B¹²⁸. The intensities of the SiC peaks assigned at ~790 and ~970 cm⁻¹ were reduced significantly from oxidation of the fiber.

The spectrum from analysis of the oxidized borosilicate glass coated fiber, shown in Figure 99 D, has notable differences from the spectrum acquired from oxidized uncoated coupon, shown in Figure 99 C. The region for Si-O-B, B-O-B, and Si-O-Si was

very broad, ranging from 200 – 600 cm^{-1} , including an overlap with peaks assigned to TiO_2 . The peak tentatively assigned to Si-O-B at $\sim 610 \text{ cm}^{-1}$ present in the thermally grown borosilicate oxide was also present in the glass coated fiber oxide. The intensities of the peaks assigned to SiC at ~ 790 and $\sim 970 \text{ cm}^{-1}$ were also lower. Two new peaks at 840 and 945 cm^{-1} were present. These are both assigned to Si-O-B peaks from the borosilicate glass coating^{66, 119}. These results show that the sol-gel derived borosilicate glass coating altered the molecular bonding of the thermally grown borosilicate oxide.

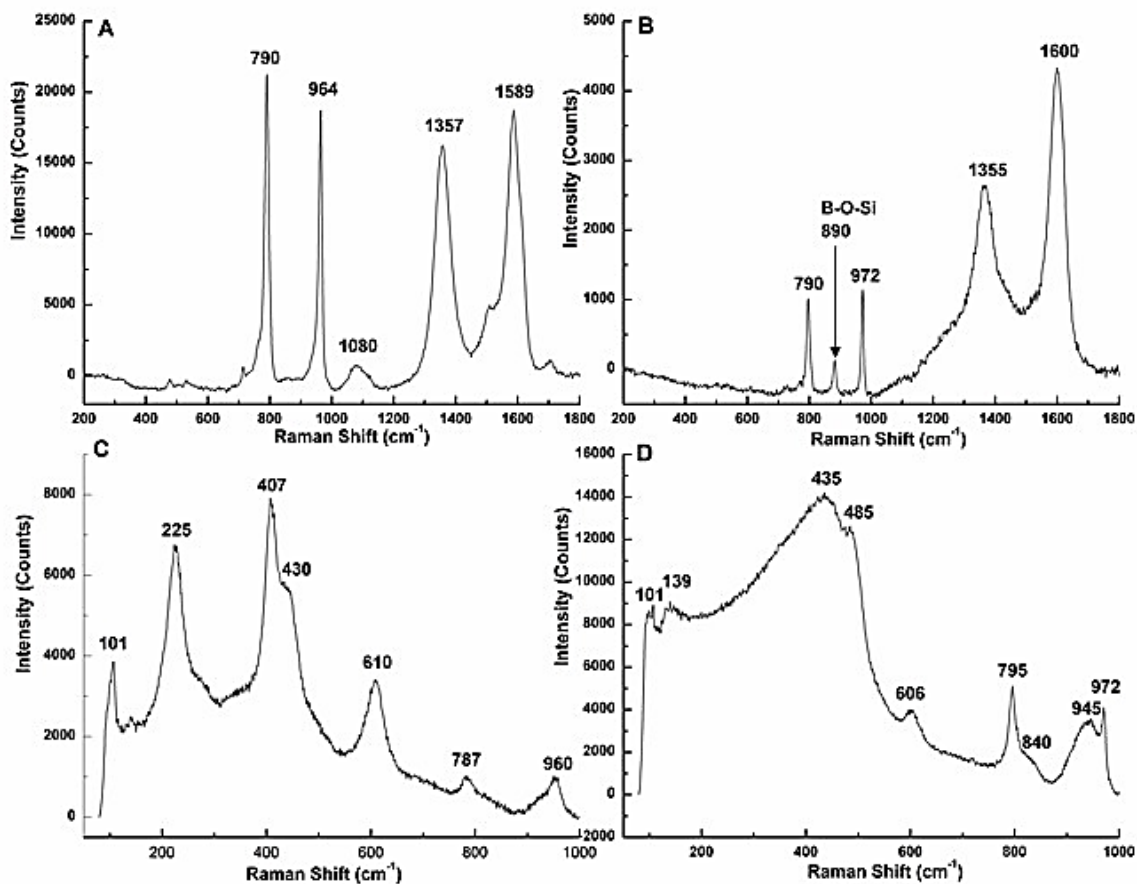


Figure 99: Raman spectra of uncoated and borosilicate glass coated Sylramic fibers (F 12) before and after oxidation at 1200 °C for 100 h in dry O₂. A) uncoated, unoxidized Sylramic SiC fiber, B) unoxidized borosilicate glass coated Sylramic SiC fiber (F 12), C) uncoated, oxidized Sylramic SiC fiber, and D) oxidized borosilicate glass coated Sylramic SiC fiber (F 12).

The peak assignments from the Raman spectra shown are listed in Table 30 for reference.

Table 30: Raman peak assignments

Uncoated and borosilicate glass coated Sylramic SiC fibers (Figure 90 A and B)		
Raman peaks (cm ⁻¹)	Molecular bond assignments	References
790	SiC	87
890	Si-O-B from borosilicate glass coating	119
964, 972	SiC	87
1080	B ₄ C	87
1357, 1355	Free carbon, D peak	87
1589, 1600	Free carbon, G peak	87
Oxides from oxidation of uncoated and borosilicate glass coated Sylramic SiC fibers (Figure 90 C and D)		
Raman peaks (cm ⁻¹)	Molecular bond assignments	References
101	TiO ₂ – anatase	129
139	Unknown	--
225	TiO ₂ - rutile	130
407 - 485	Si-O-Si, Si-O-B, B-O-B	66, 119
606, 610	Tentatively assigned to Si-O-B	128
787, 795	SiC signal from the fiber	87
945	Tentatively assigned to Si-O-B	66
960, 972	SiC signal from the fiber	87

8.3.7.4 Bulk oxide composition

The uncoated, silica-, and borosilicate glass coated Sylramic fibers were digested in HF solutions following oxidation at 800 and 1200°C for 100 h in dry O₂. The glass compositions were determined from ICP-OES analysis of digestions from glass coated fibers that were not oxidized. Analysis of digestions from uncoated fibers that were not oxidized detected some Si, B, and Ti. Their combined concentrations were < 1 wt.% of the total lanyard weight. The amount of species lost to some instability of the fiber to HF solution was considered negligible.

The compositions of digested coated fibers before oxidation and digested oxides after oxidation were determined by ICP-OES, provided in Table 31. The B concentration in the oxides formed after oxidation of the borosilicate glass coated fibers was considerably higher than the B concentrations in the thermally grown borosilicate oxide. This higher B concentration did not result in accelerating the oxidation kinetics of the borosilicate glass coated fibers.

Table 31: ICP-OES results of the bulk B concentration in oxides digested from uncoated and glass coated Sylramic fibers oxidized for 100 h in dry O₂ at 800 and 1200 °C

Formulation	B concentration in sol-gel derived borosilicate glass coating	B concentration in oxide following 100 h TGA exposures (mol%)	
		800°C (2 – 4 repeats)	1200°C (2 repeats)
Uncoated	--	13 ± 5.3	5.7 ± 0.1
Silica glass coating F 3	9.7	5.4 ± 0.3	7.1 ± 1.5
Boria-synthesized glass coating F 12	43	28 ± 2.9	9.5 ± 0.03

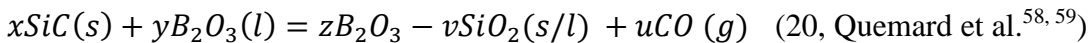
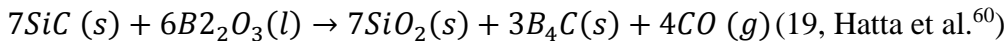
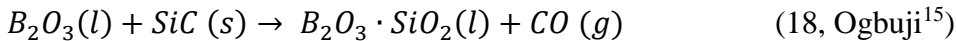
The oxides formed after oxidation of the borosilicate glass coated fibers were different from the thermally grown borosilicate oxides with respect to oxide thickness, composition, and molecular bonding. The thermally grown borosilicate oxide could not be reproduced with sol-gel derived borosilicate glass coatings. The sol-gel derived

borosilicate glass coatings are not found to be good models for thermally grown borosilicate oxides.

8.4 Discussion

8.4.1 Boria fluxing of SiC: a review of chemical reactions

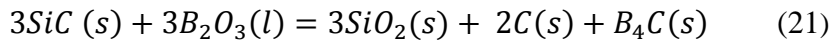
The rapid SiC oxidation observed when CVD-SiC coupons were coated with the boria glass layers is hypothesized to be due to boria fluxing of the SiC, which triggers accelerated SiC oxidation¹³. The boria fluxing results from dissolution of SiC in contact with molten boria^{13, 15, 23, 58-60}. Chemical reactions between boria (B₂O₃) and SiC were proposed by Ogbuji¹⁵, Hatta et al.⁶⁰, and Quemard et al.^{58, 59}. Results from Hatta et al. showed that the reaction between B₂O₃ and SiC took place in Ar as well as in dry O₂⁶⁰. The chemical reactions from literature are reviewed, given by Reactions 18 – 20^{15, 58-60}:



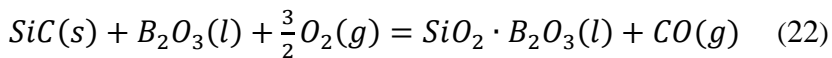
Ogbuji and Hatta et al. proposed the reaction to strongly favor products, whereas Quemard proposed an equilibrium reaction. Hatta et al. predicted the formation of SiO₂ that modifies the B₂O₃ structure leading to faster O₂ diffusion through the oxide, and were in agreement with Fergus and Schlichting^{41, 56, 60}.

Equilibrium reactions were conducted in this study with FactSage¹⁰⁰ to predict what products will form from reactions of 1) SiC + B₂O₃, and 2) SiC + B₂O₃ + O₂ at 800°C in ambient pressure. The FactPS and FToxid databases were used. For the reaction between SiC + B₂O₃, the moles of B₂O₃ had to be reduced to <66% of the moles of SiC in order to maintain equilibrium with SiC. Equilibrium with B₂O₃ could not be

established. All solid products have unit activity. Gas pressures greater than 10^{-6} atm are considered significant. The activity of CO (g) was 1.5×10^{-6} atm, but was not included as a product of the reaction as that yielded a positive Gibb's free energy of reaction. A negative Gibb's free energy of reaction of -13 kJ at 800°C and standard pressure is yielded by Reaction 21:



A borosilicate liquid was additionally predicted to form from the reaction of SiC + B₂O₃ + O₂. The products are strongly favored. Equilibrium with SiC could not be established even when the moles of B₂O₃ were reduced to 1/ 100th the moles of SiC. A negative Gibb's free energy of reaction of -86 kJ at 800°C and standard pressure is yielded by Reaction 22:



The FactSage calculations in this study are in agreement with literature showing that molten B₂O₃ is reactive with SiC, leading to formation of silica and boron carbide (B₄C) in the absence of O₂ and to a borosilicate glass in the presence of O₂. The calculations support the findings in this study that showed the boron coatings to flux the CVD-SiC, resulting in substantial SiC oxidation.

8.4.2 Role of SiO₂ on the B₂O₃ chemical reactivity with SiC

The effects of boron fluxing the CVD-SiC substrate were strongly reduced when the coupon was pre-oxidized prior application with boron glass coatings. These results indicate that additions of SiO₂ to B₂O₃ change the chemical reactivity of B₂O₃ with SiC, suggesting that SiO₂ and SiC are in competition to react with B₂O₃. The pre-oxidized CVD-SiC substrate was not as substantially oxidized in comparison with the CVD-SiC

substrate that was not pre-oxidized prior to application of the boria glass coating. The thermally grown silica limited the fluxing of the B_2O_3 glass coating with the SiC substrate by reacting with the B_2O_3 coating to form a borosilicate glass in the O_2 environment. The borosilicate glass must have a lower reactivity with SiC; otherwise the reduction in the actual oxide growth would not have occurred on those coupons that had been pre-oxidized prior to application of the boria coating. Nevertheless, the SiC parabolic oxidation rate constant, k_p , was 13 – 60 times greater for boria coated CVD-SiC that was pre-oxidized than expected for pure CVD-SiC oxidized under these same conditions. Consequently, the reaction of the boria coating with the thermally grown silica glass modified the silica structure that allowed for more rapid O_2 transport and accelerated the SiC oxidation rate, in accord with Schlichting⁴¹. The following section provides insights from literature on the structural modifications that occur between B_2O_3 and SiO_2 glasses when they react together to form a borosilicate glass. Compositional and temperature effects are considered as they relate to boria fluxing of SiC and to O_2 transport rates through a silica scale.

8.4.3 Structural insights into the fluxing mechanism

Vitreous boria is comprised of 75 % of the B atoms bonded in boroxol ring configurations⁵¹. The remaining B atoms are bonded in planar triangle configurations⁵¹. The boroxol rings decompose into a random network of planar triangles when boria is heated up past its molten state^{49, 50}. A comparison of the vitreous and molten boria structures proposed by Hwang et al.⁴⁸ and Mackenzie⁵⁶ are shown in Figure 100 A and B, respectively. Mackenzie found evidence for B=O bonds to form from the decomposition of BO_3 triangles as the boria temperature was further increased⁵². Mackenzie's analysis

of the molten boria structure was conducted by FTIR on a boria glass quenched from 1000°C. It is hypothesized here that formation of unsaturated B=O bonds in the boria glass coating are highly reactive, which if formed in the boria glass coating during exposures at 800°C in dry O₂ resulted in boria fluxing of SiC. The possible reaction of –B=O + SiC, presumably given by Reaction 21 in the form of B₂O₃ + SiC, has not been confirmed.

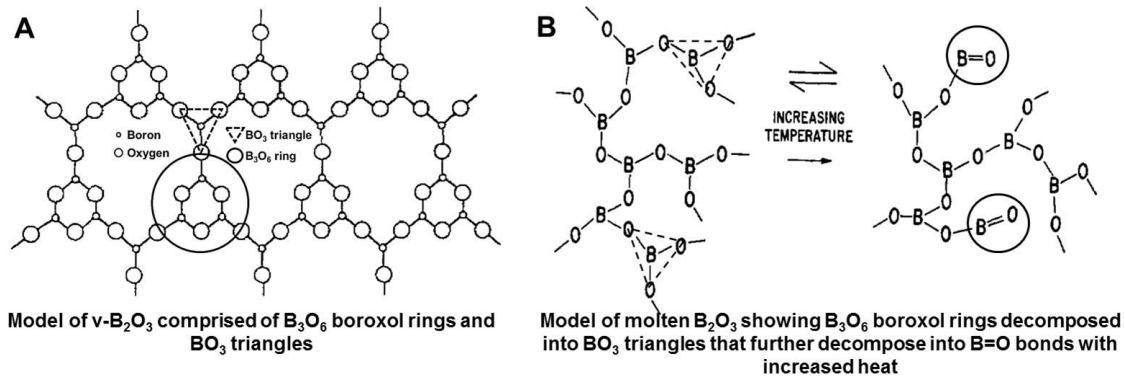


Figure 100: Proposed structures of boria. A) Proposed structure of ν -B₂O₃ by Hwang et al.⁴⁸, and B) Proposed changes in the molten B₂O₃ structure by Mackenzie showing further decomposition of BO₃ triangles into B=O bonds resulting from increased heating of the glass⁵². Figure was annotated from the original to identify B and O atoms, and B=O bonds.

The boria fluxing of SiC was curbed when a thermally grown silica oxide was present in between the boria glass coating and the SiC substrate. In a binary SiO₂-B₂O₃ borosilicate glasses, the Si and B atoms compete to bond with the available oxygen atoms⁵³. The bridging oxygens form Si-O-Si, B-O-B, and Si-O-B structural units⁶⁵. Lee and Stebbins found that intermixing of Si-O-Si (from SiO₂) and B-O-B (from B₂O₃) units result in the increased formation of Si-O-B units with increased boria concentration⁶⁵. Further, Furukawa and White found that the Si-O-B bond formation was favored when B₂O₃-SiO₂ glasses were heated⁶⁶. Furukawa and White ascribed the formation of the Si-O-B bonds to the thermal decomposition of boroxol rings into planar triangles that bonded to Si through bridging oxygens. Both of these conditions by Lee and

Stebbins⁶⁵ and Furukawa and White⁶⁶ that promote bonding between B_2O_3 and SiO_2 were set up in this study when the pre-oxidized CVD-SiC coupons coated with the boria glass layer were exposed to the high temperature oxidation environment. These results from literature provide insight into how the thermally grown silica oxide may have been incorporated into the boria glass structure, which is hypothesized here to have 1) reduced the boria fluxing of SiC by lowering the reactivity of B_2O_3 with SiC; and 2) increased O_2 transport through silica by the disruption of the silica structure via Si-O-B bonds.

8.4.4 Implications of the boria fluxing mechanism on CMC degradation

The components of CMCs – SiC fibers, BN interphase, and SiC matrix – will oxidize at different O_2 pressures under conditions in which the availability of O_2 is limited. A crack in the CMC is a condition that limits the availability of O_2 ¹². The SiC will get the O_2 in low O_2 pressure conditions and oxidize to form SiO_2 while the BN interphase remains intact unless the O_2 pressure in the crack is enough to trigger BN oxidation^{40, 101}. Although higher O_2 pressures are needed to oxidize BN, the BN oxidation kinetics are faster than SiC oxidation kinetics because O_2 diffusion is very rapid in B_2O_3 ⁹⁵. Further, BN oxidizes at temperatures as low as $\sim 450^\circ C$, whereas SiC will oxidize simultaneously with BN at higher temperatures of $\sim 900^\circ C$. Faster BN oxidation at lower temperature exposures results in more rapid B_2O_3 formation by comparison. Importantly, the crack limits the ability of B_2O_3 to volatilize outward. This situation is favorable for the boria fluxing of the adjacent SiC fibers and matrix.

This study showed that the oxidation kinetics of SiC adjacent to B_2O_3 are rapidly accelerated due to B_2O_3 fluxing of SiC at $800^\circ C$ in dry O_2 . The actual oxide growth calculated in this study ranged from 1.1 to 8.6 μm , which is much higher than the 0.3 μm

oxide thickness estimated for pure CVD-SiC oxidized in these same conditions²¹.

Assuming that the boria glass coated CVD-SiC was oxidized by parabolic oxidation kinetics, the rate constants calculated from the actual oxide growth measurements range from $1 \times 10^{-2} \mu\text{m}^2 \text{h}^{-1}$ to $7 \times 10^{-1} \mu\text{m}^2 \text{h}^{-1}$ at 800°C . These rates are faster by 13 – 811 times in comparison with rates expected for pure SiC ($9 \times 10^{-4} \mu\text{m}^2 \text{h}^{-1}$)²¹. A SiC fiber $10 \mu\text{m}$ in diameter adjacent to a B_2O_3 scale formed from oxidation of the BN interphase at 800°C would be fully oxidized within 108 – 6,550 h, assuming oxidation rate constants of $7 \times 10^{-1} \mu\text{m}^2 \text{h}^{-1}$ and $1 \times 10^{-2} \mu\text{m}^2 \text{h}^{-1}$, respectively. These rate constants are expected to increase in proportion with the elevated pressures in the combustion environment, which could be devastating for the lifetime of aircraft engine components made from CMCs. Aircraft engines are expected to be in service for several thousands of hours.

8.4.5 Critique of Schlichting's approach⁴¹

Schlichting's results could not be reproduced in this study because the borosilicate glass coatings, adapted from Schlichting's approach, were less reactive to the SiC substrate surface in comparison with the boria glass coatings. While it was shown here that boria coatings accelerated the CVD-SiC oxidation kinetics by up to 800 times greater than would be observed for pure CVD-SiC, the orders of magnitude increases in the borosilicate glass coated Si coupons reported in Schlichting's study were never observed in this study. It is projected from the results of this study that at a critical thickness (not presently known), the thermally grown silica glass from pre-oxidation the SiC substrate will prevent any boria fluxing of the SiC and significant modification of the silica structure that enhances O_2 transport. The combination of SiC oxidation and boria volatility from the borosilicate glass coating diminishes the ability of borosilicate glass

coatings to accelerate SiC oxidation. In addition, borosilicate glass coatings were prone to dewetting and cracking, especially if applied thickly.

The retained carbon was one of many factors that contributed to the inability of the sol-gel derived borosilicate glass coatings to model thermally grown borosilicate oxides. It was shown that the oxides formed from oxidation of borosilicate glass coated Sylramic fibers differed in composition and molecular bonding from the thermally grown borosilicate glass that formed from oxidation of the uncoated fibers. These results in show that Schlichting's approach of coating SiC substrates with sol-gel derived borosilicate glass coatings cannot be used to observe the effects of boria on SiC oxidation or to model the thermally grown borosilicate glass. However, increasing the boron concentration in the sol-gel derived glass coatings to levels exceedingly higher than reported in Schlichting's study did show evidence of excessive SiC oxidation in the presence of boria. It was shown here that boria glass coatings accelerated the CVD-SiC oxidation kinetics by up to 800 times greater than would be observed for pure CVD-SiC, but the orders of magnitude increases in the borosilicate glass coated Si coupons reported in Schlichting's study were never observed in this study. Importantly, however, the sol-gel method to synthesize glass coatings of well-defined boron concentration allowed for investigations of the interactions between B_2O_3 and SiC and B_2O_3 with thermally grown SiO_2 that could not be investigated with thermally grown borosilicate glasses.

8.5 *Conclusions*

The CVD-SiC oxidation kinetics were accelerated by a boria fluxing mechanism from application of a concentrated boria glass coatings. The presence of a thermally grown silica formed from pre-oxidation of the CVD-SiC coupon prior to application of

boria glass coatings substantially curbed the oxide growth. The chemical reactivity of the boria glass coating with the SiC substrate was reduced by reaction of the thermally grown silica with the boria coating to form a borosilicate glass. The boria effects on accelerating the oxidation kinetics of SiC materials not protected with a thermally grown silica can be devastating for CMC's under conditions in which the BN interphase has oxidized much faster than adjacent SiC fibers or matrix. The results from Schlichting's study were not replicated here due to a combination of 1) a borosilicate glass coating with negligible reactivity to SiC in comparison with boria glass coatings, and 2) boria volatility from the glass coating surface that occurred during high temperature oxidation exposures in combination with SiC oxidation that together enrich the SiO₂ concentration in the oxide. Oxides formed from the oxidation of borosilicate glass coated Sylramic fibers differed from the thermally grown borosilicate oxides formed on uncoated Sylramic fibers in many ways, including thickness, composition, and molecular bonding. The sol-gel derived borosilicate glass coatings are not good models for thermally grown borosilicate oxides.

8.6 *Recommendations for future work*

The boria fluxing mechanism has not been confirmed. TGA exposure of the boria coated CVD-SiC to high temperature inert environments such as Argon is one idea to isolate the chemical reactivity of boria with SiC. Characterization of the boria coated CVD-SiC coupon after Argon exposures with SEM/ EDS, XRD, Raman spectroscopy, and ICP-OES will help elucidate the products formed from the chemical reaction of boria and SiC. Oxidation of boria glass coated CVD-SiC coupons at 1200°C is recommended to understand the effects of the boria fluxing of SiC at temperatures in which both boria

vaporization and SiC oxidation kinetics are encouraged. These high temperatures, however, will also significantly reduce the viscosity of the melted boria coating, and will have to be carefully conducted. Raman spectroscopic investigations of the molecular bonding in oxides formed from the oxidation of boria coated CVD-SiC coupons that were pre-oxidized prior to coating application is also recommended to better understand the interactions of the thermally grown silica oxide with the boria coating that reduces reactivity of boria with SiC. Studies should also be conducted to determine the thickness of the thermally grown oxide needed to shut down the ability of boria to flux the SiC substrate.

9 Summation of research project findings

The goal of this research project was to determine how boria accelerated the oxidation of SiC. The findings from this study are directly applicable to understanding the mechanisms and oxidation conditions that will lead to CMC degradation. Three objectives were set forth to advance the current state of knowledge on how the SiC oxidation is increased by the presence of boria.

The first objective sought to determine the boron concentration in the thermally grown borosilicate glass that leads to SiC degradation. Thermally grown oxide compositions were determined from a systematic oxidation study in dry O₂, in which temperature and time were varied. Although the oxide compositions yielded as much as 35 mol% boron, accelerated SiC oxidation kinetics were only observed in a transient period of rapid weight gain that did not lead to excessive SiC oxidation. A sol-gel method was utilized to synthesize borosilicate glass coatings with well-defined boron concentrations. The boron concentrations in the glass coatings could be varied and were synthesized at higher concentrations of boron than could be obtained from thermally grown borosilicate glasses. The oxidation of CVD-SiC coupons coated with sol-gel derived boria glass layers containing boron concentrations > 95 mol% provided evidence for the boria fluxing of SiC leading to rapid SiC oxidation. Further, they were amenable for studying the interactions between boria and silica that would not be feasible with the thermally grown oxides. Although the sol-gel derived borosilicate glass coatings were too different in composition and bonding to act as good models for thermally grown oxides, they did help further the understanding of the relationship between oxygen transport rates and borosilicate glass structure.

The second objective sought to determine the oxidation conditions: time, temperature, and gas environment that result in excessive borosilicate glass formation. This study showed that excessive borosilicate glass formation occurs at short times (< 100 h) and at low temperatures (800 – 900°C) in dry O₂. The excessive borosilicate glass formation from oxidized reaction-bonded silicon carbide coupons was increased by elevated O₂ pressure, where it manifested as subsurface oxidation in the presence of relatively low concentrations of boron. Weight gain and oxide growth on SiC fibers were increased with temperature and time due to the presence of a boron nitride layer, but excessive borosilicate glass formation was not observed due to rapid boria volatilization occurring at either longer times or higher exposure temperatures.

The third objective was to determine the mechanisms that cause excessive SiC oxidation. These mechanisms are twofold. The first is the change in the oxygen transport rates in silica by the chemical alteration of the silica glass structure with the incorporation of boron. The second is the high reactivity of boria with SiC which produces silica from the excessive formation of borosilicate glass. The findings in this research project showed that rapid SiC oxidation was triggered by boron coating concentrations > 95 mol%, hypothetically due to a boria fluxing mechanism. The boria fluxing mechanism was active on unoxidized SiC surfaces adjacent to nearly 100% sol-gel derived boria compositions. The ability of boria to flux SiC was reduced by the presence of a thermally grown oxide that itself is reactive with boria and acted a barrier to hinder the reaction of boria with the SiC substrate.

The implications of these findings on CMCs can be beneficial or devastating as follows. A protective oxide is produced when boron nitride and silicon carbide are

oxidized on an exterior portion of the CMC. The transient period of accelerated SiC oxidation kinetics induced by oxidation of the boron nitride interphase will rapidly seal the CMC exterior, followed by rapid boria volatilization that enriches the oxide surface with silica, which significantly slows O₂ transport through the oxide. In contrast, oxidation of the CMC interior via a surface accessing crack provides access for sufficient O₂ pressures to oxidize the boron nitride interphase, which rapidly produces boria. The boria volatility is significantly more restricted in the CMC interior than it is at the CMC exterior. The potential for the boria glass to flux adjacent SiC fibers and matrix is increased, which can lead to rapid SiC oxidation, excessive borosilicate glass formation, and CMC degradation.

References

- ¹ F.W. Zok, "Ceramic-matrix composites enable revolutionary gains in turbine engine efficiency," *Am. Ceram. Soc. Bull.*, 95 [5] (2016).
- ² N.P. Padture, "Advanced structural ceramics in aerospace propulsion," *Nat. Mater.*, 15 [8] 804–809 (2016).
- ³ E.J. Opila, R.C. Robinson, and M.J. Verrilli, "Borosilicate Glass-Induced Fiber Degradation of SiC/BN/SiC Composites Exposed in Combustion Environments," *Int. J. Appl. Ceram. Technol.*, 13 [3] 434–442 (2016).
- ⁴ R. Naslain, A. Guette, F. Rebillat, R. Pailler, F. Langlais, and X. Bourrat, "Boron-bearing species in ceramic matrix composites for long-term aerospace applications," *Boron Borides Relat. Compd. Proc. 14th International Symp. Boron Borides Relat. Compd.*, 177 [2] 449–456 (2004).
- ⁵ J.A. DiCarlo, H.-M. Yun, G.N. Morscher, and R.T. Bhatt, "SiC/SiC Composites for 1200°C and Above;" pp. 77–98 in *Handb. Ceram. Compos.* Edited by N.P. Bansal. Springer US, Boston, MA, 2005.
- ⁶ K.N. Lee, D.S. Fox, and N.P. Bansal, "Rare earth silicate environmental barrier coatings for SiC/SiC composites and Si₃N₄ ceramics," *Corros. Ceram. Matrix Compos.*, 25 [10] 1705–1715 (2005).
- ⁷ E.J. Opila and Q.N. Nguyen, "Oxidation of Chemically-Vapor-Deposited Silicon Carbide in Carbon Dioxide," *J. Am. Ceram. Soc.*, 81 [7] 1949–1952 (1998).
- ⁸ L.U.J.T. Ogbuji, "A Pervasive Mode of Oxidative Degradation in a SiC-SiC Composite," *J. Am. Ceram. Soc.*, 81 [11] 2777–2784 (1998).
- ⁹ E.J. Opila, "Oxidation and Volatilization of Silica Formers in Water Vapor," *J. Am. Ceram. Soc.*, 86 [8] 1238–1248 (2003).
- ¹⁰ X. Hou, Z. Yu, Z. Chen, K.-C. Chou, and B. Zhao, "The Reaction Mechanism and Kinetics of α -BN Powder in Wet Air at 1273 K," *J. Am. Ceram. Soc.*, 96 [6] 1877–1882 (2013).
- ¹¹ N. Jacobson, S. Farmer, A. Moore, and H. Sayir, "High-Temperature Oxidation of Boron Nitride: I, Monolithic Boron Nitride," *J. Am. Ceram. Soc.*, 82 [2] 393–398 (1999).
- ¹² B.W. Sheldon, E.Y. Sun, S.R. Nutt, and J.J. Brennan, "Oxidation of BN-Coated SiC Fibers in Ceramic Matrix Composites," *J. Am. Ceram. Soc.*, 79 [2] 539–543 (1996).
- ¹³ Elizabeth Opila and M. Boyd, "Oxidation of SiC Fiber-Reinforced SiC Matrix Composites With a BN Interphase;" pp. 342–347 in *Mater. Sci. Forum.* 2011.
- ¹⁴ N.S. Jacobson, G.N. Morscher, D.R. Bryant, and R.E. Tressler, "High-Temperature Oxidation of Boron Nitride: II, Boron Nitride Layers in Composites," *J. Am. Ceram. Soc.*, 82 [6] 1473–1482 (1999).
- ¹⁵ L.U.J.T. Ogbuji, "A Pervasive Mode of Oxidative Degradation in a SiC-SiC Composite," *J. Am. Ceram. Soc.*, 81 [11] 2777–2784 (1998).
- ¹⁶ K. Nickel, E. Butchereit, and C. Schumacher, "On The Role of Boron in the oxidation of Si-C-N-B ceramics;" p. 365 in *The Electrochemical Society*, 2000.
- ¹⁷ L.U.J.T. Ogbuji and E.J. Opila, "A Comparison of the Oxidation Kinetics of SiC and Si₃N₄," *J. Electrochem. Soc.*, 142 [3] 925–930 (1995).

- 18 K.L. More, K.S. Ailey, R.A. Lowden, and H.T. Lin, "Evaluating the effect of oxygen content in BN interfacial coatings on the stability of SiC/BN/SiC composites," *Compos. Part Appl. Sci. Manuf.*, 30 [4] 463–470 (1999).
- 19 L. Ogbuji, "Oxidative pest degradation of Hi-Nicalon/BN/SiC composite as a function of temperature and time in the burner rig;" p. 105 in John Wiley & Sons, 2009.
- 20 G.N. Morscher and J.D. Cawley, "Intermediate temperature strength degradation in SiC/SiC composites," *J. Eur. Ceram. Soc.*, 22 [14–15] 2777–2787 (2002).
- 21 C.E. Ramberg, G. Cruciani, K.E. Spear, R.E. Tressler, and C.F. Ramberg, "Passive-Oxidation Kinetics of High-Purity Silicon Carbide from 800° to 1100°C," *J. Am. Ceram. Soc.*, 79 [11] 2897–2911 (1996).
- 22 B.E. Deal and A.S. Grove, "General Relationship for the Thermal Oxidation of Silicon," *J. Appl. Phys.*, 36 [12] 3770–3778 (1965).
- 23 F. Rebillat, E. Garltte, and A. Guette, "Quantification of High SiC Fiber Oxidation Rates In The Presence of B₂O₃ Under Air," *Des. Dev. Appl. Eng. Ceram. Compos. Ceram. Trans.*, 215 135 (2010).
- 24 J.A. Costello and R.E. Tressler, "Oxidation Kinetics of Silicon Carbide Crystals and Ceramics: I, In Dry Oxygen," *J. Am. Ceram. Soc.*, 69 [9] 674–681 (1986).
- 25 F.J. Norton, "Permeation of Gaseous Oxygen through Vitreous Silica," *Nature*, 191 [4789] 701–701 (1961).
- 26 L.N. Lie, R.R. Razouk, and B.E. Deal, "High Pressure Oxidation of Silicon in Dry Oxygen," *J. Electrochem. Soc.*, 129 [12] 2828–2834 (1982).
- 27 E.J. Opila and R.E. Hann, "Paralinear Oxidation of CVD SiC in Water Vapor," *J. Am. Ceram. Soc.*, 80 [1] 197–205 (1997).
- 28 V.A. Lavrenko and A.F. Alexeev, "High-temperature oxidation of boron nitride," *Ceram. Int.*, 12 [1] 25–31 (1986).
- 29 O. Flores, R.K. Bordia, D. Nestler, W. Krenkel, and G. Motz, "Ceramic Fibers Based on SiC and SiCN Systems: Current Research, Development, and Commercial Status," *Adv. Eng. Mater.*, 16 [6] 621–636 (2014).
- 30 M. Wilson and E. Opila, "A Review of SiC Fiber Oxidation with a New Study of Hi-Nicalon SiC Fiber Oxidation," *Adv. Eng. Mater.*, n/a-n/a (2016).
- 31 J. Yuan, M. Galetz, X.G. Luan, C. Fasel, R. Riedel, and E. Ionescu, "High-temperature oxidation behavior of polymer-derived SiHfBCN ceramic nanocomposites," *Eng. Ceram. 2015 Materials Better Life Engineering Ceram. 2015 Mater. Better Life*, 36 [12] 3021–3028 (2016).
- 32 N.S. Jacobson, E.J. Opila, and K.N. Lee, "Oxidation and corrosion of ceramics and ceramic matrix composites," *Curr. Opin. Solid State Mater. Sci.*, 5 [4] 301–309 (2001).
- 33 K.G. Nickel, "Corrosion: No Problem for Precursor-Derived Covalent Ceramics?" pp. 188–196 in *Precursor-Deriv. Ceram.* Wiley-VCH Verlag GmbH, 1999.
- 34 J. Lipowitz, J.A. Rabe, A. Zangvil, and Y. Xu, "Structure and Properties of Sylramic™ Silicon Carbide Fiber—A Polycrystalline, Stoichiometric β-SiC Composition;" pp. 147–157 in *Proc. 21st Annu. Conf. Compos. Adv. Ceram. Mater. Struct. Ceram. Eng. Sci. Proc.* John Wiley & Sons, Inc., 1997.
- 35 J.A. Costello and R.E. Tressler, "Oxidation Kinetics of Hot-Pressed and Sintered α-SiC," *J. Am. Ceram. Soc.*, 64 [6] 327–331 (1981).

- 36 R. Naslain, J. Lamon, R. Pailler, X. Bourrat, A. Guette, and F. Langlais, "Micro/minicomposites: a useful approach to the design and development of non-oxide CMCs," *Compos. Part Appl. Sci. Manuf.*, 30 [4] 537–547 (1999).
- 37 R. Naslain, A. Guette, F. Rebillat, S. Le Gallet, F. Lamouroux, L. Filipuzzi, and C. Louchet, "Oxidation mechanisms and kinetics of SiC-matrix composites and their constituents," *J. Mater. Sci.*, 39 [24] 7303–7316 (2004).
- 38 S. Baskaran and J.W. Halloran, "Fibrous Monolithic Ceramics: III, Mechanical Properties and Oxidation Behavior of the Silicon Carbide/Boron Nitride System," *J. Am. Ceram. Soc.*, 77 [5] 1249–1255 (1994).
- 39 T. Narushima, T. Goto, M. Maruyama, H. Arashi, and Y. Iguchi, "Oxidation of boron carbide-silicon carbide composite at 1073 to 1773 K," *Mater. Trans.*, 44 [3] 401–406 (2003).
- 40 N.S. Jacobson, G.N. Morscher, D.R. Bryant, and R.E. Tressler, "High-Temperature Oxidation of Boron Nitride: II, Boron Nitride Layers in Composites," *J. Am. Ceram. Soc.*, 82 [6] 1473–1482 (1999).
- 41 J. Schlichting, "Oxygen transport through glass layers formed by a gel process," *J. Non-Cryst. Solids*, 63 [1–2] 173–181 (1984).
- 42 V.R. Bruckner and J.F. Navarro, "Physikalisch-chemisch Untersuchungen im System B_2O_3 - SiO_2 ," *Glastech. Berichte*, 39 [6] 283–293 (1966).
- 43 C. Büchner, L. Lichtenstein, M. Heyde, and H.-J. Freund, "The Atomic Structure of Two-Dimensional Silica," pp. 327–353 in *Noncontact At. Force Microsc.* Springer, 2015.
- 44 L. Lichtenstein, M. Heyde, and H.-J. Freund, "Atomic Arrangement in Two-Dimensional Silica: From Crystalline to Vitreous Structures," *J. Phys. Chem. C*, 116 [38] 20426–20432 (2012).
- 45 V. Presser, A. Loges, Y. Hemberger, and K.G. Nickel, "Microstructural Evolution of Silica on Single-Crystal Silicon Carbide. Part I: Devitrification and Oxidation Rates," *J. Am. Ceram. Soc.*, 92 [3] 724–731 (2009).
- 46 T.J. Rockett and W.R. Foster, "Phase Relations in the System Boron Oxide–Silica," *J. Am. Ceram. Soc.*, 48 [2] 75–80 (1965).
- 47 A.C. Hannon, D.I. Grimley, R.A. Hulme, A.C. Wright, and R.N. Sinclair, "Boroxol groups in vitreous boron oxide: new evidence from neutron diffraction and inelastic neutron scattering studies," *First PAC RIM Meet. Glass Opt. Mater.*, 177 299–316 (1994).
- 48 S.-J. Hwang, C. Fernandez, J.P. Amoureux, J. Cho, S.W. Martin, and M. Pruski, "Quantitative study of the short range order in B_2O_3 and B_2S_3 by MAS and two-dimensional triple-quantum MAS ^{11}B NMR," *Solid State Nucl. Magn. Reson.*, 8 [2] 109–121 (1997).
- 49 J. Krogh-Moe, "The structure of vitreous and liquid boron oxide," *J. Non-Cryst. Solids*, 1 [4] 269–284 (1969).
- 50 G.E. Walrafen, S.R. Samanta, and P.N. Krishnan, "Raman investigation of vitreous and molten boric oxide," *J. Chem. Phys.*, 72 [1] 113–120 (1980).
- 51 G. Ferlat, T. Charpentier, A.P. Seitsonen, A. Takada, M. Lazzeri, L. Cormier, G. Calas, and F. Mauri, "Boroxol Rings in Liquid and Vitreous B_2O_3 from First Principles," *Phys. Rev. Lett.*, 101 [6] 065504 (2008).

- 52 J. Mackenzie, "Structure of liquid boron trioxide," *J. Phys. Chem.*, 63 [11] 1875–1878 (1959).
- 53 E.F. Riebling, "Structure of Borosilicate and Borogermanate Melts at 1300°C; a Viscosity and Density Study," *J. Am. Ceram. Soc.*, 47 [10] 478–483 (1964).
- 54 A.K. Hassan, L.M. Torell, L. Börjesson, and H. Doweidar, "Structural changes of B₂O₃ through the liquid-glass transition range: A Raman-scattering study," *Phys. Rev. B*, 45 [22] 12797–12805 (1992).
- 55 M.F. Yan, J.B. Macchesney, S.R. Nagel, and W.W. Rhodes, "Sintering of optical wave-guide glasses," *J. Mater. Sci.*, 15 [6] 1371–1378 (1980).
- 56 J.W. Fergus and W.L. Worrell, "Silicon-carbide/boron-containing coatings for the oxidation protection of graphite," *Oxid. Prot. Carbon Compos.*, 33 [4] 537–543 (1995).
- 57 T. Piquero, H. Vincent, C. Vincent, and J. Bouix, "Influence of carbide coatings on the oxidation behavior of carbon fibers," *Oxid. Prot. Carbon Compos.*, 33 [4] 455–467 (1995).
- 58 L. Quemard, F. Rebillat, A. Guette, H. Tawil, and C. Louchet-Pouillier, "Self-healing mechanisms of a SiC fiber reinforced multi-layered ceramic matrix composite in high pressure steam environments," *J. Eur. Ceram. Soc.*, 27 [4] 2085–2094 (2007).
- 59 L. Quemard, F. Rebillat, A. Guette, H. Tawil, and C. Louchet-Pouillier, "Degradation mechanisms of a SiC fiber reinforced self-sealing matrix composite in simulated combustor environments," *J. Eur. Ceram. Soc.*, 27 [1] 377–388 (2007).
- 60 H. Hatta, T. Sohtome, Y. Sawada, and A. Shida, "High temperature crack sealant based on SiO₂-B₂O₃ for SiC coating on carbon-carbon composites," *Adv. Compos. Mater.*, 12 [2–3] 93–106 (2003).
- 61 J. Shelby and R. Wayne, "Gas migration in vitreous B₂O₃," *J. Appl. Phys.*, 45 [6] (1974).
- 62 R.H. Doremus, "Transport of oxygen in silicate glasses," *Glass Sci. High Technol. 16th Univ. Conf. Glass Sci.*, 349 242–247 (2004).
- 63 R.B. Brown and R.H. Doremus, "Growth and Dissolution of Gas Bubbles in Molten Boric Oxide," *J. Am. Ceram. Soc.*, 59 [11–12] 510–514 (1976).
- 64 R.J. Bell, A. Carnevale, C.R. Kurkjian, and G.E. Peterson, "Structure and Phonon Spectra of SiO₂, B₂O₃, and Mixed SiO₂-B₂O₃ Glasses," *J. Non-Cryst. Solids*, 35&36 1185–1190 (1980).
- 65 S.K. Lee and J.F. Stebbins, "Extent of intermixing among framework units in silicate glasses and melts," *Geochim. Cosmochim. Acta*, 66 [2] 303–309 (2002).
- 66 T. Furukawa and W. White, "Raman Spectroscopy of Heat-Treated B₂O₃-SiO₂ Glasses," *J. Am. Ceram. Soc.*, 64 [8] 443–447 (2006).
- 67 G.N. Morscher, D.R. Bryant, and R.E. Tressler, "Environmental Durability of BN-Based Interphases (for SiCf/SiCm Composites) in H₂O Containing Atmospheres at Intermediate Temperatures," pp. 525–534 in *Proc. 21st Annu. Conf. Compos. Adv. Ceram. Mater. Struct. Ceram. Eng. Sci. Proc.* John Wiley & Sons, Inc., 1997.
- 68 S. Grandi, C. Tomasi, V. Cassinelli, L. Cucca, A. Profumo, P. Mustarelli, and C. Balduini, "SiO₂-B₂O₃ xerogels: The problem of boron leaching," *J. Non-Cryst. Solids*, 358 [14] 1631–1637 (2012).

- 69 M. Nogami and Y. Moriya, "Glass formation Of The SiO₂-B₂O₃ System By The Gel Process From Metal Oxides," *J. Non-Cryst. Solids*, 48 359–366 (1982).
- 70 G.D. Sorarù, N. Dallabona, C. Gervais, and F. Babonneau, "Organically Modified SiO₂-B₂O₃ Gels Displaying a High Content of Borosiloxane (B-O-Si) Bonds," *Chem. Mater.*, 11 [4] 910–919 (1999).
- 71 David Haaland and J. Brinker, "In Situ FT-IR Studies of Oxide and Oxynitride Sol-Gel Derived Thin Films," *MRS Proc.*, 32 (1984).
- 72 A.D. Irwin, J.S. Holmgren, and J. Jonas, "Solid state ²⁹Si and ¹¹B NMR studies of sol-gel derived borosilicates," *J. Non-Cryst. Solids*, 101 [2–3] 249–254 (1988).
- 73 M.A. Villegas and J.M.F. Navarro, "Characterization of B₂O₃-SiO₂ glasses prepared via sol-gel," *J. Mater. Sci.*, 23 [7] 2464–2478 (1988).
- 74 C.J. Brinker and G.W. Scherer, *Sol-Gel Science: The Physics and Chemistry of Sol-Gel processing*. Academic Press, Inc., San Diego, CA, 1990.
- 75 R. Peña-Alonso, G. Mariotto, C. Gervais, F. Babonneau, and G.D. Soraru, "New Insights on the High-Temperature Nanostructure Evolution of SiOC and B-Doped SiBOC Polymer-Derived Glasses," *Chem. Mater.*, 19 [23] 5694–5702 (2007).
- 76 C. Gervais, F. Babonneau, N. Dallabonna, and G. Sorarù, "Sol-Gel-Derived Silicon-Boron Oxycarbide Glasses Containing Mixed Silicon Oxycarbide (SiC_xO_{4-x}) and Boron Oxycarbide (BC_yO_{3-y}) Units," *J. Am. Ceram. Soc.*, 84 [10] 2160–2164 (2001).
- 77 S. Modena, G.D. Sorarù, Y. Blum, and R. Raj, "Passive Oxidation of an Effluent System: The Case of Polymer-Derived SiCO," *J. Am. Ceram. Soc.*, 88 [2] 339–345 (2005).
- 78 C.J. Brinker and S.P. Mukherjee, "Conversion of monolithic gels to glasses in a multicomponent silicate glass system," *J. Mater. Sci.*, 16 [7] 1980–1988 (1981).
- 79 C.J.R. Gonzalez-Oliver, P.F. James, and H. Rawson, "Silica and silica-titania glasses prepared by the sol-gel process," *J. Non-Cryst. Solids*, 48 [1] 129–152 (1982).
- 80 T. Liang, Y.-L. Li, D. Su, and H.-B. Du, "Silicon oxycarbide ceramics with reduced carbon by pyrolysis of polysiloxanes in water vapor," *J. Eur. Ceram. Soc.*, 30 [12] 2677–2682 (2010).
- 81 M. Narisawa, T. Kawai, S. Watase, K. Matsukawa, and A. Iwase, "Investigation of photoluminescence of Si-O-C(-H) ceramics at an early stage of decarbonization by using high energy excitation," *AIP Adv.*, 4 [1] (2014).
- 82 M. Narisawa, K. Terauds, R. Raj, Y. Kawamoto, T. Matsui, and A. Iwase, "Oxidation process of white Si-O-C(-H) ceramics with various hydrogen contents," *Scr. Mater.*, 69 [8] 602–605 (2013).
- 83 A.H. Tavakoli, M.M. Armentrout, M. Narisawa, S. Sen, and A. Navrotsky, "White Si-O-C Ceramic: Structure and Thermodynamic Stability," *J. Am. Ceram. Soc.*, 98 [1] 242–246 (2015).
- 84 A.C. Ferrari and J. Robertson, "Interpretation of Raman spectra of disordered and amorphous carbon," *Phys Rev B*, 61 [20] 14095–14107 (2000).
- 85 P. Kroll, "Searching insight into the atomistic structure of SiCO ceramics," *J. Mater. Chem.*, 20 [46] 10528–10534 (2010).
- 86 C.G. Pantano, A.K. Singh, and H. Zhang, "Silicon Oxycarbide Glasses," *J. Sol-Gel Sci. Technol.*, 14 [1] 7–25 (1999).

- 87 S.M. Dong, G. Chollon, C. Labrugère, M. Lahaye, A. Guette, J.L. Bruneel, M. Couzi, R. Naslain, *et al.*, “Characterization of nearly stoichiometric SiC ceramic fibres,” *J. Mater. Sci.*, 36 [10] 2371–2381 (2001).
- 88 J.A. DiCarlo and H.M. Yun, *Methods for producing high-performance silicon carbide fibers, architectural preforms, and high-temperature composite structures*; 2014.
- 89 J.A. DiCarlo and H. Yun, *Methods for producing silicon carbide architectural preforms*; 2010.
- 90 K.S. Varma, *Sol-gel synthesis of alkali-free borosilicate glass*; 1998.
- 91 V.K. Parashar, J.-B. Orhan, A. Sayah, M. Cantoni, and M.A.M. Gijs, “Borosilicate nanoparticles prepared by exothermic phase separation,” *Nat Nano*, 3 [10] 589–594 (2008).
- 92 D.M. Knotter, “Etching Mechanism of Vitreous Silicon Dioxide in HF-Based Solutions,” *J. Am. Chem. Soc.*, 122 [18] 4345–4351 (2000).
- 93 W. Kern and R. Heim, “Chemical Vapor Deposition of Silicate Glasses for Use with Silicon Devices: II. Film Properties,” *J. Electrochem. Soc.*, 117 [4] 568–573 (1970).
- 94 G.A.C.M. Spierings, “Wet chemical etching of silicate glasses in hydrofluoric acid based solutions,” *J. Mater. Sci.*, 28 [23] 6261–6273 (1993).
- 95 N. Jacobson, S. Farmer, A. Moore, and H. Sayir, “High-Temperature Oxidation of Boron Nitride: I, Monolithic Boron Nitride,” *J. Am. Ceram. Soc.*, 82 [2] 393–398 (1999).
- 96 T. Matsuda, “Stability to moisture for chemically vapour-deposited boron nitride,” *J. Mater. Sci.*, 24 [7] 2353–2357 (1989).
- 97 T.A. Anutgan, M. Anutgan, I. Atilgan, and B. Katircioglu, “Stability and degradation of plasma deposited boron nitride thin films in ambient atmosphere,” *Thin Solid Films*, 518 [1] 419–425 (2009).
- 98 R.S. Hay, G.E. Fair, R. Bouffieux, E. Urban, J. Morrow, A. Hart, and M. Wilson, “Hi-Nicalon™-SSiC Fiber Oxidation and Scale Crystallization Kinetics,” *J. Am. Ceram. Soc.*, 94 [11] 3983–3991 (2011).
- 99 Y.-H. Koh, S.-Y. Lee, and H.-E. Kim, “Oxidation Behavior of Titanium Boride at Elevated Temperatures,” *J. Am. Ceram. Soc.*, 84 [1] 239–241 (2001).
- 100 C.W. Bale, E. Bélisle, P. Chartrand, S.A. Deckerov, G. Eriksson, A.E. Gheribi, K. Hack, I.-H. Jung, *et al.*, “FactSage thermochemical software and databases, 2010–2016,” *Calphad*, 54 35–53 (2016).
- 101 D.L. Poerschke, M.N. Rossol, and F.W. Zok, “Intermediate Temperature Internal Oxidation of a SiC/SiCN Composite with a Polymer-Derived Matrix,” *J. Am. Ceram. Soc.*, 99 [9] 3120–3128 (2016).
- 102 H.-W. Kim, H.-E. Kim, H. Song, and J. Ha, “Effect of Oxidation on the Room-Temperature Flexural Strength of Reaction-Bonded Silicon Carbides,” *J. Am. Ceram. Soc.*, 82 [6] 1601–1604 (1999).
- 103 R.J. Charles and F.E. Wagstaff, “Metastable Immiscibility in the B₂O₃–SiO₂ System,” *J. Am. Ceram. Soc.*, 51 [1] 16–20 (1968).
- 104 D. Luo and Z. Shen, “Wetting and spreading behavior of borosilicate glass on Kovar,” *J. Alloys Compd.*, 477 [1–2] 407–413 (2009).
- 105 V. Presser, A. Loges, R. Wirth, and K.G. Nickel, “Microstructural Evolution of Silica on Single Crystal Silicon Carbide. Part II: Influence of Impurities and Defects,” *J. Am. Ceram. Soc.*, 92 [8] 1796–1805 (2009).

- ¹⁰⁶ E. Opila, "Influence of Alumina Reaction Tube Impurities on the Oxidation of Chemically-Vapor-Deposited Silicon Carbide," *J. Am. Ceram. Soc.*, 78 [4] 1107–1110 (1995).
- ¹⁰⁷ T.A. Ramanarayanan, M. Raghavan, and R. Petkovic-Luton, "The Characteristics of Alumina Scales Formed on Fe-Based Ytria-Dispersed Alloys," *J. Electrochem. Soc.*, 131 [4] 923–931 (1984).
- ¹⁰⁸ L.U. Ogbuji and M. Singh, "High-temperature oxidation behavior of reaction-formed silicon carbide ceramics," *J. Mater. Res.*, 10 [12] 3232–3240 (1995).
- ¹⁰⁹ M.-C. Chu, S.-J. Cho, H.-M. Park, K.-J. Yoon, and H. Ryu, "Crack-healing in reaction-bonded silicon carbide," *Mater. Lett.*, 58 [7–8] 1313–1316 (2004).
- ¹¹⁰ D. Lynch, "Winning the global race for solar silicon," *JOM*, 61 [11] 41–48 (2009).
- ¹¹¹ B. Pieraggi, "Calculations of parabolic reaction rate constants," *Oxid. Met.*, 27 [3] 177–185 (1987).
- ¹¹² C.-R. Chang and J.-H. Jean, "Crystallization Kinetics and Mechanism of Low-Dielectric, Low-Temperature, Cofirable CaO-B₂O₃-SiO₂ Glass-Ceramics," *J. Am. Ceram. Soc.*, 82 [7] 1725–1732 (1999).
- ¹¹³ A. Strachota, M. Černý, Z. Chlup, M. Šlouf, J. Hromádková, J. Pleštil, H. Šandová, P. Glogar, *et al.*, "Optimization of sol-gel/pyrolysis routes to silicon oxycarbide glasses," *J. Non-Cryst. Solids*, 358 [20] 2771–2782 (2012).
- ¹¹⁴ F. Sevim, F. Demir, M. Bilen, and H. Okur, "Kinetic analysis of thermal decomposition of boric acid from thermogravimetric data," *Korean J. Chem. Eng.*, 23 [5] 736–740 (2006).
- ¹¹⁵ M. Boike, K. Hilpert, and F. Müller, "Thermodynamic Activities in B₂O₃-SiO₂ Melts at 1475 K," *J. Am. Ceram. Soc.*, 76 [11] 2809–2812 (1993).
- ¹¹⁶ G. Socrates, *Infrared Characteristic Group Frequencies: Tables and Charts*. Wiley, 1994.
- ¹¹⁷ R. Peña-Alonso and G.D. Sorarù, "Synthesis and characterization of hybrid borosiloxane gels as precursors for Si-B-O-C fibers," *J. Sol-Gel Sci. Technol.*, 43 [3] 313–319 (2007).
- ¹¹⁸ A. Tenney and J. Wong, "Vibrational Spectra of Vapor-Deposited Binary Borosilicate Glasses," *J. Chem. Phys.*, 56 5516–5523 (1972).
- ¹¹⁹ A. Tamayo, R. Peña-Alonso, F. Rubio, J. Rubio, and J.L. Oteo, "Synthesis and characterization of boron silicon oxycarbide glass fibers," *J. Non-Cryst. Solids*, 358 [2] 155–162 (2012).
- ¹²⁰ A.D. Irwin, J.S. Holmgren, T.W. Zerda, and J. Jonas, "Spectroscopic investigations of borosiloxane bond formation in the sol-gel process," *J. Non-Cryst. Solids*, 89 [1–2] 191–205 (1987).
- ¹²¹ G.D. Sorarù, G. D'Andrea, R. Campostrini, F. Babonneau, and G. Mariotto, "Structural Characterization and High-Temperature Behavior of Silicon Oxycarbide Glasses Prepared from Sol-Gel Precursors Containing Si-H Bonds," *J. Am. Ceram. Soc.*, 78 [2] 379–387 (1995).
- ¹²² A. Saha, R. Raj, and D.L. Williamson, "A Model for the Nanodomains in Polymer-Derived SiCO," *J. Am. Ceram. Soc.*, 89 [7] 2188–2195 (2006).
- ¹²³ P. Kroll, "Modeling the 'free carbon' phase in amorphous silicon oxycarbide," *Proc. Int. Conf. Non-Cryst. Mater. CONCIM International Conf. Non-Cryst. Mater. CONCIM*, 351 [12–13] 1121–1126 (2005).

- ¹²⁴ S. Kaur, G. Mera, R. Riedel, and E. Ionescu, "Effect of boron incorporation on the phase composition and high-temperature behavior of polymer-derived silicon carbide," *J. Eur. Ceram. Soc.*, 36 [4] 967–977 (2016).
- ¹²⁵ B. McFarland and E.J. Opila, "Sol-gel derived borosilicate glasses and thin film coatings on SiC substrates: Boron loss and carbon retention due to processing and heat treatment," *J. Non-Cryst. Solids*, 449 59–69 (2016).
- ¹²⁶ A. Bongiorno and A. Pasquarello, "Oxygen Diffusion through the Disordered Oxide Network during Silicon Oxidation," *Phys. Rev. Lett.*, 88 [12] 125901 (2002).
- ¹²⁷ E.J. Opila and J.L. Serra, "Oxidation of Carbon Fiber-Reinforced Silicon Carbide Matrix Composites at Reduced Oxygen Partial Pressures," *J. Am. Ceram. Soc.*, 94 [7] 2185–2192 (2011).
- ¹²⁸ D. Manara, A. Grandjean, and D.R. Neuville, "Advances in understanding the structure of borosilicate glasses: A Raman spectroscopy study," *Am. Mineral.*, 94 [5–6] 777–784 (2009).
- ¹²⁹ A.S. Attar and Z. Hassani, "Fabrication and Growth Mechanism of Single-crystalline Rutile TiO₂ Nanowires by Liquid-phase Deposition Process in a Porous Alumina Template," *J. Mater. Sci. Technol.*, 31 [8] 828–833 (2015).
- ¹³⁰ C. Mille, E.C. Tyrode, and R.W. Corkery, "3D titania photonic crystals replicated from gyroid structures in butterfly wing scales: approaching full band gaps at visible wavelengths," *RSC Adv.*, 3 [9] 3109–3117 (2013).

Appendix

Sol-gel formulation examples

1. Formulation 2 from Table 3: Silica sol-gel

a. Synthesis calculations for a 0.025 mol batch with 90 vol% solvent; Si produced from 95 mol% TEOS and 5 mol% APTES; and 2.7: 1 molar ratio of water catalyst to silane

TEOS: $(0.025 \text{ mol} * 0.95) * 208.33 \text{ g/mol} / 0.933 \text{ g/mL} = 5.3031 \text{ mL}$

APTES: $(0.025 \text{ mol} * 0.05) * 221.37 \text{ g/mol} / 0.946 \text{ g/mL} = 0.2925 \text{ mL}$

200 proof EtOH:

1. $(5.2918 + 0.2925) / 0.1 = \text{total batch volume of } 55.843 \text{ mL}$

2. $55.843 - (5.2918 + 0.2925) = 50.2588 \text{ mL volume of EtOH}$

1 N HCl catalyst: $(2.674 \text{ mol} * 0.025 \text{ mol}) * 18 \text{ g/mol} / 1 \text{ g/mL} = 1.2033 \text{ mL}$

b. Synthesis steps

1. Mix together 5.3031 mL TEOS with 25.1294 mL 200 proof EtOH (half the total volume of EtOH) on a magnetic stir plate/ hot plate at room temperature.
2. Add 1.2033 mL 1N HCl catalyst to the TEOS/ EtOH mixture
3. Let TEOS hydrolyze for 4 h
4. Add remaining EtOH and 0.2925 mL APTES
5. Stir 5 minutes longer
6. Pipette ~ 15 mL of sol into a 16 mL short-style shell vial and immerse lanyards secured with a thin gold-coated Cu wire suspended from caps
 - a. Coat lanyards under vacuum
 - b. Dry for ≥ 1 week then convert to glass by heat treatment
7. Pipette 7 mL of sol into polyethylene molds, cap, and leave to gel overnight and dry in the hood for 1 week.
 - a. Follow convection oven drying procedure: 48 h at 40°C, 24 – 48 h at 50 – 60°C, 24 – 48 h back down to 40°C
 - b. Then heat treat in Ar/ H₂ atmosphere in the HTF with a max heat treatment temperature of 1000°C held for 4 h

2. Formulation 10 from Table 3: TMBX Borosilicate sol-gel with a nominal concentration of 60 mol% Boria and 40 mol% Silica

a. Synthesis calculations for a sol formulated at 95 vol% solvent; Si produced from 75 mol% TEOS and 25 mol% APTES; and 1.5: 1 molar ratio of water catalyst to TEOS

TEOS: $(0.02 \text{ mol} * 0.75) * 208.33 \text{ g/mol} / 0.933 \text{ g/mL} = 3.3494 \text{ mL}$

APTES: $(0.02 \text{ mol} * 0.25) * 221.37 \text{ g/mol} / 0.946 \text{ g/mL} = 1.17003 \text{ mL}$

TMBX: $(0.02 \text{ mol} / 1.00145) * 173.53 \text{ g/mol} / 1.195 \text{ g/mL} = 2.9001 \text{ mL}$

Check calculations:

Mol Si from TEOS: $[(3.3494 \text{ mL} * 0.933 \text{ g/mL}) * (28.0855 \text{ g/mol Si} / 208.33 \text{ g/mol TEOS})] / 28.0855 \text{ g/mol} = 0.015 \text{ mol Si}$

Mol Si from APTES: $[(1.17003 \text{ mL} * 0.946 \text{ g/mL}) * (28.0855 \text{ g/mol Si} / 221.37 \text{ g/mol TEOS})] / 28.0855 \text{ g/mol} = 0.005 \text{ mol Si}$

Total mol Si = 0.02 = mol SiO₂ (1 mol Si = 1 mol SiO₂)

Mol B₂O₃ from TMBX: $[(2.9001 \text{ mL} * 1.195 \text{ g/mL}) * ((3 * 10.811 \text{ g/mol B}) / 173.53 \text{ g/mol TMBX})] / 10.811 \text{ g/mol} = 0.05991 \text{ mol B} = 0.02996 \text{ mol B}_2\text{O}_3$ (1 mol B = 0.5 mol B₂O₃)

Mol% B₂O₃: $100 * [(0.02996 \text{ mol B}_2\text{O}_3) / (0.02996 \text{ mol B}_2\text{O}_3 + 0.02 \text{ mol SiO}_2)] = \mathbf{60\%}$

200 proof EtOH:

1. $(3.3422 + 1.17003 + 2.9001) / 0.05 = \text{total batch volume of } 148.2457 \text{ mL}$

2. $148.2457 - (5.2918 + 0.2925 + 2.9001) = 140.8334 \text{ mL volume of EtOH}$

3 N HCl catalyst: $(1.5 \text{ mol} * 0.02 \text{ mol}) * [(18 \text{ g/mol}) / 1 \text{ g/mL}] = 0.54 \text{ mL}$

b. Synthesis steps

1. Start heating up a water bath
2. Mix together 3.3422 mL TEOS with 70.4167 mL 200 proof EtOH (half the total volume of EtOH) on a magnetic stir plate/ hot plate
3. Add 0.54 mL 3 N HCl catalyst to the TEOS/ EtOH mixture
4. Heat up batch to 40°C
5. Let TEOS hydrolyze for 16 – 24 h
6. Add TMBX and remaining half of EtOH. Heat up batch to 60°C and stir for 24h
7. Turn off heat and add 1.17003 mL APTES
8. Stir 5 minutes longer
9. Pipette ~ 15 mL of sol into a 16 mL short-style shell vial and immerse CVD-SiC or Si coupons secured with a thin gold-coated Cu wire suspended from caps
10. Let coated CVD-SiC or Si coupons dry for 5 min, dip-coat again, dry for 5 min, and dip-coat 3rd time
11. Dry \geq 1 week in ambient lab conditions then convert to glass by heat treatment

3. Formulation 12 from Table 3: Boria Borosilicate sol-gel with a nominal concentration of 60 mol% Boria and 40 mol% Silica

a. Synthesis calculations for a sol formulated at 90 – 95 vol% solvent; Si produced from 75 mol% TEOS and 25 mol% APTES; and 1.5: 1 molar ratio of water catalyst to TEOS

Boria: $(0.1 \text{ mol} * 0.6) * 69.62 \text{ g/mol} = 4.1772 \text{ g}$ to weigh out

$4.1772 \text{ g} / 2.46 \text{ g/mL} = 1.69805 \text{ mL}$ for EtOH calculations

Silica: $(0.1 \text{ mol} * 0.4) = 0.04 \text{ mol SiO}_2 = 0.04 \text{ mol Si}$

TEOS: $(0.04 * 0.75) * 208.33 \text{ g/mol} / 0.933 \text{ g/mL} = 6.6987 \text{ mL}$

APTES: $(0.04 \text{ mol} * 0.25) * 221.37 \text{ g/mol} / 0.946 \text{ g/mL} = 2.34006 \text{ mL}$

200 proof EtOH: Split up batch into 90 vol% reactants diluted with 90 vol% EtOH and 10 vol% of reactants diluted with 95 vol% EtOH

90 vol% EtOH:

1. $(1.69805+6.6987+2.34006) * 0.9 = 9.6631 \text{ mL}$
2. $9.6631 \text{ mL} / 0.1 = \text{total batch volume of } 96.6313 \text{ mL}$
3. $96.6313 - 9.6631 = 86.9682 \text{ mL volume of EtOH}$

95 vol% EtOH:

1. $(1.69805+6.6987+2.34006) * 0.1 = 1.0737 \text{ mL}$
2. $1.0737 \text{ mL} / 0.05 = \text{total batch volume of } 21.4736 \text{ mL}$
3. $21.4736 - 1.0737 = 20.39994 \text{ mL volume of EtOH}$

Total EtOH volume: $86.9682 + 20.39994 = 107.3681 \text{ mL}$

3 N HCl catalyst: $(1.5 \text{ mol} * 0.03 \text{ mol}) * [(18 \text{ g/mol}) / 1 \text{ g/mL}] = 0.81 \text{ mL}$

b. Synthesis steps

1. Start heating up a water bath
2. Mix together 6.6987 mL TEOS with 53.6841 mL 200 proof EtOH on a magnetic stir plate/ hot plate
3. Add 0.81 mL 1N HCl catalyst to the TEOS/ EtOH mixture
4. Heat up batch to 60°C
5. Let TEOS hydrolyze for 24 h
6. Add TMBX and 36.947 mL EtOH. Stir for 24h at 60°C
7. Turn off heat and add 2.34006 mL APTES
8. Stir 5 minutes longer
9. Remove 10 mL of sol and dilute to 95 vol% EtOH
 - a. $[(10 \text{ mL} * 0.1) / 0.05] - [10 \text{ mL} * 0.9] = 11 \text{ mL EtOH}$ to add to 10 mL of sol
8. Pipette ~ 15 mL of 90 vol% EtOH sol into a 16 mL short-style shell vial and immerse lanyards secured with a thin gold-coated Cu wire suspended from caps
 - a. Coat lanyards under vacuum
10. Pipette 7 mL of sol into polyethylene molds, cap, and leave to gel overnight and dry in the hood for 1 week
 - a. Follow convection oven drying procedure then heat treat in Ar/ H₂ atmosphere in the HTF with a max heat treatment temperature of 550°C held for 4 h

11. Pipette ~ 15 mL of 95 vol% EtOH sol into a 16 mL short-style shell vial and immerse CVD-SiC coupons secured with a thin gold-coated Cu wire suspended from caps
12. Let coated CVD-SiC coupon dry for 5 min, dip-coat again, dry for 5 min, and dip-coat 3rd time
13. Dry lanyards and coupons for ≥ 1 week in ambient lab conditions then convert to glass by heat treatment in the HTF with a max heat treatment temperature of 550°C held for 4 h

4. Formulation 13 from Table 3: Boria sol-gel with a nominal concentration of 96.4 mol% Boria and 3.6 mol% Silica

a. Synthesis calculations for a sol formulated at 70 vol% solvent; Si produced from 75 mol% TEOS and 25 mol% APTES; and 1.5: 1 molar ratio of water catalyst to TEOS

b. TMBX calculations starting with 96.4 mol% B₂O₃

1. 0.1 mol * 0.964 = 0.0964 mol B₂O₃
2. g B₂O₃: 0.0964 mol * 69.9622 g/mol = 6.71156 g
3. g B in 6.71156 g B₂O₃: $6.71156 \text{ g} * \left(\frac{2 * 10.811 \text{ g/mol}}{69.622 \text{ g/mol}} \right) = 6.71156 \text{ g} * 0.31056 = 2.0843 \text{ g}$
4. mol B in 2.0843 g B: 2.0843 g / 10.811 g/ mol = 0.19279 mol B
5. every mol B = 0.5 mol B₂O₃; therefore, 0.0964 / 0.19279 mol = 0.5
6. Calculate mL TMBX to get 0.19279 mol B in the glass; note there are 3 B in one molecule of TMBX
7. First, calculate g TMBX: 0.19279 mol B * 10.811 g/ mol = 2.0843 g B
8. Next, calculate g TMBX from 2.0843 g B using 3 B per TMBX molecule:

$$2.0843 \text{ g B} \div \frac{3 * 10.811 \text{ g/mol}}{173.53 \text{ g/mol}} = 2.0843 \div 0.1869 = 11.1517 \text{ g TMBX}$$

9. Then, calculate mL TMBX: 11.1517 g / 1.195 g/mL = 9.3312 mL TMBX

c. Silane calculations starting with 3.6 mol% SiO₂ (showing 1 mol SiO₂ = 1 mol Si)

1. 0.1 mol * 0.036 = 0.0036 mol SiO₂
2. g SiO₂: 0.0036 mol SiO₂ * 60.0855 g/ mol = 0.2163 g SiO₂
3. Calculate g Si in 0.2163 g SiO₂:

$$0.2163 \text{ g SiO}_2 * \frac{28.0855 \text{ g/mol}}{60.0855 \text{ g/mol}} = 0.2163 * 0.467426 = 0.1011 \text{ g Si}$$

4. Convert g Si to mol Si: 0.1011 g / 28.0855 g/ mol = 0.0036 mol Si (equal to mol SiO₂)

d. Calculate mL TEOS from 75 mol% Si as follows:

1. 0.0036 mol Si * 0.75 = 0.0027 mol Si from TEOS
2. mL TEOS: 0.0027 mol * 208.33 g/ mol = 0.5625 g TEOS / 0.933 g/ mL = 0.6029 mL TEOS

e. Calculate mL APTES from 25 mol% Si as follows:

1. 0.0036 mol Si * 0.25 = 0.0009 mol Si from APTES
2. mL APTES: 0.0009 mol * 221.37 g/mol = 0.19923 g APTES / 0.946 g/ mL = 0.2106 mL APTES

f. Calculate 70 vol% 200 proof EtOH as follows:

1. Add up mL precursors: 9.3312 + 0.6029 + 0.2106 = 10.1447 mL
2. Calculate total batch volume (divide by 100 – 70 vol% = 30 vol%):
10.1447 mL / 0.3 = 33.8157 mL

3. Calculate mL EtOH: 33.8157 mL – 10.1447 mL = 23.701 mL EtOH

g. Calculate 1 N HCl catalyst assuming a 1.5: 1 mol ratio of H₂O: TEOS as follows:

$$1.5 \text{ mol} * 0.0027 \text{ mol TEOS} = 0.00405 \text{ mol H}_2\text{O} * 18 \text{ g/ mol} = 0.0729 \text{ mL H}_2\text{O}$$

h. Make 1 N HCl fresh prior to synthesis: mix 0.8211 mL 37% HCl with 9.1789 mL H₂O

Check calculations:

Mol Si from TEOS: $[(0.603 \text{ mL} \cdot 0.933 \text{ g/mL}) \cdot (28.0855 \text{ g/mol Si} / 208.33 \text{ g/mol TEOS})] / 28.0855 \text{ g/mol} = 0.0027 \text{ mol Si}$

Mol Si from APTES: $[(0.211 \text{ mL} \cdot 0.946 \text{ g/mL}) \cdot (28.0855 \text{ g/mol Si} / 221.37 \text{ g/mol TEOS})] / 28.0855 \text{ g/mol} = 0.000953 \text{ mol Si}$

Total mol Si = 0.003653 = mol SiO₂ (1 mol Si = 1 mol SiO₂)

Mol B₂O₃ from TMBX: $[(9.331 \text{ mL} \cdot 1.195 \text{ g/mL}) \cdot (3 \cdot 10.811 \text{ g/mol B}) / 173.53 \text{ g/mol TMBX}] / 10.811 \text{ g/mol} = 0.19277 \text{ mol B} = 0.096385 \text{ mol B}_2\text{O}_3$ (1 mol B = 0.5 mol B₂O₃)

Mol% B₂O₃: $100 \cdot [(0.096385 \text{ mol B}_2\text{O}_3) / (0.096385 \text{ mol B}_2\text{O}_3 + 0.003653 \text{ mol SiO}_2)] =$
96.3%

b. Synthesis steps

1. Start heating up a water bath
2. Make 1 N HCl water catalyst
3. Mix together 0.603 mL TEOS with 23.701 mL 200 proof EtOH on a magnetic stir plate/ hot plate
4. Add 0.073 mL 1N HCl catalyst to the TEOS/ EtOH mixture
5. Heat up batch to 40°C
6. Let TEOS hydrolyze for 4 h while batch is heating up to 40°C (~ 1 h)
7. Add 9.3312 mL TMBX. Stir for another 4 h at 40°C
8. Turn off heat and remove water bath
9. Add 0.211 mL APTES
10. Stir 5 minutes longer
11. Pipette ~ 15 mL of sol into a 16 mL short-style shell vial and immerse CVD-SiC coupons secured with a thin gold-coated Cu wire suspended from caps
12. Let coated CVD-SiC coupon dry for 5 min, dip-coat again, dry for 5 min, and dip-coat a total of seven times with ~ 5 min dry times in between dip coats
13. Dry coupons overnight in desiccator.
14. Heat treat in 95 vol% Ar/ 5 vol% H₂ gas in a horizontal tube furnace with a max heat treatment temperature of 400°C.
15. Store in desiccator until oxidation tests are to commence.
16. Heat treat a second time right before oxidation testing as follows:
 - a. Weigh coated coupon
 - b. Suspend in TGA and raise furnace at room temperature so that coupon is located in the furnace hot zone
 - c. Flush the TGA gas lines with 95 vol% Ar/ 5 vol% H₂ gas
 - d. Turn on data acquisition and heat furnace to 500°C
 - e. The weight drops quickly during first 10 – 15 min of heat treatment, then weight change levels off ~ 1 h exposure at 500°C
 - f. Lower furnace and turn it off letting coupon cool, then reweigh